UNIVERSITÀ DEGLI STUDI DI MILANO

FACOLTÀ DI SCIENZE E TECNOLOGIE

Ph.D. school in Physics, Astrophysics and Applied Physics,
Cycle XXXIII

Exploring the origin of substructures in planet forming discs

The role of protoplanets and gravitational instabilities

Disciplinary Scientfic Sector FIS/05

Supervisor of the Ph.D Thesis:
Prof. Giuseppe Lodato

Ph.D. Thesis of:
Benedetta Maria Augusta Veronesi

Director of the School:
Prof. Matteo Paris

Anno Accademico 2019-2020

Referees:
Dr. Leonardo Testi
Dr. Carlo Manara

Examiners:
Prof. Phil Armitage
Prof. Richard Alexander
Prof. Giuseppe Lodato

Final examination:

Date 30 April 2021

Università degli Studi di Milano, Dipartimento di Fisica, Milano, Italy

Codice PACS: 98.62.-g, 96.35.-j

The cover has been designed and produced by Benedetta Maria Augusta Veronesi (with the help of Cristiano Longarini), as well as the photographies included in this thesis.

Contents

Preface

Star trails under the sky of Nevada (2018)

Let the adventure begin...

A zoo of disc substructures

Motivation

Since the beginning of humanity, we have always pushed our gaze to the depths of the Universe, trying to perceive the mysteries enclosed within it. Ironically, today finding a sky like the one shown in Fig. 1 is increasingly difficult, due to the light pollution that now characterizes our cities. Nonetheless, there are still some places on Earth where a view like that is possible, and where the atmospheric conditions necessary for (radio-)telescopes do exist. One of these location can be found in the Altiplano de Chajnantor, a plateau at an altitude of 5000 meters, in the Chilean Atacama desert. Here, the Atacama Large Millimeter Array-ALMA has been developed, and from 2015 it is now collecting amazing and breakthrough images of a wide range of astronomical objects at an incredibly high resolution and high sensitivity. Those that will be of interest in this Thesis are protoplanetary discs. These systems are the cradle where planet formation takes place, and studying them allows us to understand how the Solar System was formed. In particular, we know that protoplanetary discs are accretion disc that forms during the star formation process. There are two main actors in this game. The first one is the gas, which dominates the disc dynamic, and the second one is the dust, which dominates the opacity budget and mainly determines the thermal structure of the disc. Typically, micron-sized dust grains follow the same distribution of the gas, and they are observed with various instruments including SPHERE, an instrument mounted on the Very Large Telescope. Instead, the millimeter grains, whose distribution is detected by ALMA, settle towards the midplane and tend to drift radially and to concentrate into the local pressure maxima of the gas. With ALMA we are also able to investigate the gas kinematics, by looking for the CO molecular line emission. But what was there before ALMA and SPHERE? On the millimetre side, we could count on the Submillimeter Array (SMA), the Plateau de

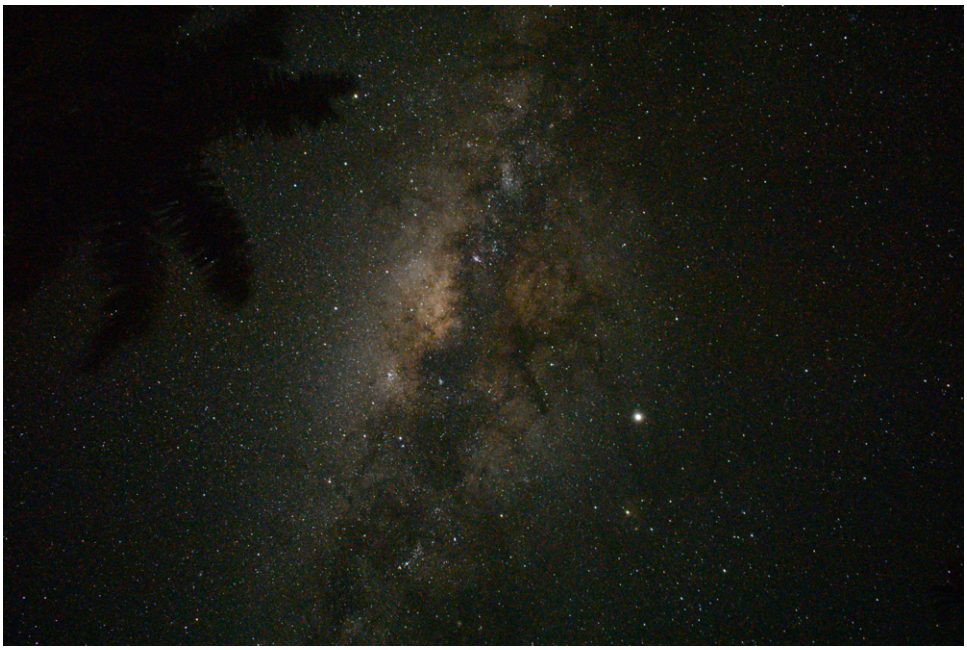

Figure 1: The Milky Way as observed from Cardwell (Australia, 2019).

Bure Interferometer (PdBI) and the Combined Array for Research in Millimeter-wave Astronomy (CARMA), while on the near-infrared side the first one able to detect protoplanetary discs has been the Hubble Space Telescope (HST), followed by the Subaru telescope (with the project SEEDS) and NaCo (NAos-COnica, Lenzen et al. 2003) at the Very Large Telescope (VLT). To have an idea of the incredible progress that has been reached from an observational point of view, we can compare some of the first images collected by the HST in Fig. 2 and the ones from ALMA and SPHERE in Fig. 3. While in the first ones we can barely see the edge-on silhouette of the disc around the protostars, in the second ones we are able to detect a wide zoo of substructures inside the discs, going from small asymmetries to grand design spirals, from rings and gaps to cavities. Another impressive example could be given with the HL Tau protoplanetary disc. In Fig. 4 are collected images of this system obtained from 1994 to 2015, with different instruments and telescopes and with increasing resolution: from a "blobby" disc to a well resolved source, showing very narrow rings and gaps.

But these images by themselves cannot disclose all their potential and cannot tell us the whole story of planet formation. In order to really unlock the puzzle, it is of paramount importance to develop theories starting from the observed images. Today, this is increasingly possible thanks to the development of more powerful and complete codes (e.g. hydrodynamics codes such as PHANTOM - Price et al. 2018b - and FARGO - Benítez-Llambay & Masset 2016, and radiative transfer codes such as RADMC-3D - Dullemond et al. 2012, MCFOST - Pinte et al. 2006, 2009, and many others), in which the physical processes at play in protoplanetary discs are treated with a better level of precision. The combination of observations and theoretical studies is starting to give us constraints on the planet formation and

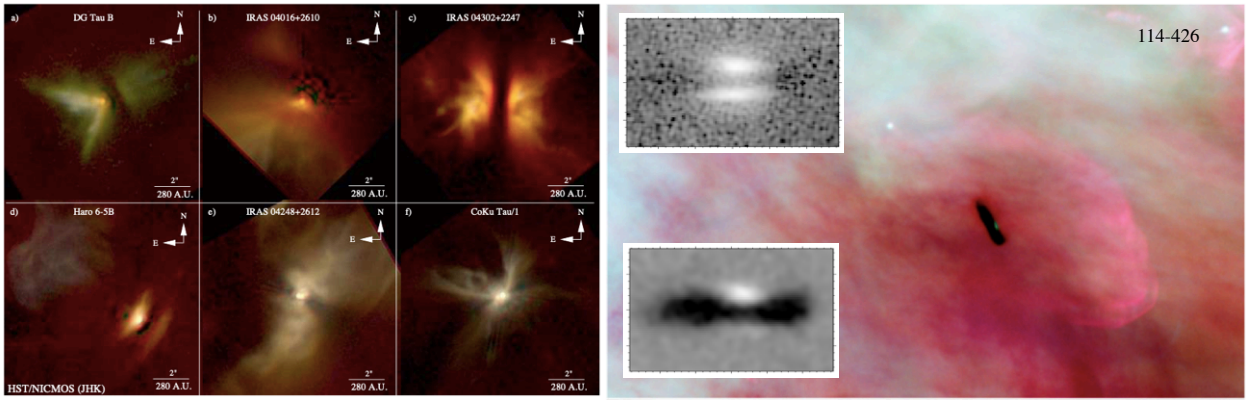

Figure 2: Left: HST/NICMOS edge-on images of Taurus young stellar objects (Padgett et al. 1999). Right: HST/ACS and HST/NICMOS images of the 114-426 protoplanetary disc in its environment (McCaughrean et al. 1998; Miotello et al. 2012).

evolution in a completely different perspective and in a way that was unthinkable only five years ago, when ALMA opened its eyes for the first time.

Going a bit more in detail, we can fast-track the history of the study of planetary formation, where the first theories saw the light in the 17/18th century, with the so called "nebula hypothesis", developed by Emanuel Swedenborg, then refined by Kant (1755) and later by Laplace (1796). This theory states that the formation of stars is the result of the collapse of a primordial nebula. After the collapse phase, a gaseous and dusty protoplanetary disc remains, orbiting around the young star. They also proposed that planets could be born and have grown in these protoplanetary discs.

This idea of a flattened, rotating structure as the origin of the observed coplanar planetary orbits in the Solar System was then physically motivated by Hoyle (1960), who described the disc formation process as the natural outcome of gravitational collapse of a rotating molecular cloud core. One of the key points of this theory is that the dynamic evolution of the collapse is linked to the conservation of angular momentum. Thus, during this initial stage, we see the formation of an accretion disc. It is important to highlight that the disc properties are directly related to the angular momentum content of the molecular cloud core within which the star forms. For this reason, the study of protostellar discs has to be directly connected with the study of its natal environment. These first theories have been confirmed by the discoveries of the first protoplanetary discs observed around protostars in the Orion Nebula (see Fig. 2).

Moreover, in 1995, Mayor & Queloz (1995) detected the first exoplanet around a main sequence star (51 Peg), and for this discovery they were awarded a Nobel Price in Physics in 2019. Since then, thousands of exoplanets have been detected with different methods, reaching the number of ∼4000 at the end of 2020. This sample of planets shows a huge variety of properties, going from hot Jupiters (massive planets orbiting around their host star) to super-Earths (planets with a mass in the range of 2-10 $M_{\oplus}$), from planets orbiting around one star, to bina-

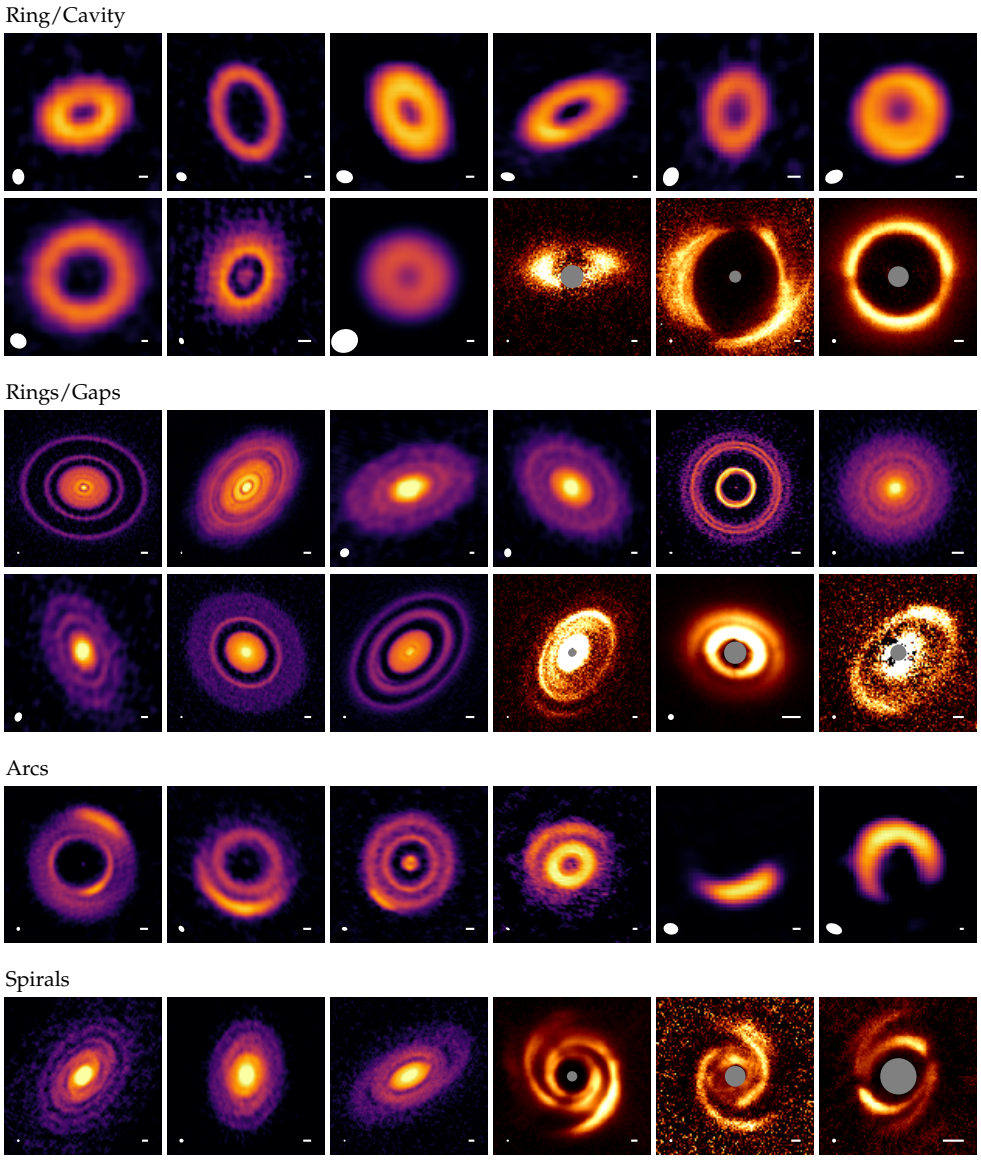

Figure 3: An example of the wide zoo of disc substructure morphologies, as collected in the continuum and in scattered light. White ellipses indicate resolutions. It is important to note that the spatial scale of these images differs from those showed in Fig. 2, and it is indicated by the white scalebar of 10 au in the lower right corners. Image taken from Andrews (2020).

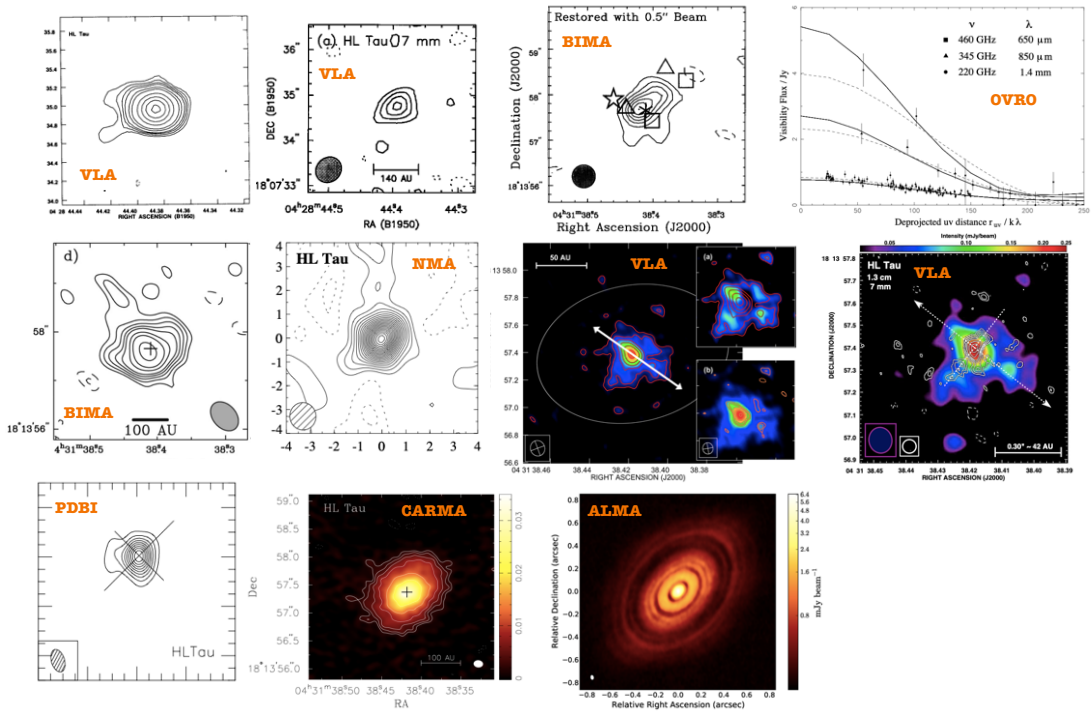

Figure 4: An overview of observations of HL Tau (first discoverd by Sargent & Beckwith 1987)taken with different telescopes and instruments, from 1994 with the VLA to 2015 with ALMA. From left to right, and from top to bottom: Rodriguez et al. (1994); Wilner et al. (1996); Mundy et al. (1996); Lay et al. (1997); Looney et al. (2000); Kitamura et al. (2002); Greaves et al. (2008); Carrasco-González et al. (2009); Guilloteau et al. (2011); Kwon et al. (2011); ALMA Partnership et al. (2015a).

ries. One of the main question related to the properties of this new population of discovered exoplanets was if our Solar System is an outsider (Winn & Fabrycky 2015; Morbidelli & Raymond 2016). The answer is that, in order to deeply understand the exoplanets population and its characteristics, one should also study the natal environment of these planets, looking in particular at the composition, the evolution and the interaction between all the main actors playing a role.

This evolution and interaction can be understood through the study of the substructures observed in a wide sample of discs. Indeed, while at the first dawn of ALMA we were able to collect just few images of protoplanetary discs, we are now beginning to explore star formation regions through more complete surveys, such as the DSHARP one (Andrews et al. 2018b), the survey of the population of discs in the Taurus (Long et al. 2018b, 2019) and in the Lupus (Ansdell et al. 2016) star-forming region, among those carried out with ALMA and many other obtained with several instruments (e.g., with X-shooter, Manara et al. 2020). It is important to highlight that between all the observed systems, substructures are detected in a large number of them (if not all), at different evolutive stages (from Class I to debris disc, see e.g., Fig. 3). At near-IR and mm wavelengths, a small selection comprises spirals (e.g., Muto et al. 2012a; Pérez et al. 2016; Benisty et al.

2017; Rosotti et al. 2019a), rings and gaps (e.g., ALMA Partnership et al. 2015a; Andrews et al. 2016; Fedele et al. 2018; Pérez et al. 2019), horseshoes and arcs (e.g., van der Marel et al. 2013, 2016a; Cazzoletti et al. 2018), and shadows (e.g., Marino et al. 2015; Stolker et al. 2016; Benisty et al. 2018; Casassus et al. 2018; Muro-Arena et al. 2020a), where some systems display many of these features at the same time. Nowadays, the origin of the sub-structures around pre main sequence stars has multiple explanations: planetary or sub-stellar companions orbiting around the central star (e.g. Paardekooper & Mellema 2004; Ataiee et al. 2013; Jin et al. 2016; Ragusa et al. 2017; Dipierro et al. 2018a; Price et al. 2018b; Liu et al. 2018b; Zhang et al. 2018), fly-bys (e.g. Cuello et al. 2019, 2020), dust growth near the snow lines (e.g., Ros & Johansen 2013; Okuzumi et al. 2016; Stammler et al. 2017; van der Marel et al. 2018b), or variable illumination (Montesinos et al. 2016; Montesinos & Cuello 2018) due to disc self-shadowing. Some of them can be also explained through dead zones and vortices (Pinilla et al. 2016; Cazzoletti et al. 2018) and some others could be due to a disc misalignment between the inner and outer regions (e.g., Facchini et al. 2018a; Nealon et al. 2019, 2020b). Last, but not less important, there are also disc instabilities (e.g., Regály et al. 2012; Kratter & Lodato 2016) and chemical processes, such as photoevaporation (e.g., Alexander et al. 2014) or MHD winds (e.g., Riols & Lesur 2019; Riols et al. 2020), that can be counted as the origin of the observed structures. Curiously, it should be noted that these structures seem to be present ubiquitously in protoplanetary discs. This could be a sign that we are observing planet hosting rather than planet forming disc. The idea is that protoplanets could start to form earlier, when discs are more massive and are still accreting material from the molecular cloud core (e.g., Greaves & Rice 2010; Manara et al. 2018; Segura-Cox et al. 2020; Tychoniec et al. 2020). Nevertheless, this is based on surveying the brightest discs in the stellar vicinity, while the fainter ones are often less studied, and when resolved they do not present large sub-structures (see e.g., Long et al. 2019).

However, the origin of such substructures is still very debated, in particular it is not clear how their morphological features depend on the composition, the disc mass and on the coupling between the gas and the dust component of the disc. A way to disentangle the knots that still exist, is to look at these systems at multiple wavelengths, and with different instruments, to capture all the possible information that would otherwise remain hidden. As an example, a protoplanetary disc which has been deeply "dug" is PDS 70 (see Fig. 5), where the combination of images of the micrometric and millimetric dust, of the gas, and of two planets (PDS 70 b, Keppler et al. 2018 - PDS 70 c, Haffert et al. 2019) detected inside a gap by SPHERE and MUSE (H-α emission) has allowed astronomers to confirm some of the above mentioned theories.

Another nice example of what different wavelengths could tell us is the one of HL Tau. Fig. 6 collects images of this system at different wavelengths, showing in particular that for an increasing dust grain size (since $\lambda \propto 2\pi a$, where a is the dust grain size), the radial extent of the disc decreases. This is a proof of the dynamical process of radial drift (Weidenschilling 1977, see Chapter 2). Moreover, not only the radial extent of the disc changes, but also the width of the gaps/rings, and this can be a sign of dust trapping and grain growth.

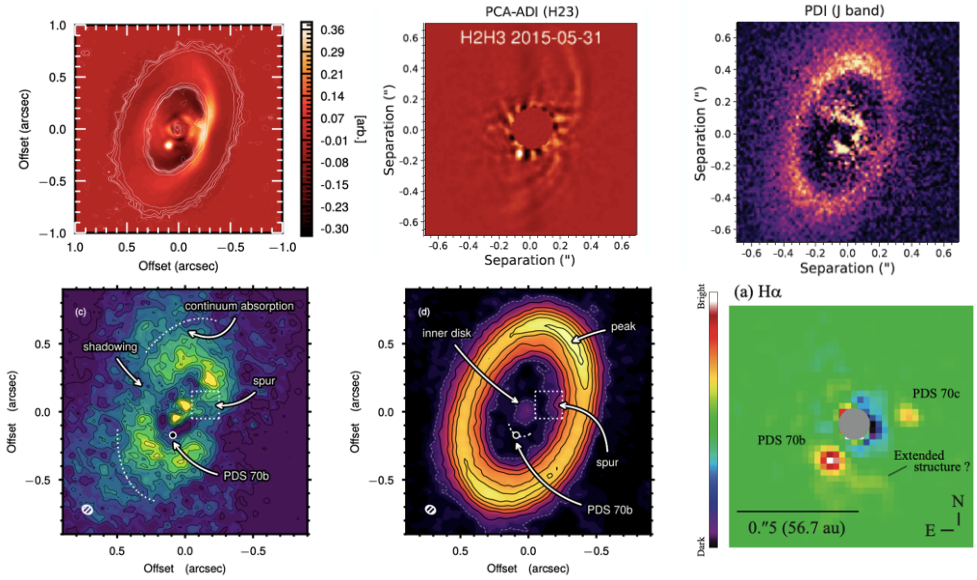

Figure 5: The protoplanetary disc orbiting around PDS 70 observed at different wavelengths and with different instruments. From left to right, and from top to bottom: IRDIS from Müller et al. (2018), IRDIS H2H3-band from Keppler et al. (2018), SPHERE PDI observations from Keppler et al. (2018), ALMA ^{12}CO observation from Keppler et al. (2019), ALMA continuum image from Keppler et al. (2019), Hα observations with VLT/MUSE from Hashimoto et al. (2020),

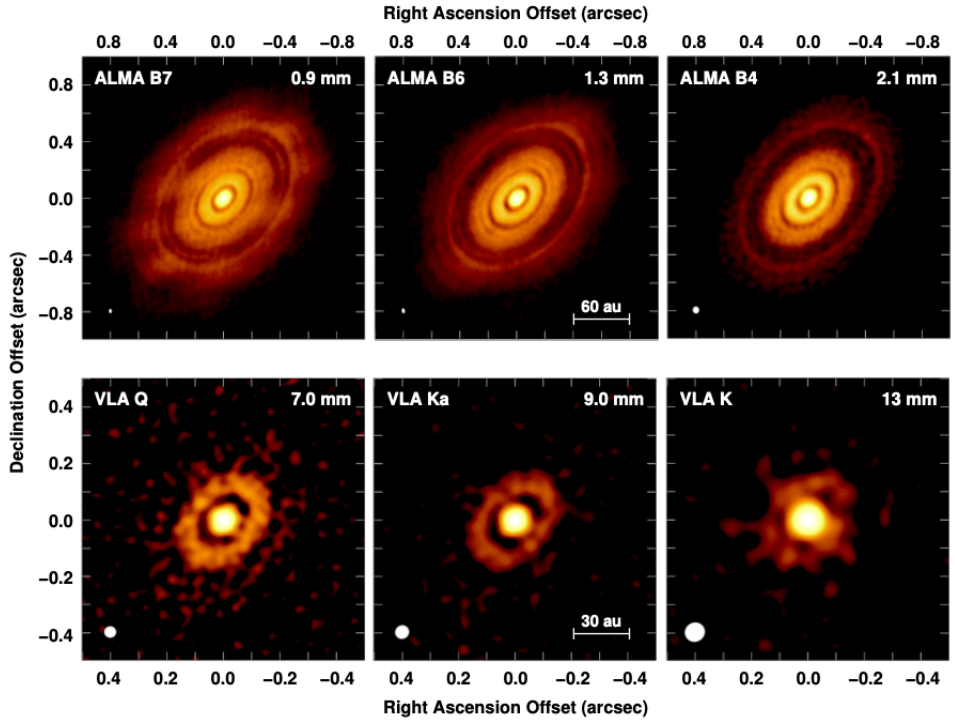

Figure 6: The protoplanetary disc orbiting around HL Tau observed at different wavelengths with ALMA and VLA (Carrasco-González et al. 2019).

Together with high resolution images, in the last two years we have also learnt how to extract from them more and more information by combining different diagnostics. An illustrative case is given by the protoplanetary disc HD 97048 (Pinte et al. 2019). This system presents one gap between two bright rings. A plausible explanation to this structure is that the gap has been carved by an embedded planet (e.g Dipierro et al. 2015a; Rosotti et al. 2016; Bae et al. 2017; Dong & Fung 2017a; Dipierro et al. 2018a). With this assumption, the morphologies of gaps could be related with the mass of the carving planet (Kanagawa et al. 2015; Dong & Fung 2017a; Dipierro & Laibe 2017; Lodato et al. 2019; Auddy & Lin 2020), but some uncertainties remain. In particular, depending on the gas viscosity and on the grain density one could find different planet masses given the same gap width (Facchini et al. 2018b; Pinte et al. 2019). Recent studies (Pinte et al. 2018b; Teague et al. 2018; Pinte et al. 2019; Casassus & Pérez 2019; Pinte et al. 2020) inferred the location and mass of some planets from the gas kinematics of the discs they were embedded in. Specifically, these studies search in different ways for velocity deviations (localised in both space and velocity) from the unperturbed Keplerian flow of the disc, induced by the presence of a planet, known as "kinks" and "Doppler flips". These studies revealed giant planets in HD 163216 and HD 97048 (see Fig. 7). In this second case, the interesting fact is that the planet inferred from the gas kinematics coincides with the gap observed in the continuum, further confirming the theory that gaps can be the signature of embedded protoplanets.

Just by looking at these few examples, we can understand why the study of this variety of disc morphologies (see Chapter 5) is crucial to connect the perturbed dust and gas surface density with the presence of a companion or with some other physical processes which are ongoing in the system. In this framework, a disc instability which plays an important role is generated by self-gravity, particularly during the first phases of the disc lifetime, when the disc is still accreting material from the parental cloud. At this stage, the disc could be massive enough that its contribution to the gravitational potential of the system cannot be neglected with respect to the star contribution. In these conditions, the disc could develop gravitational instabilities (GI) and the propagation of density waves leads to the formation of prominent structures in the form of one or more spiral arms. These morphologies have been detected by ALMA and VLT-SPHERE in both Class 0/I and Class II systems, and they are usually assumed to be originated by embedded companions (e.g. HD 135344B, Dong et al. 2015b; Veronesi et al. 2019, MWC 758, Calcino et al. 2020), by an external body via a fly-by (e.g. Cuello et al. 2019), or by self-gravity (e.g. Elias 2-27, Pérez et al. 2016; Huang et al. 2018b). Investigating whether some discs can be self-gravitating is important. In fact, some studies (Rice et al. 2004; Rice et al. 2006b; Clarke & Lodato 2009) have shown that GI spirals can trap dust and solid cores can form rapidly at their location. This could be crucial in the planetesimal formation process.

Given the complexity of the systems considered, and thus the incredible amount of information that can be extracted from just one observation, the only way we can unravel the mystery of planet formation is through the cooperation between theory and observations. Hydrodynamical simulations including gas and dust

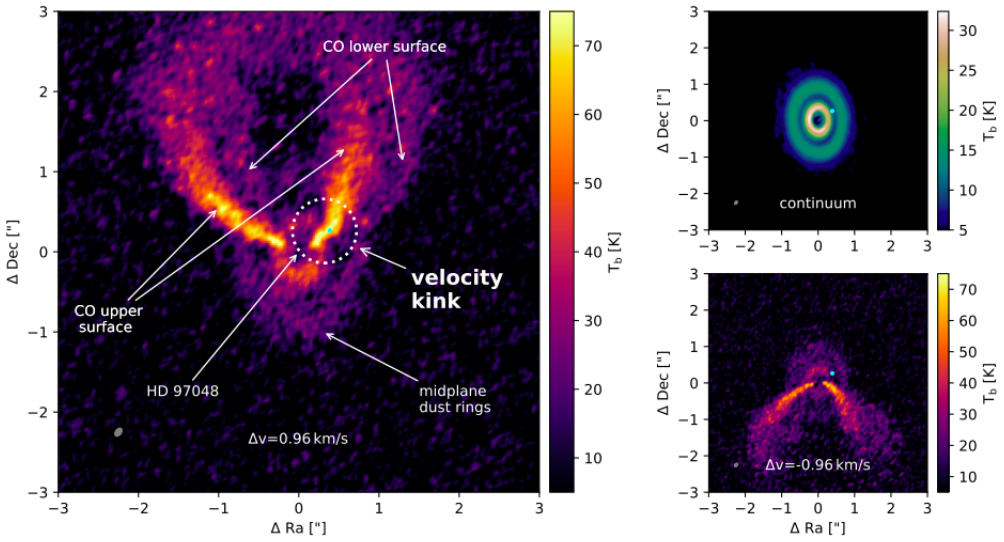

Figure 7: ALMA observations of the dust and gas disc surrounding HD 97048. Left panel: ^{13}CO 3-2 emission showing the velocity perturbation (i.e. kink). The velocity kink is connected to the presence of an embedded protoplanet, which is marked in the picture with a cyan dot. The upper right panel shows the dust continuum, where the planet has been marked and it appears to be located in the continuum gap. Lower right panel: ^{13}CO 3-2 emission at the opposite velocity with respect to the kink one: no velocity deviation is detected here. Image taken from (Pinte et al. 2019).

with one or more embedded stellar/substellar companions are needed to constrain the properties of these objects and to determine the origin of the substructures. Finally, in order to explain the origin and evolution of the studied systems, it is also important to accurately implement in our codes the physical mechanisms that regulate the planet formation process, focusing in particular on the disc evolution. It is only by considering the full picture of what we already know that, thanks to the development of increasingly powerful codes and telescopes, we will be able to answer the questions that still remain unanswered, and which I will try to cover in this Thesis.

Thesis outline

In light of recent breakthrough observational results, this Thesis work is aimed at linking the observed disc substructures with some of the open questions in the planet formation field. This has been done by investigating numerically and analytically some of the phenomena occuring in protoplanetary discs. In particular, I focused on the study of the dust and gas interaction within a disc with an embedded planet. A second topic of this work is related to the study of one of the primordial planet formation phases, when discs were self-gravitating.

This work is focused at reproducing and understanding the observational prediction of two classes of discs: discs hosting planets and gravitationally unstable

discs. For each of these models, we investigate the spatial distribution of gas and dust and analyze the observational predictions for different wavelengths in order to verify if recent high resolution observations can be interpreted according to these models. I study the dynamics of gas and dust with Smoothed Particle Hydrodynamics (SPH)-based (Price et al. 2018a) simulations adopting the previously mentioned models. Moreover, given the crucial role of the observational signatures of protoplanetary discs, Monte Carlo radiative transfer simulations have been performed (with RADMC-3D, Dullemond et al. 2012; and MCFOST, Pinte et al. 2006, 2009) to compute the expected emission of disc models. Finally, in order to compare the numerical results with observational results, I simulate realistic observations for some of the obtained disc models. In the last project collected in this Thesis, I have also performed analytical computations in order to fit velocity data with a disc rotation curve model and get constraints for what concern the disc mass.

This thesis is organized in 3 parts as follows:

Part I provides an introduction to the research theme of this Thesis, focusing on the theoretical and observational essentials of protoplanetary discs. The aim of this part is to give a background of the theoretical and observational investigations developed in this Thesis. **Chapter 1** describes the general framework behind the planet formation process. **Chapter 2** focuses on gas and dust dynamics in protoplanetary discs.

Part II explores the different physical process that could have given origin to the plethora of observed disc substructures, in particular spirals, rings and gaps. **Chapter 3** discusses systems where the disc is massive enough to induce gravitational instabilities that could be detected as spiral density waves. **Chapter 4** describes the tidal interaction between the disc and an embedded planet, whose outcome could be both gaps or spirals. Finally, **Chapter 5** focuses on the observations of the previously described phenomena, both from a morphological and kinematical point of view. In this Chapter I also summarize some results obtained in collaboration with Cassandra Hall, Teresa Paneque-Carreño and Laura Perez. The first work refers to Hall et al. (2020) published on the *AstroPhysical Journal*, with the title "Predicting the kinematic evidence of gravitational instability". The main aim of this work is to show how spiral induced by gravitational instabilities can be detected in the gas kinematic. The second work has been submitted as Paneque-Carreno et al. (2021) on the *AstroPhysical Journal*, and it titles "Spiral arms and a massive dust disk with non-Keplerian kinematics: Possible evidence for gravitational instability in the disk of Elias 2-27".

After this theoretical overview linking disc substructures to physical processes, in **Part III** I collect the main results obtained during this Thesis, aiming to constrain disc dynamics from observations of substructures. I will explore in **Chapter 6** if there could be a relation between substructures observed at different wavelengths in protoplanetary disc and the gas disc mass. This Chapter is based on an article published on the *Monthly Notices of the Royal Astronomical Society* (Veronesi et al. 2019). **Chapter 7** focuses on the study of the protoplanetary disc orbiting around the DS Tau star (Long et al. 2018b, 2020). In particular, I will present a modeling of this source in order to unveil the mass of an hypothetical

planet embedded in the disc and responsible for the observed gap. This work is based on an article published in *Monthly Notices of the Royal Astronomical Society* (Veronesi et al. 2020). Finally, in **Chapter 8** we investigate if the spirals observed by ALMA in the protoplanetary disc orbiting around Elias 2-27 (Pérez et al. 2016) can be related to gravitational instabilities. To achieve this, I present an analytical model of the velocity data collected by (Paneque-Carreno et al. 2021). Starting from an early work of Bertin & Lodato (1999), I fit the rotation curve of the disc with both a Keplerian and a self-gravitating model. From this fit we obtain a constraint for the disc mass, compatible with the disc being self-gravitating unstable. The work has been submitted to the *AstroPhysical Journal Letter* with the title "A dynamical measurement of the protoplanetary disk mass in Elias 2-27", and is currently under review.

Finally, I present the **Conclusions** of this Thesis, briefly discussing the obtained results, and focusing on future developments. The appendix is divided into two parts: **Appendix A** presents the derivation of the disc gravitational potential introduced in Chapter 4 and then used in Chapter 8, and **Appendix B** presents a work done in collaboration with Giulia Ballabio and Giovanni Dipierro that has been published in the *Monthly Notices of the Royal Academy Society*, with the title "Enforcing dust mass conservation in 3D simulations of tightly-coupled grains with the PHANTOM SPH code". The work presented here has also been implemented in the PHANTOM SPH code, used in Chapter 6 and Chapter 7 of this Thesis.

Part I

Introduction

Chapter

1

Planet formation in a nutshell: protoplanetary discs

The beginning (sprout growing out of a seed during the first lockdown of 2020).

It was in 1995 that Mayor & Queloz (1995) detected the first exoplanet around a main-sequence star, 51 Pegasi b. Since then, an incredible variety of planets and planetary systems have been collected. Up to September 2020, we can count more than 4000 confirmed exoplanets, and it can be said that the Solar System is distinctly atypical (see Fig. 1.1, where the confirmed exoplanets up to Sept. 2020 are represented, Winn & Fabrycky 2015), even if for a complete discussion it would be necessary to consider observational biases (see e.g. for a deeper discus-

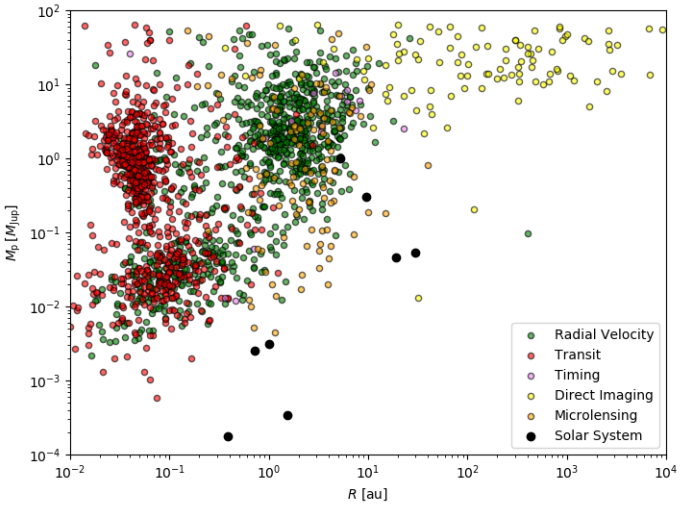

Figure 1.1: Mass (in Jupiter masses) vs separation (in au) of confirmed exoplanets up to September 2020. Different colours represent different detection techniques: radial velocity (green), transit (red), purple (timing), direct imaging (yellow) and microlensing (orange). The planets of the Solar System are shown in black. The catalogue of exoplanets detection has been taken from exoplanets.eu.

sion Morbidelli & Raymond 2016).[1] To understand this diversity of planets and planetary systems, we must understand the planet formation process, and this could be done by investigating the cradle of planet formation: the protoplanetary disc.

This has been made possible by recent technological developments in the (sub-)mm interferometry (Atacama Large sub-Millimeter Array, ALMA) and by several instruments in the field of adaptive optics (for example GPI on Gemini, SPHERE on VLT, Hi- CIAO on Subaru and MagAO(x) on Magellan), which have disclosed a comparable level of diversity in the physical structure of these potentially planet-forming/hosting discs.

1.1 Star and disc formation

A star forms from the collapse of a molecular cloud core (Hoyle 1960), a mixture of dust and gas, itself a substructure of the interstellar medium, ISM. In Fig. 1.2 we can see a schematic representation of the star-disc formation process. At the onset of collapse, the initial core has a non-zero angular momentum contribution, meaning that the infalling material will not fall directly onto the protostar, but it

[1] An observational bias is related to the detection of low-mass planets (e.g.,mass equal to the Earth) at large separation.

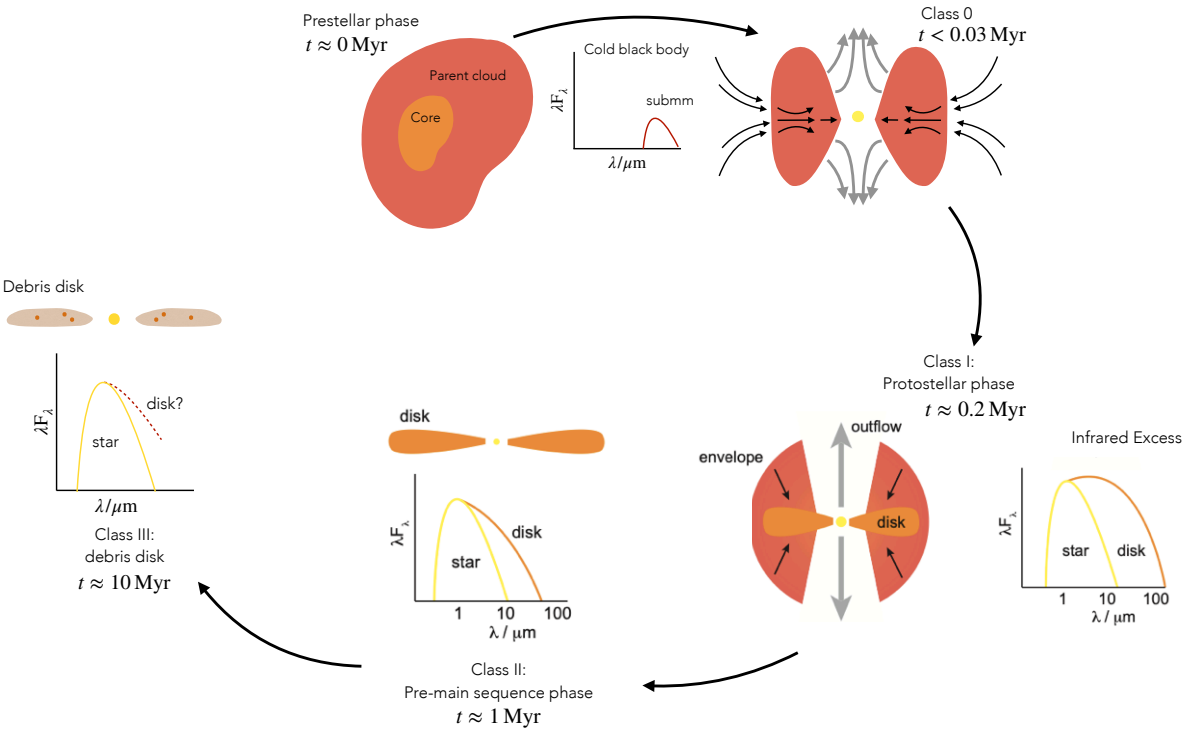

Figure 1.2: Phases of the star and disc formation processes, going from a core inside the parental cloud to a system formed by a star and a disc surrounding it. For each phase is showed a schematic Spectral Energy distribution. Image readapted from André (2002) and Armitage (2015).

will form a disc around it (e.g., Terebey et al. 1984; Yorke et al. 1993) or fragment into a multiple stellar system (e.g., Matsumoto & Hanawa 2003).

More in detail, the process begins with a Giant Molecular Cloud (GMC), emitting in the IR and sub-mm, with a gaseous mass of $10^4 - 10^6 M_\odot$ and a radius between $1 - 100$ pc. These clouds are composed by molecular hydrogen, and they show many complex and filamentary substructures (André et al. 2010; Molinari et al. 2010; Toci & Galli 2015). The fundamental forces acting at this stage on the GMC are the gravitational attraction, which leads to the cloud collapse, the thermal pressure, magnetic field forces (e.g., for a review Galli 2005) and bulk motions, which leads to the cloud dispersion. Turbulence is another mechanism able to counterbalance gravity on global scales, but it could provoke collapse locally (e.g. Larson 2003 for a review). All the observed GMC are in the same quasi-equilibrium state, showing an initial contraction process.

During this contraction, at a typical dimension, turbulence becomes negligible compared to thermal motion, leading to the formation of more dense and round substructures, called Molecular Cloud Cores (MCC). This typical size can be estimated through a first-order perturbation analysis of the response of the medium to small perturbations (Jeans 1902). In this way, one can evaluate the maximum

wavelength of small perturbations below which the cloud is stable, called the Jeans length λ_J, given by

$$\lambda_J = \frac{\sqrt{\pi} c_\mathrm{s}}{\sqrt{\mathcal{G}\rho_\mathrm{g}}}\,, \tag{1.1}$$

where ρ_g is the medium density (assumed as infinite, static and homogeneous), c_s is the sound speed and $\mathcal{G}$ is the gravitational constant. In other terms, this criterion determines the critical size above which initial inhomogeneities in the cloud become gravitationally unstable and fragment to form protostars. With typical values for the temperature, $T = 10\,\mathrm{K}$, and for the molecular cloud density, $\rho_\mathrm{g} \simeq 3 \cdot 10^{-19}\,\mathrm{gcm}^{-3}$, the Jeans length is $\lambda_J \simeq 0.05\,\mathrm{pc}$. The correspondent minimum mass value for this fragmentation process, the Jeans mass, is $\propto {\lambda_J}^3$, and it depends on the density and the temperature of the medium. For the same values of before, a typical Jeans mass is of the order of $0.4\,M_\odot$. We highlight that individual MCCs collapse, rather than the GMC itself.

After this stage, different models have been developed to explain how stars finally form, and what determines the mass distribution of stars at their formation (Initial Mass Function - IMF). One of the most accredited is the core gravitational collapse model. According to this model, every MCC gives birth to a single protostar via the gravitational collapse. Several observations of star forming regions have demonstrated that cloud cores are characterized by rotation (Goodman et al. 1993), confirming that angular momentum plays a major role in the system evolution. This means that the collapse cannot be completely free. Therefore, in a typical timescale of $10^4 - 10^5$ yrs (estimated from the free fall timescale $t_\mathrm{ff} \sim (G\rho_\mathrm{g})^{-1/2} \sim GM_\odot/c_\mathrm{s}^3$), the conservation of angular momentum determines the formation of a disc around the protostar, called *protostellar disc*, with an extension of the order of hundreds of AU. This disc is composed by gas and dust, where the gas component is usually assumed to be the $\sim 99\%$ of the total mass (with a typical dust-to-gas ratio of 0.01, as in the ISM). It is important to highlight that, nowadays, there is a lot of uncertainty with respect to this value (see Sec. 1.2.1). The transition between the first evolutionary stage and this one is called "main infall phase". During this phase some fundamental processes determine the future system evolution. First of all, a residual surrounding gas envelope accretes chaotically onto the forming disc for approximately 10^5 yrs. As a consequence, during this stage the disc could be massive enough to be self-gravitating (see Chapter 3), and the chaotic accretion could be responsible for geometrically warped discs or for the formation of multiple systems (Bate et al. 2010; Bate 2018). Moreover, different mechanisms of angular momentum redistribution across the disc are present, allowing the accretion onto the central protostar (Pringle 1981; Frank et al. 2002). Some of these mechanisms are viscosity, turbulence and jets/outflows. At this stage, the disc luminosity is due to viscous accretion heating and the disc is defined as "active".

After a few 10^5 years, most of the disc matter has accreted onto the star. The remaining disc is still an accretion disc, but with a mass $M_\mathrm{disc} \ll M_\star$ (where $M_\star$ is the mass of the star), made of gas and dust, called *protoplanetary disc*. The disc emission at this stage is mostly based on the irradiation it receives from the

star, meaning that the disc is "passive". Typically, these discs have an accretion rate $\leq 10^{-8}\,M_{\odot}/\mathrm{yr}$, while active discs (see Sec. 1.2.3) show $\dot{M} > 10^{-8}\,M_{\odot}/\mathrm{yr}$ (Gullbring et al. 1998; Armitage 2013). The fact that this disc is still visible for $\sim 10\,\mathrm{Myr}$ means that there is enough time for planets to form out from the disc (Fedele et al. 2010). These discs surround a significant fraction of young pre-main sequence stars (PMS) with ages less than a few ~ 10 Myr, known as Classical T-Tauri (CTT) stars and Herbig Ae/Be stars (Evans et al. 2009). [2] The physical characteristics of the disc in these last stages are essentially dependent on the angular momentum content of the parent molecular cloud core. In the last stage, the main actor is the central protostar, surrounded by a disc, made of almost completely solid materials, which is called *debris disc* (Wyatt et al. 2015; Wyatt 2018). The mass content of these discs can be described as second generation dust, formed after the collision and fragmentation of larger bodies. Systems in this phase are known as Weak T-Tauri (WTT) star.

If we consider the star/disc formation phases described until now, each of them can be characterised by a signature, observable in the Spectral Energy Distribution (SED, see Sec. 1.2.3.1). The SED describes how the energy radiated from the system is distributed over frequencies, after being reprocessed through the disc material. In Figure 1.2 is schematically represented the star and disc formation process, highlighting the difference between the SED of each phases, and what is the main component of the system giving its energetic contribution. This SED-based classification relies on the evaluation of the spectral index s of the emitted flux F_{λ} of the object at wavelength λ, defined as

$$s = \frac{\partial \log(\lambda F_{\lambda})}{\partial \log \lambda}\,. \tag{1.2}$$

The spectral index is typically measured in the near-far Infrared, from 2 up to $100\,\mu$m. From this classification, we note that the shape of the SED varies depending on the dominant component of the forming system, since they are at different temperatures. We briefly summarize the main characteristics of the three classes (Class I,II,III identified by Lada & Wilking 1984; Lada 1987, Class 0 identified by André 2002):

- Class 0: $s > 0$ (i.e. the emission increases with wavelength in the considered waveband), typical of systems where the dominant component is the cool dust of the envelope ($T \leq 30 - 50K$) with its emission in the sub-millimetre range.

- Class I: $s > 0$, typical of cold objects in which the dominant component is the envelope. It emits in the near-infrared with a rising spectrum towards long wavelengths. They are also characterized by a "infrared-excess" emission, which is due to the reprocessing of the star radiation by the circumstellar dust (Hartmann 2009). Indeed, the dust absorbs energy from the star at

[2] T-Tauri are solar analogs with strong magnetic fields, violent stellar activity, X-ray radiation and intense FUV (Bertout 1989). They might be considered as low-mass pre-main sequence stars (Walker 1956). Herbig stars are, instead, defined as the stars with spectral type A or B, with emission lines, infrared excess due to hot or/and cool circumstellar dust and with luminosity class from III to V (Waters & Waelkens 1998).

short wavelengths and re-emits it at far-infrared wavelengths, where the envelope is sufficiently optically thin for the radiation to escape;

- Class II: $-\frac{4}{3} < s < 0$, we can distinguish two components: the protostar, that emits in the UV/optical range, and the disc, which is the most relevant component in the IR/mm. The disc results optically thin in the millimetre range of wavelengths, while it is optically thick in the infrared. In these systems, emission lines can trace accretion onto the central star.

- Class III: $s < -\frac{4}{3}$, the emission is dominated by the black body of the pre-main sequence star, with no infrared excess.

We can read this classification both as a structural and evolutionary sequence. From Class 0 and Class I YSOs, which are accreting from discs, still being fed by gas falling in from envelopes, to Class II YSOs (also called Classical T Tauri stars), which are pre-main-sequence stars with surrounding discs. From Class II to Class III YSOs (or Weak-lined T Tauri stars), which are pre-main-sequence stars with little or no primordial gas remaining in orbit around them.

1.2 Protoplanetary discs properties

With the advent of powerful telescope and instruments, such as ALMA and VLT/SPHERE, we are now able to better characterise the properties of protoplanetary discs. This is fundamental if we want to explain the observed exoplanets population and the process of planet formation. The starting point, has already mentioned before, is that these discs are mainly composed by gas ($\sim$ 99%) and dust ($\sim$ 1%). The dust-to-gas ratio it is usually assumed to be equal to 10^{-2}, coming from the interstellar medium - ISM (Mathis et al. 1977). In the last years, new studies and comparison between theories and observations are suggesting that this value could be different, globally (Tricco et al. 2017), but also locally, in particular due to a different spatial distribution of gas and dust (Birnstiel & Andrews 2014; Ansdell et al. 2016), both vertically (i.e. vertical settling) and radially (i.e. radial drift). Interestingly, this different dust-to-gas ratio could be related to the primordial collapse phase, and could thus determine the entire evolution process of these systems (Bate & Lorén-Aguilar 2017). It is important to emphasise that, although the dust is present in much smaller quantities, it plays a fundamental role as it dominates the opacity of the disc, and to best explain ALMA observations it is therefore necessary to accurately determine its chemical composition (Draine 2006). Moreover, knowing the dust budget and the evolution of the dust grains is necessary in order to describe the starting and ending points of planet formation. At the same time, gas, and in particular the angular momentum transport of the accreting gas, is thought to be the primary source of disc viscosity, although recent studies have proposed new mechanisms. We will address the viscosity topic in Sec. 2.1.3. In this section I will give an overview of the main properties of protoplanetary discs that have been obtained by the sinergy between observations and theory, such as the disc mass, the mass accretion rate onto the central star, the radial extent and the disc thermal structure.

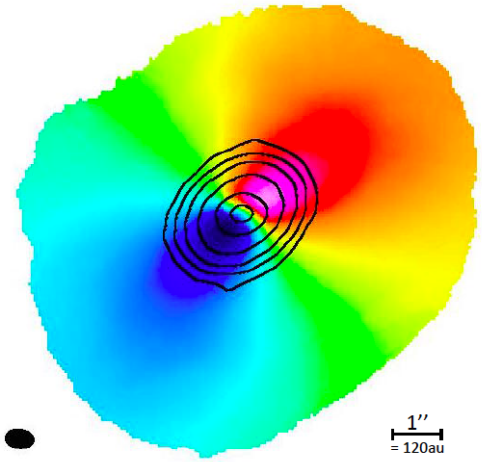

Figure 1.3: The dust and gas component in the HD 163296 protoplanetary disc. The continuum emission from dust is shown as contours, while the color-coded first moment map of CO represent the gas component. Image taken from (de Gregorio-Monsalvo et al. 2013).

1.2.1 A mass problem

How massive are protoplanetary discs? This is one of the most crucial, unsolved question in the field of planet formation (Bergin & Williams 2018). Indeed, the gas mass affects how planets form, how they migrate inside the disc (Baruteau et al. 2016), what would be their final composition, and what is the origin of the substructures we observe in protoplanetary discs (see Chapter 6, Veronesi et al. 2019). At the same time, dust is also essential to build the core of the future protoplanets (Manara et al. 2018). For a disc, mass is also one of the discriminating factor for the development of gravitational instabilities and thus for the arising of spiral structures, which can act as dust traps and increase grain growth (Rice et al. 2004; Kratter & Lodato 2016).

As anticipated, the spatial distribution of dust and gas is not trivial. This is clear, for example, in Fig. 1.3, where the continuum emission is represented by black contours lines, while the gas component is represented with the color-coded first moment map of CO. The more compact size of the dust continuum can be explained by the radial drift of dust grains (Weidenschilling 1977). This example illustrates in a simple way the importance of measuring independently the gas and dust components. Indeed, different techniques have been developed to properly capture the amount of material inside the disc.

1.2.1.1 Dust

Also if less abundant than the gas, dust is one of the building blocks of planets. Dust emits over a continuum rather than the narrow spectral lines from gaseous species. Consequently, it is easier to detect it in the cold dusty regions in the outer disc (> 50 au) (Beckwith et al. 1990). We refer the reader to numerous reviews on this subject (Testi et al. 2014; Andrews 2015). Briefly, the dust component can be measured under two main assumptions. The first one is that the emission is optically thin, which is true at (sub-)millimetre wavelengths for $\Sigma_{\rm dust} \leq 3\,{\rm g cm^{-2}}$ (Bergin & Williams 2018) for most discs, even if it is worth noting that in massive

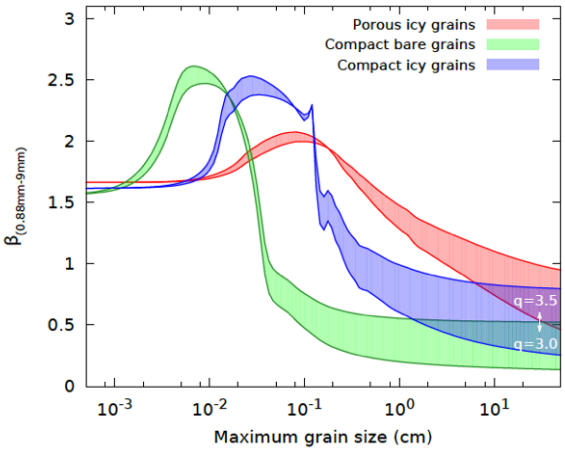

Figure 1.4: Spectral index β of Eq. 1.5 calculated between two wavelengths as a function of the maximum grain size $a_{\max}$, for a power-law grain size distribution. Different colors correspond to different chemical composition and porosity, while the colored band shows the scattering between two different power-law indeces for the grain size distribution (Testi et al. 2014).

discs this value could be exceeded in the inner tens of au. Starting from the observed flux F_ν at a frequency ν, we can derive the dust mass as

$$M_{\rm dust} = \frac{F_\nu d^2}{\kappa_\nu B_\nu \left(T_{\rm dust}\right)} , \tag{1.3}$$

where d is the distance from the observer. B_ν is the Plank function and τ_ν is the optical depth (i.e. the absorption cross-section per unit mass, see Rybicki & Lightman 1979 for a full derivation) at frequency ν which can be directly derived from the opacity as

$$\tau_\nu = \kappa_\nu \Sigma_{\rm dust} , \tag{1.4}$$

with $\Sigma_{\rm dust}$ being the dust surface density. This last relation is correct under the assumption that the optical depth is dominated by the optically thin dust fraction. This computation of the dust mass depends on some quantities, in particular the dust temperature and the optical depth. The temperature could be derived from the Spectral Energy Distribution (SED) of the system, and generally this is a function of both the radial and vertical direction (r, z). Indeed, the surface layers are warmer than the midplane. Anyway, the millimetre emission comes mostly from the midplane, where large dust grains have settled (see Sec. 2.2.3), and their temperature is low and can be considered as constant ($\sim$ 20 K, i.e. the average dust temperature found in the outer disc in the Taurus star forming region from Andrews & Williams 2005). Instead, the dust opacity can be approximated by a power law of the frequency (Beckwith et al. 1990) as

$$\kappa_\nu = \kappa_0 \left(\frac{\nu}{\nu_0}\right)^\beta , \tag{1.5}$$

where κ_0 is a normalization factor, and β is the spectral index. Both κ_0 and β depend on the dust grains composition, porosity, shape and size distribution (Pollack et al. 1994; Kataoka et al. 2014), where the latter is usually assumed to be a power law $n(a) \propto a^{-q}$, with q varying from 3.5 in the surface layer (Mathis et al. 1977) to 3 in the midplane (Tanaka et al. 2005). Specifically, β is obtained by opacity measurements at millimetre wavelengths, and in protoplanetary discs

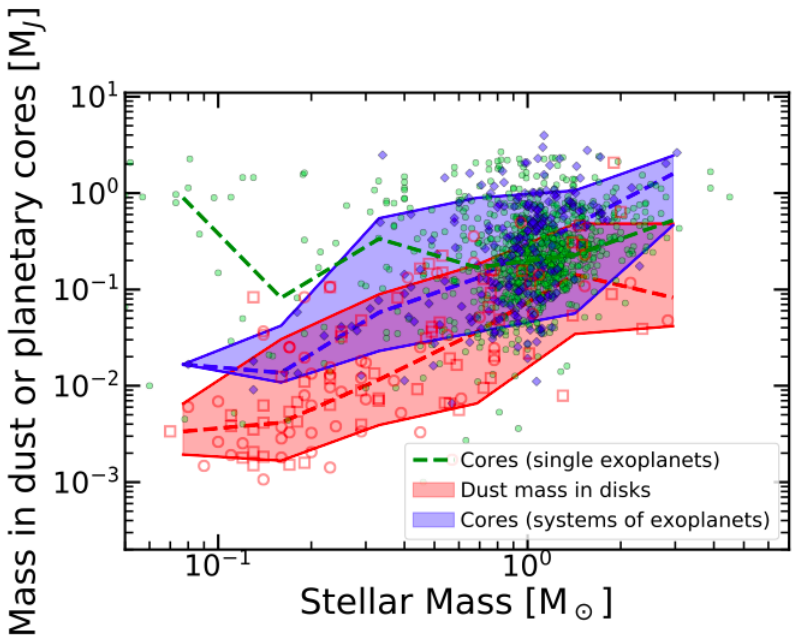

Figure 1.5: Masses of the cores of single exoplanets (green), the sum of the cores in exoplanetary systems (blue) and disc masses (red), each one as a function of the mass of their host star. The colored regions comprises the 10th and 90th percentiles of the distributions, while the dashed lines represent the median of the distributions (Manara et al. 2018).

$\beta \simeq 1$ (Beckwith et al. 1990; Testi et al. 2003; Natta et al. 2004; Ricci et al. 2010). It can be related to the measured spectral index α, as $\beta = \alpha - 2$, where α could be obtained by multi-wavelength continuum observations (in the optically thin and Rayleigh-Jeans regime). Fig. 1.4 resumes the dependence of β from the dust composition, geometry and size (Testi et al. 2014; Natta et al. 2004). An analytical prescription for the dust opacity is presented by Bell & Lin (1994), where they consider differ dust grains compositions. This model has been used in self-consistent modeling of self-gravitating discs (e.g., Clarke & Lodato 2009; Rice et al. 2010).

Another aspect one has to keep in mind is that any measurement of dust mass is, practically, a measure of the amount of particles with sizes comparable to the observing wavelength ($\sim a/2\pi$ with a the grain size, e.g. Draine 2006). In particular, millimeter and larger-sized particles can be found at the midplane (settling), also drifting toward the center at different rates, with a size-segregation outcome. This means that different range of grain sizes and different regions in the disc could be probed, enriching the study of the physical processes happening during the disc formation and evolution. This has also a "con": when measuring dust disc masses one should take these processes into account.

Finally, despite the apparent facility with which the mass of dust in the discs can be weighed, Manara et al. (2018) showed that there could be some issues.

They collected the masses of the confirmed exoplanets and compared their dependence on stellar mass with the same dependence for protoplanetary disc masses measured in $\sim 1-3$ Myr old star-forming regions (Lupus and Chamaeleon I, from Ansdell et al. 2016; Pascucci et al. 2016). The obtained result, showed in Fig. 1.5, highlights that protoplanetary discs appear not having enough mass to form planets when they have the above-mentioned age. This could be a "dangerous" issue, since all theoretical models that try to explain planetesimal formation are based on inefficient processes (such as pebble accretion, see Guillot et al. 2014). There are a few possible solutions to this "cat biting its own tail". The first one is that disc dust masses could be highly underestimated, while the second one is that planets should actually start forming much earlier (<0.1-1 Myr), when the disc is still rich in dust (Segura-Cox et al. 2020). Another way out is that the disc could be continuously replenished by material from the external environment (Kuffmeier et al. 2017). To determine which one is the actual scenario one should observe the disc neighbourhood, looking in particular to younger and more embedded regions (Class 0/I). A similar conclusion has been also reached by (Cazzoletti et al. 2019) in the Corona Australis region. The previously cited ALMA surveys, Lupus and Chamaeleon I (i.e. young sources), also showed that there is a decreasing trend with age of the dust mass with respect to the older systems of, for example, the Orionis cluster (Ansdell et al. 2017) and Upper Sco (Barenfeld et al. 2016). As a proof of this relation, analysing both ALMA and VLA data, Tychoniec et al. (2020) found that the dust masses of young Class 0 and I discs are larger by at least a factor of 10 and 3, respectively, compared with dust masses inferred for older Class II discs in Lupus and other regions. This means that in younger systems (Class 0/I) there should be enough mass to produce the observed exoplanet population (see their Fig. 6).

1.2.1.2 Gas

The gas is the main component in protoplanetary discs, and it is usually assumed to be 100 times the dust. Nevertheless, as already mentioned, this is only a simplistic approximation. It should also be noted that although gas is a key player in the overall picture of planetary formation, it is the component less constrained, and this is due to the nature of the gas chemical composition. Indeed, the most abundant constituent of gas is molecular hydrogen (H_2), which emission is weak or undetectable in most disc regions (Carmona et al. 2008)[3]. The weak emission of H_2 is caused by the absence of a dipole moment, whereas only weaker quadrupole transitions are allowed. It could be possible to detect it in the inner regions of the disc, closer to the star where temperatures are higher (>100 K), but these regions are optically thick, due to the large dust column densities (Pascucci et al. 2006). Thanks to the upcoming James Webb Space Telescope, we would be able to detect in the mid-infrared also the hot gas closer to the star, and at the same time warmer material at greater distances. Hopefully, this would help us to weigh also those regions that now are missing from our data. Moreover, to put more constraints on the disc masses, other methods independent from chemistry are under explorations

[3]Protoplanetary discs are generally cold ($T \simeq 20$ K) molecule-dominated regions, making the emission of H_2 not detectable.

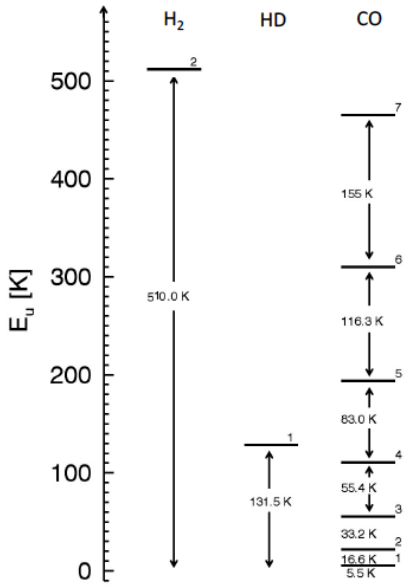

Figure 1.6: Rotational energy levels for H_2 (left), HD (middle) and CO (right). It is evident that the energy needed to excite the different transitions (shown in Kelvin) are much higher for H_2, than for HD and CO. Image taken from Miotello A. PhD Thesis (https://openaccess.leidenuniv.nl/handle/1887/61006).

in the last years. For example, this could be done by searching for deviation from Keplerianity in the disc rotation curve (e.g. Bertin & Lodato 1999; Lodato & Bertin 2003 in the context of AGN, and Veronesi et al. 2021, see Chapter 8), or by looking at multi-wavelengths observations and comparing substructures to get an estimation (with fixed dust grain size) for the Stokes number, and thus on the disc mass (Powell et al. 2019; Veronesi et al. 2019).

Tracing H_2. Due to the high difficulty in detecting H_2, the focus has been on finding other tracers of the gas mass budget, such as carbon monoxide (CO), hydrogen deuteride (HD) and the dust itself. Starting from the latter, the idea is to infer the disc mass from the observed (sub-)millimetre flux F_ν (Eq. 1.3), under an assumption on the dust-to-gas ratio (e.g., 100, such as in the ISM) for the conversion between the two components. However, as already discussed, this value is highly uncertain, mainly due to the spatial segregation between dust and gas, and this often results in under-estimation of the gas mass. Another source of uncertainty comes from the optical depth as discussed in Sec. 1.2.1.1.

Going back to the other two tracers, HD and CO, since they have lower excitation energy with respect to H_2 (see Fig. 1.6 for a schematic comparison), they result being more detectable. However, there are some issues when measuring the gas mass from CO and HD. A critical point in using optically thin lines of various molecules to probe H_2 is that their abundance must be known with a reasonably high precision. Moreover, these molecules are affected by chemical processes that "hide" part of the mass budget. In Fig. 1.7 are schematically showed the dust and gas component of a flared protoplanetary discs, highlighting the main composition and some of the chemical processes at play. Here I will briefly summarise the results obtained with the two tracers, also listing the physical processes that characterise them and that may in some way affect the mass estimate.

HD is the closest molecule to H_2. It is its less abundant isotopologue and

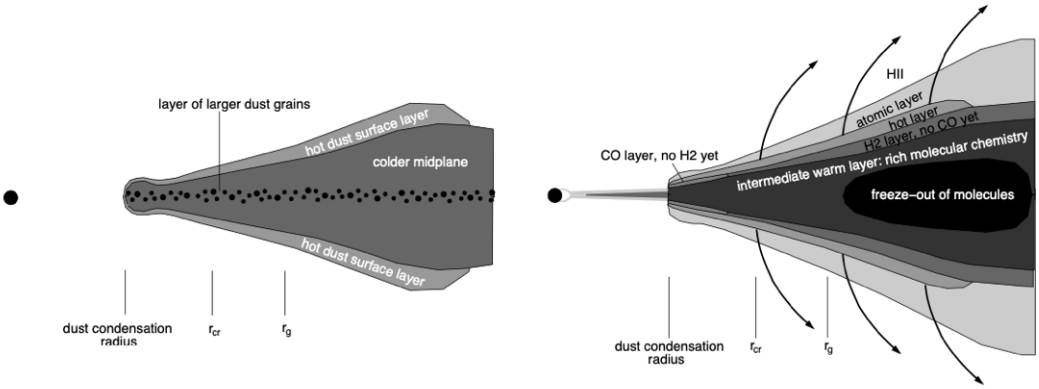

Figure 1.7: Schematic picture of a flared protoplanetary disc showing the dust and gas main composition and some of the chemical processes involved (Dullemond et al. 2007).

their chemistry is similar, meaning that they both self-shield themselves from photodissociating UV photons (Wolcott-Green et al. 2011), and they do not freeze-out onto grains, unlike CO and less volatile species. Indeed, at low temperatures, when freeze-out occurs, the CO-isotopologues stick onto icy grains and they are not anymore counted as gas budget. The abundance of HD with respect to H_2 is $\approx 3 \times 10^{-5}$. When estimating the gas mass from HD, one should also take into account that the HD emitting line is found in an elevated region above the midplane, where the gas is warmer than 30 K. Thus, to properly estimate the disc mass from HD, it is necessary to investigate the disc vertical structure (Trapman et al. 2017). Finally, until now this transition has been detected in a small sample of close and bright discs, such as TWHya (Bergin et al. 2013), DM Tau and GM Aur (McClure et al. 2016). In particular for what concern the TW Hya detection, Bergin et al. (2013) obtained a disc mass larger than $5 \times 10^{-2}\, M_\odot$, which is very high for quite an old disc ($\sim$ 10Myr).

CO, is the second most abundant molecule in protoplanetary discs. It emits rotational lines at millimetre wavelengths, observed in discs with a high signal-to-noise ratio (e.g., Dent et al. 2005). The emission from the ^{12}CO lines is so abundant that it could be optically thick, meaning that it is more sensitive to temperature than to column density. It is possible to use less abundant CO isotopologues (^{13}CO, C^{18}O, C^{17}O and ^{13}C^{18}O) to infer the gas mass (van Zadelhoff et al. 2001). CO and its isotopologues are also stable molecules and for all these reasons they are often used as tracers of gas properties, structure and kinematics in discs and in other astronomical contexts. Also in this case, to measure the gas mass, it is required a CO-H_2 conversion factor (i.e. the abundance ratio). Usually, CO abundances in molecular clouds are found in a range between $\approx 0.5 - 4 \times 10^{-4}$ (Bergin & Williams 2018). However, this conversion seems to underestimate the mass budget (Ansdell et al. 2016; Miotello et al. 2017; Ubeira Gabellini et al. 2019), for example with respect to HD measurements (Bergin et al. 2013; McClure et al. 2016). This is probably due to an high levels of carbon depletion (Favre et al. 2013). Speaking about CO spatial distribution inside the disc, Aikawa et al.

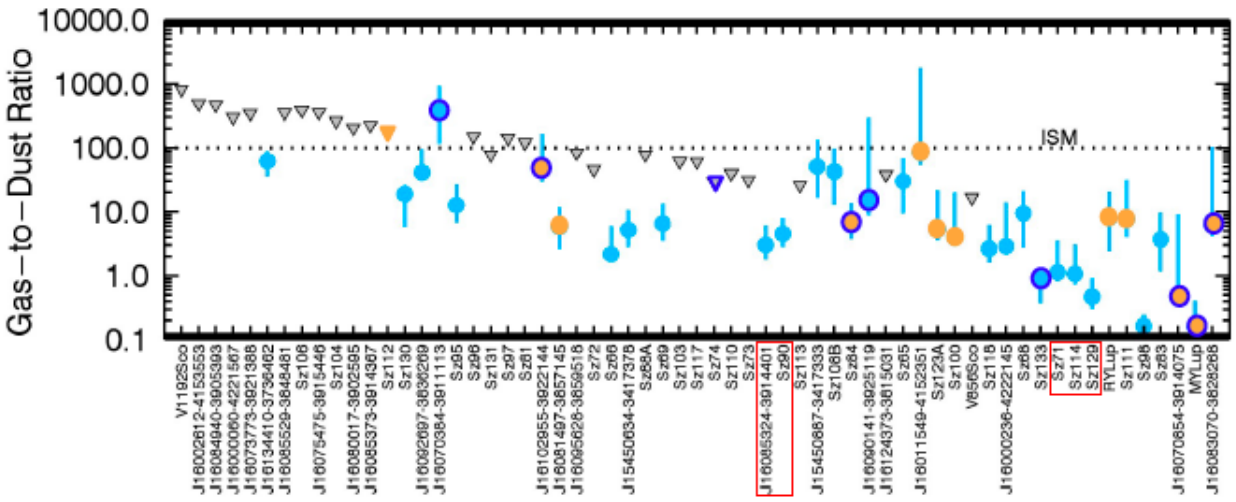

Figure 1.8: Gas-to-dust ratios for all the sources detected in the continuum (Lupus survey). Gas non-detections are shown with gray triangles, while all detections are presented as filled circles. Different colors represent transitional disc (orange) and edge on disc (blue) (Miotello et al. 2017).

(2002) proposed CO and other molecules to be found in a warm molecular layer with two boundaries. The lower one set by the freeze-out of molecules onto dust grains, and corresponding to the cold disc midplane. This phenomenon is expected to lock a significant fraction of CO on grains (Tielens et al. 1991; Qi et al. 2013, 2015). The upper one set by photo-dissociation from the central star or from the external environment. This is an isotope-selective process subject to self-shielding (van Dishoeck & Black 1988), meaning that different isotopologues would photodissociate at different location of the disc, due to their abundance (Miotello et al. 2014). Considering these two processes (Visser et al. 2009; Williams & Best 2014; Miotello et al. 2014; Woitke et al. 2016) that control the survival of carbon monoxide in the gas-phase may affect the abundance ratio. Some recent works have taken into account these processes, with worrying results. Miotello et al. (2017) found that CO based estimates result in very low gas masses (even $< 1\,M_{\rm J}$), when volatile carbon in not depleted. As a consequence, global gas-to-dust ratios are much lower ($\simeq 1 - 10$) than the expected ISM value of 100 (see Fig. 1.8). These two results may indicate rapid loss of gas, or chemical evolution, for example, through sequestering of carbon from CO to more complex molecules, or carbon locked-up in larger bodies. It is interesting to note that the observations statistics show that the CO line-to-continuum ratio varies widely from disc to disc within a single star-forming region. As a drastic example, Fig. 1.9 from Bergin & Williams (2018) shows two CO-derived gas-to-dust ratios in the Lupus disc survey. While in the left column there is the continuum emission (top panel: the large and bright Sz 98 disc; bottom panel: the low mass J1607- 3911 disc), in the right one it is presented the integrated ^{13}CO emission, with dust continuum contours overlaid. The resulting ^{13}CO line-to-continuum ratio is substantially different for the two systems, suggesting either that we are missing some chemical/physical

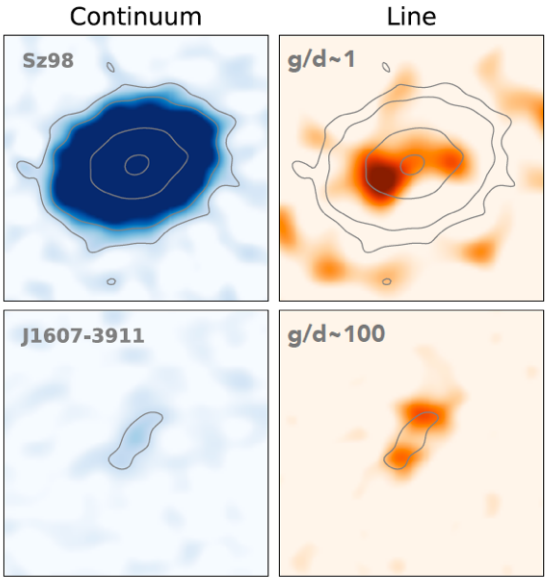

Figure 1.9: Two CO-derived gas-to-dust ratios in the Lupus disc survey (Ansdell et al. 2016). Left column: continuum emission (top panel: the large and bright Sz 98 disc; bottom panel: the low mass J1607- 3911 disc). Right column: integrated ^{13}CO emission, with dust continuum contours overlaid (Bergin & Williams 2018).

process or that this difference is real.

1.2.1.3 Mass accretion rates

Another indirect way in which we can have information about the disc masses and about physical processes happening inside the disc is by looking at the mass accretion rate onto the star (e.g. Hartmann et al. 2016). In particular, mass accretion rates are nowadays measured through spectroscopic observation from near UV to near IR with instruments such as X-shooter (Manara et al. 2016b; Alcalá et al. 2014, 2017; Herczeg & Hillenbrand 2008). To properly explain these data is not easy, since there are uncertainties related to the mechanism for angular momentum removal/redistribution and its associated timescales (Turner et al. 2014), combined with further uncertainties associated with the roles of internal/external photoevaporation (Alexander et al. 2014).

However, some interesting results have been found. First Manara et al. (2016b), and then also Rosotti et al. (2017), show that CO based disc masses estimates, which are systematically low, result in accretion efficiencies above unity, in contrast with the viscous theory. This strengthens the idea that CO based measurements underestimate the disc mass (Miotello et al. 2017). Moreover, they demonstrate that dust masses estimates are enough accurate to reveal higher accretion efficiencies in the Trapezium cluster, explaining this as an evidence of the external photoevaporation process. Different surveys have explored star formation regions such as Chamaeleon (see e.g., Manara et al. 2016a,b, 2017 or Pascucci et al. 2016), Lupus (see e.g., Ansdell et al. 2016; Alcalá et al. 2017; Tazzari et al. 2020a) and Upper Scorpius (see e.g., Barenfeld et al. 2016; Manara et al. 2020). The main outcome of these studies is that mass accretion rates and disc mass are two correlated quantities (Manara et al. 2016b). Mulders et al. (2017b) found a slope slightly shallower than linear and a spread larger than expected from α-constant viscous evolution models. However, both Lodato et al. (2017) and Mulders et al.

(2017b) demonstrate that the observed relation can be reproduced by viscous models (Lynden-Bell & Pringle 1974; Hartmann et al. 1998) under some assumptions for the viscous timescale (i.e. the average viscous evolutionary timescale of the discs should be comparable to the cluster age).

Another nice outcome of the study of accretion rates is that they could help us in understanding the physical processes that originated the so-called transitional discs (TD), where the inner regions have been depleted in dust creating large cavities. Manara et al. (2014) found that the accretion rates and wind properties of 80% of the TD in their sample are comparable to those of classical T Tauri stars, meaning that despite the dust depletion, gas can still be transferred to the inner region. Finally, in a recent work, Manara et al. (2020) investigated accretion rates for 36 young stars, with still surviving discs in the 5-10 Myr old UpperSco region, revealing that accretion rates do not decrease with time (they are similar to those of the younger SFR of Lupus and Chamaeleon I), as would be expected from viscous theories, and that they have a large $M_{\rm acc} - M_{\rm disc}$ spread. The obtained high value of $10^{-9}\,M_{\odot}$/yr for the accretion rate together with measured low disc masses could not be explained by internal photoevaporation (Somigliana et al. 2020), but could be related to external photoevaporation (Rosotti et al. 2017; Winter et al. 2018a; Sellek et al. 2020a). To better understand these data in the picture of the secular evolution of protoplanetary disc, it would be necessary to account for several interconnected processes, such as dust evolution, external and internal photoevaporation and MHD winds (Armitage 2013; Bai & Stone 2013; Sellek et al. 2020b). Another independent constraint on viscous models in the outer region of protoplanetary disc could be given by a comparison between wind mass-loss and stellar accretion rates (Winter et al. 2020).

1.2.2 Radial extent

Already from Fig. 1.3 it is clear that the dust and gas radial extents could be very different between each other. This is generally explained by the fact that their dynamic and evolution is dominated by different processes (see Chapter 2 and Testi et al. 2014 for a review on dust dynamics). In particular, radial drift (Weidenschilling 1977) and vertical settling (Nakagawa et al. 1986) determines the compactness of the dust disc with respect to the gas component, which often is more spread out due to the viscous evolution of the gas (for a review on gas accretion dynamics see Lodato 2008 and Chapter 2.1 of this Thesis). Thus, studying the radial extent of the two components can give us information about the internal and external processes that dominates the disc evolution, in particular focusing on alternative angular momentum removal mechanisms (Turner et al. 2014; Najita & Bergin 2018). The latter include among others, external photoevaporation, dynamical encounters with other objects for example in multiple systems (Clarke & Pringle 1993; Bate 2018), interaction with the external environment and processes involving magnetic fields. Moreover, as already mentioned in Sec. 1.2.1, being able to detect resolved discs allows us to put more constraints onto the gas-to-dust ratio, and thus onto the gas mass. Together with observation of single objects, ALMA in the last years started conducting surveys in many star forming regions (see Fig. 1.10, e.g. Ansdell et al. 2016, 2018; Pascucci et al. 2016; Barenfeld et al.

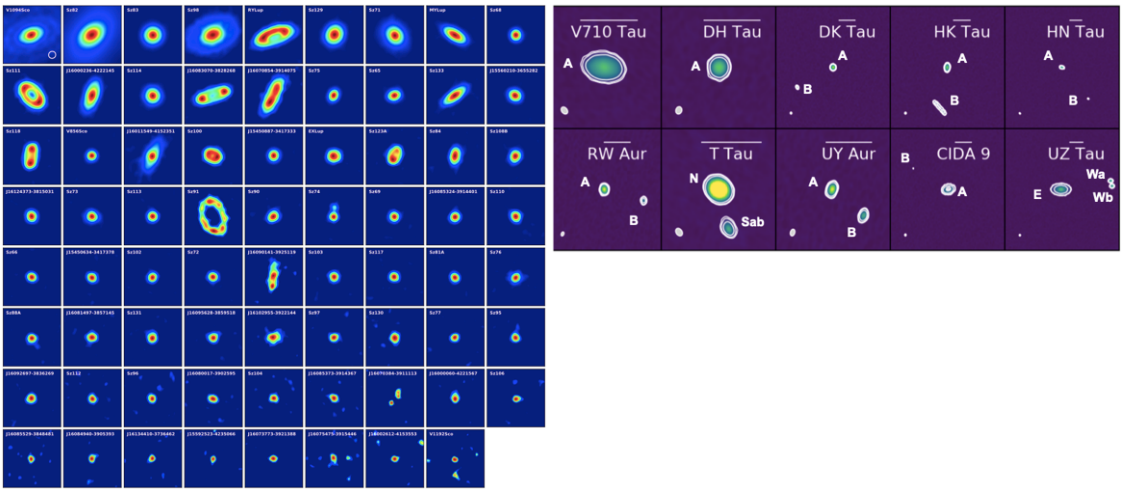

Figure 1.10: Left panels: 1.33 continuum images of the 71 protoplanetary discs (ordered by decreasing continuum flux density) detected in the Lupus survey by Ansdell et al. (2018). Right panels: continuum images of the discs in multiple stellar systems in the Taurus star forming region (Manara et al. 2019a).

2016; Cieza et al. 2019; Maury et al. 2019; Tobin et al. 2019), allowing the derivation of statistical properties, which are fundamental to build a complete picture of the evolution of these system (we cannot observe the evolution of individual objects, as the evolutionary timescales are much too long) and of the planetesimal formation process. A first finding of these studies is that many discs show rather compact and faint (luminosity-size relation, Tripathi et al. 2017; Tazzari et al. 2017; Andrews et al. 2018a) continuum emission at (sub-)millimetre wavelengths (e.g. in Lupus and Ophiucus 40% of the detected sources are still spatially unresolved at a resolution of $\sim$ 30 au, see left panels in Fig. 1.10). As previously mentioned, an explanation to the compactness of this large sample of discs is radial drift, that in the case of a smooth pressure profile results in the accumulation of dust in the inner regions. Instead, if we observe brighter discs, substructures are almost ubiquitous (Andrews et al. 2018a), in particular rings and gaps, and the discs appear to be larger with respect to the previous case. This is suggesting that radial drift accumulates dust pebbles at local pressure maxima at large radii (e.g., Pinilla et al. 2012a; Dullemond et al. 2018). In isolate systems, the difference between the dust and gas disc size is mainly due to the opacity in the CO being higher than in the dust and to the growth and drift of dust grains (Dutrey et al. 1998; Birnstiel & Andrews 2014; Facchini et al. 2017; Trapman et al. 2019, 2020). The observed ratio is typically $\sim 1.5 - 3$ (Ansdell et al. 2018), confirming theoretical hypothesis. An extreme example is given by the faint disc around CX Tau, which shows no (at the moment) detectable substructures, and a very large (> 5) ratio between the gas and dust disc size (Facchini et al. 2019). In multiple systems, the sizes of the disc gaseous component are expected to be truncated to sizes that are a fraction of the distance between the two components, where this result depends on the eccentricity and coplanarity of the orbit, the stellar mass ratio, the viscosity and temperature of the disc (e.g., Papaloizou & Pringle 1977;

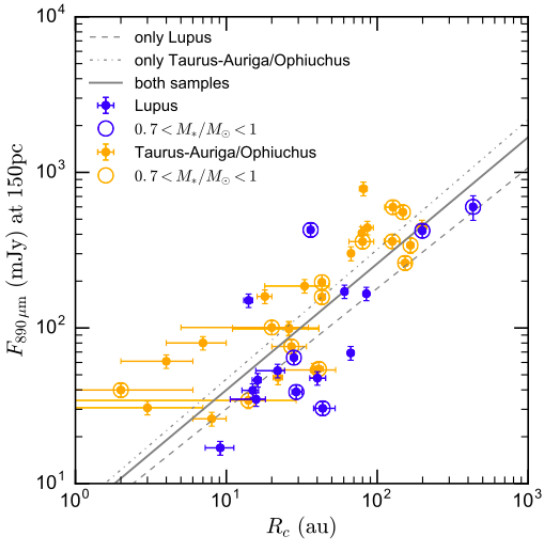

Figure 1.11: 890 μm integrated flux as a function of cut-off radius for the sample of Taurus-Auriga/Ophiuchus (yellow points) and Lupus (blue points) discs. The data have been collected from previous observations (Andrews et al. 2009, 2010; Isella et al. 2010; Guilloteau et al. 2011; Piétu et al. 2014). The disc size have been determined by fitting the spatially resolved observations with an exponentially tapered power-law profile, and correspond to the exponential cut-off radius Rc (Tazzari et al. 2017).

Artymowicz & Lubow 1994; Lubow et al. 2015; Miranda & Lai 2015). It would be interesting to understand if these very small (in the continuum) and faint disc apparently without substructures are hiding a more complex structure or if they really are what they appear to be. Instruments with higher angular resolution would be necessary to solve the mystery. For what concern the dust, Manara et al. (2019a) explored 10 disc structures in multiple stellar systems (collected in the right panel of Fig. 1.10), taken from the Taurus survey (Long et al. 2018b). As expected, the dust radii of disc around multiple stellar systems are smaller with respect to those around singlets in the same stellar mass range and region. The tidal truncation due to the interaction between protoplanetary discs in a multiple system appears to produce a decay of the millimetre continuum emission at the outer radius steeper than discs around single stars. Tazzari et al. (2017) analysed 36 protoplanetary discs in the Lupus star forming region, finding that there is a correlation (see Fig. 1.11) between the integrated sub-mm flux (i.e. the disc mass) and the exponential cut-off radii (i.e. the disc size). They also compared these results with data from the Taurus-Auriga/Ophiuchus region, observing that the Lupus discs are generally fainter and larger. Since these regions have an age difference of 1−2 Myr, a possibility is that the offset in $M_{\rm disc} - R_{\rm disc}$ is due to the viscous spreading of the gas (and thus partially also of the - small coupled - dust). In this work, gas and dust has been assumed as co-localised in space, but observations are often showing that this is an approximation too simplistic. Moreover, Facchini et al. (2017) highlighted how different turbulence values (i.e. viscosity) can drastically affect the estimate of the disc gas outer radius. The left panel of Fig. 1.12 shows the ratio $R_{\rm CO}/R_{\rm mm}$ derived from their models as a function of α: the gas outer radius probed by the CO emission can differ by a factor of ~ 3 for $\alpha = 10^{-4} - 10^{-2}$, and the ratio between the CO and mm emission increases with turbulence. Recently, Rota et al. (to be submitted) analysed new high-resolution Band 6 ALMA observations of line and continuum emission in seven multiple stellar systems in the Taurus region, obtaining that gas radii

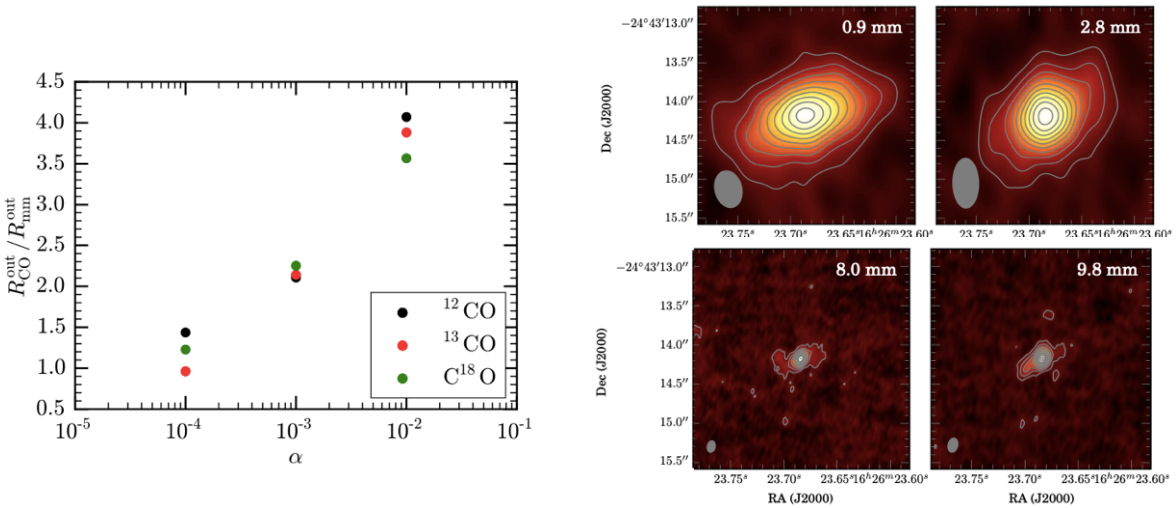

Figure 1.12: Left panel: R_{CO}/R_{mm} derived from their models as a function of α, for different CO isotopologues (Facchini et al. 2017). Right panel:Observation at λ =0.9, 2.8, 8.0, and 9.8 mm of the DoAr 25 protostellar disc. Observations have been made with the Combined Array for Research in Millimeter-wave Astronomy (CARMA), the Sub-Millimeter Array (SMA), and the Very Large Array (VLA) as part of the Disks@EVLA collaboration (Perez et al. 2015a).

in multiple systems are typically $\sim 2-3$ times the dust radii, same as in singles (Sanchis et al. 2021). Another nice link between the disc radial extent and the disc mass has been explored by Powell et al. (2019). In this work, they presented a novel method to determine the disc surface density via the disc "dust lines", which indicate the observed disc radial scale, at different wavelengths.

Finally, also when considering dust disc extent, it is crucial to observe a same protoplanetary discs at different wavelengths. For example, Pinilla et al. (2015) found an evidence for grain growth and radial drift in the circumstellar discs aroung CY Tau and DoAr 25. In the right panel of Fig. 1.12 we report their comparison between four different wavelengths (0.9, 2.8, 8.0, and 9.8 mm) for the DoAr 25 disc.

1.2.3 Disc thermal structure

As a first consideration, one can think that discs are primarily irradiated by the central star, especially in the outer regions (e.g. Adams & Shu 1986). Dusty protostellar envelopes are extremely opaque at the ultraviolet wavelengths at which most of the energy of protostars is emitted. The energy emitted by the central star is therefore absorbed, and since the dust temperature is much lower than the temperature of the central star, it reradiates the absorbed energy at longer wavelengths where the dust opacity is lower. This explain the infrared emission of many protostellar discs (i.e. infrared excess, Kenyon & Hartmann 1987; Chiang & Goldreich 1997). At the same time, we know that protoplanetary discs evolve through viscous accretion of the gas onto the central star. This accretion is an

heating source of the disc, and contributes to the thermal structure. This accretion can explain the strong excess of optical and ultraviolet continuum emission that is observed in some discs (Basri & Bertout 1989).

Thus, we can identify two main source of heating in a protostellar disc, that regulate its thermal structure:

- the dissipation of gravitational potential energy of the accreting material, due to the viscous forces,
- the radiation emitted from the star, and then intercepted and reprocessed by the disc.

Both sources contribute significantly to the thermal balance of the disc. Discs for which the thermal structure is dominated by the intercepted stellar radiation are called "passive" discs. Instead, if the luminosity is due to the internal heating related to the accretion process, they are called "active" discs. Since the accretion process is strictly dependent on the amount of material inside the disc, and so on the mass accretion rate, we expect to observe an evolution in the disc thermal structure. At early epochs discs should be dominated by internal heating, while at later times, when the disc mass is depleted, the protostar mostly irradiates the disc. The general picture of a protostellar discs is that the two sources of heating are both active and their efficiency depends on the disc structure and stellar emission properties (D'Alessio et al. 1998). If the disc extent is large enough, we can identify another heating source coming from nearby stars. The radial temperature profile for an active dis is a power-law, and generally for a protostellar disc we have $T_{\rm disc,visc} \propto (R/R_{\rm in})^{-q}$, with $q = 3/4$ in the Keplerian case. For an irradiated disc, it can be demonstrated that the temperature profile has the same radial behaviour of the active case. These two profiles are derived in the case of a flat disc, but it is known that protoplanetary discs are usually flared (i.e. $H(R)$, where H/R is an increasing function of radius). Indeed, if we take the derived temperature, we have that the sound speed $c_{\rm s} \propto T_{\rm disc,irr}^{1/2} \propto R^{-3/8}$ and the thickness $H = c_{\rm s}/\Omega \propto R^{9/8}$. The disc is puffed up, due to the radiation absorption, and in this way interceps a larger fraction of stellar irradiation, resulting in a less steeper temperature profile (Kenyon & Hartmann 1987; Chiang & Goldreich 1997). By doing some assumption on the irradiation angle, one can derive that for a flared disc $T_{\rm disc,irr} \propto R^{-3/7}$, while Kenyon & Hartmann (1987) have shown that at larger radii it becomes $T_{\rm disc,irr} \propto R^{-1/2}$, reconciling models and observations.

1.2.3.1 Spectral Energy Distribution

Once the temperature profile is known, one can compute the spectral energy distribution (SED), that is what we observe. It can be shown that this will be a superposition of various blackbodies, each one at a different radius R of the disc, with a given $T(R)$ (a multicolor black body spectrum). So, in order to obtain the total disc energy distribution we need to integrate over all the disc extent. The left panel in Fig. 1.13 shows the spectral energy distribution of a flared protoplanetary disc. It is clear that the different components of the system affect the SED in a

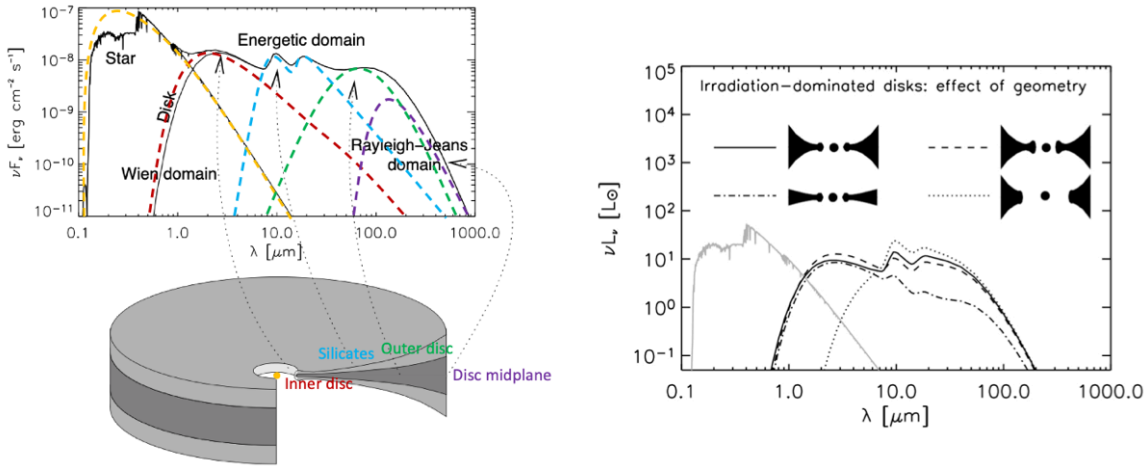

Figure 1.13: Left: Spectral Energy Distribution of a flared protoplanetary disc. Different disc contributions are highlighted with different colours. In yellow it is shown the stellar emission, in red the inner disc, in light-blue the silicates signature, in green the outer disc and in violet the thermal emission of the midplane. Right: different lines represent SEDs for different disc geometries (from flat to flared, with a cavity or with a puffed inner rim). Image adapted from Dullemond et al. (2007).

different way, resulting in a peculiar signature. The yellow lines represent the stellar emission, the red one the inner disc, the light-blue is for the silicates signature, the green for the outer disc and in violet is pictured the thermal emission of the midplane. At the same time, we can note that also different geometries of the disc end up in different SEDs (right panel of Fig. 1.13). The disc blackbody spectrum is given by

$$B_\nu(T) = \frac{2h\nu^3}{c^2}\frac{1}{e^{\frac{h\nu}{KT}} - 1}\,, \tag{1.6}$$

where ν is the radiation frequency. The total flux emitted by the disc (emitted luminosity as function of the frequency) will be

$$I_\nu = \int_{R_{\rm in}}^{R_{\rm out}} B_\nu(T_s) 2\pi R \mathrm{d}R\,, \tag{1.7}$$

where T_s is the disc temperature profile in the general case (that is, a power-law with index q).

We can thus identify three different regimes (see Figure 1.13): the Wien regime, the Rayleigh-Jeans regime, and an intermediate one. In the Wien regime $h\nu \gg KT(R_{\rm in})$ (where $T(R_{\rm in}) = T_{\rm in}$), and so Eq. 1.7 tells us that $I_\nu \propto \exp(-h\nu/KT_{\rm in})$. Instead, in the Rayleigh-Jeans, $h\nu \ll KT(R_{\rm out})$, and we have that $I_\nu \propto \nu^2$. Finally we can describe an intermediate regime, with $KT_{\rm out} \ll h\nu \ll KT_{\rm in}$. In this last case, after a change of variables and some algebraic step, the equation for the total flux gives us

$$I_\nu \propto \nu^{3-\frac{2}{q}}\,. \tag{1.8}$$

If we have a Keplerian disc with $q = 3/4$, then the total flux will be $\propto \nu^{1/3}$. In summary, the full SED of an accreting protostar is given by the spectrum of the star, that, to a first approximation, can be represented by a single blackbody spectrum at the temperature of the stellar photosphere, plus the spectrum of the accretion discs, whose temperature is much lower, so that the SED extends down to longer wavelengths, in the near and mid infrared. The first evidence for the existence of discs around young stars came from observations of infrared excess with IRAS (Beichman et al. 1986).

1.3 Other physical processes related to the disc evoution

Since they are not directly connected with the development of this Thesis, but they are still important in the general context of disc evolution and planetesimal formation, I will briefly mention other physical processes. I refer the interested reader to other readings (for some reviews, Armitage 2013; Alexander et al. 2014; Armitage 2018; Wurster 2021). In particular, Alexander et al. (2014) reviewed the processes that regulate the disc dispersal during its evolution, and that contribute to determine the outcome of planet formation. Specifically, during the planet-forming epoch, the disc evolution is driven by accretion and mass-loss due to winds (Ballabio et al. 2020; Pascucci et al. 2020). Also, photoevaporation by high energy radiation from the central star is thought to dominate the final gas dispersal phase. Together with the internal photoevaporation, there is also the far-ultraviolet (FUV) driven external one (Scally & Clarke 2001; Winter et al. 2018a). Tidal encounters with external objects likely could set the protoplanetary disc initial conditions during the evolution of stellar multiple systems (Winter et al. 2018b; Bate 2018), when the disc is still largely embedded in the molecular cloud core and it is interacting with other protostars/protostellar discs.

In Fig. 1.14 it is schematically described the disc evolution and dispersal phase. Initially, in the Class I phase, accretion onto the star (and still from the envelope onto the disc) is the dominant process. Strong jets and outflows, originated from the inner regions by magnetic effects, characterise this first step. The disc evolves towards a more quiescent phase (Class II phase), where accretion and mass-loss in low-velocity winds are the main processes at play. These winds arise from a combination of X-ray/FUV photovaporation and from magnetic fields (Armitage 2013). Their effect onto the disc is still to be properly understood, and it may vary, but they contribute to the depletion and truncation of the disc. The final disc dispersal phase starts when mass-loss (driven by other kinds of photoevaporation) begins to dominate over accretion. This evolutionary phase is associated with the transition from Class II to Class III SEDs. At this point, the disc is rapidly cleared from inside-out, altering the spatial distribution of the remaining solids. From this point onwards the nascent planetary system is dominated by gravitational and collisional dynamics, and evolves through the debris disc (Wyatt 2018) phase to stability as a mature planetary system.

Armitage (2013, 2015) reviewed also other processes connected to magnetic fields and turbulence. Among others there are magnetic braking, dead zones and vortices (Barge & Sommeria 1995; Balbus & Hawley 1998; Brauer et al. 2007;

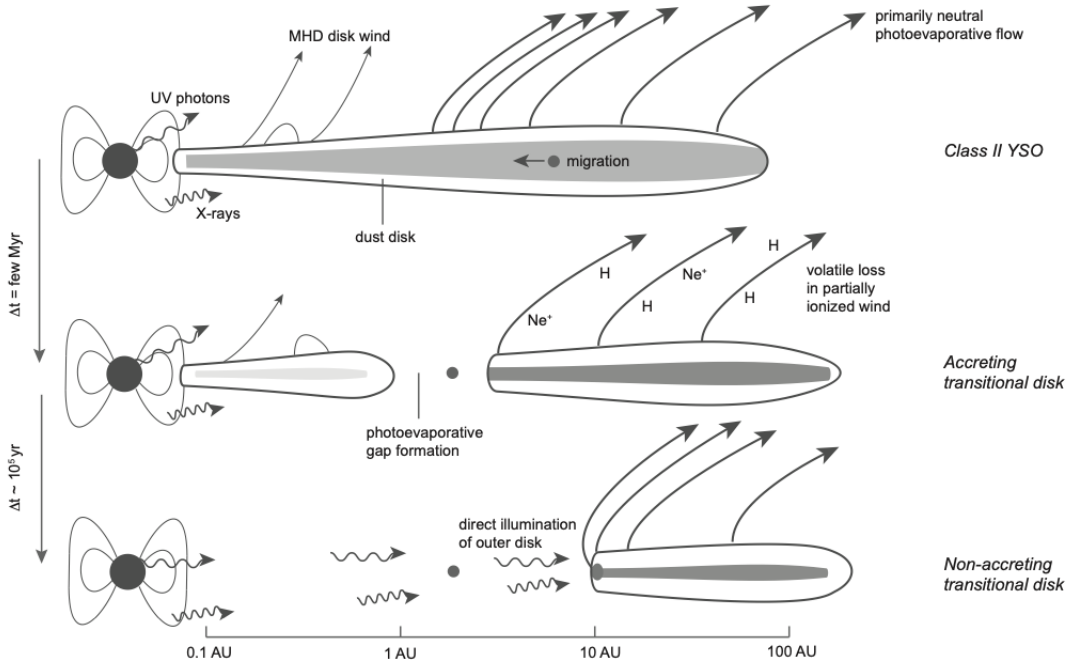

Figure 1.14: Schematic representation of the disc evolution and dispersal sequence. At early times accretion dominates the evolution, while mass-loss is dominated by some combination of X-ray and/or FUV photoevaporation and magnetic fields. At later times the photoevaporative flow is at least partially ionized, driven by EUV and/or X-ray irradiation, and once this wind overcomes the accretion flow the disc is rapidly cleared from the inside-out (Alexander et al. 2014).

Turner et al. 2014). It is interesting to note that measurements of the local strength and coherence of magnetic fields can bring some constraints on the relative importance of internal versus external angular momentum transport, and on the nature of turbulence. Turbulence itself can be counted as one of the potential source of viscosity (see Sec. 2.1.3). It plays a crucial role in the formation and evolution of planets, through its influence on processes ranging from the collisional velocity of small dust grains to the ability of gas-giant planets to open gaps in the disc. Unfortunately, there are very few constraints on its value. In the last year, Flaherty et al. (2020) measured turbulence using new observations of CO emission, finding that it could be weaker than expected ($\alpha < 10^{-3} - 10^{-4}$, see Sec. 2.1.3.3), thus raising new questions on what are the physical mechanisms driving the accretion and evolution of protoplanetary discs.

1.4 How do planets form?

Finally, in this section we briefly review the main processes that regulate planet formation: gravitational instabilities (see also Chapter 3 for a more complete de-

scription) and core accretion (Armitage 2013, 2018). In the first mechanism the dominant actor is the gas, while in the second one the dust, due to its aerodynamical coupling with gas and to its complex dynamics.

1.4.1 The gravitational instability (GI)

The GI scenario for planet formation prescribes that planet formation is a consequence of disc fragmentation when the gaseous disc is massive enough to become gravitationally unstable (Rice et al. 2004; Rice et al. 2006a; Kratter & Lodato 2016). This could happen when the ratio between the disc mass and the star mass $M_{\rm disc}/M_\star$ is greater or of the same order of the disc thickness H/R. This criterion comes directly from the local instability criterion which requires that the Toomre parameter $\mathcal{Q}$ should be lower than 1 (see Sec. 3.1, Toomre 1964), and it can be derived from the dispersion relation of density waves in discs. When this happens, gravitational instabilities excite spiral density waves. At the same time, to properly describe this process, we should take into account the disc cooling mechanism that regulate the evolution of GI in the disc. Indeed, if the gas is not able to cool, the system temperature increases under the effect of contraction induced by self-gravity, and the stability of the system increases. Moreover, the spiral arms generated by the onset of GI produce shocks, which in turn provide a source of heating (and thus of stabilitiy). To describe with a simple toy model the gas cooling mechanism, it is introduced a dimensionless parameter β (Gammie 2001), which is defined as the ratio between the cooling timescale and the dynamical one. Since the instability provides heat on a timescale that is of order the dynamical timescale in the disc, in order to develop fragmentation, one should have both $\beta \gg 1$, the cooling timescale should be shorter than the dynamical one, and $\mathcal{Q} \ll 1$, the disc should be massive enough. By assuming at $\mathcal{Q} = 1$ that the most unstable wavelength is $2\pi H$ (H= disc thickness), we can obtain the fragment mass as

$$M_{\rm frag} = \pi\Sigma\lambda^2 = 4\pi \left(\frac{H}{R}\right)^2 M_{\rm d} = 4\pi \left(\frac{H}{R}\right)^3 M_\star \approx 10\, M_{\rm J} \tag{1.9}$$

where the last identity assumes the disc to be gravitationally unstable. This crude estimate tells us that the gravitational instability can explain mainly the formation of massive planets, or even of low mass star companions (Durisen et al. 2007; Zhu et al. 2012a).

1.4.2 Core accretion

The mechanism of core accretion models the formation of planets as a four step process:

- **Dust growth**: during this initial phase the micrometric dust is dominated by the collisional coagulation process, where thanks to the Van der Walls/electrostatic forces grains stick together reaching dimension of $\sim$ millimetre. This process can be indirectly detected by observations: at (sub-)mm wavelengths the disc is optically thin, and since the dust opacity is a function of the grain size, by measuring the slope of the SED we can extract information about the dust population.

- **Formation of planetesimal**: we go from mm grains to km bodies (i.e. planetesimals). This phase is poorly understood since it is not clear through which mechanism the dust growth in this size range (Blum & Wurm 2008; Youdin 2010). Moreover, we come across the so-called "meter size problem": the migration of meter sized bodies occurs on timescales of the order of ~ 100 yr (Weidenschilling 1977), meaning that the coagulation of dust grains should be extremely (and unrealistically) fast, in order for grains to grow before being accreted onto the star. Possible solutions to this problems have been proposed (such as the streaming instability, Youdin & Goodman 2005, or the existence of dust traps Haghighipour & Boss 2003a,b), but there is still a long way to go to really understand this stage.

- **Formation of rocky cores**: the size of planetesimal continues to grow up to the size of terrestrial planets or of giant planet cores. The growth in this phase is driven by the gravitational attraction and collision of dust grains, known at this stage as "pebbles" (~ 1 cm sized grains, see Ormel 2017 for a review), on to already existing planetesimals.

- **Core accretion**: the body has become a planet. At this stage the disc-planet interaction is dominated by gravitational forces. If the core becomes massive enough its gravitational field is sufficiently strong to retain an atmosphere, i.e. a core envelope in hydrostatic equilibrium. The core mass continues its growth by accreting smaller planetesimal, and when it reaches a critical value of $10\,M_\oplus$, the planet enters a phase of runaway accretion which is modulated by a circumplanetary disc. Accretion onto the planet decreases gradually, until it stopped after a deep gap in the gas has been carved (see Chapter 4) or as a consequence of the disc dispersal caused by e.g., photoevaporation.

Chapter

2

Gas and dust disc dynamics

A vision of gas and dust in Milan skies (lockdown of 2020).

As anticipated in the previous chapter, protoplanetary discs are astronomical objects mainly composed by gas and dust, that originate from substructures in the interstellar medium. Once molecular cloud cores collapse during the star formation phase, they form an accreting disc because of angular momentum conservation. Inside the disc, gas and dust evolve and interact. The dust, in particular, constitutes the building block for planetesimal formation (see Sec. 1.4.2 and 2.2): it is reprocessed and it grows from micrometers to centimetres, up to kilometers size. We note that these two components undergo different but linked physical and chemical processes, and it is crucial to understand them if we want to explain the substructures we observe in protoplanetary discs. The gas dynamics is dominated by accretion onto the central star, and in the late life stages also by dispersal due to photoevaporation and MHD winds. Depending on the amount of gas, the disc can be self-gravitating, and this is the first step in order to develop gravitational instabilities, which are observable in the shape of spiral structures. On the contrary, if the dust-to-gas ratio is high, the gas can be affected by the dust dynamics

(i.e. the back-reaction). Moreover, dust particles dominate the disc opacity, governing their thermal structure and affecting our observations. For this reason, it is necessary to shed light on the interaction between dust and gas and their evolution, and thus investigate the spatial distribution of these two components.

In this Chapter we discuss the gas and dust dynamics and their sometimes interconnected evolution. For the gas description, we follow the approach used by Frank et al. (2002); Lodato (2008); Armitage (2013), while for the dust component we mainly refer to Armitage (2013). We refer the reader to this references for a more detailed description.

2.1 Gas dynamics

At the beginning of the star formation process, the dust, which has a sub-micrometric size, coexists with the gas all over the molecular cloud, and it is not segregated in a specific region. At this stage, the gas-to-dust ratio is typically of 100, of the same order of the interstellar medium (Bohlin et al. 1978). It is because of the following evolution of the system that this value will eventually decrease locally and/or globally, down to value of $10^{-4} - 10^{-1}$ (Moór et al. 2015) in debris discs (i.e. discs mainly composed by solids where the detected gas is thought to be a "second generation" reprocessed gas, Hughes et al. 2018). Therefore, it is correct to firstly investigate the gas dynamics. In a second step (see Sec. 2.2) we will address also the dust dynamics and its more or less coupled evolution with the gas. The main process regulating the gas component in a protoplentary disc is the accretion onto the central star (Pringle 1981). What is causing this accretion motion? The question is still open, but the important thing to keep in mind is that there should be some physical processes able to dissipate gravitational energy, transport outward the angular momentum and thus enabling the gas inward motion. Different mechanisms have been proposed to explain this motion, including the turbulent motion of the gas, which we will refer to as viscosity. Before starting, in order to build a complete physical model for a protoplanetary gaseous accretion disc, we need to make some assumptions.

The thin-disc approximation. We assume that the radial distance R is greater than the vertical typical length scale H, by introducing $H/R \ll 1$, a quantity called aspect ratio of the disc. This approximation is confirmed by observations of discs around protostars, showing a value of $H/R \simeq 0.1$ (if instead we consider disc around AGN the value would be even smaller, i.e. $\simeq 0.001-0.01$). In particular, in the case of protoplanetary disc, it is often assumed an aspect ratio consistent with these values, as reported by Andrews & Williams (2007b,a), who have studied a sample of protoplanetary disc to collect their physical properties. This allows us to consider equations integrated in the vertical direction, using quantities evaluated per unit area (surface density Σ), instead of quantities per unit volume (density ρ):

$$\Sigma = \int \rho \mathrm{d}z \,. \tag{2.1}$$

Axisymmetric discs. In this part, we will consider all the quantities as independent on the azimuthal coordinate ϕ. This assumption should be relaxed when studying actual observations, since asymmetries and peculiar substructures (such as spirals and clumps) are almost ubiquitous in protoplanetary discs (except, up to now, in the fainter and more compact discs).

Non self-graviting discs. We assume for the moment that the gravity of the disc does not influence the disc dynamics and structure, which translates in requiring that,

$$\frac{M_{\rm disc}}{M_\star} \ll \frac{H}{R}\,, \tag{2.2}$$

with $M_{\rm disc}$ and $M_\star$ being the disc and star masses, and H/R the disc aspect ratio. This condition corresponds to $\mathcal{Q} \gg 1$, where $\mathcal{Q}$ is the "Toomre parameter" (see Eq. 3.19 and Chapter 3). However, in the disc early stage this effect could be important and could set the conditions for the birth of planetesimal (Rice et al. 2004; Rice et al. 2006a). Thus, in a second moment, we will also consider the effect of self-gravity on discs (see Chapter 3), a signature of which could be the presence of spiral structures (Kratter & Lodato 2016).

Velocities assumption. Starting from the previous assumptions, particularly the thin-disc one, we can also simplify the discussion on the velocities within the disc. The $H(R)/R \ll 1$ relation corresponds to an equivalent ordering in terms of velocities. We are assuming that the sound speed $c_{\rm s}$ is much smaller than the rotational velocity v_ϕ. This means that the disc rotation is highly supersonic. Another important relation between velocities can be derived by requiring that accretion takes place on a long timescale ($t_\nu \gg t_{\rm dyn}$, where t_ν is the accretion timescale and $t_{\rm dyn}$ is the dynamic one). This condition implies that the radial velocity v_R should be smaller than both the sound speed and the rotational speed, and this leads in a first approximation to orbits that stay circular. So, the final relation for the relevant disc velocities is:

$$v_R \ll c_{\rm s} \ll v_\phi\,. \tag{2.3}$$

Moreover, in the description of our system, we will use cylindrical polar coordinates (R, ϕ, z), with the $z = 0$ plane in the midplane of the disc, and the origin in the central star. So, because we are assuming a fluid gaseous disc, the equations we will use are the fluid dynamics equations, particularly the continuity equation and the Navier-Stokes equations.

2.1.1 Disc fluid dynamics equation

The disc evolution obeys to two fundamental equations:

$$\frac{\partial \rho}{\partial t} + (\boldsymbol{v}\cdot\nabla)\rho = -\rho\nabla\cdot\boldsymbol{v}\,, \tag{2.4}$$

which is the continuity equation (mass conservation law), and

$$\frac{\partial \mathbf{v}}{\partial t} + (\mathbf{v}\cdot\nabla)\mathbf{v} = -\frac{1}{\rho}(\nabla p - \nabla\cdot\sigma) - \nabla\Phi\,, \tag{2.5}$$

which is the momentum conservation law, also known as Navier-Stokes equation. ρ is the gas mass density, $\mathbf{v}$ is the fluid velocity, P is the pressure, σ is the stress tensor, and Φ is the gravitational potential. This last term can be calculated by solving the Poisson equation,

$$\nabla^2\Phi = 4\pi\mathcal{G}\rho\,, \tag{2.6}$$

where $\mathcal{G}$ is the gravitational constant. Φ may be written as $\Phi_\star + \Phi_{\rm disc}$, where $\Phi_\star$ is the central star (or stars if there is a binary system) contribution and $\Phi_{\rm disc}$ the disc contribution, when the disc is self-gravitating (Bertin & Lodato 1999, and see Chapter 3). Given the previous assumption on the gravitational potential, in this first part we will focus on

$$\Phi = \Phi_\star = -\frac{\mathcal{G}M_\star}{r}\,. \tag{2.7}$$

The stress tensor describes the effect of viscous forces, which is a very important ingredient in the accretion process. Viscosity is one of the most complex and studied topics in the field of accretion discs, and it has not been completely understood yet (for a more detailed discussion see section 2.1.3). It may include non-local mechanisms of angular momentum transport, but in the simplest case, σ is assumed to be the shear viscosity[1]. Indeed, the gas in a disc is characterised by differential rotation, where each annuli communicates with its neighbours via some physical mechanism, such as chaotic thermal motion or turbulent motion. Thus, in cylindrical coordinates, the only one non-vanishing component in a circular shearing flow is the $R\phi$ component:

$$\sigma_{R\phi} = \eta R\frac{\mathrm{d}\Omega}{\mathrm{d}R}\,, \qquad \nabla\cdot\sigma|_\phi = \left(\frac{\partial}{\partial R} + \frac{2}{R}\right)\sigma_{R\phi} \tag{2.8}$$

where $\Omega = v_\phi/R$ is the angular velocity and η is the shear viscosity coefficient.

Given the approximation of thin disc, we can integrate both Eq. 2.4 and Eq. 2.5 in the vertical direction, obtaining:

$$\frac{\partial\Sigma}{\partial t} + \frac{1}{R}\frac{\partial}{\partial R}(R\Sigma v_R) = 0\,, \tag{2.9}$$

$$\Sigma\left[\frac{\partial v_R}{\partial t} - \frac{v_\varphi^2}{R}\right] = -\frac{\partial P}{\partial R} - \Sigma\frac{\partial\Phi}{\partial R}, \tag{2.10}$$

$$\Sigma\left[\frac{\partial v_\varphi}{\partial t} + v_R\frac{\partial v_\varphi}{\partial R} + \frac{v_R v_\varphi}{R}\right] = \frac{1}{R^2}\frac{\partial}{\partial R}(R^2\ \mathrm{T}_{R\varphi})\,, \tag{2.11}$$

where Σ, P and $T_{R\varphi}$ are the vertically integrated versions of, respectively, ρ, p and $\sigma_{R\varphi}$. In particular, $T_{R\varphi}$ (the only non vanishing component) can be written as,

$$T_{R\phi} = \nu\Sigma R\frac{\partial\Omega}{\partial R}\,. \tag{2.12}$$

[1] Another term contributing to the stress tensor can be the bulk viscosity, related to the compression of the fluid. In our case, since we are considering an ideal fluid, this term can be neglected. This is not the case when including also non-ideal MHD effects.

The shear viscosity coefficient η in Eq. 2.8 has been integrated on the vertical direction, becoming the vertical averaged kinematic viscosity $\nu = \Sigma^{-1} \int_z \eta \mathrm{d}z$.

The Navier-Stokes equation (Eq. 2.5) has three components in the radial, vertical and azimuthal directions. Through the study of each component, we can derive some important properties of accretion disc (in Figure 2.1 we can see a geometrical sketch of the disc structure).

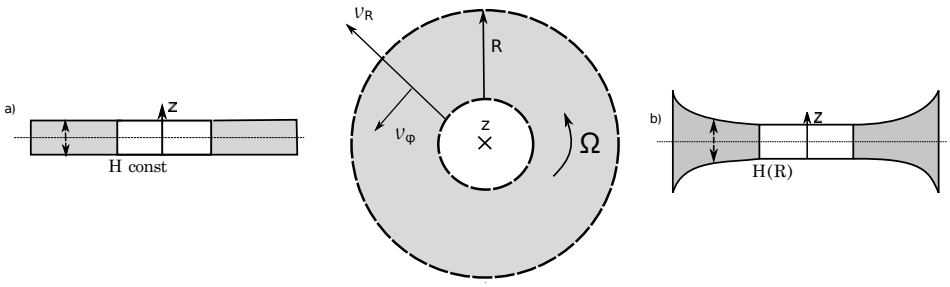

Figure 2.1: Geometric representation of the disc structure in cylindrical coordinates (R, z, ϕ). a) shows a flat disc profile, with constant disc thickness H. b) shows a flares disc profile, with $H(R)$ varying with the radial direction R ($H(R)$ increasing with R). Usually discs are observed to have a flaring angle (see Sec. 1.2.3).

2.1.1.1 The radial structure: centrifugal balance

Firstly, we consider the radial projection of the Navier-Stokes equation 2.5. Because of the velocity assumptions previously made ($v_R \ll v_\varphi$, otherwise, the disc would accrete onto the central object in less than the time required for an orbit) the only non-zero term in the left hand side (l.h.s.) is the centrifugal one, $-v_\phi^2/R$. On the right hand side (r.h.s.) the stress tensor term vanishes, because viscosity does not act in the radial direction. We thus get the centrifugal balance,

$$\frac{v_\phi^2}{R} \simeq \frac{\partial \Phi}{\partial R} + \frac{1}{\rho}\frac{\partial P}{\partial R}\,, \tag{2.13}$$

where for the case of a non self-gravitating disc (in the thin disc approximation) the contribution of the central star to the gravitational potential is given by,

$$\frac{\partial \Phi}{\partial R} = \frac{\mathcal{G} M_\star R}{(R^2 + z^2)^{3/2}} \underset{z \ll R}{\approx} \frac{\mathcal{G} M_\star}{R^2}\,. \tag{2.14}$$

Therefore, through the centrifugal balance we describe the disc rotation curve as an azimuthal velocity, given by the Keplerian velocity $v_\mathrm{k} = \sqrt{\mathcal{G} M_\star / R}$ (with an angular velocity $\Omega_\mathrm{k} = \sqrt{\mathcal{G} M_\star / R^3}$) plus a pressure correction term. To quantify the pressure term, we can assume a power-law profile for the surface density ($\Sigma \propto R^{-p}$) and for the temperature ($T \propto R^{-q}$), a barotropic disc, and we define the disc aspect ratio as $H/R = c_\mathrm{s}/v_\mathrm{k}$. By substituting them in Eq. 2.13, we derive

$$v_\phi = v_\mathrm{k} \left[1 + \zeta \left(\frac{H}{R} \right)^2 \right]^{1/2}\,, \tag{2.15}$$

where

$$\zeta = \frac{\partial \ln \rho}{\partial \ln R} = -\left(p + \frac{q}{2} + \frac{3}{2}\right) . \tag{2.16}$$

In typical protoplanetary disc $p = 1$ and $q = 1/2$, giving $\zeta < 0$. Moreover, $(H/R)^2 \ll 1$ ($H/R \sim 0.1$ for protostellar disc, and $\simeq 0.05$ for protoplanetary discs, Andrews & Williams 2007b), thus, when considering the small contribution given by pressure, the gas would be sub-Keplerian. This characteristic is important, because in the context of protoplanetary disc, where dust and gas partially co-exist, the solids are not subject to pressure, and would move on Keplerian orbits. In Sec. 2.3 we will see that this difference in velocity is the starting point for crucial interactions between dust and gas, in particular it determines a fast inward migration of the solid bodies (Weidenschilling 1977).

It is interesting to note (see Fig. 2.2 for two examples) that other deviations from the Keplerian velocity field come from the disc being self-gravitating (see Chapter 3 and Chapter 8, e.g. Lodato & Bertin 2003), or from a planet embedded in the disc (Pinte et al. 2018b; Teague et al. 2018; Pinte et al. 2019; Casassus & Pérez 2019; Pinte et al. 2020). In the first case, it can be demonstrated that the deviation is actually larger than the pressure correction, while in the second case it is a local deviation, both in space and velocity (see Chapter 5).

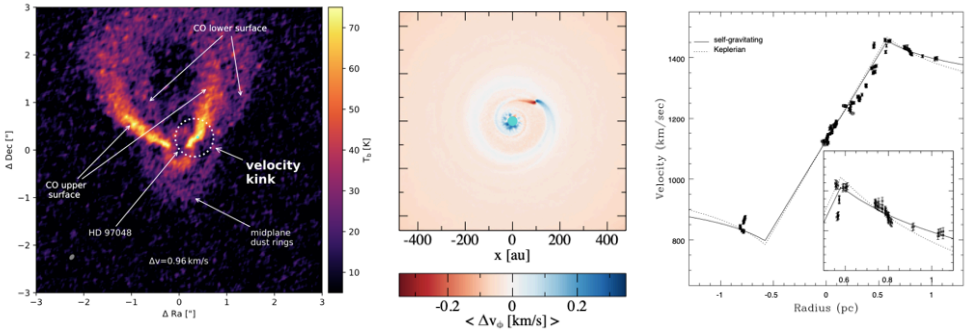

Figure 2.2: Left and center: ALMA observation of the dust and gas disc surrounding HD 97048, and modeling of the gas azimuthal velocity offset compared to the Keplerian velocity (Pinte et al. 2019). Right: fit with a self-gravitating model to the rotation curve of the accretion disc surrounding the active galactic nuclei NGC 1068 (Lodato & Bertin 2003).

2.1.1.2 The vertical structure: hydrostatic equilibrium

When considering the vertical projection of the Navier-Stokes equation 2.5, we can describes the vertical structure of the disc. The z component of the velocity can be neglected, since we made the assumption of thin-disc approximation. The viscous force vanishes as well, since the non-zero component of the stress is in the $R\phi$ direction. The remaining terms are the gravitational force and the pressure force that balance themselves in the vertical direction (i.e. hydrostatic equilibrium):

$$\frac{1}{\rho}\frac{\partial P}{\partial z} = -\frac{\partial \Phi}{\partial z} . \tag{2.17}$$

Moreover, in the non self-graviting disc approximation, the vertical component of the gravitational force becomes $g_z = \mathrm{d}\Phi/\mathrm{d}z = {\Omega_\mathrm{k}}^2 z$. Assuming also a barotropic fluid and using the definition of the disc thickness $H = c_\mathrm{s}/\Omega_\mathrm{k}$, we can derive the density profile of the gaseous disc in the vertical direction:

$$\rho(z) = \rho_0 \exp\left(-\frac{z^2}{2H^2}\right). \tag{2.18}$$

From this relation we see that the density profile is a gaussian, and we can write the density at the midplane ρ_0 as $\Sigma/\sqrt{2\pi}H$. Considering the definition of the disc thickness, since $H \propto c_\mathrm{s} \propto T^{1/2}$, there is a relation between the thickness and the disc temperature: due to thermal pressure, the disc expands in the vertical direction, counteracting gravity. This means that the shape of the disc depends upon $H(R)/R = c_\mathrm{s}/v_\varphi$, where at a first approximation (see Eq. 2.15) $v_\varphi \approx v_\mathrm{k} = \Omega_\mathrm{k} R$. Therefore, in order to build a complete description of the disc, we need to know how does this quantity (related to the temperature T) vary with radius. Parametrizing the radial variation of the sound speed with $c_\mathrm{s} \propto R^{-q}$, we can write the aspect ratio as

$$\frac{H(R)}{R} \propto R^{1/2-q}. \tag{2.19}$$

Depending on q, we can have two different shape (for a schematic representation see also Figure 2.1): if $q = 1/2$ the disc will be flat, while if $q < 1/2$ the disc will be flared, and as a consequence it will intercept a larger fraction of the stellar radiation. To resume, to obtain a complete description for the disc geometry, we need to know how these parameters (aspect ratio, temperature) vary with radius. In particular, considering the vertical structure of the disc, we need to know how does the temperature vary with R. This quantity can assume significantly different values, and in particular it strongly depends on whether the disc is "active" (heated by the accretion process), or "passive", (heated by the central star), as discussed in Sec 1.2.3. Finally, we note that the aspect ratio is the inverse of the Mach number of the gas, thus $H/R \ll 1$ implies that the gas azimuthal motion is highly supersonic, $v_\varphi = v_\mathrm{k} \gg c_\mathrm{s}$.

2.1.1.3 Azimuthal component: angular momentum conservation

Finally, we discuss the last component of the Navier-Stokes equation, strictly linked to the angular momentum conservation. First, we assume that along the azimuthal direction, the pressure and gravitational force does not give any contribution due to the axisymmetry of the disc, and we integrate the equation along the vertical direction. Then, by combining Eq. 2.11 with the continuity equation 2.9 and the definition of the stress tensor (Eq. 2.12), the angular momentum conservation equation becomes:

$$\frac{\partial}{\partial t}(R\Sigma v_\phi) + \frac{1}{R}\frac{\partial}{\partial R}(R v_R \Sigma R v_\phi) = \frac{1}{R}\frac{\partial}{\partial R}(\nu \Sigma R^3 \Omega'), \tag{2.20}$$

where in the l.h.s. we have the Lagrangian derivative of the angular momentum per unit mass (angular momentum time derivative + radial advection), while in

the r.h.s. there is the torque exerted by the viscous forces.[2] In this equation the viscous forces are a term of angular momentum transfer and redistribution inside the disc. We will see how this physical mechanism happens, and how it is related to the accretion process (see Sec. 2.1.3).

Density evolution By means of the continuity (Eq. 2.9) and the angular momentum conservation (Eq. 2.11) equations, and assuming that the disc is Keplerian, $\partial_t v_\varphi = \partial_t \Omega = 0$, one can derive the radial velocity v_R[3] as,

$$v_R = \frac{1}{R\Sigma(\Omega R^2)'} \frac{\partial}{\partial R} \left(\nu \Sigma R^3 \Omega' \right) , \tag{2.22}$$

where $(\Omega R^2)' = \mathrm{d}(\Omega R^2)/\mathrm{d}R$. Inserting back this relation in the continuity equation, we find the time evolution for the surface density of the gas

$$\frac{\partial \Sigma}{\partial t} = \frac{3}{R} \frac{\partial}{\partial R} \left[R^{1/2} \frac{\partial}{\partial R} (\nu \Sigma R^{1/2}) \right] , \tag{2.23}$$

which is a diffusion equation, where ν is the quantity that determines the evolution of the disc density, through the accretion process. From a simple dimensional analysis, the viscous evolution timescale is $t_\nu = R^2/\nu$. We can compare this timescale with the dynamical timescale $t_{\mathrm{dyn}} = \Omega^{-1}$, obtaining

$$\frac{t_\nu}{t_{\mathrm{dyn}}} = \frac{R^2 \Omega}{\nu} . \tag{2.24}$$

Then, through the velocity ordering ($v_\phi \gg v_R$), we find a relationship between the viscous and the dynamical timescale, that is $t_\nu \gg t_{\mathrm{dyn}}$. It means that accretion through viscosity is a slow process. We can define the ratio between the two timescale (Eq. 2.24) as the Reynolds number of the flow which is essentially a measure of the ratio of inertial forces (acting on a dynamical timescale) to viscous forces (acting on the viscous timescale). Starting from this definition one can describes different flow regimes: at low Reynolds numbers, where viscous forces are dominant, the fluid is characterized by a laminar flow, while for high Reynolds numbers inertial forces tend to produce turbulence phenomena (i.e. turbulent flow). The diffusion equation can be analytically solved for some particular cases, leading to two time-dependent solutions (the "spreading ring" and the self-similar solution) and one time-independent (the steady-state solution).

2.1.2 Accretion disc evolution

Find the solutions for the diffusion equation 2.23, which describes the temporal evolution for the surface density of the gas, is not trivial. Indeed we do not

[2] Keep in mind that for a Keplerian disc, $v_\phi = \sqrt{GM/R}$, $\Omega = v_\phi/R = \sqrt{GM/R^3}$, and $Rv_\phi = \sqrt{GMR}$

[3] In the case of a Keplerian disc the radial velocity equation becomes,

$$v_R = -\frac{3}{\Sigma R^{1/2}} \frac{\partial}{\partial R} \left(\nu \Sigma R^{1/2} \right) \sim \frac{\nu}{R} . \tag{2.21}$$

have any information about ν, and generally we would have $\nu = \nu(\Sigma, R)$. In the following, we resume the analytical solutions that can be found for time-dependent and steady-state configurations, under specific assumptions for the functional form of ν. In particular, we assume that ν does not depend on Σ, and that its radial dependence is just a simple power-law, $\nu \propto R^b$.

2.1.2.1 Time dependent solutions

A first possible solution is given by considering an initial mass distribution in the shape of an infinitesimally thin ring of mass m centered at a certain radius, with constant ν, and Σ with the shape of a Dirac δ function. The solution to Eq. 2.23 in this case was found by Lynden-Bell & Pringle (1974), and it takes the name of "spreading-ring solution" (see left panel in Figure 2.3). Ideally, in order to have accretion, and at the same time to respect the angular momentum conservation, a little bit of material has to go to infinity with all the angular momentum: the disc spreads, inward and outward, due to viscous forces.

A second kind of solutions have been found for $b > 0$. Here we just describe for brevity the case $b = 1$, so the viscosity has a linear dependence on radius. The initial mass distribution is a power law truncated exponentially at a given radius. The solution, showed in the right panel of Fig. 2.3, is a time dependent truncated exponential ("self-similar solution", Lynden-Bell & Pringle 1974; Hartmann et al. 1998), with a normalisation constant that decreases with increasing time, while the exponential truncation moves outward increasing time. We note that in this solution, the timescale is evaluated at the truncation radius, and so it is a local quantity. Moreover, after some manipulation one can find that the transition radius between inward and outward moving flow, is $R_{\rm tr} \sim R_1\,[1 + t/t_\nu]$, that moves outwards with time. This solution comes to be very useful from an observational point of view, for the description of the protostellar disc evolution. Usually, it can be used to derive the level of disc viscosity by measuring the radial extent of the gaseous disc (by means of spatially resolved observations) and by estimating the viscous timescale (e.g., by looking at the fraction of young stars with discs, at different ages). Finally, this class of solutions has been used to derive the disc properties by comparing high-resolution observations with the predictions of models of flared discs.

2.1.2.2 Steady-state solutions

A third class includes time-independent solutions for the diffusion equation of a Keplerian disc, with $\partial\Sigma/\partial t = 0$. This solution may not seem accurate to describe system which actually have a time evolution, but it can help us to understand some of the disc properties. From this assumption, the continuity and the angular momentum conservation equations (Eqs. 2.9 and 2.20) become

$$\dot{M} = -2\pi R v_R \Sigma\,, \tag{2.25}$$

$$\dot{M} R^2 \Omega - 3\pi\nu\Sigma R^2\Omega = \dot{J}\,, \tag{2.26}$$

where two new quantities have been introduced as $\dot{M}$, i.e. the mass accretion rate, and $\dot{J}$, i.e. the net flux of angular momentum. The signs have been chosen

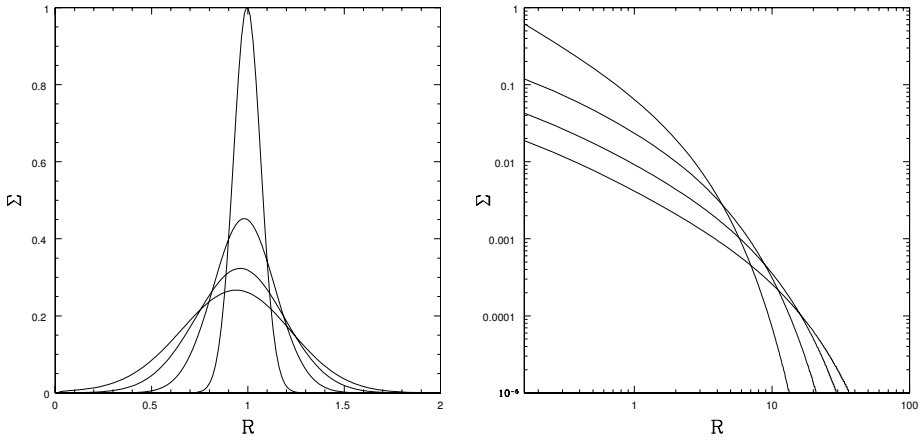

Figure 2.3: Two time-dependent solutions to the diffusion equation: in the left panel, the evolution of the spreading ring solution, in the right one, the self similar solution, arranged from Lodato (2008). The two lines tell us that if our instrument has different (low/high) sensitivity to a surface density, we would see our disc getting contracted or expanded, at larger time.

such that for $v_R < 0$ (directed inward), then $\dot{M} > 0$, which means accretion. In the second equation, in the l.h.s. we find the angular momentum transported by the accretion process plus the outward flux material originated by the viscous forces. We can determine in a more explicit way $\dot{J}$ by means of the "no-torque" boundary condition. This condition states that there is a boundary region between the central object and the disc where the gas angular velocity profile flattens as it reach the (lower) velocity of the star. Indeed, it should be $\Omega_\star \ll \Omega_{\rm k}(R_{\rm in})$, where $\Omega_{\rm k}(R_{\rm in})$ is the break-out velocity at which the star would be disrupted by the centrifugal force (Frank et al. 2002). We point out that in general for protostellar discs, one does not expect to have a boundary layer, but magnetospheric accretion. Although, for our derivation, we still use the no-torque condition, obtaining

$$\dot{J} = \dot{M} {R_{\rm in}}^2 \Omega(R_{\rm in})\,. \tag{2.27}$$

By using the Keplerian velocity and inserting $\dot{J}$ in equation 2.26, we find the steady-state solution:

$$3\pi\nu\Sigma = \dot{M}\left(1 - \sqrt{\frac{R_{\rm in}}{R}}\right)\,. \tag{2.28}$$

For $R \gg R_{\rm in}$, the solution becomes

$$\dot{M} = 3\pi\nu\Sigma\,, \tag{2.29}$$

where $\dot{M}$ has a constant value. It means that the quantity $\nu\Sigma$ is constant, and if we know something about the surface density profile we can infer also the radial viscosity profile, and this can be very useful in order to deepen our knowledge on the disc properties. In particular, this relation has been often used in observational investigations of protostellar discs to derive estimates of the disc viscosity starting

from the measured value of the mass accretion rate (Andrews & Williams 2007b,a; Andrews et al. 2009; Pinte et al. 2016).

2.1.2.3 Accretion disc energetics

Another important aspect to consider when describing the accretion dynamics of protoplanetary disc (but also more in general of accretion discs) is the disc energetics. First of all, we consider how much energy is dissipated by a disc during the angular momentum redistribution ("active disc", see Sec. 1.2.3). Indeed, viscous torques convect energy between neighbouring annuli across the disc and dissipate gravitational potential energy into heat. Following the approach from Frank et al. (2002), one can compute the dissipation effect, and so the energy dissipated per unit time and surface, from both the disc sides, as

$$D(R) = \frac{G\Omega'}{2\pi R} = \nu\Sigma(R\Omega')^2 \tag{2.30}$$

and by inserting the Keplerian velocity, we obtain

$$D(R) = \frac{9}{4}\nu\Sigma\Omega^2 \,. \tag{2.31}$$

Assuming a steady-state solution for the disc surface density (see Eq. 2.28), we can calculate the total power emitted by a Keplerian disc with an infinite extent,

$$L = \int_{R_{\rm in}}^{\infty} 2\pi R D(R) \mathrm{d}R = \int_{R_{\rm in}}^{\infty} \frac{3}{2}\frac{GM\dot{M}}{R^2}\left(1-\sqrt{\frac{R_{\rm in}}{R}}\right)\mathrm{d}R = \frac{1}{2}\frac{GM\dot{M}}{R_{\rm in}} \,. \tag{2.32}$$

So, we can note that while we gain $GM/R_{\rm in}$ of gravitational energy, a half remains as kinetic energy in order to support the disc in centrifugal equilibrium, and the other half is dissipated due to the viscous forces. For a deepen discussion we refer to Lodato (2008). From this energetics argument, it is possible to recover the thermal structure of active accretion discs (see Sec. 1.2.3, also for the "passive" thermal structure).

2.1.3 Turbulent angular momentum transport and viscosity

Until now we have highlighted how fundamental is viscosity in the accretion process in discs (both around protostars but also around, for example, black holes). But what do we know about viscosity? What are the physical mechanisms that produce it? Is viscosity in accretion discs the same physical quantity we know here on Earth? What is its magnitude and on what timescale does it play a role? The discussion that arises from all these questions has been and still is quite active in the scientific community. So far, it is not yet clear which process is mainly responsible for governing the theory of viscous accretion.

To understand what are the key points behind the angular momentum transport in accretion disc, we can start by looking at the ratio between the viscous and the dynamical timescale, also known as Reynolds number (see Eq. 2.24). This quantity is found to be quite large in accretion discs. Indeed, we can consider molecular collisions as a first candidate to explain the viscous disc evolution,

as they generate a viscosity $\nu_{\rm mol}$ in a shear flow because of the finite mean-free path λ in the gas. In this case, when computing the Reynolds number, using values typical in protostellar discs, one can found a viscous timescale of the order of 10^{13} yrs, which is much longer with respect to the disc lifetime. This is due to the fact the the gas density in this system is very low. As a consequence, the Reynolds number is $\approx 10^{10}$ (Armitage 2013), meaning that $\nu_{\rm mol}$ is not a good candidate. However, it is interesting to note that fluids with such an high Re numbers are expected to develop turbulence (i.e. strong fluctuations in the velocity field). This turbulence, whatever is the physical origin, could be the responsible for the angular momentum transport we are seeking.

2.1.3.1 Turbulence

It is known that the transport mechanism is more effective in turbulent flows with respect to laminar ones. Indeed, in the first case, the angular momentum is transported through the violent mixing (Turner et al. 2014) of fluid elements (that in some cases, belong to regions very distant between them[4]), while in the second one the angular momentum is exchanged through collisions of individual gas molecules on a timescale that exceeds the Hubble time. Then, assuming that there exist some mechanism that extract energy from the mean flow and inject the latter in the fluctuations, we can compute the torque exerted by these fluctuations to measure the flux of angular momentum. Balbus & Hawley (1998), assuming an inviscid disc ($T_{R\varphi} = 0$, i.e. molecular viscosity is a negligible component), and separating the fluid velocity in a secular varying average component v plus a rapidly varying fluctuating component u (i.e. a velocity perturbation has been introduced), computed the vertically integrated perturbed Navier-Stokes equation (see Eq. 2.11) as,

$$\frac{\partial}{\partial t}\left(\Sigma R v_\varphi\right) + \frac{1}{R}\frac{\partial}{\partial R}\left[R u_R \Sigma R v_{\varphi,0}\right] = -\frac{1}{R}\frac{\partial}{\partial R}\left[\Sigma R^2 \left\langle u_\varphi u_R \right\rangle_\varphi\right] \tag{2.33}$$

where the angle brackets indicate an azimuthal average. We can see that even without explicitly including any form of viscous transport of angular momentum ($T_{R\varphi} = 0$), if a positive correlation between u_φ and u_R exists, one can write the Reynolds stress as,

$$T_{R\phi}^{\rm Reyn} = -\Sigma_{\rm g} \left\langle u_{{\rm g},R} u_{{\rm g},\phi} \right\rangle \ . \tag{2.34}$$

This turbulence related stress acts in the same way of the viscous stress tensor $T_{R\phi}$. This means that velocity fluctuations are sufficient to provide a stress, which is at the origin of the angular momentum transport in a purely hydrodynamical flow. However, this is not enough to describe how accretion discs work. Together with a turbulent fluid, it is required a mechanism able to constantly inject energy in it, otherwise turbulence would gradually decrease as a consequence of dissipative effects. Such a mechanism could be found, for example in disc instabilities that might produce disturbances of the velocity field. Up to now, there are several

[4] Indeed, the typical collisional mean free path can be several orders of magnitudes smaller than the lengthtscale of turbulent processes, and angular momentum transport can be much more effective.

candidates: the magneto rotational instability (MRI), the gravitational instability (GI), the Rayleigh-Taylor (RTI) instability induced in magnetically arrested discs (MAD, Narayan et al. 2003; Marshall et al. 2018) and many others mechanisms (with the requirement of producing a non vanishing $\langle u_\varphi u_R \rangle_\varphi$). In particular, if the disc is magnetized and fully ionized, the perturbed magnetic field B provides an angular momentum transport, leading to the so-called "Maxwell" stress,

$$T^{\mathrm{M}}_{R\phi} = -\Sigma_{\mathrm{g}} \left\langle u^A_R u^A_\varphi \right\rangle , \tag{2.35}$$

where u^{A} is called Alfven velocity. Instead, if the disc is self-gravitating, the perturbed gravitational field provides a stress in the form,

$$T^{\mathrm{grav}}_{R\phi} = -\Sigma_g \left\langle u^g_R u^g_\varphi \right\rangle , \tag{2.36}$$

By bringing all these elements together, in steady state, the angular momentum flux in a magnetized and self-gravitating inviscid disc is therefore given by

$$\dot{J} = \dot{M} R^2 \Omega - 2\pi \Sigma_{\mathrm{g}} R^2 \left(\langle u_R u_\varphi \rangle + \left\langle u^A_R u^A_\varphi \right\rangle + \left\langle u^g_R u^g_\varphi \right\rangle \right) , \tag{2.37}$$

where this expression accounts for the angular momentum flux advected with the inward flow and generated from internal stresses, including Reynolds stress, Maxwell stress, and stress arising from perturbations in the gravitational fields.

It is important to highlight that the presence (or not) of turbulence in protoplanetary discs has strong implications for a range of planet formation stages, including the vertical settling and the collisional growth of dust grains (Fromang & Papaloizou 2006; Youdin & Lithwick 2007; Birnstiel et al. 2010b), the radial diffusion (Clarke & Pringle 1988), the concentration of dust particles (Cuzzi et al. 2008; Johansen et al. 2009; Simon & Armitage 2014), the trapping of dust in asymmetric vortices (Pinilla et al. 2015), and the migration of planetary bodies (Nelson & Papaloizou 2004; Baruteau et al. 2011; Paardekooper et al. 2011). Moreover, turbulence is expected to affect the sharpness and morphology of dark gaps and dust rings (Pinte et al. 2016; Huang et al. 2018a; Dullemond et al. 2018).

2.1.3.2 Disc instabilities

As mentioned above, disc instabilities that satisfy the requirement of producing a non zero correlation between the radial and the azimuthal velocities of the fluid can produce an effective transport of angular momentum, acting as a source of viscosity. It is also interesting to note that a completely different perspective can be taken. One can indeed assume that the evolution of the disc is driven by the loss, and not the redistribution (as assumed so far), of the angular momentum. The loss of angular momentum may be mediated by magnetic field lines crossing the disc and thus generating magnetic winds (see right panel, Fig. 2.4). We briefly present here some of the possible candidates (for a review check Armitage 2013; Lyra & Umurhan 2019), which are schematically pictured in Fig. 2.4 (Hartmann 2009).

The Rayleigh criterion. The linear stability of a shearing flow with a smoothly varying $\Omega(R)$ against axisymmetric perturbations, in a non-magnetized, non-self-gravitating disc, is given by the Rayleigh criterion (Pringle & King 2007). The stability analysis can be done though a perturbation analysis, searching for exponentially growing or decaying modes for which the frequency of the perturbation is imaginary. The stability requirement is that

$$\frac{\mathrm{d}l}{\mathrm{d}r} = \frac{\mathrm{d}}{\mathrm{d}r}\left(r^2\Omega\right) > 0 \tag{2.38}$$

where l is the disc specific angular momentum, which in a Keplerian disc is an increasing function of radius, $\propto \sqrt{r}$. This means that the flow is predicted to be hydrodynamically stable, despite the huge value obtained for the Re number. Thus, the viscosity source should be searched elsewhere.

Magneto-rotational instability: MRI. One good candidate is given by the magneto-rotational instability (Balbus & Hawley 1991; Hawley & Balbus 1991; Balbus & Hawley 1998), described schematically in the left panel of Fig. 2.4. When temperature is high enough for the gas to be ionized, the disc is made of plasma (ionized gas) in differential rotation, and if it is subject to a weak magnetic field, it becomes unstable. Indeed, the magnetic field lines are stretched by differential rotation ($\Omega \propto R^{-3/2}$): if we consider two fluid elements in neighbouring annuli, they will tend to increase their distance as time increases. Instead, the magnetic field line that connects the two points will tend to shorten the distance between them, accelerating the outer ring and decelerating the inner one. As a consequence, we have a transfer of angular momentum from the inner ring of the disc, to the outer ones. Indeed, it can be shown that the condition for MRI instability to arise is given by $\partial\Omega^2/\partial R < 0$, which is usually satisfied in accreting disc (except for the disc boundary layer) when assuming a perfect coupling between the gas and the magnetic field. This is possible when the gas reaches a very high temperature ($T \geq 1000$ K). The problem is that the majority of the disc mass is located in regions near the midplane or in the outer part of the disc (Bai 2011; Bai & Stone 2011), where the temperatures are much lower. This leads to the formation of large "dead zones" in which MRI is not effective (Gammie 1996; Martin & Lubow 2011). Thus, in order for MRI to be effective a ionization mechanism (for examples, X-ray and cosmic ray from the star) should be necessary. Moreover, these dead-zones could produce axisymmetric (mostly known as zonal flows) and non-axisymmetric density structures which might be identified with ALMA (Flock et al. 2015; Ruge et al. 2016).

Gravitational instability. Another possibility in order to find a source of energy to feed the turbulence, comes from the gravitational instability (for a review see Lodato 2007; Kratter & Lodato 2016). We refer the reader to Chapter 3 for a deeper introduction and discussion to self-gravitating discs and to its importance for what concern angular momentum transport. Qualitatively speaking, we can suppose that instead of a magnetic field line, as in the previous case, there is a radially extended mass concentration (central panel of Fig. 2.4). The gravitational

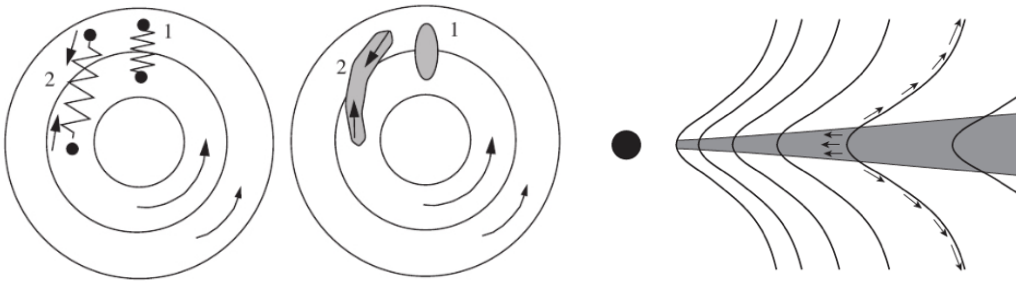

Figure 2.4: Left panel: MRI can be seen as a spring connecting two regions of the disc with a different velocity. The restoring force of the spring spin up the outer annulus and spin down the inner annulus (i.e. transferring angular momentum outward). Central panel: it is the case of the gravitational instability, where an excess of material gets sheared out by the differential rotation; the gravitational attraction on the sheared excess (spiral arm pattern) exerts a restoring force in the same sense as the magnetic case, again transferring angular momentum outward. Image taken from Hartmann (2009). Right panel: open magnetic field lines connect the disc to a disc corona. A small fraction of the accreting matter is accelerated outward along the field lines to form a magnetically launched disc wind, while the magnetic torque exerted by the field at the disc surface withdraw the disc of angular momentum, driving accretion (Armitage 2013).

instability can keep the mass clump together despite the shearing effects of the disc and tidal acceleration, confining it to a trailing spiral arm. Gravitational forces set up by the spiral arms act like the magnetic tension in an MRI-unstable disc: the inner part of the spiral arm pulls on the outer part of the spiral arm, trying to accelerate the outer regions. This tendency to accelerate outer regions in the direction of motion causes a net flow of angular momentum outward, and thus in principle can produce the torque needed for mass accretion.

2.1.3.3 Quantifying our "ignorance": the α-prescription

At this point, we can understand how complex is this discussion about angular momentum transport, and why theoretician have not come to a comprehensive understanding of its origin. In the previous section, we reviewed the turbulence driven angular momentum transport, and some of the disc instabilities that can "feed" this turbulence. Nevertheless, in order to model accretion discs, we need to find a way to estimate the magnitude of such an important physical process. But before, we need to understand if the stress provided by velocity fluctuations (Eq. 2.34) is a proper viscous stress.[5] Two aspects define a stress as viscous: the first one is that turbulence associated stresses need to dissipate energy as a viscous stress would do (i.e. according to Eq. 2.30), while the second one is that fluctuations are readily dissipated locally. Balbus & Papaloizou (1999) have shown that the energy dissipation associated to the Reynolds and Maxwell stress is the same as it would be dissipated in a viscous process. However, due to the

[5] We want to characterize it, as well as noting that it takes the place of viscous stress in the equation for conservation of angular momentum (Eqs. 2.11 and 2.33)

fact that gravity is a global phenomena, the gravitational stresses might introduce anomalous energy transport (i.e. fluctuations are able to travel significantly before being dissipated). Numerical investigations performed to date found that the level of non-local transport induced by gravitational instabilities is negligible for low mass discs, thus suggesting that "gravo turbulent" transport does behave to first approximation as an "anomalous" viscosity (see Sec. 3.2.4, Lodato & Rice 2004, 2005; Forgan et al. 2011).

Once this aspect has been clarified, we can quantify turbulence. Shakura & Sunyaev (1973) presented a simple and elegant parameterization of viscosity in terms of an unknown dimensionless parameter, called α. From a dimensional analysis, the kinematical viscosity parameter ν is proportional to a length times a velocity. The magnitude of turbulent viscosity is thus given roughly by $\nu \sim \bar{v}l$, where l is the typical size of turbulent eddies ($l < H$) and $\bar{v}$ is the typical turbulent velocity ($\bar{v} < c_{\rm s}$). Then, we introduce a dimensionless proportionality factor α and write the prescription as,

$$\nu = \alpha c_{\rm s} H \,, \tag{2.39}$$

where $c_{\rm s}$ is the sound speed and H is the disc thickness. Through this parametrization we move the uncertainty from ν, which is the fundamental physic parameter, to α, and from simple physical arguments we can put some constraints on it. As we said, l has to be necessarily smaller than the disc thickness H (assuming isotropic turbulence), and $\bar{v}$ cannot by supersonic, since a supersonic turbulence would dissipate due to shocks. We can conclude that $\alpha \leq 1$. Moreover, the parameter α is also often assumed to be constant, while in general this might not be true, and it could be a function of other disc parameters, such as radius, density, temperature. Using the prescription for the viscosity, we can estimate how large it should be to reproduce the observed timescale for disc evolution (Fedele et al. 2010). Indeed, if we look at the viscous timescale

$$t_{\rm visc} = \frac{R^2}{\nu} = \left(\frac{H}{R}\right)^{-2} \frac{1}{\alpha\Omega} \,, \tag{2.40}$$

where the α viscosity prescription has been used. In order to reproduce the expected disc lifetime for typical disc parameters we should be in the range $\alpha \sim [10^{-4}, 10^{-2}]$.

From an observational point of view, we have that the measurement of α can be derived by observing protostellar statistical samples of differently aged disc. Through the analysis of accretion indicators such as ultraviolet excess and/or Hα emission over the stellar photosphere (Hartmann et al. 1998) and/or by spatially resolved (sub-)millimetre observations (Andrews & Williams 2007b; Andrews et al. 2009), we are able to find typical values of the order of $[10^{-3}, 10^{-2}]$, though there remain uncertainties in its exact value due to observational limitations. A number of studies have examined various predictions of viscous evolution using samples of 30-50 sources (Andrews & Williams 2007b; Mulders et al. 2017b; Lodato et al. 2017; Rafikov 2017; Ansdell et al. 2018; Najita & Bergin 2018) finding a wide range of α values ($10^{-4} - 0.1$). In the first two panels of Fig. 2.5 we show two α estimates obtained by Flaherty et al. (2020) from high resolution ALMA CO J=2-1 line observations. The first one is a detection around DM Tau, while the

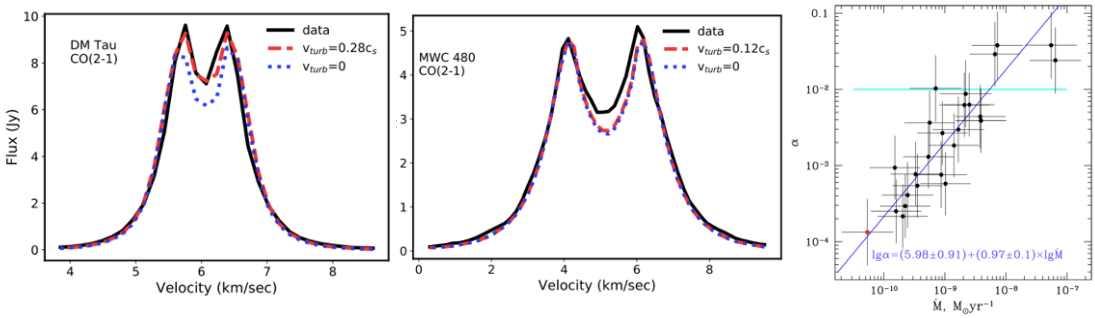

Figure 2.5: Left and central panels: spectra of the DM Tau and MWC 480 CO(2-1) emission (black line) and best $\alpha-$fit model (red line). The blue line indicates a model fit in which turbulence has been fixed at zero (Flaherty et al. 2020). Right panel: effective viscosity α, computed for a fixed temperature (20 K), as a function of the central mass accretion rate $\dot{M}$ (Rafikov 2017).

second one is a non-detection around MWC 480. Using parametric models of disc structure, they detected non-thermal gas motions around DM Tau with $\alpha \simeq 0.08$, while for MWC 480 they were able to put an upper limit, $\alpha < 0.006$. Other sources have been analysed in the same way (Hughes et al. 2011; Guilloteau et al. 2012; Flaherty et al. 2015, 2017) finding upper limits on the turbulence of $5-10\%$ of the local sound speed for gas at distances of $\sim$30 au. In the third panel of Fig. 2.5 we report the result obtained by Rafikov (2017). By using a sample of 26 protoplanetary discs resolved by ALMA with measured (dust-based) masses and stellar accretion rates, he derived the dimensionless α-viscosity values for individual objects, finding that the inferred values of α do not cluster around a single value, but instead have a broad distribution extending from 10^{-4} to 0.04. He also found a correlation between α and the mass accretion rate, which origin is still to be properly understood. Drawing some conclusions, the value for α obtained from observation and statistical studies is still extremely uncertain, and some more steps need to be done in order to understand the actual amount of turbulence in protoplanetary discs, and its physical origin. Finally, the α-prescription is of paramount importance because we can now collect the relevant equations we have derived so far, obtaining a set of equations that could be solved algebraically, and thus finding the physical parameters of the disc as function of radius (e.g., Σ, T, ρ, H, c_s, P, ν), with α as parameter. This kind of disc modeling is known as "Shakura & Sunyaev" disc model, and it is often used for black holes accretion discs (Shakura & Sunyaev 1973).

2.2 Dust dynamics

In Chapter 2.1 we described the gas dynamics in protoplanetary disc, which is the 99% in mass of the total disc mass, neglecting the influence of the dust phase on the gas dynamics. However, as already mentioned, dust is fundamental in the process of planet formation and its dynamic is not completely independent from the gas. Indeed, a key point in the development of a planet formation theory is the

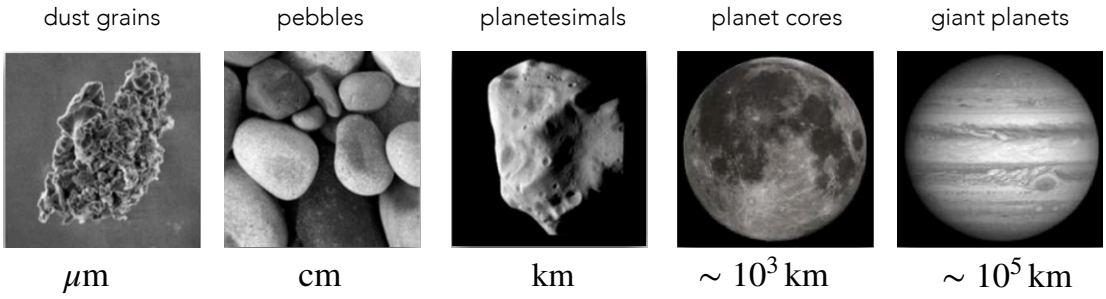

Figure 2.6: The main dust phases during the planet formation process, going from the micrometric dust, well coupled to the gas, to centimeters pebbles, slightly decoupled from the gas, to large planetesimal and planet cores, that interact via gravitational forces.

"meter size barrier" problem. While in the molecular cloud core dust grains have a ∼sub-micron size, in protoplanetary discs, they grow, and they are expected to cover in size a wide range of values, from sub-micron grains to objects with sizes of hundreds of meters (see Fig. 2.6). Once dust grains reach the ∼meters size, they are more prone to radial drift and experience an inward migration in a time which is much shorter than the disc lifetime (see Sec. 2.3). This means that there would not be material available for the formation of planetesimals.[6] Investigating the connection between gas and dust motion can bring solutions to this problem (e.g. see Sec. 2.3.1). The final phase of this growth process are planets, with a mass comparable to the one of Jupiter. We can think at this process as happening in three phases: the grain growth, the planetesimal formation, and the terrestrial and giant planet formation. Each one of these phases is characterized by different regime of solid bodies, where different processes dominate their dynamics. So, we can see why dust is a fundamental ingredient in the planet formation recipe. Furthermore, dust is also important because it dominates the disc opacity, and so it is the disc component we see more from observations. In particular dust gives us information about the thermal and chemical composition of the disc: the scattering and thermal emission at different wavelengths, produced by dust of various dimension, gives us an insight on the solids dimension and spatial distribution (see Fig. 2.7). For example, ALMA observe usually the large dust settled at the midplane, while SPHERE observe the micrometric dust that is still coupled with the gas in the upper layers. Starting from this information, we could be able to infer the gas dynamics from the dust observations (for a deeper description of protoplanetary discs observations related to the dust evolution we refer to Testi et al. 2014). In this Section, we will focus on some of the mechanisms regulating the dust-gas dynamical interaction, in particular the vertical settling and the radial drift, which are represented schematically in Fig. 2.7. We base our discussion on

[6] Another issue arises during the terrestrial planet formation stage. Indeed, this is a very slow process, with a timescale comparable to the (accretion) viscous timescale ($t \sim 10^6$ yr and $t_\nu \sim 10^7$ yr), with the consequence that at the end of this phase no more gas is left for the core accretion process, and we could not be able to form giant gaseous planets. So, the physical processes governing this phase are still under debate.

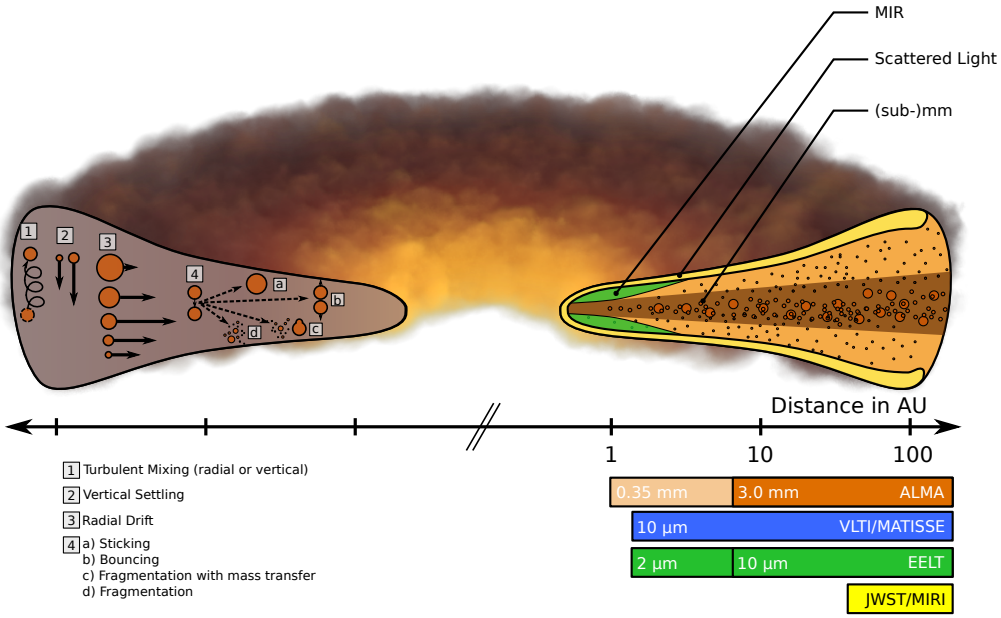

Figure 2.7: Illustration from Testi et al. (2014) of the structure, grain evolution processes and observational constraints for protoplanetary discs. On the left side are represented the main grain transport and collision mechanism properties. The different lengths of the arrows illustrate the different velocities of the different grains. On the right hand side, are showed the areas of the disc that can be probed by the various techniques, through different instruments. The axis shows the logarithmic radial distance from the central star. The horizontal bars show the highest angular resolutions (left edge of the bars) that can be achieved with a set of upcoming facilities and instruments for at the typical distance of the nearest star forming regions.

Chapter 4 of Armitage (2013).

2.2.1 Gas and dust dynamics: aerodynamical drag

Dust particles in protoplanetary discs can be considered as a pressureless (i.e. the frequency of collisions between dust particles is very low compared to collisions between particles and gas) and viscousless (i.e. the interaction between dust particles is neglected) fluid, subject to gravity and centrifugal forces. Dust also feels an aerodynamical drag from the gas, and vice-versa (even for dust-to-gas ratios of just a few per cent, Dipierro et al. 2018b). We also make an assumption on the gas flow being laminar (non turbulent) and on the "dust fluid" being composed by one single size grain. We will see that these two hypothesis should be relaxed in order to match what is really happening inside a protoplenatary disc. Considering the system as a dust-gas mixture in a thin, axisymmetric, non-magnetic, non-self-gravitating, viscous and vertically isothermal disc, we can (re-)write the dust and gas equations of motion (Nakagawa et al. 1986) as

$$\frac{\partial \rho_\mathrm{g}}{\partial t} + \nabla \cdot (\rho_\mathrm{g} \mathrm{v}_\mathrm{g}) = 0\,, \tag{2.41}$$

$$\frac{\partial \rho_\mathrm{d}}{\partial t} + \nabla \cdot (\rho_\mathrm{d} \mathrm{v}_\mathrm{d}) = 0\,, \tag{2.42}$$

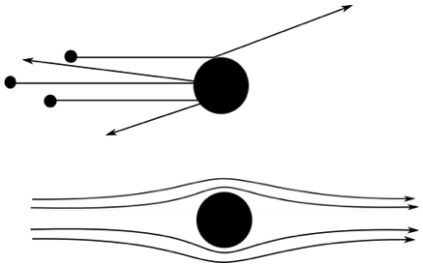

Figure 2.8: Gas-dust aerodynamical interaction in the Epstein regime (top) and in the Stokes regime (bottom).

$$\frac{\partial \mathrm{v_g}}{\partial t} + (\mathbf{v_g} \cdot \nabla)\, \mathrm{v_g} = -\frac{1}{\rho_\mathrm{g}} \mathrm{F_{drag}} - \frac{1}{\rho_\mathrm{g}} (\nabla P - \nabla \cdot \sigma) - \nabla \Phi \,, \tag{2.43}$$

$$\frac{\partial \mathrm{v_d}}{\partial t} + (\mathbf{v_d} \cdot \nabla)\, \mathrm{v_d} = \frac{1}{\rho_\mathrm{d}} \mathrm{F_{drag}} - \nabla \Phi \,, \tag{2.44}$$

where the indices g and d refer to the gas and the dust phases, Φ is the star gravitational potential, P and σ describe the pressure and the gas viscous tensor. We highlight that Eq. 2.43 is the Navier-Stokes equation already discussed in Sec. 2.1 (see Eq. 2.5) with an additional force given by the dust back-reaction on the gas flow. It is important to include this term, since in general it can give origin to several phenomena, such as the streaming instability (Youdin & Goodman 2005; Jacquet et al. 2011), and the destruction of vortices (Fu et al. 2014). In general, all these phenomena determines an evolution of the dust-gas disc which is different compared to the pure viscous evolution (Kanagawa et al. 2017; Dipierro et al. 2018b). The aerodynamical drag per unit volume can be written as,

$$\mathbf{F_{drag}} = -K^V \mathbf{v}_\mathrm{rel} \,, \tag{2.45}$$

where $\mathbf{v}_\mathrm{rel} = (\mathbf{v_d} - \mathbf{v_g})$, and the drag coefficient K^V (mass per unit volume per unit time) is related to the drag coefficient on a single grain K, as $K^V = \rho_\mathrm{d} K/m$ (ρ_d is the dust volume density and m is the particle mass). These coefficients depends mainly on the grain size. Indeed, we can define two regimes: the Epstein (Epstein 1924) and the Stokes (Stepinski & Valageas 1996) regimes (see for a schematic description Fig. 2.8). In the first one, grains are smaller than the mean free path of the gas molecule ($a < 9\lambda_\mathrm{mfp}/4$), so we can consider the gas as a collection of particles randomly colliding with the dust grain, and exchanging angular momentum. In the second one, the dust particles are larger than the mean free path ($a > 9\lambda_\mathrm{mfp}/4$), so one needs to consider the flow of gas around the particles. In this case the transfer of kinetic energy to a dust particle occurs trough viscous friction. Depending on the laminar or turbulent regime of the flow, we can find three other sub-regimes (known as Stokes I, Stokes II and Stokes III). It can be shown (Weidenschilling 1977) that in the Epstein regime the drag coefficient on a single grain K is

$$K = -\frac{4}{3} f \pi a^2 \rho_\mathrm{g} v_\mathrm{th} \tag{2.46}$$

while in the Stokes regime is

$$K = -\frac{\mathrm{C_D}}{2} \pi a^2 \rho_\mathrm{g} \left|\mathbf{v}_\mathrm{rel}\right| \,, \tag{2.47}$$

where $v_{\rm th}$ is the gas thermal velocity[7], $\rho_{\rm g}$ is the gas density, a is the grain size, and f is a correction term that takes into account if the motion between the dust and the gas is supersonic (in protoplanetary disc $f \sim 1$). Finally, $\mathrm{C_D}$ is a coefficient that describes the aerodynamics of a particle, and depends on its shape. For a spherical grain it depends only on the Reynolds number of the particle[8]

$$\mathrm{C_D} \simeq \begin{cases} 24 Re^{-1}\,, & Re < 1 \quad (\text{Stokes I}) \\ 24 Re^{-0.6}\,, & 1 < Re < 800 \quad (\text{Stokes II}) \\ 0.44\,, & Re > 800 \quad (\text{Stokes III})\,. \end{cases} \tag{2.50}$$

We highlight that the fundamental difference between the Epstein and the Stokes (with $Re > 1$) regimes is the different type of proportionality with $v_{\rm rel}$: in the first case the drag force remains linear, while in the others the drag force is non-linear. Using typical physical quantities to estimate the mean free path in protoplanetary discs (around classical T Tauri star, CTTS), it can be shown that drag forces for particles smaller than ~ 10 m are well described according to the Epstein regime (Garaud et al. 2004; Laibe et al. 2012). However, there might be regions close to the star where the gas is dense enough to interact with the dust according to the Stokes I drag law regime.

2.2.2 The stopping time

In order to study how strong is the interaction between the gas and solid component of the disc, we can introduce two typical timescales. The first one, called friction timescale, or "stopping time", is given by,

$$t_{\rm stop} = \frac{m\,|\mathbf{v}_{\rm rel}|}{|\mathrm{F}_{\rm drag}|}\,, \tag{2.51}$$

where $m = 4/3\pi a^3 \rho_{\rm gr}$ (a = grain size, $\rho_{\rm gr}$ =intrinsic grain density) is the dust grain mass, $\mathbf{v}_{\rm rel}$ is the relative velocity between dust and gas, and $\mathrm{F}_{\rm drag}$ is the drag force (see Eq. 2.45), depending on the particle size and on the gas density. We can also rewrite $t_{\rm stop} = m/K = \rho_{\rm d}/K^V$, where we used Eq. 2.45 and the relation between the drag coefficients K and K^V. This timescale is defined as the typical timescale on which drag significantly modifies the relative velocity between a single grain and the gas. Indeed, we stress that a particle, due to its inertia,

[7] The thermal gas velocity

$$v_{\rm th} = \sqrt{\frac{8 k_B T}{\pi \mu m_{\rm H}}} = \sqrt{\frac{8}{\pi\gamma}} c_{\rm s}\,, \tag{2.48}$$

where T is the gas temperature, k_B is the Boltzmann's constant, γ is the adiabatic index and $c_{\rm s}$ is the sound speed. The thermal velocity is the typical velocity of the thermal motion of particles of a gaseous or liquid medium; indirectly is a measure of the gas temperature.

[8] The Reynolds number for a particle embedded in a fluid can be written as

$$Re = \frac{vL}{\nu}\,, \tag{2.49}$$

where v is the relative velocity between the fluid and the particle, L is a characteristic length-scale and ν is the kinematical viscosity.

does not instantaneously follow the gas motion but it requires a certain time. Considering all the regimes previously described, it can be derived (Laibe et al. 2012) that

$$t_{\rm stop} = \begin{cases} \frac{\rho_{\rm gr} a}{\rho_{\rm g} c_{\rm s}} \sqrt{\frac{\pi\gamma}{8}}, & \text{Epstein regime,} \\ \frac{0.2 \rho_{\rm gr} a^2}{\nu \rho_{\rm g}}, & \text{Stokes regime I} \\ \frac{0.17 \rho_{\rm gr} a^{1.6}}{\nu^{0.6} \rho_{\rm g}^{1.4} |\mathbf{v}_{\rm rel}|^{0.4}}, & \text{Stokes regime II,} \\ \frac{6 \rho_{\rm gr}}{\rho_{\rm g} |\mathbf{v}_{\rm rel}|}, & \text{Stokes regime III.} \end{cases} \tag{2.52}$$

We note that in the context of protoplanetary discs the relevant stopping time is mainly the one found within the Epstein regime. Thus, considering the Epstein regime and inserting in Eq. 2.52 some typical values for a particle in the midplane, with a size of $a = 1\,\mu$m, with gas density $\rho_g \sim 10^{-9}\,\mathrm{g\,cm^{-3}}$, a grain intrinsic density of $\rho_p \sim 3\,\mathrm{g\,cm^{-3}}$, a thermal velocity of $v_{\rm th} \sim 10^5\,\mathrm{cm\,s^{-1}}$, we obtain that the stopping timescale is of the order of $t_{\rm stop} \approx 3\,$sec. Since $t_{\rm stop}$ is lower than the typical dynamical timescale $t_{\rm dyn} \sim \Omega^{-1}$, for particle of that dimension, gas and dust are well coupled. We note that the stopping time increases (decreases) with the particle size (gas density), and so, larger grains become uncoupled with the gas and tend to move with their own velocity. Thus, if we consider the evolution of the grains, i.e. the growth/fragmentation process, we understand how this could influence the aerodynamical coupling (Laibe et al. 2014). In particular, particles of the order of $\sim$ mm or cm sizes (also depending on the disc gas density) would be partially or totally decoupled from the gas.

It comes naturally to define another parameter, called Stokes number, in order to quantify the coupling between gas and dust,

$$\mathrm{St} = \frac{t_{\rm stop}}{t_{\rm dyn}} = \Omega_{\rm k} t_{\rm stop}\,, \tag{2.53}$$

which is the ratio between two typical timescale of the system, the friction timescale, and the dynamical one. We can refer to this parameter also as a dimensionless stopping time. If we rewrite Eq. 2.53 using the expression we found for the stopping timescale (see Eq. 2.52), and assuming $\rho_g(z=0) = \Sigma_{\rm g}/(\sqrt{2\pi}H)$, we get the Stokes number as a function of disc physical quantities,

$$\mathrm{St} = \frac{a\rho_{\rm gr}}{\rho_{\rm g}} \frac{\Omega_{\rm k}}{c_{\rm s}} \sqrt{\frac{\pi}{8}} = \frac{a\rho_{\rm gr}}{\Sigma_{\rm g}} \frac{\pi}{2}\,, \tag{2.54}$$

where all the quantities have been previously defined. While for small grains or/and for a high gas density, the Stokes number is small (the two phases are strongly coupled), for bigger grains or/and a low gas density, the Stokes number is high (the two phases are decoupled). This property should be taken into account when we want to explain the substructures observed in discs. We base the work presented in Chapter 6 on this parameter. It is important to note that until now we considered a laminar flow, but it has been demonstrated (see Sec. 2.1.3.1) that the gas should be a turbulent medium. As a consequence, the definition of coupling between dust and gas would change, and the Stokes number would measure the coupling of the dust particles to the turbulent medium.

Dust-to-gas ratio ϵ It is useful to introduce a parameter defined as dust-to-gas ratio $\epsilon \equiv \rho_{\rm d}/\rho_{\rm g}$. Usually, in our dust and gas dynamics description we assume a value for the dust-to-gas ratio of $\sim 10^{-2}$ (i.e. the density of one phase is negligible compared to the density of the other one). This assumption basically means that the dust feels the drag force by the gas, but the dust back-reaction on the gas velocity is negligible. However, we already mentioned that the dust back-reaction can be very important when describing the evolution of a disc (Dipierro et al. 2018b). The equations of motions and the velocities for arbitrary dust to gas ratios can be found in Nakagawa et al. (1986). They define the stopping time and hence the drag coefficient for a mixture of dust and gas as

$$K^V \equiv \frac{\rho_{\rm d}\rho_{\rm g}}{{\rm t}_{\rm stop,mix}\,(\rho_{\rm d}+\rho_{\rm g})}\,. \tag{2.55}$$

Rewriting the above equation in term of the dust to gas density ratio, we obtain

$$t_{\rm stop,mix} = \frac{t_{\rm stop}}{1+\epsilon}\,. \tag{2.56}$$

This expression for the stopping time extends the previous formulation based on the interaction between a single grain and the gas flow. The latest is obtained from Eq. 2.56 by assuming that $\epsilon \ll 1$, meaning that the dust component is negligible enough to does not affect the gas dynamics. This assumption becomes erroneous in the case where the two fluids have densities of the same order of magnitude, as expected in the midplane of the inner disc regions. We can also define the Stokes number (see Eq. 2.53 and 2.54) for a mixture of dust and gas ${\rm St}= t_{\rm stop,mix}\Omega_{\rm k}$, as

$${\rm St} = \frac{a\rho_{\rm gr}}{(1+\varepsilon)\rho_{\rm g}}\frac{\Omega_{\rm k}}{c_{\rm s}}\sqrt{\frac{\pi}{8}}\,. \tag{2.57}$$

To resume, it is important to keep in mind that in principle, the dust back-reaction could be non negligible. Indeed, it can be shown that in different situation ϵ can increase. For example, defining $\epsilon_0 = 10^{-2}$ the initial dust-to-gas ratio, in the case of a dust disc more compact with respect to the gas one (due to radial drift), $\epsilon_{\rm drift} \approx 6\epsilon_0$. On top of this, considering also the dust settling onto the midplane, the dust-to-gas ratio becomes $\epsilon_{\rm drift+settle} \approx 2$.[9] Finally, ϵ can change further when adding the growth process.

2.2.3 Dust settling

Aerodynamical coupling allows us to better explain both the vertical distribution and radial motion of dust within the protoplanetary disc, but is not the only physical mechanism that determines the grains motion and evolution. Indeed, one of the most important motion to consider, is the vertical one under the action of the gravitational and drag force (Safronov 1969; Goldreich & Ward 1973; Weidenschilling 1980; Nakagawa et al. 1986; Cuzzi et al. 1993; Johansen & Klahr 2005; Carballido et al. 2006; Bai & Stone 2010). This motion is important because it determines a size-segregation in the vertical distribution (smaller grains would settle

[9] Where it was assumed $\alpha = 10^{-3}$, since the settling process is directly related to the turbulence of the medium, which affects the dust scale height, and ${\rm St} = 1$.

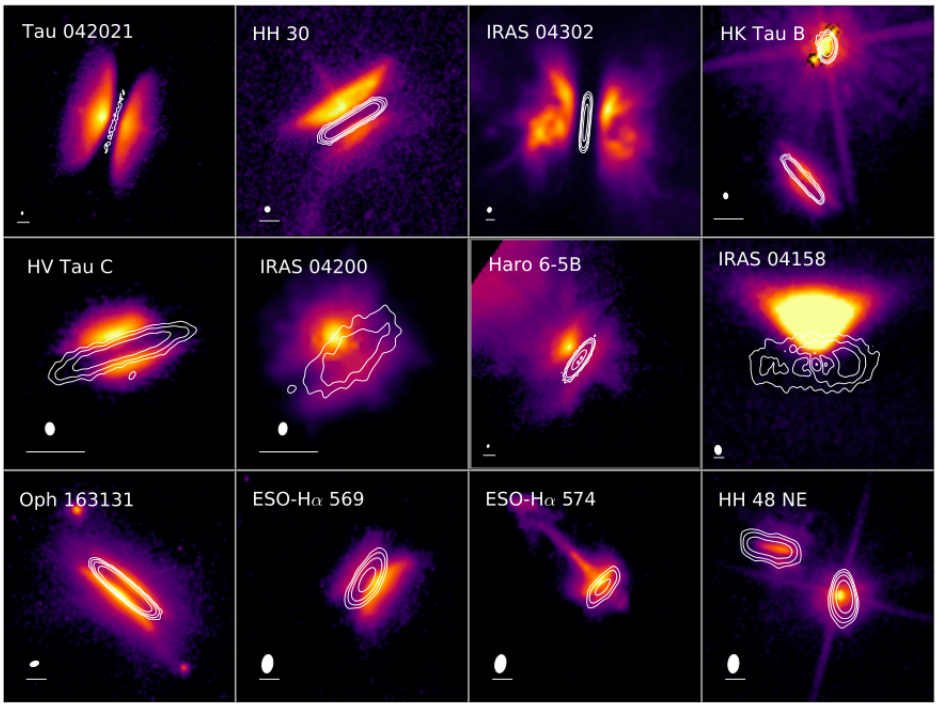

Figure 2.9: Scattered light (colors, in logarithmic scales) and ALMA band 7 continuum images (5, 10, 20, and 50σ contours) for all the sources in Villenave et al. (2020), except for Oph 163131 for which band 6 it is shown.

higher with respect to larger grains), which could affect the radial dust motion (both the aerodynamical grains properties and the gravitational force scale with the radial distance), and that will be detected in the slope of the SEDs. However, by considering a timescale argument (long-term corrections due to radial drift are negligible, $t_{\rm r,drift} \gg t_{\rm z,settle}$, Garaud et al. 2004; Laibe et al. 2014), it can be shown that, in typical protoplanetary discs, there is a separation between the radial and vertical motion of the dust grains. Thus, we will consider separately these two motions. A nice direct prove of dust settling can also be found in observations, such those presented by Villenave et al. (2020), where they compare ALMA observations of the dust continuum with scattered light observation of several edge-on discs (see Fig. 2.9). As expected, μm-sized grains, detected through scattered light, have a larger vertical sizes with respect to mm-sized grains, pointing out to different optical depths and to vertical dust settling.

We will consider a non-turbulent, non-self-gravitating disc (keeping in mind that it is indeed important to relax these approximations). While the gas in the disc is supported against the gravitational force by a pressure gradient directed upward, the particle "fluid" is assumed to be pressureless. Then, if the particle is initially at rest, it accelerates until the gravity exerted by the star is balanced by the aerodynamical drag, in the vertical direction. By inserting typical values (for micrometric particles), we thus obtain a settling timescale of the order of $\approx 1.5\times10^5$ yrs, which is short compared to the disc lifetime (the viscous timescale). It can be also shown that, when assuming a Gaussian vertical density profile, dust

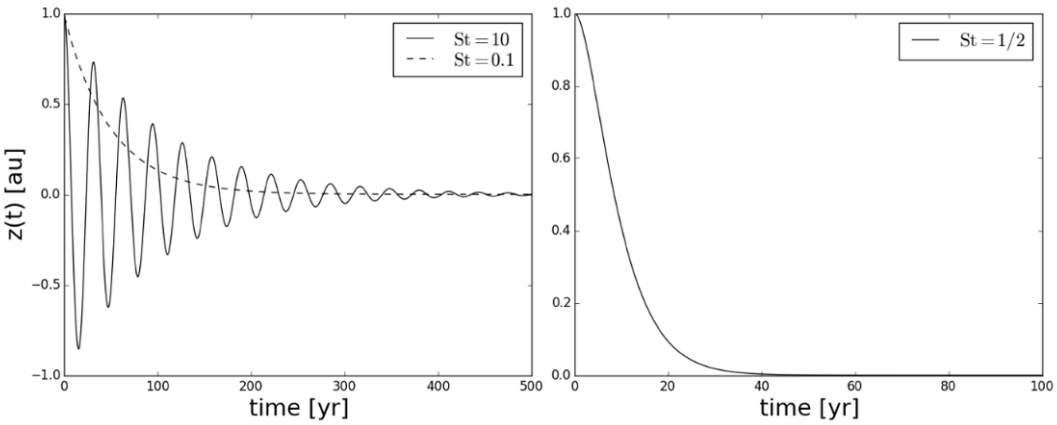

Figure 2.10: Vertical motion of a dust particle starting at $z(0) = 1$ au with St $= 10$ (left panel - solid line), St $= 0.1$ (left panel - dashed line) and St $= 1/2$ (right panel) expressed in Eq. 2.59, at a radial distance of 10 au from a central star with mass $1\,M_\odot$. Image taken by Dipierro et al. (2016).

particles settle out in the upper layers of the disc much faster with respect to the lower layers. We remind the reader that this is obtained for a disc in absence of turbulence, whose effect would be a general mixing of different layers, that could slow down/change the settling velocity.

It is instructive also to look at the time evolution of the vertical settling process. With the previous assumption on the disc (no turbulence, thin disc approximation) one can find that close to the midplane ($z \ll H$, where we can assume ρ_g to be constant) the equation of motion for dust particles in the vertical direction is a damped harmonic oscillator,

$$\frac{\mathrm{d}^2 z}{\mathrm{d}t^2} + \frac{1}{t_\mathrm{fric}}\frac{\mathrm{d}z}{\mathrm{d}t} + \Omega_\mathrm{k}^2 z = 0\,, \tag{2.58}$$

where three different Stokes number regimes can be identified. The three solutions are showed in Figure 2.10. From the analysis of these different regimes, we understand that, in general, dust grains settle towards the midplane with a timescale that depends on their size. For small/large grains, the dimensionless settling time is defined as $\sim 1/\mathrm{St}$ and St, respectively, while the fastest settling time (Ω_k^{-1}) occurs for grains with St $= 0.5$. Merging together these three cases, the settling timescale can be well approximated by (e.g. Youdin & Lithwick 2007; Laibe et al. 2014),

$$\Omega_\mathrm{k} t_\mathrm{settle} \simeq \mathrm{St} + \frac{1}{\mathrm{St}}\,. \tag{2.59}$$

Loosely coupled particle (St $\gg 1/2$) at a height z above the disc mid-plane would move on an inclined Keplerian orbit, thus oscillating around the midplane. In the intermediate regime (St $= 1/2$), the dust settling occurs on the fastest timescale, Ω_k^{-1}; the motion is not oscillatory and goes quickly to the steady state on an orbital timescale. Particles which are strongly coupled to the gas (St $\ll 1/2$), instead of oscillating around the midplane, slowly settle toward the midplane on a timescale of a few hundred thousand years, in typical disc conditions.

Dust settling with gas stratification In Sec. 2.1.1.2 we derived that the gas density has a Gaussian vertical profile, thus it would be necessary to relax the assumption we made of constant density. By doing this, it is interesting to note that the Stokes number can be written as

$$\mathrm{St} = t_{\mathrm{fric}}\Omega_{\mathrm{k}} = \frac{\rho_g r a}{\Sigma_g}\frac{\pi}{2}\sqrt{\gamma}\exp\left[\frac{z^2}{2H^2}\right] = \mathrm{St}_0\exp\left[\frac{z^2}{2H^2}\right] \tag{2.60}$$

where we used the vertical density profile given by Eq. 2.18, the density at the midplane $\rho_0 = \Sigma/\sqrt{2\pi}H$, and where we define the Stokes number at the midplane St_0. It is clear that the Stokes number is a function of z, through the density profile. Therefore, due to the low density of the gas at the surface layers, and to a higher density at the midplane, we would find that micron sized grains could have a large Stokes number at the disc surface (not coupled to the gas), and a smaller Stokes number at the midplane (strongly coupled to the gas). As we can see also from Eq. 2.60, while the dust settles to the midplane, its Stokes number will decrease due to the increased gas densities. Therefore, in the assumption of non-growing grains, they will decelerate their motion. From the Stokes number we can also derive some information about the settling timescale. In particular, for small particles (in the assumption of steady state for the vertical motion), it can be shown that dust settling depletes the upper layers of a disc surface much faster compared to the lower layers, especially in the outer disc region where the gas density is lower and St is higher. Unless a mixing process counteracts the settling, the upper disc layer should become depleted of dust quickly, heavily affecting the radiative processes at the disc surface and, thus, the disc appearance (Dullemond & Dominik 2004).

Dust settling with coagulation However, we do know that the dust in protoplanetary discs undergoes a process of growth via collisions, and consequently coagulation (or fragmentation, depending on the relative velocities). This has been also investigated by means of observations, since the wavelength-dependent absorption and scattering properties of dust grains change as they grow in size. Indeed, if grains grow while settling down, their increase in size can partly balance the increase in gas density. It can be shown (e.g. Laibe et al. 2014) that including the dust coagulation process, depending on the initial grain size considered, can change significantly the settling timescale. This result is presented in the left panel of Fig. 2.11, where solutions corresponding to different growth efficiency are collected, for small particles with initial Stokes $\sim 10^{-2}$ (which are supposed to populate the initial disc phase). The main point is that particles settle to the disc midplane on a time scale of the order of 10^3 yr, more than two orders of magnitude faster than the equivalent timescale in the absence of particle growth (see Sec. 2.2.3. It is also interesting to look closely at the different solutions. While in the slow growth regime, $\gamma \ll 1/2$, the vertical motion is damped efficiently (particles settle before they have time to grow and decouple from gas), increasing γ, grains start to decouple slowly from they gas. Therefore, as they settle, the drag becomes weaker, meaning that their settling time is shorter if compared to the one of non-growing grain. Instead, if we go to $\gamma > 1/2$, in the fast growth regime, dust particles grow fast enough to decouple from the gas before they feel the gas drag

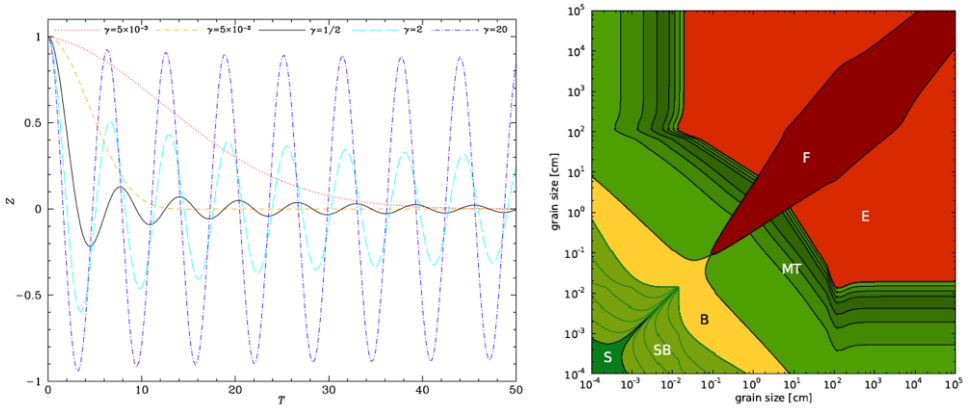

Figure 2.11: Left panel: vertical motion of a growing dust particle with time T starting at $Z_0 = 1$, with $\mathrm{St}_0 = 10^{-2}$ and $\gamma = 5 \times 10^{-3}, 5 \times 10^{-2}, 0.5, 2, 20$. The most efficient settling is obtained for $\gamma = 1/2$. Image from Laibe et al. (2014). Right panel: Windmark et al. (2012) derived the collisions outcomes parameter space by interpolating the results of the laboratory experiments across the entire parameter space (where F stays for fragmentation, B for bouncing, S for sticking, E for erosion, MT for mass transfer).

and their settling time-scale becomes much longer. In the intermediate case, with $\gamma = 1/2$, dust particles grow in the same timescale as they settle to the midplane, where they finally decouple from the gas, after having reached macroscopic sizes (Dullemond & Dominik 2004). This is the most efficient regime for settling. For a more detailed description of this process including coagulation, we also refer the reader to a simple single particle model proposed by Safronov (1972). An analytical model is instead provided by the Smoluchowski (1916) equation. Moreover, we note that while initial model used to take into account a single grain dust population, we now know that protoplanetary disc should be populated by a dust distribution $n^a \propto a^{-q}$, where q is usually assumed to be equal to $3 - 3.5$ (Natta et al. 2007; Testi et al. 2014). This is also due to the fact that other processes should be considered together with the growth process, such as fragmentation, bouncing, erosion (see right panel in Fig. 2.11). Different studies have been made including at least also the fragmentation (Tanaka et al. 1996; Dominik et al. 2007; Ormel & Cuzzi 2007; Birnstiel et al. 2010b). Including fragmentation (as the outcome of very energetic collisions) in dust evolution models is one of the possible explanation to the question of how the observed population of small grains managed to survive to late times, without being completely reprocessed in larger grains settled to the midplane (Dullemond & Dominik 2004). Other answers can be found in considering a non-laminar gas flow or by assuming that the upper layers of the disc are constantly replenished by infalling material (Mizuno et al. 1988; Dominik & Dullemond 2008).

Dust settling with turbulence Although this model is a big improvement, it is not enough. Indeed, we are neglecting turbulence, and we are assuming that collisions between particles happen only because they have different vertical veloc-

ities. It is clear that other phenomena have a role in the particle growth process, like the Brownian motion of the particle, the turbulence, and the differential radial velocity. Though the result obtained from Safronov (1972) has been confirmed by more complex models, taking into account more physical ingredients is important in order to build an accurate description. When considering settling in a laminar fluid, the main outcome is that the disc flatten. Indeed, there is clear evidence for settling and flattening of discs as they age (Chiang et al. 2001; D'Alessio et al. 2001; Dullemond & Dominik 2004; Furlan et al. 2006), but this is a weak effect and takes place over millions of years, not thousands! This over-estimate of the settling rate is due to the fact that we have considered only a laminar disc, while real discs are turbulent. Settling of dust in a turbulent disc is a much more complex problem, as the turbulent motions can bring the grains to a certain height z on relatively short timescales. In general the effect of turbulence is to drive diffusion of dust in the vertical direction, counteracting the effect of vertical settling. This effect is dependent on the velocity of the gas fluctuations, and on the level of coupling between dust and gas. Detailed models generally suggest that the vertical distribution of small grains in discs is sustained by a quasi-equilibrium between turbulent diffusion and sedimentation (Dubrulle et al. 1995; Carballido et al. 2006; Fromang & Nelson 2009). The dust density evolution due to the dust settling and diffusion can thus be computed in terms of an advection diffusion equation, and it can be derived that the dust concentration scale height - close to the midplane - resulting from these models (with the assumption of isothermal disc with $H = c_\mathrm{s}/\Omega$) is

$$H_\mathrm{dust} = H\sqrt{\frac{\alpha_\mathrm{diff}}{\alpha_\mathrm{diff} + \mathrm{St}}}, \tag{2.61}$$

where α_diff is assumed to be an anomalous diffusion coefficient, related to turbulence in the vertical direction of the disc. From this equation we can see that in the vertical direction, perpendicular to the disc midplane, dust settling towards the midplane is balanced by turbulent diffusion, which determines the thickness of the dust disc.

2.3 Dust radial drift

Another fundamental process that concerns dust particles, is the radial drift (Whipple 1972; Weidenschilling 1977), which we have to take in account, in order to give a complete description of the planet formation process. Indeed, we will see that this mechanism can critically compromise the growth process, and then the planetesimal formation. In Sec. 2.1.1 we derived that a gas particle feels a balance of centrifugal acceleration, gravity and pressure. We recall the reader that at a first approximation[10] the velocity of the gas particle can be assumed as Keplerian, but taking into account also the pressure support, it becomes slightly sub-Keplerian (the pressure gradient is pointing outward since densities and temperatures are

[10] If we consider typical disc parameters for a flaring disc with temperature profile $T \propto R^{-1/2}$, i.e. $H/R = c_\mathrm{s}/v_\mathrm{k} = 0.05$ and $\zeta = 11/4$, we find that this correction is very small, with $(1-\eta)^{1/2} \sim 0.0034$ (with $\eta = \zeta(H/R)^2$).

higher in the inner disc),

$$v_\phi = v_\mathrm{k}\left[1 + \frac{R}{v_\mathrm{k}^2\rho_\mathrm{g}}\nabla P\right]^{1/2} = v_\mathrm{k}\left[1 - \zeta\left(\frac{H}{R}\right)^2\right]^{1/2}, \tag{2.62}$$

where the second equality stands when assuming a barotropic gas ($P = P(\rho_\mathrm{g})$) and power-law profiles for the surface density ($\Sigma_\mathrm{g} \propto R^{-p}$) and temperature ($T \propto R^{-q}$), and where

$$\zeta = \frac{\partial \ln \rho}{\partial \ln R} = -\left(p + \frac{q}{2} + \frac{3}{2}\right). \tag{2.63}$$

Moreover, we highlight that the disc is assumed to be non-self-gravitating and the gravitational contribution comes from the central object. Indeed, including also the self-gravity effect would introduce another correction term (see Chapter 3). Instead, as already mentioned, dust particle are not subjected to ∇P, consequently having a Keplerian velocity. Therefore, we have solid dust particles, with a certain velocity, which are embedded in gas, flowing with a smaller velocity. This means that the dust particles will experience a headwind, which will differ according to their size. They will be decelerated by the tangential drag force (see Eq. 2.45), which is proportional to the relative velocity between dust and gas, Δv. This drag force will produce a torque on the dust grain that will cause its change in angular momentum and its migration (inwards or outwards, depending on the sign of the Δv, which in protoplanetary disc is negative). The migration itself will develop another drag force in the radial direction, due to a radial velocity difference between the two species.

Briefly, the two equations describing the system, in the radial and azimuthal direction (assuming $z = 0$) are

$$\begin{cases} \dfrac{\mathrm{d}v_R}{\mathrm{d}t} = \dfrac{v_\phi^2}{R} - \dfrac{v_\mathrm{k}^2}{R} - \dfrac{1}{t_\mathrm{stop}}\left(v_R - v_{R,g}\right) \\ \dfrac{\mathrm{d}Rv_\phi}{\mathrm{d}t} = -\dfrac{R}{t_\mathrm{stop}}\left(v_\phi - v_{\phi,g}\right) \end{cases}, \tag{2.64}$$

where v_R and v_ϕ are the radial and azimuthal velocity of the dust, $v_{R,g}$ and $v_{\phi,g}$ are the gas radial and azimuthal velocity, and t_stop is the stopping time previously defined in Eq. 2.51, via a dimensionless parameter (the Stokes nuber, $\mathrm{St} = t_\mathrm{stop}\Omega_\mathrm{k}$). By making some approximations and assumptions[11] we can derive the particle radial velocity, which in the steady state, $\mathrm{d}v_R/\mathrm{d}t = 0$, is,

$$v_R = \frac{v_\mathrm{r,g}}{\mathrm{St}^2 + 1} - \eta\frac{v_\mathrm{k}}{\mathrm{St} + \mathrm{St}^{-1}} \tag{2.65}$$

where we used the dimensionless stopping timescale and where $\eta = \zeta(c_\mathrm{s}/v_\mathrm{k})^2$. Using the first equality of Eq. 2.62, and generalising for non negligible dust-to-gas

[11] The two main assumptions are:

- $v_\phi = v_{\phi,g} = v_\mathrm{k}$, angular momentum in the azimuthal direction remains always quasi-Keplerian, which means that the particles spiral inwards through a succession of quasi circular orbits;
- $v_{R,g} \ll v_R$, the net radial acceleration of the gas can be neglected

ratio ϵ (Nakagawa et al. 1986), we can rewrite Eq. 2.65 in term of a typical optimal drift velocity Δv

$$v_R = \frac{1}{1+\epsilon}\left[\frac{v_{\rm r,g}}{1+{\rm St}^2} + \frac{\Delta v}{{\rm St}+{\rm St}^{-1}}\right] \tag{2.66}$$

where

$$\Delta v \equiv \frac{1}{\rho_{\rm g}\Omega_{\rm k}}\frac{\partial P}{\partial R}\,. \tag{2.67}$$

From this relation it is clear that the principal sources for the radial drift motion are the pressure and the viscous forces, since the radial component of the gas velocity $v_{\rm r,g}$ is a viscous velocity (see Eq. 2.22). We can say that the dust particle feels a continuous headwind from the gas in the azimuthal direction and a crosswind towards inner radii due to the radial inward motion of the gas (since the gas is secularly accreting towards the star, i.e. $v_{\rm r,g} < 0$). The headwind causes the dust particle to lose its angular momentum and to spiral towards the star (for the law of action-reaction the gas acquires this angular momentum, slowly drifting outwards). This motion is mostly referred to as **radial drift** and it is the second term in the right hand side of the equation. The crosswind forces the dust particles to move toward inner radii due to the induced direct pushing. This component, the first term in the r.h.s. of the equation, is mostly referred to as **viscous drag**. Comparing the orders of magnitude of the different velocity terms, we obtain

$$|\Delta v| \sim \left(\frac{H_{\rm g}}{R}\right)^2 v_{\rm k} \quad \text{and} \quad |v_{\rm R,g}| \sim \alpha\left(\frac{H_{\rm g}}{R}\right)^2 v_{\rm k}\,, \tag{2.68}$$

where we have used the $\alpha-$prescription for the turbulent viscosity, $\nu = \alpha c_{\rm s} H$ (Shakura & Sunyaev 1973). The relative contribution of the radial drift to the drag component scales with $|\Delta v| \,/\, |v_{\rm R,g}| \sim \alpha^{-1} \gg 1$. Thus, to a first approximation, since typically in protoplanetary discs $\alpha^{-1} = [10^2, 10^4]$, the radial drift component is expected to dominate the dust motion for a large range of Stokes number. Starting from the expression for the dust radial velocity (Eq. 2.66, with $\epsilon \ll 1$), we can identify three regimes:

- ${\rm St} \gg 1$: for large particles, we find that the radial drift velocity tends to

$$v_{\rm R} \simeq \frac{\Delta v}{\rm St} \underset{{\rm St}\to\infty}{\approx} 0\,, \tag{2.69}$$

  which means that since the particles are (totally) decoupled from the gas, the drag force between the two components is negligible and there is no dust radial motions.

- ${\rm St} \ll 1$: for small particles, the radial drift occurs at the velocity

$$v_{\rm R} \simeq v_{\rm R,g} - {\rm St}\Delta v \underset{{\rm St}\to 0}{\approx} v_{\rm R,g}\,, \tag{2.70}$$

  which means that the dust particles, which are strongly coupled to the gas, are dragged in with the gas, and it can be shown that their azimuthal velocity will equal the gas one. Since this is sub-Keplerian, the centrifugal force will be insufficient to balance gravity, and the particle will spiral inwards at its radial velocity.

It is interesting to note that, in both the regimes, the ratio between the dust radial velocity and the Keplerian gives $|v_R/v_\mathrm{k}| \ll 1$, as we can see in Fig. 2.12, where it is shown the logarithmic behavior of the ratio between the two velocities as a function of the dimensionless stopping timescale (St).

- This means that a real inward migration happens in a third, intermediate regime, where $\mathrm{St} \approx 1$. In this case, from Eq. 2.65 we find that

$$v_R \simeq \frac{v_{R,g}}{2} + \frac{\Delta v}{2}\,, \tag{2.71}$$

where we highlight the dependence of the radial velocity from the disc pressure gradients ($\Delta v \propto \nabla P$). In this case, from Eq. 2.68 we have that $\Delta v \gg v_\mathrm{R,g}$, and thus Eq. 2.71 becomes

$$v_{\mathrm{d},R,\ \mathrm{peak}} \simeq \frac{\Delta v}{2} = \frac{\zeta v_\mathrm{k}}{2}\left(\frac{H_\mathrm{g}}{R}\right)^2\,, \tag{2.72}$$

where ζ has been defined in Eq. 2.16. The particles affected by this "real" inward migration are the ones marginally coupled to the gas. Thus, as one can see from Fig. 2.12, the radial drift velocity peaks at $\mathrm{St} \approx 1$, and we can calculate in the Epstein regime the particle size relative to this peak, as

$$a(\mathrm{St}=1) = \frac{\rho_g v_\mathrm{th}}{\rho_\mathrm{gr}\Omega_\mathrm{k}}\,, \tag{2.73}$$

where for typical disc parameters ($R = 5$ au, $\rho_g = 10^{-9}\mathrm{g\,cm^{-3}}$, $\rho_\mathrm{gr} = 3 \times$ $\mathrm{g\,cm^{-3}}$ and $H/R = 0.05$), we find $a \approx 20\,\mathrm{cm}$. Generally, for $R \simeq 1 \div 10$ au, the particle size results to be $s \simeq 10\,\mathrm{cm} \div 1\,\mathrm{m}$. We can also derive the timescale related to the maximum grain radial drift, as

$$t_\mathrm{drift} = \frac{R}{|v_{R,\mathrm{max}}|} = \frac{R}{v_\mathrm{k}}\left(\frac{H}{R}\right)^{-2}\,, \tag{2.74}$$

which is defined as a function of the radial distance from the star, and where $v_{R,\mathrm{max}} \approx \Delta v$. With typical values, within the main planet-forming regions of the disc, $t_\mathrm{drift} \leq 10^3$ yrs, which is extremely short compared to other timescales. Therefore, once dust particles have migrated inward, they are accreted onto the central star and they are no more available for grain growth (Takeuchi & Lin 2002, 2005; Brauer et al. 2008).

From these results, two observations come spontaneously. The first one is that the planetesimal formation has to be rapid, otherwise it seems that not enough material would be available. Probably, this process occurs through a cascade of collisions that lead to growth. This is commonly known as the "meter-size barrier" problem, and how to overcome radial drift remains one of the major unsolved issue in planet formation. A possible solution to this problem comes from the "particle traps" mechanism (see Section 2.3.1). A second solution is that there should be a radial redistribution of solids within the disc. Indeed, the radial drift of grains is characterised by $t_\mathrm{drift} \ll t_\nu$ not only at the velocity peak, but also for substantially

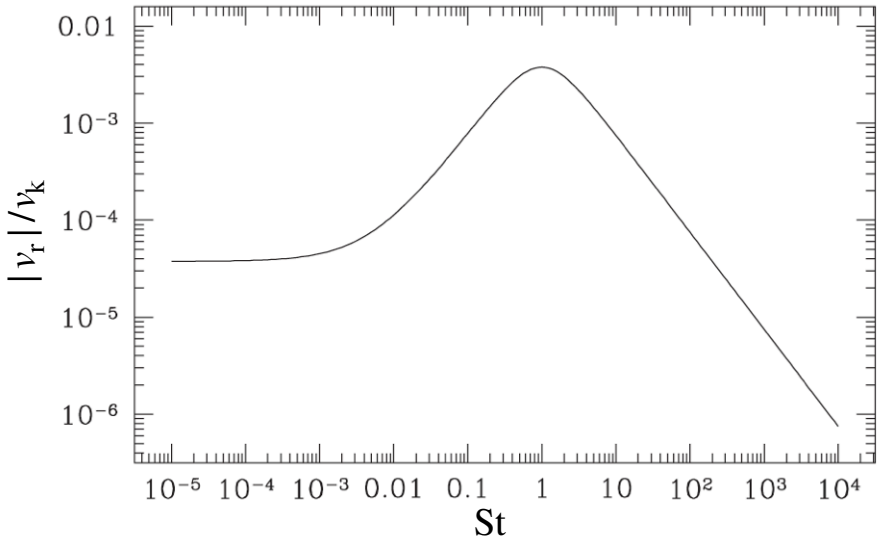

Figure 2.12: The radial drift velocity of dust particles at the midplane of the protoplanetary disc, plotted as a function of the dimensionless stopping time $\mathrm{St} = t_{\mathrm{stop}}\Omega_{rmk}$. The model refers to a system with $\eta = \beta(c_\mathrm{s}/v_\mathrm{k})^2 = 7.5 \times 10^{-3}$, where for $\mathrm{St} \to 0$, we have that $v_R/v_\mathrm{k} \to v_{R,g}/v_\mathrm{k} = -3.75 \times 10^{-5}$. These values are appropriate for a disc with $H/R = 0.05$ and $\alpha = 10^{-2}$ at 5 au.

smaller and larger particles. This leads to a local enhancements or depletions of solids (relative to the gas surface density). Moreover, in this derivation we did not consider the dust growth (e.g. via coagulation), and this process could potentially be beneficial for radial drift. Indeed, if grains grow fast enough (or fragment at the right size), the velocity peak could be in some way overcame, not affecting dangerously the disc evolution.

Including the grain coagulation to the previous derivation, it can be shown that $t_{\mathrm{growth}} < t_{\mathrm{drift}}$ when

$$a \lesssim \frac{3\epsilon}{4\sqrt{2\pi}} \left(\frac{H}{R}\right)^{-1} \frac{\Sigma}{\rho_{\mathrm{gr}}}, \tag{2.75}$$

where ϵ is the dust-to-gas ratio at the disc midplane. For typical values in protoplanetary discs $a_{\mathrm{crit}} \sim 2$ m. This means that a particle with a size lower than a critical value would have time to grow via collision, before it would have migrate inward, with the consequently accretion onto the star. This implies that the peak value of the radial drift speed is not an insurmountable barrier to ongoing growth, provided that vertical settling has taken place. However, we also know that the outcome of particles collisions does not correspond always to growth, but it can produce fragmentation depending on the grain sizes and collision velocities. Different models including also fragmentation has been proposed, but this remains an open issue in the planetesimal formation process.

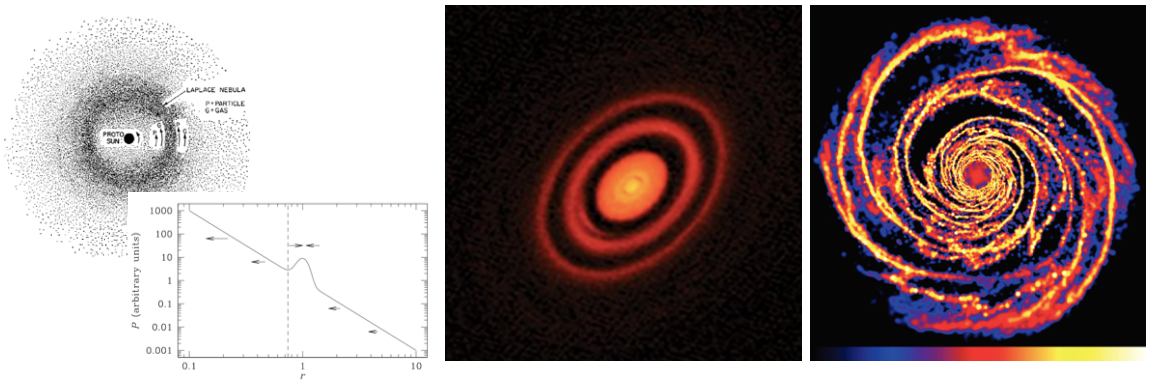

Figure 2.13: Left panel: Mechanism of particles pile-up, due to the presence of a local maximum in the pressure profile (non-monotonic) of the disc. Dust particles tend to drift towards the location of the pressure maximum from both sides, resulting in a rapid concentration of solids at that point. Image readapted from Armitage (2013) and Whipple (1972). Right panels: two examples of substructures that could be linked to dust trapping, such as rings and gaps observed in HD 163296 (Rosotti et al. 2020b) or spirals generated by gravitational instabilities (simulation from Rice et al. 2006b).

2.3.1 Dust particle concentration at $P_{\max}$

A solution to the "meter size problem" arises from the so called "particle traps" (Whipple 1972). In the left panel of Fig. 2.13, one can see that there is a mechanism allowing particles to concentrate in some regions, which are pressure maxima. This could provide a way in order to overcome the radial drift problem. Indeed, a high particle concentration turns out in increased collision rates, and (consequently) in a more rapid particles growth. How does this mechanism take place? First of all, we note that the equations of motion in the previous section do not explicitly predict inward radial drift; rather, solid particles drift towards regions of high pressure ($v_{\rm R} \approx \Delta v \propto \nabla P$). Indeed, if we consider a local radial pressure maximum at radius R_0, the gas is sub-Keplerian for $R > R_0$ ($\nabla P < 0$) but super-Keplerian for $R < R_0$ ($\nabla P > 0$) . Dust particles are generally Keplerian, so they experience a headwind at $R > R_0$, and at the same time they receive a tailwind if $R < R_0$. Therefore, the headwind torque removes angular momentum and causes inward drift, while the tailwind adds angular momentum and drives outward drift. The net effect is that dust migrates towards the pressure maximum (which corresponds to an overdensity) from both directions. This is why the pressure maxima is called a "dust trap" (Rice et al. 2006b; Pinilla et al. 2012a). One can characterize two positive outcomes: the first one is that the radial inward migration slows down, if not halted at all. The second one is that at pressure maxima the density increases, and this, as we said, leads to a higher number of collisions, and to a faster grain growth. Other possible ways of going from pebbles to planetesimal in these dust traps are the streaming instability (Youdin & Goodman 2005; Johansen et al. 2007) or the direct gravitational collapse (Goldreich & Ward 1973; Youdin & Shu 2002). These pressure maxima can be created locally either via small-scale

structures or through turbulence. In particular, likely scenario where such a pressure bump can arise are given by the edges of dead zones (e.g. Varnière & Tagger 2006), the edges of gas gaps cleared by massive planets (Zhu et al. 2012b; Pinilla et al. 2012b, see Chaper 4, and for an example see central panel in Fig. 2.13), in zonal flows (with azimuthal dust trap, e.g. Barge & Sommeria 1995; Klahr & Henning 1997), which can be the result of a Rossby Wave Instability of a radial pressure bump (e.g. Lovelace et al. 1999; Wolf & Klahr 2002; Lyra et al. 2009; Regály et al. 2012). It has been shown that also spiral waves originated by gravitational instabilities could trap dust (e.g. see right panels of Fig. 2.13, Rice et al. 2006b, and Dipierro et al. 2014 for observational prediction of ALMA continuum observation of dust trapped in GI spirals). It is interesting to note that a practical way to investigate the presence of dust trapping in protoplanetary disc is to look at the same system at different wavelengths (Cazzoletti et al. 2018; Long et al. 2020) and to study the dust spectral index (Testi et al. 2014).

We can give an estimate of the pile-up timescale. If the pressure gradient has a scale length ΔR, the local radial dust velocity is (see Eq. 2.65, assuming $v_{R,\mathrm{g}} = 0$) $|v_R| \propto \eta v_\mathrm{k} \propto \partial P/\partial R \sim P/\Delta R$, while the unperturbed radial dust motion is $\propto P/R$. The timescale for solids to pile-up at the pressure maximum is further reduced by a factor $\Delta R/R$ because the planetesimals have to move only of a distance $\sim \Delta R < R$ to reach the density maxima. Moreover, typical density/pressure inhomogeneities are characterized by a typical length scale $\sim H$ (the height scale of the disc). Therefore, the timescale to concentrate solids at the pressure maximum is shorter than the global drift timescale by a factor of $(\Delta R/R)^2 \sim (H/R)^2 \sim 0.01$, approaching values of the order of $\sim$ one year for marginally coupled particles ($\mathrm{St} \approx 1$) in typical discs, given a drift timescale $t_\mathrm{drift}\Omega_\mathrm{k}$ of the order of 10^2 (see Fig. 2.6 of Dipierro et al. 2016). Moreover, we can also provide an estimate for the minimum Stokes number below which particles are no more trapped. With $\mathrm{St} \ll 1$, the condition on the dust velocity for having trapped particles is $v_\mathrm{R} > 0$ (with v_R given by Eq. 2.70), which yields

$$\mathrm{St} > \frac{\alpha}{|\zeta|}\left(\frac{\mathrm{H}}{\mathrm{R}}\right)^2, \tag{2.76}$$

where it has been assumed a gas velocity $v_{\mathrm{g,R}} \sim \nu/R$ and the Shakura-Sunyaev α-prescription. For Stokes number greater than this value, particles are trapped in the pressure maxima, otherwise they filter through the gap, reaching the disc inner region.

2.3.2 Radial drift in disc observations

It is interesting to observe the general picture given by dust observations. The first point to note is that while discs with substructures (such as rings or spirals) have a larger radial extent, discs with no detected substructures are generally smaller. One should also say that these discs are also fainter, thus it could be that the lack of substructures is just a resolution issue. However, this difference in size can in principle be explained by looking at the gas and dust evolution. Indeed, gas viscously spread and evolve, slowly accreting on the central star, while dust is affected by the radial drift mechanism. If a substructure is present, this could

correspond to a pressure maximum and thus to a dust trap. Consequently, the dust would stop (or at least decrease) its inward radial motion. Instead, discs with no detected substructures appear to be smaller, since they do not host dust traps. Though, it is important to remember that this is just a simplicistic description, since many more mechanisms involving both dust and gas play a main role in the evolution of the disc. For example, we could think to the shrinking of the radial dust extent as an outcome of radial drift, but one should consider that, even if radial drift promotes a rapid inspiral of the fastest-drifting dust, it is ineffective in the overall picture. Indeed, models of grain growth predict that the dust in the outer parts of discs is small enough to be relatively well coupled to the gas, thus following the viscous, outwards flow. We can investigate what are the processes regulating the disc evolution by looking at a wide sample of disc, making for example a population synthesis study (e.g. Rosotti et al. 2019b; Sellek et al. 2020a and Toci et al. 2021 in prep). Here we are going to present, in a non exhaustive way, some of the last works connecting radial drift and the observed disc extent.

Birnstiel et al. (2010a) found that radial drift leaves a distinctive "fingerprint" in the dust surface density profile that is directly accessible through current observational facilities. Using an analytical framework for dust evolution, they demonstrate that the combined effects of drift and (viscous) gas drag naturally produce a sharp outer edge in the dust distribution. This edge feature forms during the earliest phase in the evolution of disc solids, before grain growth in the outer disc has made much progress, and is preserved over longer timescales when both growth and transport effects are more substantial. Pinte & Laibe (2014) showed, as expected, that the outcome of the dust migration process is very sensitive to the physical conditions within the disc (such as the aspect ratio of the disc, the dust-to-gas ratio and the surface density profile). More recent works highlighted correlations between disc properties and managed to explain some of them through the radial drift process. By using models of grain growth and radial drift, Rosotti et al. (2019b) showed that the observed disc radii is tracing where the dust grains are large enough to have a significant sub-mm opacity ("opacity cliff", see right panel in Fig. 2.14). They also concluded that the prediction of viscous models is that the dust flux radius increases with time, but only when considering relatively high fractions (95%) of the disc flux, otherwise (with the 68%) it is observed a shrinking (see left panel of Fig. 2.14). This is a consequence of the small dust opacity (and therefore surface brightness) in the outer part of the disc. At the current state, observations are not able to detect the viscous spreading expected when observing the radius corresponding to the 95% of the flux (see the right panels in Fig. 9 of Rosotti et al. 2019b), and we would need deeper surveys to detect it. In contrast, the 68% flux radius traces where the grains are large, probably large enough to be linked to radial drift. Finally, they also show that if the maximum grain size is set by radial drift, this implies relatively low values of the viscous parameter $\alpha \simeq 10^{-3}$ (in agreement with Flaherty et al. 2020). At the same time, Sellek et al. (2020a) found that for turbulent viscosities with $\alpha \simeq 10^{-3}$, the depletion of dust from the disc due to radial drift allows to reproduce the range of masses and accretion rates seen in the Lupus and Upper Sco

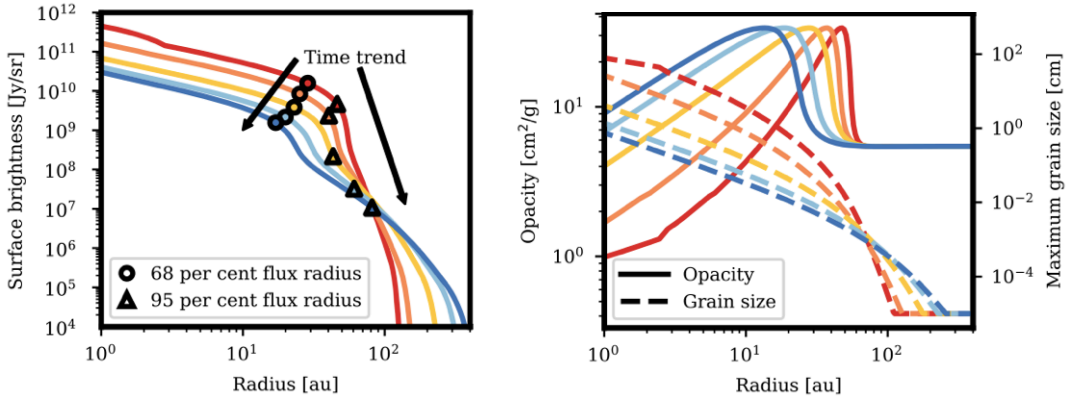

Figure 2.14: Time evolution of the flux, opacity and grain size as a function of the radial extent of the disc. While the 68 per cent flux radii shrink (and at this location it corresponds a drop in flux), the 95 per cent expand. The location of the abrupt change in the surface brightness in the top panel corresponds to the location of the peak in the opacity (Rosotti et al. 2019b).

datasets. Moreover, radial drift and radially dependent grain growth lead to a dependence between the extent of the continuum emission and the wavelength of the observations, with emission at longer wavelengths being more compact (see e.g., Tripathi et al. 2018). On the wake of these studies, Trapman et al. (2019) required that discs should be observed at high enough angular resolution in order to distinguish between observed radial extent due to radial drift and grain growth or from line optical depth. Trapman et al. (2020) investigated the occurrence of common radial drift and radially dependent grain growth across the Lupus disc population. For half of the sample disc, they need both dust evolution and optical depth effects to explain the observed gas-dust size difference. Their analysis shows that most of the discs in their sample, which represent the bright ones of the Lupus disc population, are consistent with radial drift and grain growth. Furthermore, they also find six faint discs with ^{12}CO emission beyond four times their dust disc size, suggesting that radial drift could be a common feature among bright and faint discs. Instead, Tazzari et al. (2020b), in their study at 0.9,1.3 and 3.1 mm of the 26 brightest disc in the Lupus survey, note that when observed at 3.1 mm the discs appear to be only 9% smaller than when observed at 0.9 mm, appearing not in agreement with models of dust evolution which predict a sharper difference (26% smaller radius at 1.3 mm and a 64% smaller radius at 3.1 mm.).

It should be noted that many of the models developed in the literature, when studying the dust evolution, consider each radius to be populated at a first approximation by the larger grain size (Birnstiel et al. 2012), neglecting the fact that due to turbulence, dust growth, vertical settling and radial drift, at each radii there is a size distribution of grains, which interact with the gas, and between themselves in different ways.

Part II

Disc substructures from dynamical processes

Chapter

3

Self-gravity: the disc mass matter

Protoplanetary disc: 10^{-2}–$10^{-4}\,M_\odot$*?*
Grey Whale (Eschrichtius robustus): $1.36 \cdot 10^{-26}\,M_\odot$ *(Los Angeles, 2018).*

In Chapter 2 we described the gas dynamics when neglecting the disc contribution to the gravitational potential. However, we do know that especially during the early stages of star formation, the protostellar disc is still accreting from the parental molecular cloud, and in general it could be massive enough to alter the disc dynamics and star formation. Adding the self-gravity ingredient to the disc evolution recipe can help explaining some of the substructures we observe today,

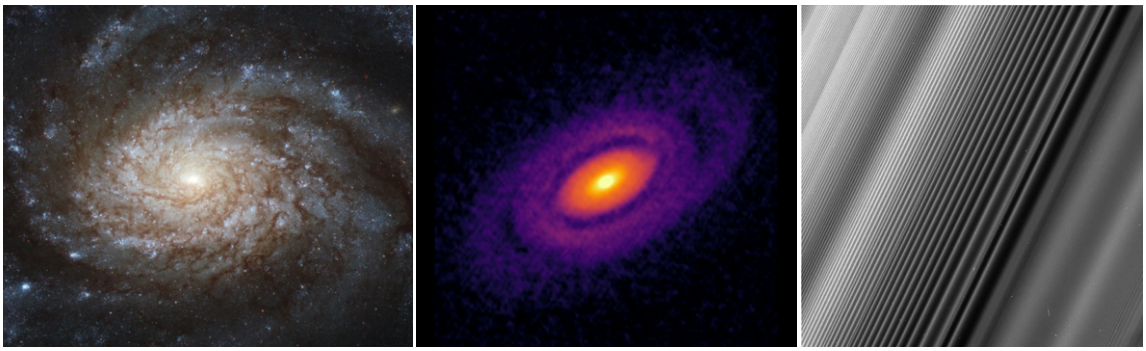

Figure 3.1: Three examples of spiral structures detected in discs system at different scales: the NGC 3810 galaxy (left panel, credit to ESA/Hubble and NASA), the protoplanetary disc Elias 2-27 (central panel, Andrews et al. 2018b) and Saturn's rings (right panel, credit to NASA/JPL-Caltech/Space Science Institute).

and in principle can also lay the foundations for the formation of planetesimals. Indeed, if the substructures observed in Class II, or even Class I, discs are due to planets, this pushes the process of planet/planetesimal formation to an era when self-gravity is important. The disc self-gravity may alter the dynamics through the propagation of density waves, leading to the formation of a prominent spiral structure. These structures may have a twofold outcome: they are thought to provide a non negligible contribution to the angular momentum transport (Lodato & Rice 2004, 2005; Cossins et al. 2009b), and the instability can be strong enough to lead to the formation of gravitationally bound clumps within the disc, and thus to determine the disc fragmentation, paving the way to the formation of gas giant planets (Rice et al. 2004; Rice et al. 2006a). Additional, such spirals may provide suitable conditions for the formation of planetesimals (Rice et al. 2005, 2006a). It is interesting to note that the disc self-gravity is important not only in the process of star and planet formation, but also in other astrophysical contexts, such as disc around Active Galactic Nuclei, galaxies, and at a smaller scale the Saturn's rings (see Fig. 3.1).

For these reasons, understanding how massive protoplanetary discs are, especially at the beginning of their life, can shed some light on the origin of the spirals we observe and on the mechanisms behind the formation of planets. In this Chapter we will go through the processes and dynamics described previously, including the self-gravity of the disc. The modern theory of gravitationally unstable discs was first described by Paczynski (1978) and Lin & Pringle (1987), and recently reviewed by Lodato (2007) and Kratter & Lodato (2016), to which we refer for a deeper discussion.

3.1 Self-gravitating disc structure

As mentioned above, in some cases, neglecting the self-gravity of the disc is not possible. This is what happens for examples in discs around young stars and

supermassive black holes. Here we derive some differences that can arise in the disc structure when considering the disc self-gravity. We remind the reader that the thin disc approximation is still valid, and that the starting point to obtain the disc structure is always the Navier-Stokes equation (see Sec. 2.1.1).

3.1.1 Vertical hydrostatic equilibrium

We consider a self-gravitating vertical isothermal and radially homogenous slab of gas, assuming that the vertical gravitational field is dominated by the disc self-gravity $\nabla\Phi = -2\pi\mathcal{G}\Sigma(z)$, which has been obtained from the Poisson equation (Eq. 2.6), where we are neglecting the gravity of the central star. Then, our relation for the hydrostatic equilibrium (Eq. 2.17) becomes:

$$\frac{c_{\rm s}^2}{\rho}\frac{\partial\rho}{\partial z} = -2\pi\mathcal{G}\Sigma(z)\,, \tag{3.1}$$

with $\Sigma = \int_{-z}^{z}\rho(z')dz'$. The vertical density profile (Spitzer 1942) can be derived as,

$$\rho(z) = \rho_0\frac{1}{\cosh^2(z/H_{\rm sg})}\,, \tag{3.2}$$

where $H_{\rm sg}$ is the thickness in the self-gravitating gas

$$H_{\rm sg} = \frac{c_{\rm s}^2}{\pi\mathcal{G}\Sigma}\,. \tag{3.3}$$

It is important to highlight that usually in a protostellar disc both the star and the disc contributes to the gravitational potential. In order to understand what is the dominant component, we need to compare the disc thickness $H_{\rm sg}$ and $H_{\rm nsg} = c_s/\Omega_k$:

$$\frac{H_{\rm sg}}{H_{\rm nsg}} = \frac{c_{\rm s}\Omega_k}{\pi\mathcal{G}\Sigma}\,, \tag{3.4}$$

where the right side of the equation is approximately equal to the stability parameter $\mathcal{Q}$ (Toomre 1964), giving us information about the stability of the disc (see Sec. 3.2 below). When $\mathcal{Q} > 1$, the disc is stable and the dominant component is the gravity of the central object. Instead, when $\mathcal{Q} < 1$, the dominant component is the self-gravity and the disc is unstable. This condition highlights the important roles played by the gas surface density, the temperature and the local orbital timescale, and it suggests that a massive and/or a cold disc will be unstable. From Eq. 3.4 we can write a relationship between the aspect ratio of disc, in the two configuration, and the ratio between the mass of the central object $M_\star$ and the mass of the disc $M_{\rm disc}$:

$$\mathcal{Q} \simeq \frac{H_{\rm nsg}}{R}\frac{M_\star}{M_{\rm disc}}\,, \tag{3.5}$$

where $M_{\rm disc} \approx 2\pi\Sigma R^2$. This relation is obtained more specifically, by analyzing and comparing the two contributions ($M_\star$ and $M_{\rm disc}$) to the vertical component of the gravitational field. We note that from Eq. 3.5 we can derive how massive the disc needs to be, in order for self-gravity to significantly affect its vertical structure. The vertical structure of the disc is affected by self-gravity already

Figure 3.2: Saturn with his rings, seen by the NASA's Cassini spacecraft (https://saturn.jpl.nasa.gov/).

when the disc mass is of the order of $M_{\rm disc}/M_\star \approx H_{\rm nsg}/R \ll 1$. Thus, for thin discs this happens even when the disc mass is much smaller than the central object mass. This is the case, for example, of the Saturn's rings, that are self-gravitating, with $H/R \sim 10^{-8}$ (Figure 3.2).

3.1.2 Centrifugal balance

As we derived in Sec. 2.1.1.1, the centrifugal balance in the radial direction gives us the disc rotation curve. For non self-gravitating discs, the gas orbital velocity is slightly sub-Keplerian, due to the pressure gradient contribution. In the same way, when the disc mass is not negligible, we need to consider its contribution to the gravitational potential. Therefore, the general equation describing centrifugal balance is

$$\Omega^2 \sim \frac{1}{R}\frac{\mathrm{d}\Phi_{\rm disc}}{\mathrm{d}R} + \frac{GM_\star}{R^3} + \frac{1}{\rho}\frac{\partial P}{\partial R}\,, \tag{3.6}$$

where $\mathrm{d}\Phi_{\rm disc}/\mathrm{d}R$ is the disc contribution to the gravitational potential, and where also the pressure correction term has been included. The disc contribution to the gravitational field depends on the matter distribution through the Poisson's equation $\nabla^2\Phi_{\rm sg} = 4\pi\mathcal{G}\Sigma\delta(z)$, where $\delta(z)$ is the Dirac δ-function which is introduced to indicate that the disc is confined to the mid-plane (thin-disc approximation). It can be derived (see Appendix A and Binney & Tremaine 1987; Bertin & Lodato 1999) that the disc self-gravity contribution to the gravitational potential is:

$$\frac{\partial\Phi_{\rm disc}}{\partial R}(R,z) = \frac{\mathcal{G}}{R}\int_0^\infty \left[K(k) - \frac{1}{4}\left(\frac{k^2}{1-k^2}\right)\left(\frac{R'}{R} - \frac{R}{R'} + \frac{z}{RR'}\right)E(k)\right]\sqrt{\frac{R'}{R}}k\Sigma\left(R'\right)\mathrm{d}R'\,, \tag{3.7}$$

with $K(k)$ and $E(k)$ being complete elliptic integrals of the first and second kind, and where

$$k^2 = \frac{4RR'}{\left[(R+R')^2 + z^2\right]} \tag{3.8}$$

(see Gradshteyn & Ryzhik 1980). Bertin & Lodato (1999) computed the field $\mathrm{d}\Phi_{\rm disc}/\mathrm{d}R$ in the equatorial plane by taking the limit $z \to 0$. This relation is rather complicated, and it can be computed numerically. However, there are a few cases where a simple analytical result is possible. For example, if we consider a Mestel disc with $\Sigma = \Sigma_0 R_0/R$ (Mestel 1963) the gravitational field is given by

$$\frac{\partial \Phi_{\rm disc}}{\partial R} = 2\pi \mathcal{G}\Sigma\,, \tag{3.9}$$

and the gas orbital velocity induced by self-gravity takes the form

$$v_\varphi^2 = R\frac{\partial \Phi_{\rm disc}}{\partial R} = 2\pi \mathcal{G}\Sigma_0 R_0\,. \tag{3.10}$$

It is interesting to note that the Mestel disc is also the solution to the accretion disc equations in a steady state, when assuming strongly self-gravitating discs (Bertin 1997). Although the mass of the central star cannot normally be neglected in accretion discs, we note that the gas density profile is often observed to be $\Sigma \propto 1/R$. Other analytic cases can be found in Binney & Tremaine (1987).

If we consider Eq. 3.6 in its totality, we can make some considerations about deviations from "Keplerianity" induced by the pressure term and the self-gravity. The pressure gradient modifies the disc rotation curve with deviation from the Keplerian motion of order $(H/R)^2$. Self-gravity also affects the centrifugal balance by a force term which is $\simeq \mathcal{G}M_{\rm disc}/R^2$, where $M_{\rm disc}$ is the disc mass contained in the disc portion of radius R, being $M_{\rm disc} = \pi\Sigma R^2$. It is worth noting from Eq. 3.5 that when the disc is marginally gravitationally stable ($Q \approx 1$), the disc mass is of the order of $(H/R)M_\star$, resulting in a deviation from Keplerian motion due to self-gravity of the order of H/R. This deviation is actually stronger than the effect of pressure gradients. From these considerations, and knowing that spiral structures can originate from gravitational instabilities, if such a structure is observed in a disc and velocity data are present, then Eqs. 3.6 and 3.7 can be used to fit the mass of the disc. This dynamical method has been used for galaxies and AGN (e.g. Lodato & Bertin 2003), and in Chapter 8 I show its application to a protoplanetary disc. This last case is of particular interest, since disc mass estimates of protoplanetary discs mainly based on the disc chemistry and dust emission are often very uncertain. Thus, finding an independent method is crucial and can help to put more limits on the value of mass in discs.

3.2 The origin of gravitational instabilities

Until now we described how the disc structure can change if self-gravity is not negligible, but we also know that one of the most important effects associated to self-gravity is the possibility to develop gravitational instabilities. A first study of this kind of instabilities has been performed by Jeans (1902) for an infinite, static and homogeneous medium at a fixed temperature, finding that there is a critical mass above which gravity overcomes the thermal pressure support (which is more effective at small scales), and the cloud becomes unstable to small perturbations. If we want to apply this study to rotating thin disc, the stability analysis is more

complex, due to the different geometry and to the additional stabilising effect of the shear, which is more effective at large scales. The outcome of gravitational instabilities can be twofold: while the non-linear outcome of the instability can be violent and lead to disc fragmentation, at the same time there is the possibility of forming a long-lived spiral structure, which is related to the fact that the instabilities have a steady transport of angular momentum and self-regulate. Both of these instabilities manifestations have an impact on the formation of planets. In fact, it has been shown that dust can concentrate in the spiral waves of a non-fragmenting gravitationally unstable disc, creating the conditions for the formation of planets (Rice et al. 2004; Rice et al. 2006a; Clarke & Lodato 2009). Indeed, this high concentration of dust grains in some regions of the disc enhances their collision rate, accelerating the process of grain growth, and thus of planet formation by means of direct gravitational collapse. On the other hand, fragmentation is a way of shutting off the instability, and it could be of great importance, as fragmentation can in principle lead to the formation of either stellar, brown dwarf, of perhaps planetary mass companions.

3.2.1 Spiral waves

We give here a brief description of spiral waves density in discs. We consider waves in razor thin discs, and consequently we only care about perturbations in the radial (R) and azimuthal (ϕ) directions. In order to describe a spiral one can use the shape function $\psi(R)$ in a way such that

$$m\phi + \psi(R) = c \mod 2\pi\,, \tag{3.11}$$

with c a constant value and

$$\psi(R) = \int_0^R k\left(R'\right) \mathrm{d}R'\,. \tag{3.12}$$

In these two equations are introduced two important wavenumbers characterising the spiral wave. The first one is the azimuthal wavenumber $m \geq 0$, which corresponds to the number of modes of the perturbations, and thus of spiral arms (see e.g., Fig. 3.3). The second one is the radial wavenumber k, and there are no restrictions for its value. Indeed, if the disc is rotating in the sense of increasing ϕ, one can identify two categories depending on the value of k: leading waves for $k < 0$ (i.e. waves pointing in the direction of rotation), and trailing waves for $k > 0$ (i.e. waves pointing counter to the rotation direction). By combining the radial and azimuthal wavenumbers we can determine the winding of the spiral, also known as pitch angle i, as

$$\tan i = \frac{m}{kR}\,. \tag{3.13}$$

From this relation, by considering $m/(kR) \ll 1$, we can define tightly wound spiral waves. For this kind of waves the radial wavenumber is very large (and thus the radial wavelength is very small) when compared with the azimuthal wavenumber. This property can be used to carry out a Wentzel-Kramers-Brillouin (WKB) expansion of the perturbed fluid equations (see next Section). We highlight that

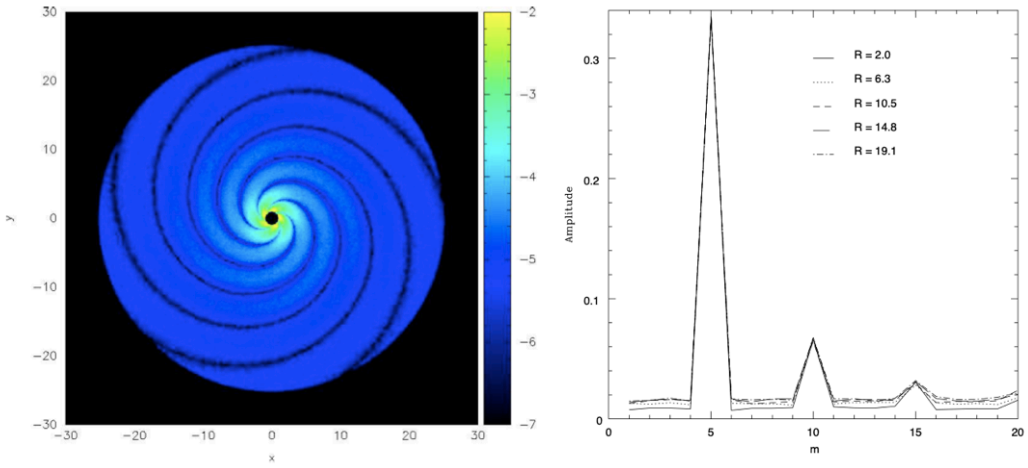

Figure 3.3: Left panel: disc surface density showing an imposed spiral waves. Right panel: results of the Fourier decomposition of test disc shown in the left panel, in terms of the azimuthal wavenumber, m. Images taken by Cossins et al. (2009b).

spirals can also be excited by the interaction between the disc and an embedded companion. It is interesting to note that these two kinds of spiral differ from each other, especially for the pitch angle, the number of modes that can be excited (see Chapter 5) and the disc dynamics and angular momentum transport.

3.2.2 Dispersion relation and disc stability

In order to understand the onset of gravitational instabilities we will start by analyzing the response of an infinitesimally thin disc under the action of small perturbations. Since the gravitational force has a long-range nature, the gravitational potential at a given location depends on the whole gas disc distribution, making the analysis difficult. To get around the problem, the idea is to perform a linear perturbation local analysis of the dynamical equations, by assuming that the density perturbations imposed on the unperturbed disc are small. Thus, for tightly wound perturbations (with a pitch angle $m/|kR| \ll 1$, where k is the radial wavenumber and m is the azimuthal one, corresponding to the number of arms of a spiral disturbance), in order to infer the features of propagating radial and azimuthal waves, one can adopt the tight-winding approximation to simplify the analysis and obtain the dispersion relation. The above-mentioned dynamical equations that are considered in such analysis are the continuity and momentum equations (see Eqs. 2.4 and 2.5), together with an equation of state (in case of barotropic gas, $c_\mathrm{s} = \mathrm{d}P/\mathrm{d}\rho$), to connect pressure and density, and with Poisson's equation (Eq. 2.6), to link the disc density to the gravitational potential. In this approximation, we perturb the equilibrium with a monochromatic perturbation

$$\Sigma' = \delta\Sigma \exp[i(m\phi - \psi(r) - \omega t)]\,, \tag{3.14}$$

where ω is the angular frequency and we used the description of spiral wave of Eq. 3.11. It can be shown that the only solution to the Poisson's equation given

this perturbation is

$$\Phi' = \delta\Phi \exp[i(m\phi - \psi(r) - \omega t)]\,, \tag{3.15}$$

and that the relation linking the potential perturbation $\delta\Phi$ to the density one is

$$\delta\Phi = -\frac{2\pi\mathcal{G}}{|k|}\delta\Sigma\,, \tag{3.16}$$

obtained by computing the integral of the Poisson's equation. By keeping only first order terms in the perturbed quantities, one can derive that for non axisymmetric disturbances ($m \neq 0$) the dispersion relation $D(\omega, k, m)$ (Lin & Shu 1964; Binney & Tremaine 1987; Bertin 2000) is

$$D(\omega, k, m) = (\omega - m\Omega)^2 - c_{\rm s}^2 k^2 + 2\pi G\Sigma|k| - \kappa^2 = 0 \tag{3.17}$$

where κ is the epicyclic frequency defined as

$$\kappa^2 = \frac{2\Omega}{R}\frac{\partial\left(\Omega R^2\right)}{\partial R} \tag{3.18}$$

which represents the oscillation frequency of a particle in a pressureless shearing non self-gravitating flow subject to a small radial displacement from equilibrium. The epicyclic frequency κ is generally of the order of the angular velocity Ω, where the exact proportionality depends on the rotation curve. For example, for Keplerian rotation we have that $\kappa = \Omega$. We highlight that this relation is similar to the dispersion relation obtained for the non-rotating, uniform, infinite and infinitely thin sheet of matter (e.g. Binney & Tremaine 1987), where the only difference can be found in the term involving the epicyclic frequency, which is related to rotation. For a detailed discussion of the physics behind the dispersion relation, we refer the interested reader to Bertin & Lin (1996) and Bertin (2000).

Starting from the dispersion relation (Eq. 3.17), we can discuss the conditions for the disc stability under the effect of the thermal pressure (first term in the rhs), the disc self-gravity (second term) and the disc rotation (third term). Let us assume axisymmetric disturbances with $m = 0$. If $\omega^2 > 0$, a given perturbation propagates in a wave-like way, otherwise if $\omega^2 < 0$ (imaginary ω) exponentially growing instabilities arise. We can categorise the right hand side terms of the dispersion relation into stabilising and destabilising, depending on their signs. Thus, the first and third terms, respectively related to pressure forces and to the disc rotation, are stabilising, while the second term, linked to the disc self-gravity, has a destabilising effect. We note that the three terms depend on three different power-laws in k, meaning that while the pressure term dominates at small wavelengths (large k), rotation stabilises the disc at large wavelengths (small k). In an intermediate regime we can find the disc self-gravity. When $\omega^2 > 0$ and the perturbation is stable, Eq. 3.17 can be solved easily (simple quadratic expression for the wave number k), finding,

$$\mathcal{Q} = \frac{c_{\rm s}\kappa}{\pi\mathcal{G}\Sigma_{\rm g}} > 1\,, \tag{3.19}$$

where $\mathcal{Q}$ is known as Toomre parameter. This parameter is thus essential to determine if an infinitesimally thin disc can be locally perturbed by gravitational

instabilities. We note that, as discussed above, the definition of $\mathcal{Q}$ contains the balance between the stabilising effects of rotation, where for a Keplerian disc $\kappa(R) = \Omega(R)$, and of thermal pressure $c_s(R)$, as well as the destabilising effect of the disc self-gravity, expressed by means of $\Sigma(R)$. From this expression for $\mathcal{Q}$ it can be derived Eq. 3.5, which for $\mathcal{Q} \sim 1$ corresponds to $M_{\rm disc}/M_\star \sim H_{\rm nsg}/R$, meaning that a relatively light thin disc can be gravitationally unstable. Starting from these relations, we can obtain the minimum mass necessary for a disc to be self-gravitating. Generally, colder and thinner discs are more susceptible to develop GI. A qualitative estimate can be given, knowing that star forming regions do not have temperatures below 10 K, and that the disc radius can be assumed between 10^2 and 10^3 au (see Sec 1.2.2). From this assumption one can find that the requirement for the onset of gravitational instabilities, $\mathcal{Q} < 1$ (Kratter & Lodato 2016) gives

$$\frac{M_d}{M_*} > 0.06 \left(\frac{f}{1}\right) \left(\frac{T}{10K}\right)^{1/2} \left(\frac{r}{100AU}\right)^{1/2} \left(\frac{M_\odot}{M_*}\right)^{1/2}, \tag{3.20}$$

where f contains numerical factors of order unity, which depend on the surface density profile. For gravitationally unstable discs, $\mathcal{Q} \sim 1$, it is also possible to compute the most unstable wavelength λ_0, by finding the radial wave number κ_0 for which the right-hand side of Eq. 3.17 has a minimum. From a simple derivation, λ_0 is given by

$$\lambda_0 = \frac{2\pi}{k_0} = \frac{2\pi c_s^2}{\pi \mathcal{G} \Sigma_g} = 2\pi H_{\rm sg}\,, \tag{3.21}$$

which is of the order of the disc thickness scale $H_{\rm sg}$.

Finally, it should be noted that massive discs that are locally stable according to the stability criterion (Eq. 3.19) might be able to generate violent, large scale non-axisymmetric perturbations. This kind of perturbations cannot be treated with the WKB tightly wound approximation, but it is possible to generalise the analysis in order to get the global dispersion relation (Lau & Bertin 1978; Kratter & Lodato 2016; Lodato 2007). This relation depends on an additional parameter, J, that being proportional to Σ, is a measure of he disc mass.

H/R and $M_{\rm disc}/M_\star$ dependence As derived above from the Lin & Shu dispersion relation, an interesting properties of perturbations excited by the disc self-gravity is that the dominant modes have a wavenumber $k \propto 1/H_{\rm sg}$. This characteristic has been confirmed in numerical simulations by performing a spectral analysis (Boley et al. 2007; Cossins et al. 2009b). At the same time, also the azimuthal wavenumber m scales with the inverse of the disc thickness $H_{\rm sg}$, meaning that thicker discs shows fewer spiral arms and a more open spiral structure. We can find the same behaviour when considering the disc mass, $q = M_{\rm disc}/M_\star \propto 1/m$ (Lodato & Rice 2004; Cossins et al. 2009a; Dong et al. 2015c). Indeed, from Eq. 3.19 we derived that the disc self-gravity starts to be important when the disc-to-star mass ratio equal the disc aspect ratio. This can be observed in Fig. 3.4, where in the left panel is presented the snapshot of a three-dimensional simulation (Kratter et al. 2010), with $M_{\rm disc}/M_\star \sim 0.5$, in which the strong left-right asymmetry is evidence of a dominant $m = 1$ mode. In the right panel is shown

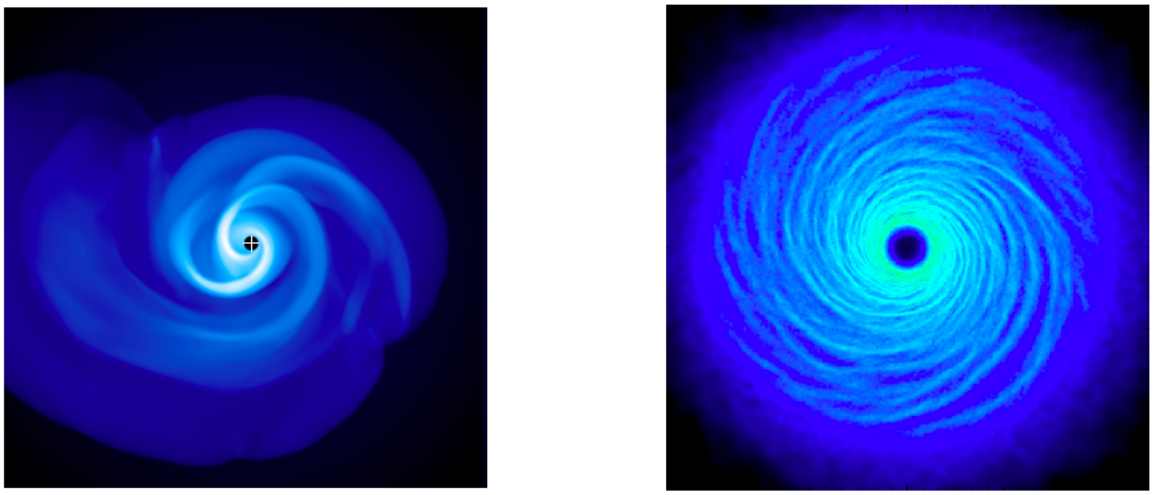

Figure 3.4: Left panel: snapshot from a simulation of a self-gravitating disc with $M_{\rm disc}/M_\star \sim 0.5$, from Kratter et al. (2010). Right panel: snapshot from a simulation of a self-gravitating disc with $M_{\rm disc}/M_\star \sim 0.1$, from Cossins et al. (2009b).

a three-dimensional simulation from Cossins et al. (2009b), with $M_{\rm disc}/M_\star \sim 0.1$, where instead the dominance of high m spiral structure is evident. This peculiar properties of gravitational instabilities could in principle be used to constraints from observations the disc-to-star mass ratio and/or the disc aspect ratio.

3.2.3 Self-regulation

The stability parameter $\mathcal{Q}$ encloses another peculiar property typical of self-gravitating discs. As described above, since $\mathcal{Q}$ is proportional to the sound speed, we expect that colder disc would be more gravitationally unstable (as shown in Eq. 3.19), thus to fully characterise the evolution of gravitational instabilities one should consider various disc properties, including the temperature and the cooling rate. We look at a disc which is initially hot enough to guarantee that $\mathcal{Q} > 1$ everywhere. The disc is thus expected to cool down simply due to radiative cooling, producing a decrease in the value of $\mathcal{Q}$ until it reach almost the order of unity. At this stage, the disc is cold enough to develop gravitational instabilities, with the consequent propagation of spiral density waves within the disc. This waves propagation provides angular momentum and energy transport, and produces compressions and shocks, that result in heating mechanisms. These shocks arise from the supersonic difference of speed between the spiral pattern and the disc. The outcome of this process is that $\mathcal{Q}$ increases. As a consequence, the disc is expected to reach the so-called *marginal stability*, with $\mathcal{Q} \sim \bar{\mathcal{Q}} \approx 1$, thanks to the heating that is switched on once the disc has cooled down below a certain threshold. We can describe this property of the stability condition as a "thermostat" which forces the instability to self-regulate, leading to thermal equilibrium state where the disc cooling is balanced by heating generated through gravitational instabilities. In this regime, spiral perturbations do not grow exponentially, but their amplitude saturates at some finite value. A large number of numerical

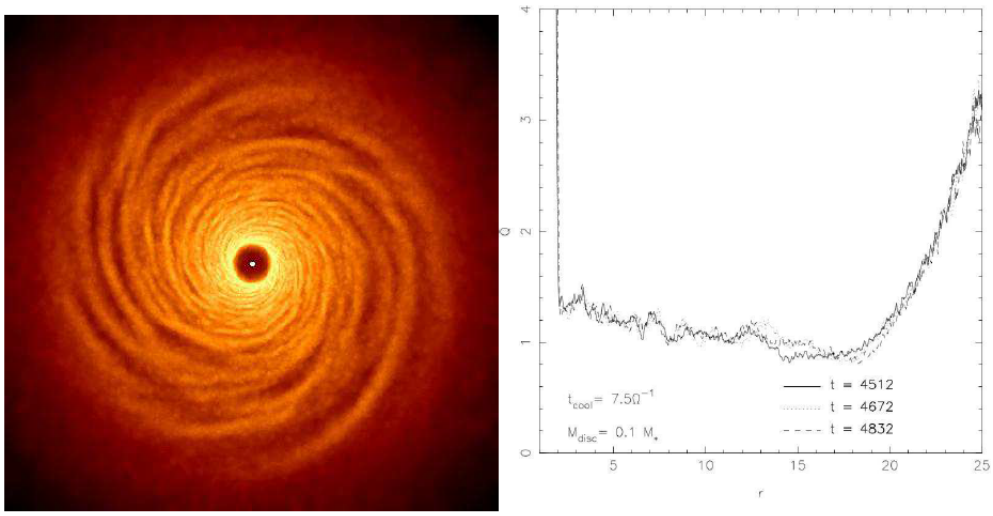

Figure 3.5: Left panel: Surface density snapshot from a simulation of a cooling self-gravitating disc. Right panel: radial profile of the azimuthal and vertical average of $\mathcal{Q}$, where it is visible that the disc has reached self-regulation over almost all its extent. Image taken from Lodato (2007).

simulation studies have studied and reproduced this peculiar feature of GI (Lodato & Rice 2004; Vorobyov & Basu 2005, 2006; Cossins et al. 2009b). Indeed, after an initial transient, the disc reaches a quasi-steady state with large scale spiral structures (see e.g., Fig. 3.5).

3.2.4 Angular momentum transport

Another aspect to keep into account when discussing gravitational instabilities is the angular momentum transport inside the disc. It is now well known that spiral waves can transport angular momentum inside a disc, providing thus accretion onto the central star. Since spiral waves are generally structures that cover a large extent of the disc, a question arises spontaneously, which is if the angular momentum transport happens locally or on a larger scale. In other words, it is important to understand if the spiral waves will be able to travel within the disc significantly away from their corotation radius or if they will interact with one another and undergo shocks and dissipation, without propagating to large radial distances. If this is as a local mechanism, gravitational instabilities can be considered as a pseudo viscous process (e.g. Lodato & Rice 2004, 2005; Clarke & Lodato 2009; Cossins et al. 2009b; Forgan et al. 2011), meaning that it can be included in the "anomalous" α viscosity discussed in Sec 2.1.3.

The crucial point is that transport that arises from gravitational instabilities could happens over long distances, so it is necessary to verify if these waves are able to propagate over significant radial distances before being dissipated. Lodato & Rice (2004) showed that for disc-to-star mass ratio $M_{\rm disc}/M_\star < 0.25$, the local analysis can be used to descrive gravitational instabilities. Instead, in massive discs where $M_{\rm disc}/M_\star > 0.25$, global effects become dynamically important (Lodato & Rice 2005), and the disc dynamics is dominated by strong transient low-m spiral

modes producing strong angular momentum transport. In this second case, the disc does not reach a quasi-steady state. It is interesting to note how, not only the development of gravitational instabilities, but also the properties of the transport mechanism induced by them depends generally on the parameter $M_{\rm disc}/M_\star$. Therefore, for relatively low disc-to-star mass ratio, the torque produced by the development of non-axisymmetric modes induced by self-gravity can be treated as the viscous torque. As in the previous case, the work done by the stress provided by these "gravitoturbulent" fluctuations is dissipated in the disc, bringing a net conversion of mechanical energy into heat which allows the flow to accrete onto the central object. In light of this effect of the gravitational instability onto the angular momentum and energetic contents of the disc, the action of self-gravity is analogous to that of viscosity.

To put this in a more quantitative form, in order to consider gravitationally unstable disc as belonging to the accreting viscous disc category, we need to prove that the rate of work done on the flow locally is entirely specified by the local torque (Cossins et al. 2009b). Indeed, by considering the Navier-Stokes equation, the viscous torque per unit area is related to the stress tensor as

$$\dot{\mathcal{L}}_\alpha = \frac{\partial}{\partial R}\left(R^2 T_{R\theta}\right) , \tag{3.22}$$

where the stress tensor is in turn linked to local disc pressure through the α-prescription

$$T_{R\phi} = \frac{\partial \log \Omega}{\partial \log R}\alpha \Sigma c_{\rm s}^2 . \tag{3.23}$$

The power per unit surface $\dot{\mathcal{E}}_\alpha$ produced by this viscous torque is then simply given by

$$\dot{\mathcal{E}}_\alpha = \Omega \dot{\mathcal{L}}_\alpha \tag{3.24}$$

This last equation links the transport of angular momentum and the associated rate of work done by torques in the case of a local process.

To prove that this is valid also in the case of gravitational instabilities, we consider the torque and power associated with a spiral wave induced by GI. Standard wave mechanics (Toomre 1969; Shu 1970; Fan & Lou 1999) link the energy and angular momentum of a wave, $\mathcal{E}_{\rm w}$ and $\mathcal{L}_{\rm w}$ respectively, to the wave action $\mathcal{A}$:

$$\mathcal{E}_{\rm w} = \omega \mathcal{A} = m \Omega_{\rm p} \mathcal{A} \tag{3.25}$$

$$\mathcal{L}_{\rm w} = m \mathcal{A} , \tag{3.26}$$

where the wave action is defined as

$$\mathcal{A} = \frac{1}{4}\frac{\partial D}{\partial \omega}|\delta\Phi|^2 = \frac{m\left(\Omega_{\rm p} - \Omega\right)}{8\pi^2 G^2 \Sigma}|\delta\Phi|^2 . \tag{3.27}$$

The last equality is obtained by combining the dispersion relation and Eq. 3.16, describing the link between the density and the potential perturbation, and by introducing $\Omega_{\rm p} = \omega/m$, as the pattern speed of the perturbation. Finally, combining Eqs. 3.25, 3.16 and 3.27, we can write

$$\mathcal{E}_{\rm W} = \frac{\Sigma v_{\rm p} \tilde{v}_{\rm p}}{2}\left(\frac{\delta\Sigma}{\Sigma}\right)^2 \tag{3.28}$$

where $v_\mathrm{p} = m\Omega_\mathrm{p}/k$ and $\tilde{v}_\mathrm{p} = m(\Omega_\mathrm{p} - \Omega)/k$ are the radial and Doppler-shifted (i.e. measured in a frame co-moving with the fluid) radial phase speeds of the wave respectively, and $\delta\Sigma/\Sigma$ is the fractional amplitude of the perturbation. From this derivation, it can be noted that the ratio of energy and angular momentum (and the ratio of power and torque exerted on a disc when launching the wave) is the wave pattern speed Ω_p, while for the viscous stress it was the local rotation Ω. This means that generally, angular momentum and energy transport via gravitational instability cannot be considered as a local mechanism, and thus it cannot be describe as a viscous process. This is only possible at the corotation region, where $\Omega = \Omega_\mathrm{p}$. A similar result has been found also by Balbus & Papaloizou (1999). Indeed, by using Eq. 3.26, we can rewrite the wave energy density (Eq. 3.28) as a sum of two terms,

$$\begin{aligned}\mathcal{E}_\mathrm{w} &= \Omega\mathcal{L}_\mathrm{w} + (\Omega_\mathrm{p} - \Omega)\,\mathcal{L}_\mathrm{w} \\ &= \frac{\Sigma}{2}\frac{m^2}{k^2}\Omega\,(\Omega_\mathrm{p} - \Omega)\left(\frac{\delta\Sigma}{\Sigma}\right)^2 + \frac{\Sigma}{2}\frac{m^2}{k^2}\,(\Omega_\mathrm{p} - \Omega)^2\left(\frac{\delta\Sigma}{\Sigma}\right)^2 .\end{aligned} \tag{3.29}$$

While the first term on the right hand side is a local, viscous-like energy transport term, characterised by the local rotation speed Ω, the second term is a non-local one, characterised by $\Omega_\mathrm{p} - \Omega$. The latter is the "anomalous" energy transport term identified by Balbus & Papaloizou (1999), that prevents self-gravitating discs from behaving as pure viscous α-discs. Therefore, the degree of non-locality of the disturbance can be measured by the ratio between the two terms, $|\Omega - \Omega_\mathrm{p}|\,/\Omega$ (where this ratio properly identifies the fractional deviation between the local flow speed and the wave's pattern speed Ω_p). If the waves are able to travel within the disc significantly away from their corotation radius before being dissipated, the transport induced by spiral waves will be global. Since, this quantity can be measured in numerical simulations of marginally stable self-gravitating discs, Cossins et al. (2009b) found that the flow speed of the gas into spiral arms is marginally sonic,

$$|\Omega - \Omega_\mathrm{p}| \approx \frac{c_\mathrm{s}}{R}\,. \tag{3.30}$$

This means that the waves almost instantaneously dissipate their energy through shocks, and consequently they are not allowed to propagate far from where they are produced. Starting from this result, we can rewrite the parameter measuring the non-locality of the perturbation in terms of the disc-to-star mass ratio, thus obtaining,

$$\frac{|\Omega - \Omega_\mathrm{p}|}{\Omega} \approx \frac{H}{R} \sim \frac{M_\mathrm{disc}}{M_\star} \lesssim 1\,, \tag{3.31}$$

where it has been used Eq. 3.5. This relation indicates that a gravitationally unstable disc in marginal state ($\mathcal{Q} \approx 1$) is characterized by a self-adjustment of the pattern speed of the perturbations in order to ensure that the normal flow speed into the arms is sonic, thus minimizing the fraction of energy non-locally dissipated. Note that when $M_\mathrm{disc} \simeq M_\star$ global transport does become important.

3.2.5 Cooling rate and fragmentation

In Sec. 3.2.3 we discussed the self-regulation mechanism, but there are some conditions for which this mechanism fails. As a consequence, the disc develops high amplitude density perturbations, leading to the formation of gravitationally unstable overdensities. These regions may eventually become Jeans unstable (the Jeans mass decreases, for a given density, with decreasing temperature) and collapse under their own gravity, with the results that the disc fragments in bound clumps. This happens if the balance between heating and cooling is broken, with the result that the gravitational heating timescale is longer than the cooling timescale. Thus, gravity has not enough time to prevent the formation of these bound objects, which could be the progenitors of future brown dwarfs or giant planets (see Sec. 1.4.1).

It is important to understand what are the conditions necessary for the disc to self-regulate. To do so, we introduce a new parameter β measuring how efficient the cooling mechanisms are. While the gravitational instabilities supply heat on a timescale of the order of the dynamical time $t_{\rm dyn} = \Omega^{-1}$, we assume that the cooling timescale is a factor β longer, so that $\beta = \Omega t_{\rm cool}$ (Gammie 2001). Therefore, we can say that β is a measure of the cooling timescale with respect to the dynamical one, and controls the evolution and saturation of the instability. To properly study the disc evolution from a stable condition to an unstable one, it is necessary to consider the disc thermodynamics and energy equation. Usually, this is done in numerical simulations by considering a simple cooling prescription where the cooling rate is given by

$$\left.\frac{{\rm d}u}{{\rm d}t}\right|_{\rm cool} = -\frac{u}{t_{\rm cool}}\,, \tag{3.32}$$

where $t_{\rm cool}$ is the cooling timescale, which is set as free parameter, and u is the internal energy of the fluid

$$u = \frac{\Sigma c_{\rm s}^2}{\gamma(\gamma-1)}\,, \tag{3.33}$$

with γ the adiabatic index. A critical value $\beta_{\rm crit}$ can be found below which the disc fragments. Numerous studies showed that this cooling parameter is dependent on the equation of state ($\beta_{\rm crit} \approx 6-7$ for discs with $\gamma = 5/3$ and $\beta_{\rm crit} \approx 12-13$ for discs with $\gamma = 7/5$, Rice et al. 2005), the disc thermal history (Clarke et al. 2007), or the temperature dependence of the chosen cooling law (Cossins et al. 2010). Meru & Bate (2010) showed that the critical value of the cooling timescale is dependent on the ratio of the surface mass density to the stellar mass. However, many of these results can also potentially be explained if the fragmentation is dependent on the number of particles used in a numerical simulation (i.e. the resolution, Lodato & Clarke 2011). This last issue has been investigated in the last years, without reaching a full point to the question. In particular, Meru & Bate (2011) performed three-dimensional Smoothed Particle Hydrodynamics (SPH) simulations obtaining that fragmentation occurs for longer cooling timescales as the resolution is increased. This result underlines that the critical value of the cooling time-scale is longer than previously thought, and actually it raises the question of whether or not a critical value exists. In a later work, Meru &

Bate (2012) reached in their simulations the convergence of the critical cooling time-scale ($\beta_{\rm crit} > 20$), showing that it could depend on the numerical viscosity employed in numerical simulations. More recently, Deng et al. (2017) by performing numerical simulations of gravitationally unstable disc with SPH (with artificial viscosity) and a with a Lagrangian meshless finite mass scheme (no artificial viscosity) showed how the non-convergence problem in SPH is caused by artificial fragmentation triggered by an excessive dissipation of angular momentum in domains with large velocity derivatives. This actually remains an open issue (e.g., Paardekooper et al. 2011; Paardekooper 2012; Rice et al. 2012, 2014; Young & Clarke 2015)

In Section 3.2.4 we presented a discussion of whether or not angular momentum transport is non-local in self-gravitating disc. The outcome of that analysis was that the transport induced by self-gravity can be described locally in terms of viscosity. We also know that the disc behaviour is strongly dependent on the cooling timescale. Indeed, for a specific value of this parameter, the disc reaches a steady thermal equilibrium state in which the heating balances the imposed cooling. In these conditions, the amplitude of the spiral instability saturates. We already derived the heating induced by viscous dissipation in Sec. 2.1.2.3 and we recall it here for clarity,

$$D(R) = \nu\Sigma \left(R\Omega'\right)^2 = \left|\frac{\mathrm{d}\ln\Omega}{\mathrm{d}\ln R}\right|^2 \nu\Sigma\Omega^2 \,. \tag{3.34}$$

By equating the heating and the cooling rate (Eq. 3.32) a relationship can be derived between the cooling time and the viscous α (in this case also indicating the gravitational stress) parameter (Gammie 2001; Rice et al. 2005),

$$\alpha_{\rm GI} = \left|\frac{\mathrm{d}\ln\Omega}{\mathrm{d}\ln R}\right|^{-2} \frac{1}{\gamma(\gamma-1)\Omega t_{\rm cool}} \,. \tag{3.35}$$

This relations tell us that the rapid cooling required for fragmentation can also be interpreted as a maximum gravitational stress that a disc can support without fragmenting. It should be noted that Eq. 3.35 holds whenever self-gravity provides the necessary heating to reach thermal equilibrium, and if transport can be described viscously.

While in the previous derivation we used the viscous dissipation rate, knowing that the heating induced by GI is due to the supersonic difference of speed between the spiral pattern and the disc, the heating rate can also be written in terms of the energy of the density wave (Eq. 3.28), and from the thermal equilibrium condition it can be derived (Cossins et al. 2009b) that

$$\left\langle \frac{\delta\Sigma}{\Sigma} \right\rangle = \chi\beta^{-1/2} \,, \tag{3.36}$$

where χ is a proportionality factor, that is of the order of unity. This condition gives us a relation between the amplitude of density perturbations and the cooling parameter, meaning that instability saturates at an amplitude $\propto 1/\sqrt{\beta}$. It also points out that the strength of the instability, and its efficiency as an angular

momentum transport process, are correlated with the thermodynamics in steady state, in particular they increase with decreasing cooling time. This relation can be theoretically justified by remarking that the energy density of sound waves is proportional to $(\delta\Sigma/\Sigma)^2$. In order to maintain the dynamic thermal equilibrium in marginally stable discs, the rate at which energy is lost due to cooling $\propto \beta^{-1}$ must be balanced by the energy dissipated by the waves, that, for low massive gravitationally unstable discs, is dissipated through shocks at the locations where they are generated.

Finally, we highlight that this discussion is valid as long as the only assumed source of heating in the disc is the one provided by the gravitational instabilities through shocks and compressions. Actually, the environment in which protostellar discs are should also be considerated. Indeed, due to the chaotic first stages of their formation and evolution, they are expected to be irradiated by the central protostar, their parental cloud, or nearby stars. Irradiation has a twofold outcome, and in general in these case the disc does not self-regulate as described in the previous Sections (Kratter & Murray-Clay 2011; Rice et al. 2011; Hall et al. 2016). On one side, due to the external heating, the temperature increases, providing extra pressure support against gravitational collapse. For this reason, in particular in the flared outer disc regions which are more affected, irradiation from the star weakens the strength of disc self-gravity, stabilising the initially marginally unstable disc. On the other side, since the cooling time of irradiated discs is lower than the one required for thermal equilibrium in a viscously heated disc (e.g. Rafikov 2005; Kratter & Murray-Clay 2011; Rafikov 2015), a very strongly irradiated disc will behave like an isothermal disc. Indeed, discs in such conditions are heated to higher temperatures by irradiation than by dissipation of accretion energy induced by gravitational stresses. Therefore, without reaching thermal balance, the over-densities induced by gravitational perturbation never become pressure supported, and this causes their free-fall collapse, since any extra heat generated by compression of the collapsing over-density is quickly radiated away. In this case, irradiation has the effect of destabilizing the disc against fragmentation, because smaller amplitude perturbations could lead to collapse (Rice et al. 2011). This aspect concerning the impact of external irradiation on the stability of self-gravitating discs is still under debate.

Chapter

4

Planet-disc interaction

Interaction between a geranium and a Macroglossum stellatarum from my balcony (lockdown of 2020).

In Chapter 2 we described protoplanetary disc dynamics, and in particular, through the assumption that their mass is at 99% made of gas, we started by studying the gas dynamic processes, neglecting the dust one. Then, we removed this approximation, studying the dust disc component, its interaction with gas, and how the physical mechanisms that arise from this interaction could influence the planet formation process. Moreover, after the planetesimal formation phase,

terrestrial and giant planets will form (see Sec. 1.4.1). One can wonder if their progenitors (i.e. the protoplanets) would modify the disc evolution. Recent high-resolution ALMA and SPHERE observations have provided evidence that a large variety of structures do exist in protoplanetary disc, particularly we can see gaps and rings-like structures, spirals features, and cavities (see Fig. 4.1 for some non exhaustive examples). The most discussed hypothesis in order to explain the origin of all these substructures, is the tidal interaction between the disc and an embedded companion, such as a planetesimal or a companion star. In an imaginative way, we can think at gaps as the marble track of planets, and at spirals as the wave the planet is surfing.

In this Chapter we focus on this hypothesis. The description of the main mechanisms involved in the coupled disc-planet evolution is based on the works of Goldreich & Tremaine (1979) and Lin & Papaloizou (1979a), and one outcome of this interaction is an inward (or outward) migration process of the planet (for a detailed review on planet-disc interaction and migration mechanism we refer to Kley & Nelson 2012). These processes are fundamental to explain, for example, how giant planets observed in exoplanet systems, could have reached the inner regions of their system. In general, this topic, together with the study of the gas and dust dynamics, can lead to a more deep understanding of the complex planet formation process.

4.1 Planetary torques

The system we study is composed of a gaseous disc, and a satellite (a planetesimal) orbiting the central star[1]. We want to understand how the dynamics of the system changes, and what is the role of the material, gas or dust, presents in the disc. Qualitatively, one can think to a planet embedded in a protoplanetary disc, which perturbs the motion of the surrounding fluid elements by deflecting their orbit due to its gravity. Therefore, the perturbation induced by the planet gives rise to oscillations of fluid particles around their circular unperturbed orbit, exciting waves that propagate across the disc far from the planet. It is important to highlight that it is the reciprocal interaction between the perturber and the wake that, exchanging/gaining angular momentum, pushes the outer disc outward and the inner disc inward, leading to the formation of an axisymmetric underdense region around the planet location, usually called as gap. It has been showed that the morphology of the gap and the ability of the planet to carve it depend on the disc local properties and on the mass of the planet (see Chapter 5 and Chapter 7 for a direct application of this dependence). Instead, propagating density waves are sheared out by the Keplerian differential rotation, and they create a wave pattern in the form of spirals. We will see that, for low mass planets, the waves can constructively interfer and form a one-armed spiral structure (Ogilvie & Lubow 2002;

[1]This problem can be described like a restricted three-body problem: we will study the angular momentum exchange between a gas particle and the satellite, both orbiting around the star.

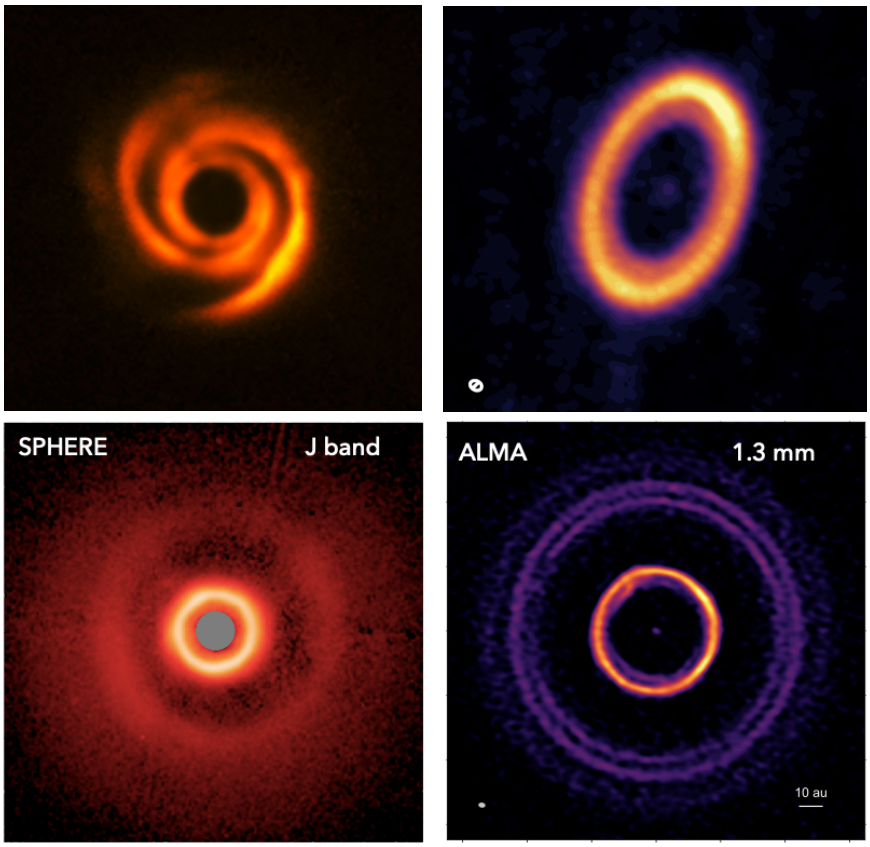

Figure 4.1: Gallery of disc substructures, probably originated via disc-planet interaction. Top left: spiral structures are observed in scattered light of HD 135344B Stolker et al. (2016). Top right: cavity observed with ALMA in the dust continuum of PDS 70 (Keppler et al. 2019). Bottom left and right: scattered light and ALMA image of HD169142 (Pohl et al. 2017; Pérez et al. 2019). All the images are on different scale.

Rafikov 2002). Instead, for higher mass planets, in a non-linear approximation, the waves could form a two-armed (or more) spiral structure (Dong et al. 2015b). Lin & Papaloizou (1979a) and Goldreich & Tremaine (1979) were the first who explained how the mutual angular momentum exchange between the gaseous disc and the binary system (star-planet) could modify both the disc structure and the planet orbit (migration), giving rise to spiral waves.

One direct evidence of these density waves, originated by the interaction between a disc and a satellite, comes from the Nasa's Cassini spacecraft, that recently observed the Saturn's moon Daphnis in its gap (see left panel in Fig. 4.2). In the right panel of Fig. 4.2 it has been observed another Saturn gap, where vertical structures are visible at the ring edge, casting long shadows on it. These structures are thought to be originated by the interaction of a moonlet with the surrounding material of the rings.

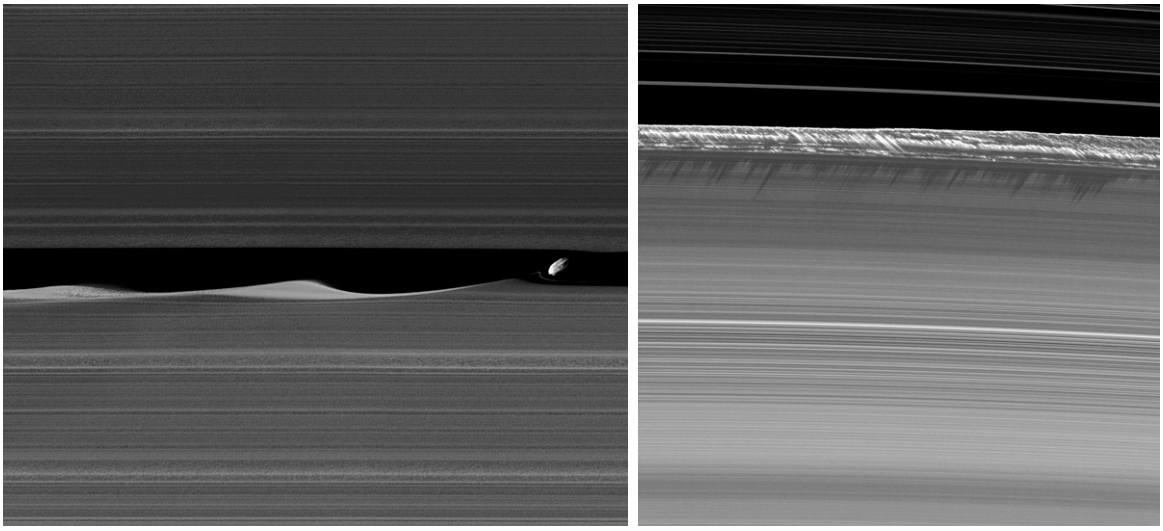

Figure 4.2: Left: the gap carved by the moon Daphnis in Saturn rings, where we can see the density waves formed by the gravitational pull of the satellite. Right: Saturn gap where also some vertical perturbations are visible. Both images have been captured by the NASA Cassini spacecraft (`https://saturn.jpl.nasa.gov/`).

4.1.1 Impulse approximation

Lin & Papaloizou (1979a) studied the case of close encounters between gas and a small satellite, described by a small mass ratio $q_\mathrm{p} = M_\mathrm{p}/M_\star$, where M_p is the satellite mass (the planet), and $M_\star$ is the primary mass (the star)[2], by making two different approximations:

- The **impulsive approximation**, which states that, if the encounter between the gas particle and the satellite is very close, one can assume that the trajectory remains unperturbed until the particle reaches its minimum distance from the satellite (called impact parameter). This means that the exchange of angular momentum, occurs over a duration much shorter than the orbital period of the planet. Then, the gravitational interaction between the two, can be approximated as impulsive;

- The **test particle approximation**, which consists in taking the gas particle like a test particle, meaning that we will neglect hydrodynamics effects, except for some dissipative effects (i.e. viscosity). This one, after each encounters (and deflection) with the secondary, will bring again the particle on an unperturbed orbit, before the following encounter.

We note that the results obtained through the "impulsive" approximation are in good agreement with more rigorous derivation (Goldreich & Tremaine 1979), and allow us to simplify a complex problem. A schematic description of the problem

[2] We note that with this assumption, we are allowed to neglect the motion of the primary, due to the secondary.

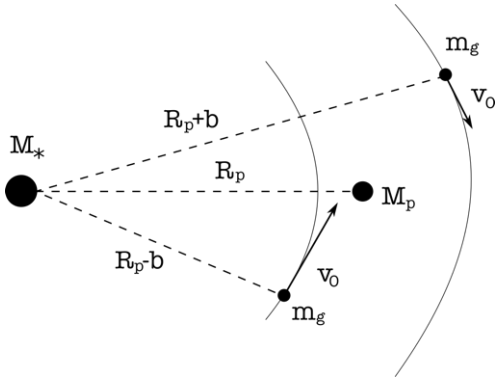

Figure 4.3: The image shows a sketch of the studied binary system in a gaseous disc. It is composed by a central star, with mass $M_\star$, and a planet with $M_\mathrm{p} < M_\star$ ($q < 1$). The planet orbits around the star on an orbital radius R_p. There are also two gas particle, on an inner $R_\mathrm{p}-b$ and outer $R_\mathrm{p}+b$ radius. The inner gas particle, with $R < R_\mathrm{p}$ moves faster than the planet, and so it seams to overcome it, while the outer one, with $R > R_\mathrm{p}$ moves slower than the planet, and so it is left behind.

is given in Fig. 4.3 and 4.4. We start our derivation considering a gas particle of mass m_g, on a circular orbit around the star (with mass $M_\star$), with orbital radius $R_\mathrm{g} = R_\mathrm{p} \pm b$, where $b \ll R_\mathrm{p}$ is the so called impact parameter, and R_p is the orbital radius of the satellite. The particle must approach the planet, with an orbital radius sufficiently different from R_p to allow it to freely pass by the planet, with only a small deflection. We set our frame of reference comoving with the planet. It means that the planet is assumed to be at rest, and the relative gas velocity with respect to the satellite turns out to be $v_0 = v_\mathrm{g} - v_\mathrm{p}$, where v_p is the planet velocity measured on the inertial frame centered on the central star. This is known as heliocentric frame. Then, the interaction between the gas particle

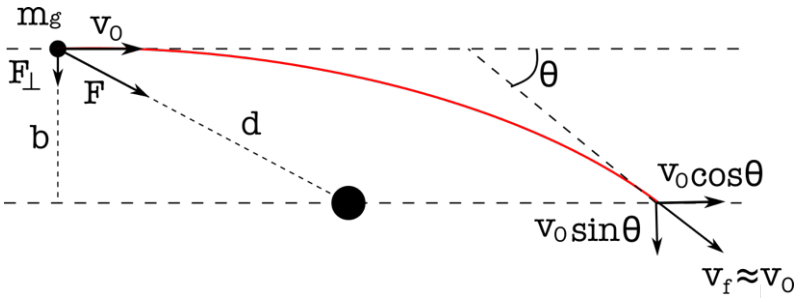

Figure 4.4: Schematic representation of the gravitational interaction between a gas particle and a planet, as seen by the reference frame of the planet. The gas particle has an initial velocity v_0, and it has an initial orbital radius $R = R_\mathrm{p} \pm b$, where $b \ll R_\mathrm{p}$ is the impact parameter.

and the planet can be described by the initial velocity of the particle v_0 in the corotating frame, the impact parameter $b = R - R_\mathrm{p}$, and the deflection angle θ

$$\cot\left(\frac{\theta}{2}\right) = \frac{v_0^2}{\mathcal{G}M_\mathrm{p}}\,. \tag{4.1}$$

This angle tells us how much the orbit of the particle changes, due to the gravitational interaction, and it is assumed to be small (this relation is nothing else than

the Rutherford scattering formula). A consequence of the deflection is that the particle gains a velocity $v_\perp$ in the radial direction (i.e. the direction perpendicular to its unperturbed motion) given by

$$|v_\perp| = \int_\infty^\infty \frac{F_\perp}{m_\mathrm{g}} \mathrm{d}t = \frac{2\mathcal{G}M_\mathrm{p}}{bv_0}\,, \tag{4.2}$$

where $F_\perp$ is the radial component of the gravitational force. At the same time, the gas particle velocity in the tangential direction (i.e. parallel to the unperturbed motion) decreases from v_0 to $v_\parallel = v_0 \cos\theta$, due to the increase of the radial component from a zero value to $|v_\perp| = v_0 \sin\theta$, which is expressed in Eq. 4.2. This means that, during the interaction, the value of the particle velocity does not change, but only its direction. This turns out from the conservation of kinetic energy of the particle before and after the interaction with the planet. Then, the deflection angle could be rewritten as,

$$\theta \approx \frac{|v_\perp|}{v_0} \sim \frac{2\mathcal{G}M_\mathrm{p}}{bv_0^2}\,. \tag{4.3}$$

Because of the variation of the two velocity component, a change of the particle angular momentum per unit mass occurs

$$\Delta j_\mathrm{g} = Rv_\parallel - Rv_0 = Rv_0(\cos\theta - 1) < Rv_0\,, \tag{4.4}$$

where we assumed that the orbital radius of the particle has not changed significantly, and where $R = R_\mathrm{p} + b \approx R_\mathrm{p}$ (for $b \ll R_\mathrm{p}$). Due to the approximations we did at the beginning of this section, after the deflection the particle is assumed to recover its circular orbit corresponding to the new value of its angular momentum via some dissipative effects, which allow to remove the eccentricity gained by the particle during the encounter. This happens before the following encounter. Since the deflection angle is assumed to be small, $\cos\theta - 1 \approx -\theta^2/2$, the angular momentum variation is

$$\Delta j_\mathrm{g} \approx -Rv_0\frac{\theta^2}{2} = -\frac{2\mathcal{G}^2M_\mathrm{p}^2R}{b^2v_0^3}\,, \tag{4.5}$$

depending from an odd power of the initial particle velocity v_0. The only force in the system is the gravitational one, therefore the total angular momentum of the system must be conserved, and the planet's angular momentum change is thus given by $\Delta j_\mathrm{p} = -\Delta j_\mathrm{g}$, where $R = R_\mathrm{p} + b \approx R_\mathrm{p}$. Looking at Fig. 4.3 and at the definition of v_0 in the corotating frame, it is interesting to distinguish between two cases: for $R \lesssim R_\mathrm{p}$, i.e. for particle on an inner orbit, $v_0 > 0$, while for $R \gtrsim R_\mathrm{p}$, i.e. for particle on an outer orbit, $v_0 < 0$. This could be easily understood if we think that, in the frame reference of the satellite, the particles orbiting on an inner orbit, have a velocity greater than the satellite one, while the outer particles have lower velocity, and this results in an opposite rotation way. Therefore, if the planet interact with gas located on different orbits, we identify two behavior:

- gas on $R > R_\mathrm{p}$: the planet loses angular momentum to the gas, $\Delta j_\mathrm{p} < 0$, and it migrates towards inner orbits, while the gas, that has gained angular momentum $\Delta j_\mathrm{g} > 0$, moves to outer regions;

- gas on $R < R_\mathrm{p}$: the planet gains angular momentum from the gas, $\Delta j_\mathrm{p} > 0$, and it migrates towards outer orbits, while the gas, that has lose angular momentum $\Delta j_\mathrm{g} < 0$, moves to inner regions.

Usually the binary system is completely embedded in a gaseous disc, thus the migration will be inwards or outwards depending on which of the two behaviour dominates. At this point, we want to calculate the total torque acting on the planet. We have defined Δj_p to be the planet specific angular momentum variation, during one interaction. The specific total torque from the disc on the planet is obtained dividing the specific angular momentum change by the time interval between two encounters, $\Delta t = 2\pi/v_0$,

$$\Lambda^T = \frac{\Delta j_\mathrm{p}}{\Delta t} = \frac{\mathcal{G}^2 M_\mathrm{p}^2}{\pi b^2 v_0^2}\,\mathrm{sgn}(v)\,. \tag{4.6}$$

Considering both the planet and particle motion to be Keplerian, the initial velocity v_0 can be rewritten in terms of the angular velocity

$$v_0 = R\Omega_\mathrm{g} - R_\mathrm{p}\Omega_\mathrm{p} = (R_\mathrm{p}+b)\Omega(R_\mathrm{p}+b) - R_\mathrm{p}\Omega(R_\mathrm{p})\,, \tag{4.7}$$

where Ω_p and Ω_g are the angular velocity of the planet and the particle, respectively. We remember that we have assumed $R/R_\mathrm{p} = (R_\mathrm{p}+b)/R_\mathrm{p} \approx 1$, so, in this limit, Eq. 4.7 can be expanded about $b = 0$, obtaining $v_0 \approx -3/2\Omega_\mathrm{p} b$, where, depending on the sign of b, we find the two behavior previously described. The physical meaning of this Taylor expansion, is that non negligible torques are found only near $R \simeq R_\mathrm{p}$. Then, inserting the new expression for the initial particle velocity, Eq. 4.6 becomes

$$\Lambda^T = \mathrm{sgn}(R_\mathrm{p}-R) f q_\mathrm{p}^2 \Omega_\mathrm{p}^2 R_\mathrm{p}^2 \left(\frac{R_\mathrm{p}}{b}\right)^4\,, \tag{4.8}$$

where q_p is the planet-to-star mass ratio and f is a numerical factor. We have derived this expression for $R \simeq R_\mathrm{p}$, but Lin & Papaloizou (1979b) showed that the error made using this approximation can be neglected, so it is valid also for $R \neq R_\mathrm{p}$. We can now integrate on the disc mass, in order to obtain the total torque exerted on the planet by the whole disc. The mass of an annulus of material close to the planet position between b and $b + \mathrm{d}b$, exterior to the planet, is given by $\mathrm{d}M = \Sigma(R) 2\pi R_\mathrm{p} \mathrm{d}b$, where $\Sigma(R) = \Sigma_\mathrm{g}$ is the surface gas density, which we assume to be constant. Then,

$$\Gamma^T = \frac{\mathrm{d}J_\mathrm{p}}{\mathrm{d}t} = \int_{b_\mathrm{min}}^{\infty} \Lambda(R_\mathrm{p}) \Sigma_\mathrm{g} 2\pi R_\mathrm{p} \mathrm{d}b\,, \tag{4.9}$$

where b_min is the minimum impact parameter below which the encounter would be not fast and weak enough to justify the impulse approximation. After a little algebra, we obtain that the total torque of the disc acting on the satellite, is given by

$$\Gamma^T = \frac{8}{27} q_\mathrm{p}^2 \Sigma_g \Omega_\mathrm{p}^2 R_\mathrm{p}^4 \left(\frac{R_\mathrm{p}}{b_\mathrm{min}}\right)^3\,. \tag{4.10}$$

Looking at Eq. 4.8 we note that we find again two different behaviours, depending on $\mathrm{sgn}(R_\mathrm{p} - R)$:

- $\Lambda < 0$ for $R > R_\mathrm{p}$: the planet loses angular momentum to the gas in the outer regions, and it tends to migrate inwards;
- $\Lambda > 0$ for $R < R_\mathrm{p}$: the planet gains angular momentum from the gas inside its orbit, and thus it is pulled to migrate outwards.

Finally, since the total angular momentum must be conserved, we find that the total torque (per unit of mass) of the satellite exerted on the disc (Λ_d^T), can be written as,

$$\Lambda_\mathrm{d}^T = -\Lambda^T = \mathrm{sgn}(R - R_\mathrm{p}) f q_\mathrm{p}^2 \Omega_\mathrm{p}^2 R_\mathrm{p}^2 \left(\frac{R_\mathrm{p}}{R - R_\mathrm{p}}\right)^4 , \tag{4.11}$$

which diverges for $R \to R_\mathrm{p}$. But this point could be easily resolved, noting that the tidal interaction does not allow the disc to occupy a region near the planet location. We have the formation of a "gap" in the gas surface density. This is due to the net effect of the angular momentum transfer between particles and the planet: the planet is subject to a migration, and the gas is repelled from the orbit of the planet, carving a hole with an approximated size given by,

$$|R - R_\mathrm{p}| \leq \max\{R_\mathrm{H}, H\} , \tag{4.12}$$

where R_H is the Hill radius, defined as the influence zone of the planet, where the dominant effect respect to the gravitational field of the star comes from the planet gravitational field. This radius could be derived resolving the restricted three-body problem, in particular searching for the equilibrium points of the system[3], obtaining that

$$R_\mathrm{H} = \left(\frac{q_\mathrm{p}}{3}\right)^{1/3} R_\mathrm{p} , \tag{4.13}$$

where q_p is the planet-to-star mass ratio. So, Eq. 4.12 tells us that if the impact parameter is smaller than this minimum value, the gas particle would be accreted onto the planet, without bringing contributions to the interaction. This result can be applied to a fluid disc, collisionless gas or a collection of dust particles.

We note that depending on the disc composition, some other effects can become important. Indeed, for a gas disc it is necessary to take into account also the possibility that the gas particle (if the relative velocity between particle and planet is less than the sound speed) is aware of the presence of the planet due to pressure effects. The outcome is that the impact parameter changes, and it can be derived that $b_\mathrm{min} = 2/3H$. By combining this value with the previous requirement of $b_\mathrm{min} > R_\mathrm{H}$, we get that in the computation of the total torque of the disc (satellite) acting on the satellite (disc), Λ^T or Λ_d^T, the minimum impact parameter is

$$\Delta_\mathrm{g} = \max\left(|R - R_\mathrm{p}|, \frac{2}{3}H, R_\mathrm{H}\right) . \tag{4.14}$$

Instead, in a pressureless fluid such as dust particles, the minimum impact parameter is simply given by $\Delta_\mathrm{d} = \max(|R - R_\mathrm{p}|, R_\mathrm{H})$.

[3] In this case our restricted three-body problem consists in the study of the equilibrium of a gas test particle, in the field of a binary system, star plus planet.

4.1.2 Resonances: the Lindblad and corotation torque

Goldreich & Tremaine (1979, 1980), through a more rigorous derivation, obtained the same expression of Eq. 4.10 for the total tidal torques. Let us summarize their results. In general, a planet embedded in a disc breaks the axial symmetry, adding a gravitational contribution to the potential of the system. This would give rise to tidal torques between the planet and the disc, that modify the Keplerian orbits of the gas, leading to a change also in the accretion mechanism. The final result is that the disc-planet exchange of angular momentum occurs only at some resonance locations[4], and the disc replies to the planet perturbation by means of the excitation of density waves. These waves propagate in the disc, carrying out energy and angular momentum, and finally they are dissipated through shocks. Considering a Keplerian disc, it can be shown that if the flow is weakly perturbed, a fluid particle oscillates around its orbit at equilibrium at a frequency given by the epicyclic frequency $\kappa = \Omega_{\rm k}$, defined in Eq. 3.18. Then, a resonance occurs, inducing a strong disc response to the perturbations. These resonances, induced by a perturbing gravitational potential in the disc, are known as Lindblad resonances (Lindblad 1927). Goldreich & Tremaine (1979, 1980) treated the problem in a linear approximation, assuming the planet to be a low-mass perturber, and evaluating the linear response of the flow to the small tidal perturbations induced by the planet in the gravitational potential of the primary object. It can be shown that the linear perturbation analysis on the response of the fluid to the perturber is valid for planets with masses satisfying (Rafikov 2002),

$$M_{\rm p} \ll M_{\rm th} = \left(\frac{H}{R}\right)^3_{\rm p} M_\star\,, \tag{4.15}$$

where the thermal mass $M_{\rm th}$ is the mass for which the Hill radius (see Eq. 4.13) is equal to the thickness of the disc H, in this case, evaluated at the planet location. The planet potential in polar coordinates centered on the star is written as $\Phi_{\rm p}(R,\phi) = -\mathcal{G}M_{\rm p}/d$, where $d = \sqrt{R^2 + R_{\rm p}^2 - 2RR_{\rm p}\cos(\phi-\phi_{\rm p})}$ the distance of the star from the planet. It follows that the potential is a $2\pi-$periodic function of the relative azimuthal position $\phi - \phi_{\rm p}$, where $\phi_{\rm p} = \Omega_{\rm p} t$ is the azimuth of the planet. Therefore, Goldreich & Tremaine (1979, 1980) treated the planet perturbation potential by means of a decomposition in Fourier modes, which if the planet has a circular orbits is given by

$$\Phi(R,\phi,t) = \sum_m \phi_m \exp[{\rm i}m(\phi(t) - \Omega_{\rm p} t)]\,, \tag{4.16}$$

where m is the azimuthal harmonic number, $\Omega_{\rm p}$ is the Keplerian planet angular velocity and $\phi_m(R)$ is a coefficient of the linear combination. If the planet has an eccentric orbit, then the decomposition modes will be of the form of

$$\Phi(R,\phi,t) = \sum_m \sum_l \phi_{m,l} \exp[{\rm i}(m\phi - l\Omega_{\rm p} t)]\,, \tag{4.17}$$

[4] We remember that a resonance is a region of the disc where a characteristic frequency of the planet motion is equal to a frequency inside the disc.

where l is a new harmonic number (time harmonic number), taking into account the system eccentricity. The pattern speed of each bar-mode $\phi_{m,l}$ is given by

$$\Omega_{l,m} = \frac{l}{m}\Omega_{\rm p}\,, \tag{4.18}$$

where the Keplerian motion assumption implies that the the planet orbital velocity is equal to the epicyclic frequency, $\Omega_{\rm p} = \kappa$. In general a resonance occurs whenever a characteristic frequency of the planet matches a frequency within the disc. Then, for each bar-mode a tidal torque arises due to the effects of the potential perturbation component of order (m, l), near the Lindblad and corotation resonances, associated to the pattern frequency:

$$\begin{aligned} \Omega(R) - \Omega_{l,m} &= \pm\frac{\kappa(R)}{m} \qquad \text{Lindblad resonance,} \\ \Omega(R) - \Omega_{l,m} &= 0 \qquad\qquad \text{Corotation resonance,} \end{aligned} \tag{4.19}$$

where $\Omega(R)$ is the orbital frequency of the gas and $\kappa(R)$ the epyciclic frequency. The first equation of Eq. 4.19 means that in order to have a "Lindblad" resonance, the angular velocity of the gas and that of the planet $\Omega_{l,m} \propto \Omega_{\rm p}$ must differ for a submultiple of the epyciclic frequency. Instead, the second equation means that when the orbital speed of the gas matches the planet one, a "corotation" resonance arises. We note that the mode $m = 0$, which is axisymmetric, is an exception and does not exert any torque on the disc. So, for $m \geq 1$, and under the assumption of Keplerian motion, Eq. 4.19 becomes

$$\begin{aligned} \Omega_k(R)\left(1 \mp \frac{1}{m}\right) &= \Omega_{l,m}\,, \\ \Omega_k(R) &= \Omega_{l,m}\,, \end{aligned} \tag{4.20}$$

and we can find the disc radial location where the resonances occur, as

$$\begin{aligned} R_L &= \left(\frac{m+\epsilon}{l}\right)^{2/3} R_{\rm p}\,, \\ R_C &= \left(\frac{m}{l}\right)^{2/3} R_{\rm p}\,, \end{aligned} \tag{4.21}$$

remembering that we have assumed Keplerian angular velocities, and where $\epsilon = \pm 1$, depending if the resonant location is inside ($\epsilon = -1$) or outside ($\epsilon = +1$) the planet orbit. Each pattern frequency (Eq. 4.18), with respect to the corotation radius, has a set of inner (inner Lindblad resonances ILRs), outer (OLRs) and corotation (CR) resonances. In particular, for $m = 2$ (and assuming $m = l$) we can identify the first ILR at $R_{\rm ILR} = 2^{-2/3} R_{\rm p} \simeq 0.63\, R_{\rm p}$ (1:2 resonance, i.e. the radius at which orbital frequency of the gas in the disc is doubled with respect to that of the binary) and for $m = 1$ the first OLR at $R_{\rm OLR} = 2^{2/3} R_{\rm p} \simeq 1.59\, R_{\rm p}$ (2:1 resonance), while for $m \to \infty$ the planet radius becomes a resonances accumulation point.

These two furthermost locations define the zone where the angular momentum exchange occurs; outer this zone, neither the disc, neither the planet, can exert

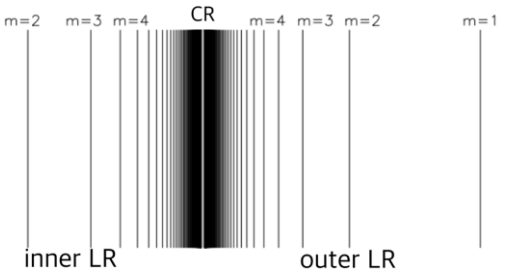

Figure 4.5: Schematic representation of the inner and outer Lindblad planet resonances (see Eq. 4.19), respect to the planet orbit, which coincides with the corotation resonance (CR). Radial distance R increases to the right, and the primary is far to the left. Only the $m \leq 4$ Lindblad resonances are labelled. Not shown is the m = 1 inner Lindblad resonance that lies at $R = 0$. We note that for $m \to \infty$, $R_{\rm p}$ tends to be a resonances accumulation point.

a tidal torque on each other. Moreover, one can find that, for the circular case (if $m = l$) the planet carries out the torque on the disc only near the Lindblad resonances, while in the eccentric case the torque will be performed out at the corotation radius, too. In particular, the angular momentum and energy exchange at the Lindblad resonance would produce an increase in the eccentricity of the planet orbit, while at the corotation radius it would produce a decrease of the orbit eccentricity. For Keplerian discs (with no non-linear effects), one can find that the corotation resonances dominate, and so the eccentricity is damped. Through this derivation, Goldreich & Tremaine (1979) found in their Eq. (13) and (14) the torque exerted by the (l, m) mode of the j-th potential, at Lindblad ($T^{\rm L}_{l,m}$) and corotation ($T^{\rm C}_{l,m}$) radius. What happens physically at each resonance location $R_{\rm L,C}$, is that m-fold density waves are launched, producing an angular momentum flux towards outer/inner radii as they propagate away from the planet. As a result, a gap is formed under the action of the tidal torques (see Section 4.3). Finally, assuming that the resonant locations are known, one can evaluate the total torques exerted on the disc, summing up over all the resonances contributions. The intensity of the torque at a given resonance is determined by the intrinsic strength of the resonance (determined by the linear perturbation theory, and then independent of physical disc conditions), and by the amount of gas at the resonance (so it will depend on ν, H). As we can see from Fig. 4.5, due to the high density of resonces, we could have a divergence of the torque at the corotation radius, for $m \to \infty$. Artymowicz (1993) showed that we can prevent this, taking into account also pressure effects that act on the Lindblad resonances, shifting them at a new location,

$$R_{\rm p} - \frac{2}{3}H \leq R_{\rm L} \leq R_{\rm p} + \frac{2}{3}H\,, \tag{4.22}$$

where H is the disc thickness.This phenomenon is known as "torque cut-off". Due to the high density of resonances near the accumulation point, Goldreich & Tremaine (1980) introduced the average torque per radial interval, or torque density, $\mathrm{d}T^{\rm L,C}_{l,m}/\mathrm{d}R$. We consider here, for simplicity, only the torques exerted by

the planet at the Lindblad resonances with $l = m$, which lead to

$$\frac{\mathrm{d}T^{\mathrm{L}}_{m,m}}{\mathrm{d}R} = f\,\mathrm{sgn}(R - R_{\mathrm{p}})\frac{\mathcal{G}^2 M_{\mathrm{p}}^2 R\Sigma}{\Omega^2(R_{\mathrm{p}} - R)^4}(2K_0(2/3) + K_1(2/3))^2 \tag{4.23}$$

$$\propto \Sigma q_{\mathrm{p}}^2 \Omega^2 R^3 \left(\frac{R}{R_{\mathrm{p}} - R}\right)^4 . \tag{4.24}$$

where f is a numerical factor, $q_{\mathrm{p}} = M_{\mathrm{p}}/M_\star$, and $K_{0,1}$ are modified Bessel functions of order 0 and 1. We note that this result, except for a numerical constant, is the same of the one we found with the impulsive approximation (see Eq. 4.8, where $\mathrm{d}T/\mathrm{d}R = \Lambda^T(2\pi)$). A further point of interest comes from considering a gaseous disc where were excited density waves with different m. Indeed, it can be shown (Ogilvie & Lubow 2002) that they can constructively interfere, leading to the formation of a one-armed spiral structure, with a pitch angle given by

$$i = \tan^{-1}\left(\frac{m}{kR}\right) , \tag{4.25}$$

where k is the radial wavenumber. The shape of this wake in polar coordinates far from the planet position (R_p, θ_p) is given by (Rafikov 2002),

$$\theta(R) = \theta_{\mathrm{p}} - \frac{\mathrm{sgn}(R - R_{\mathrm{p}})}{h_{\mathrm{p}}} \times \left[\left(\frac{R}{R_{\mathrm{p}}}\right)^{1+\beta}\left\{\frac{1}{1+\beta} - \frac{1}{1-\alpha+\beta}\left(\frac{R}{R_{\mathrm{p}}}\right)^{-\alpha}\right\} - \left(\frac{1}{1+\beta} - \frac{1}{1-\alpha+\beta}\right)\right] , \tag{4.26}$$

where h_{p} is the disc aspect ratio at $R = R_{\mathrm{p}}$, $\Omega(R) \propto R^{-\alpha}$ is the disc angular velocity, and $c_{\mathrm{s}}(R) \propto R^{-\beta}$ is the sound speed in a general case. This formula is used to fit the shape of the observed spiral structures in order to infer the local disc conditions. As an example, by measuring the pitch angle of the spiral structure, one can gain insights on the local disc temperature (Eq. 4.25) and, consequently, on the local disc aspect ratio (Muto et al. 2012a; Benisty et al. 2015). We stress that this result is valid only in the linear perturbation theory, for $M_{\mathrm{p}} \ll M_{\mathrm{th}}$. When the planet mass is higher than the thermal mass, we would have strongly nonlinear density waves generated by the planet. In this limit, the spiral wave is characterized by a larger pitch angle, and a secondary inner spiral arm appears with some azimuthal shift from the primary arm, which also appears to be dependent on the planet mass (Zhu et al. 2015; Fung & Dong 2015). However, more recent studies have shown that also in the approximation of low mass planet, and thus in the framework of linear theory, a secondary and a tertiary spiral arms can form (Bae & Zhu 2018a; Miranda & Rafikov 2019a). These additional arms are the result of the splitting of the primary arm, and arise in the regione inside the planet orbit. It is interesting to note that the secondary arm is initially weak, but it becomes stronger and narrower towards the center of the disc, eventually exceeding the strength of primary arm (Miranda & Rafikov 2019a). Probably this result was not achieved in previous works due to approximations and calculation limitations. Bae & Zhu (2018a) attribute the presence of more than one arm to the constructive interference of different sets of wave modes, where the exact

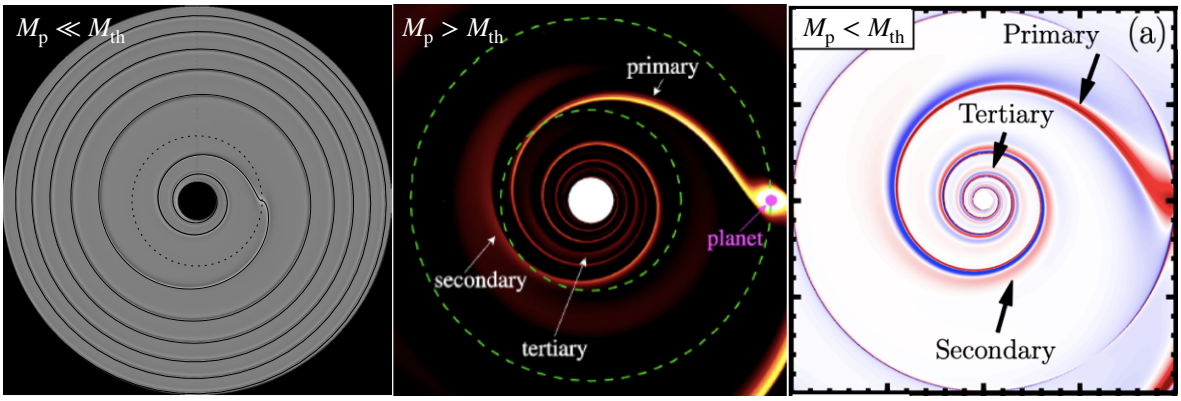

Figure 4.6: Left panel: the one-armed spiral resulting by the disc-planet interaction in the approximation of low mass planet (linear theory) obtained by Ogilvie & Lubow (2002). Central panel: result obtained by Fung & Dong (2015), showing that a planet with $M_p > M_{th}$ can excite more than one spiral arms. Right panel: result obtained by Miranda & Rafikov (2019a), showing that for $M_p < M_{th}$, in the framework of linear theory, one planet can give rise to multiple spiral arms in the region inside the planet orbit.

number and launching position of the spiral arms depend on the planet mass as well as the disc temperature profile. Fig. 4.6 resumes the above described results. In particular, the left panel shows the first result obtained by Ogilvie & Lubow (2002), with the one-armed spiral resulting by the disc-planet interaction in the approximation of low mass planet (linear theory), while the central and right panels show results obtained by Fung & Dong (2015) for $M_p > M_{th}$, and by Miranda & Rafikov (2019a), for $M_p < M_{th}$, respectively.

4.2 Planet migration

In the previous section we saw that a planet embedded in a gaseous disc, by means of tidal torques exchange angular momentum with its "host" at some specific locations (resonances). As a reaction, also the disc interacts in the same way with the planet, modifying its orbit, and so, through the resonances contributions we can compute the total torque acting on the disc/satellite, as $\Lambda_{disc} = -\Lambda_p$. This reciprocal exchange can lead to planetary migration. Depending on the planet mass and the local gas properties, we can identify different migration types, which describe how the disc evolves as angular momentum is gained or lost to the planet:

- **type I** migration affects low-mass planets whose interaction with the disc is weak enough as to leave the disc structure almost unperturbed. This condition is verified when the local exchange of angular momentum between the planet and the disc is negligible compared to the redistribution of angular momentum due to disc viscosity. As a result, the planet is not able to carve a gap, remaining thus fully embedded in the gaseous disc. This regime is described by Ward (1997) and Tanaka et al. (2002);

- **type II** migration affects high-mass planets whose gravitational torques are not anymore a small perturbation to the viscous stress, but locally dominate angular momentum transport within the disc. As discussed in the previous section, the gas in the orbit of the planet is repelled away from these gravitational torques. In this regime the planet clears an annular gap, corresponding to a drop in the gas surface density. This regime is described by Lin & Papaloizou (1986).

- **type III** migration (or runaway migration) has also being investigated (Masset & Papaloizou 2003; Artymowicz 2004). It occurs in massive discs and is relevant to partial gap-forming planets. The migration can be directed inward or outward, and under appropriate conditions it can happen very fast.

Fig. 4.7 shows the interaction between a planet and a viscous protoplanetary disc in the three different migration regimes, as obtained with two-dymensional hydrodynamic simulations (Armitage & Rice 2005). It is interesting to note that the orbital migration in each of these regimes is induced by the angular momentum exchange with disc material that occurs through disc-planet interaction. Depending on the regime, this occurs through wave excitation, as in type I migration, a combination of wave excitation and shock dissipation, as occurs in type II migration, or direct exchange with disc material traversing the orbit, as has been suggested for type III migration. We will now briefly describe type I and II migration regimes.

Finally, we emphasise how important it is to consider the process of planetary migration in order to explain the current observed population of exoplanets (for a recent work see e.g. Lodato et al. 2019), with a particular focus to the group of hot-Jupiters. These are massive planets observed very close to their host host star. The favoured theory in order to explain them is that they formed in the outer region of the disc, and then migrated inward, but other possible mechanisms have been explored (see Dawson & Johnson 2018 for a detailed review).

4.2.1 Type I migration

When the planet mass is low, the angular momentum exchanged between the planet and the disc is negligible compared to the angular momentum flux due to the disc viscosity, and then the disc structure would be almost unperturbed (the planet remains completely embedded in the gaseous disc). In order to compute the total torque acting on the planet we have to consider all the contributions coming from the corotation, and the inner and outer Lindblad resonances,

$$T = \sum_{m=2}^{\infty} T_{\rm ILR}(m) + \sum_{m=1}^{\infty} T_{\rm OLR}(m) + T_{\rm CR}(m)\,. \tag{4.27}$$

In particular, Tanaka et al. (2002), assuming an isothermal disc in the vertical and radial direction, found that the total torque is given by,

$$T \propto -q_{\rm p}^2 \Sigma \Omega_{\rm k}^2 R_{\rm p}^4 \left(\frac{H}{R}\right)^{-2}\,, \tag{4.28}$$

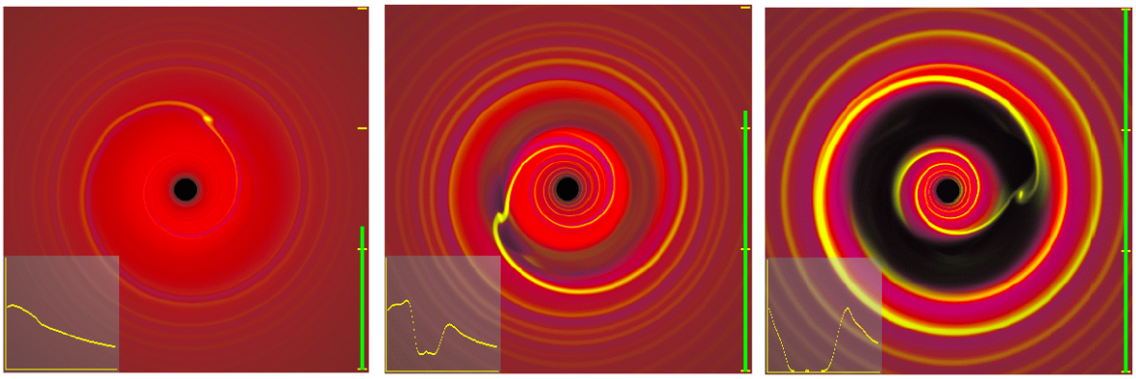

Figure 4.7: Two-dimensional hydrodynamic simulation, showing the interaction between a planet and a viscous protoplanetary disc in different migration regimes. Left panel: Type I regime, relative to low-mass planets, where it is also shown the disc surface density profile, almost unperturbed. Central panel: Type III regime, relative to partially opened gap. Right panel: Type II regime, relevant to giant planets. The disc surface density profile shows a completely depleted gap.

while with the impulsive approximation we derived in Eq. 4.10, we have found that $T \propto (H/R)^{-3}$. This difference is due to an intrinsic asymmetry between the inner and outer Lindblad torques, which is itself an increasing function of the disc thickness (Armitage 2013). We highlight here the two main behavior in the system: at the inner resonance, the planet gains angular momentum from the inner disc, while at the outer one, it loses angular momentum to the outer disc. If the two contributions do not balance, we have migration. Defining

$$f = \frac{T_{\rm ILR} + T_{\rm OLR}}{|T_{\rm ILR}| + |T_{\rm OLR}|}\,, \tag{4.29}$$

we will have inward migration when $f < 0$, and viceversa. We note that if $f = 0$ the planet is only a sort of channel for the angular momentum transport from the inner to the outer regions of the disc. In particular, we will expect the satellite to migrate outwards if the inner surface density is much higher than the outer one, due to the fact that the resonance magnitude depend on the local gas density. Actually, Ward (1997) showed that for all the physical combinations of the disc $\Sigma(R)$, $\Omega(R)$ and $T(R)$ (temperature) profile, the migration occurs always inward. This is also due to the fact that Lindbland resonances exterior to the planet orbit are stronger than the interior ones. Moreover, it should be noted that also the co-orbital torque has a role in type I migration. Indeed, the gas that is almost co-orbital with the planet, travels in horseshoe orbits (in a frame co-rotating with the planet). During the U-shaped turns at both ends of the horseshoe, the density differs between the disc trailing and leading the planet. This density variation is what switch on the torque, that arising close to the planet, can be as large or larger than the torque from the Lindblad resonances. For a schematic description of this process, see Fig. 4.8 from Armitage (2007).

The timescale for this process (which is the time the $T_{\rm tot}$ would take to force the satellite to spiral inward up to accrete on the primary object) is given by the

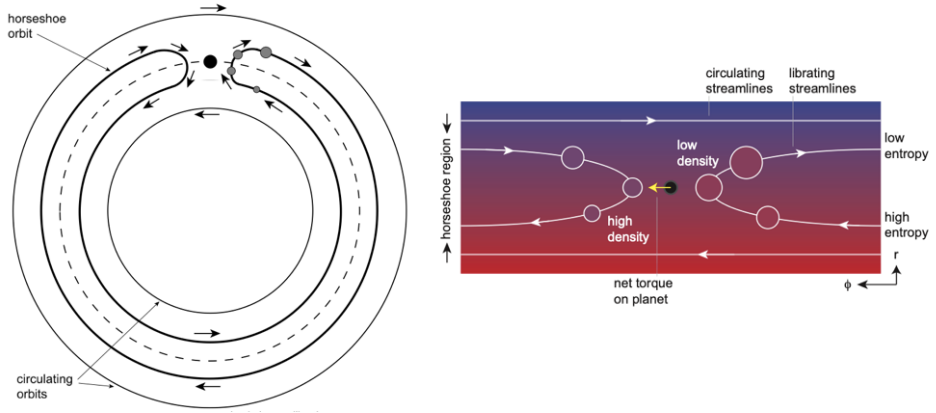

Figure 4.8: Schematic representation (in global and local view) of the gas performing an horseshoe orbit, and exerting a "co-rotation torque" onto the planet embedded in a disc. The torque arises from density variations as the gas executes the horseshoe turns, resulting in an azimuthal asymmetry in the disc near the planet.

ratio between the planet angular momentum, $J_\mathrm{p} = M_\mathrm{p}\Omega_\mathrm{p}R_\mathrm{p}^2$, and the total torque, $\dot{J}_\mathrm{p} = T_\mathrm{tot}$,

$$t_{\mathrm{type\,I}} = \frac{J_\mathrm{p}}{T_\mathrm{tot}} = 2\frac{M_\star}{M_\mathrm{disc}} q_\mathrm{p}^{-1} \left(\frac{H}{R}\right)^2 T_\mathrm{p} \simeq 200\,\mathrm{yr}\,, \tag{4.30}$$

where T_p is the satellite period, and we note that this migration process is very fast. Moreover, the fundamental dependence of the type I migration timescale is $t_{\mathrm{type\,I}} \propto M_\mathrm{p}^{-1}$, so more massive is the satellite, more faster it migrates. For an Earth mass planet at 1 au from a solar mass star (with $H/R \sim 0.05$ and a density as predicted by the MMSN $\Sigma \sim 1700\,\mathrm{gcm}^{-2}$), we obtain a migration timescale less than 1 Myr, which is lower than the typical lifetime of accretion discs surrounding a forming star, which is expected to be $\sim 1-10$ Myr. Not only, indeed the migration timescale is also extremely shorter than the gas accretion time onto the core, which is typically of the order of few Myr. This is the greater issue concerning type I migration. Some recent studies have shown that there could be some mechanisms halting or slowing down the migration. For example, Masset et al. (2006) found that planets can be halted at radially localized disc surface density jumps, such as the outer edge of cavities. Thanks to these "traps", planets rapidly accrete gas material, overcoming the critical mass threshold, and entering the type II migration regime, characterised by a slower migration.

4.2.2 Type II migration

In order to describe in a more quantitative way this process, we can compute the critical mass (and so a gap opening criterion) at which this kind of migration occurs. In order to do that, we have to find out what is the dominant torque in the process, if the tidal or the viscous one.

As the planet mass grows, and because of the dependence of the total torque

on $M_{\rm p}^2$, we expect to find at same point a critical mass, over which the disc perturbations due to the presence of the planet become relevant. Since the disc-planet interaction adds angular momentum to the disc exterior to the planet, and removes it from the interior gas, the overall effect is that a strong torque repels gas from the vicinity of the planet orbit creating a gap (see right panel of Fig. 4.7). For massive planet we can identify the gap edges to be at the Lindbald resonances with lower m, which manage to hold back the viscous disc flux. Due to this gap formation, a lack of gas is verified at the LR location, the exchange of angular momentum between the gas and the planet is weakened, and thus the migration efficiency is reduced. The consequence is that the planet is stuck inside the gap: if it approaches the inner (outer) disc, the gas will induce a positive (negative) torque, repelling the planet outward (inward). The migration of the planet cannot occur anymore only by means of the tidal interaction, and since most of the angular momentum content is in the gas rather than in the planet, it is instead controlled by the viscous evolution of the gas disc. In other words, at the inner edge, the planetary torque removes the necessary amount of angular momentum, such that the disc viscous diffusion does not overtake the wall. At the same time, at the outer edge of the gap, the planetary torque adds the necessary amount of angular momentum, such that the disc material can move at larger radii. Then, the gain of angular momentum of the outer disc should be balanced by a loss of angular momentum from the inner disc. This loss of angular momentum causes the material to accrete onto the star, moving away from the inner edge of the gap. Then, in order to maintain the gap edges near the resonant locations (i.e. where the torque acts), the planet itself has to migrate inward, following the gaseous disc. We can say that the planet role is that of a catalyst, that redistributes angular momentum from inner to outer regions, and in order to be always at the gap centre, it has to follow the local motion of the inner disc. It is like we are assuming the planet to be, to a first approximation, a fluid element of the disc, with a velocity which is equal to that of the gas in a steady state disc,

$$v_{\rm R} = -\frac{3}{\Sigma R^{1/2}}\frac{\partial}{\partial R}\left(R^1/2\nu\Sigma\right) = -\frac{3}{2}\left(\frac{H}{R}\right)^2 \alpha v_{\rm k}\,, \tag{4.31}$$

where we note that the speed of Type II migration depends on a few parameters and, importantly, appears to be independent of the mass of the planet. We refer the reader to the next Section for a more accurate evaluation of type II migration velocity.

4.2.3 Type II timescale

In the previous Section we saw that the type II migration occurs when planets embedded in the disc have a mass greater than a critical mass. This condition allows the planet to clear a gap in the disc. Therefore, we have to note that the previous time evolution equation (Eq. 2.23) for the surface density is not valid anymore in the regions near the planet orbit, because it does not take into account the planet-disc interaction. In order to give a new description for this region, we can make the assumption that the tidal torques could be considered as concentrated in a narrow annular region near the orbit of the planet, so outside

this ring the disc would be unperturbed, and the surface density time evolution would still be given by,

$$\frac{\partial \Sigma}{\partial t} = \frac{3}{R}\frac{\partial}{\partial R}\left[R^{1/2}\frac{\partial}{\partial R}\left(R^{1/2}\nu\Sigma\right)\right] . \tag{4.32}$$

This allows us to treat the planet such as one fluid annulus of the disc, at a radius $R = R_\mathrm{p}$, with mass $M_\mathrm{p} = 2\pi R_\mathrm{p}\Sigma(R_\mathrm{p})\mathrm{d}R$, an infinitesimally size $R_\mathrm{p}+\mathrm{d}R$, and with an angular rotation equal to the fluid one, $\Omega(R_\mathrm{p}) = \Omega_\mathrm{p}$. The migration timescale of the planet can be evaluated starting from the angular momentum conservation of the annulus, where the balance is reached if the sum of the two torques (viscous and tidal) acting on the fluid ring (i.e. the planet) equals the angular momentum change of the planet,

$$G(R_\mathrm{p}) - K(R_\mathrm{p}) = 2\pi v_\mathrm{R}\Sigma R_\mathrm{p}^3\Omega_\mathrm{p} , \tag{4.33}$$

where we are evaluating all the quantities at the planet orbit, to where we have limited the perturbations effect. The viscous $G(R_\mathrm{p})$ and the tidal $K(R_\mathrm{p})$ torques, are defined as,

$$G(R_\mathrm{p}) = 2\pi\nu\Sigma R^3 \left.\frac{\mathrm{d}\Omega}{\mathrm{d}R}\right|_{R=R_\mathrm{p}} \tag{4.34}$$

$$K(R_\mathrm{p}) = \frac{\mathrm{d}}{\mathrm{d}t}\left.\left(M_\mathrm{p}\Omega R^2\right)\right|_{R=R_\mathrm{p}} . \tag{4.35}$$

Through a little algebra, and assuming the planet to have the same fluid velocity of the gas ($v_\mathrm{R} = \dot{R}_\mathrm{p}$), we obtain (Syer & Clarke 1995; Ivanov et al. 1999) the type II migration timescale as,

$$t_\mathrm{typeII} = \frac{R_\mathrm{p}}{|\dot{R}_\mathrm{p}|} = \frac{3\pi R_\mathrm{p}\nu\Sigma\Omega_\mathrm{p}}{\frac{1}{2}M_\mathrm{p}\Omega_\mathrm{p}R_\mathrm{p} + 2\pi\Sigma\Omega_\mathrm{p}R_\mathrm{p}^3} , \tag{4.36}$$

which can be rewritten as (Lodato et al. 2009),

$$t_\mathrm{typeII} = \frac{M_\mathrm{p} + M_\mathrm{disc}(R_\mathrm{p})}{M_\mathrm{disc}(R_\mathrm{p})} t_\nu(R_\mathrm{p}) , \tag{4.37}$$

with $M_\mathrm{disc} = 4\pi\Sigma(R_\mathrm{p})R_\mathrm{p}^2$ the local disc mass, and with the viscous timescale $t_\nu(R_\mathrm{p}) = (2/3)(R_\mathrm{p}^2/\nu(R_\mathrm{p}))$. Let us go a little further on, by defining a dimensionless parameter$B$, defined as $M_\mathrm{disc}/M_\mathrm{p}$, that leads to a more interesting form for the type II timescale,

$$t_\mathrm{typeII} = \frac{1+B}{B} t_\nu(R_\mathrm{p}) . \tag{4.38}$$

We highlight that this migration timescale is of the order of the viscous one, while the migration type I timescale was of the order of M_p^{-1}. Two regimes can be identified:

- $B \ll 1$, where the $M_\mathrm{p} \gg M_\mathrm{disc}$, it is the so called satellite-dominated regime. The planet inertia produces a slow migration, where the satellite can be seen as a dam for the fluid material. For $B \to 0$ the timescale is given by $t_\nu/B \gg t_\nu$.

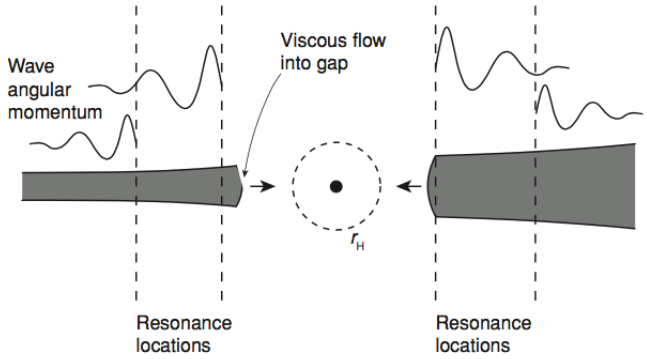

Figure 4.9: Sketch of the gap formation process under the action of the tidal and viscous forces. This mechanism can be described through a gap opening criterion, which tell us if the tidal torque is dominant respect to the viscous one. Image taken from Armitage (2013).

- $B \gg 1$, where the $M_\mathrm{p} \ll M_\mathrm{disc}$, it is the so called disc-dominated regime. The radial velocity of the planet can be approximated as the fluid radial velocity, then the migration is determined by the viscosity, and the timescale is the viscous one.

In the previous derivation we have assumed that the gas is kept outside from the gap, but in reality the picture is more complicated. Indeed, it is well known that gas does flow through gaps (Lubow & D'Angelo 2006). If this happens, the gas can also move at a different velocity from the planet one, which is not forced anymore to move at the viscous velocity. Early investigations performed with hydrodynamical simulations, where the planet was allowed to migrate, found that the migration rates were compatible with the type II estimate (Nelson & Papaloizou 2000; D'Angelo et al. 2005). Instead, more recent works (Duffell et al. 2014; Dürmann & Kley 2015) obtained as counter-trend result that the migration of a planet in this mass regime is faster than type II. Scardoni et al. (2020) re-analysed the problem by running longer simulations than Dürmann & Kley (2015). They confirmed the presence of an initial phase characterised by fast migration, but they also revealed that the migration velocity slows down and eventually reaches the theoretical prediction, if the system is allowed to evolve for enough time.

4.3 Gap opening criterion

We consider a Keplerian disc, with specific angular momentum $j(R) = \sqrt{\mathcal{G} M_\mathrm{p} R}$, and assume a gap size $\Delta \gtrsim H$, where H is the disc thickness. Indeed, this is a plausible estimate, first because Lindblad resonances are at their most effective at about this distance from the planet, and second because gaps whose radial width is much smaller than the vertical thickness of the disc could be unstable. In order to determine the gap opening criterion we have to compare the timescale relative

to the two torques acting on the system, as $t_{\rm open} \lesssim t_{\rm close}$, where $t_{\rm open}$ is the tidal timescale and $t_{\rm close}$ is the viscous one. For a schematic picture of the process see Fig. 4.9. From Section 2.1.3 we have that the viscous timescale is defined by

$$t_\nu(R_{\rm p}) = t_{\rm close} = \frac{H^2}{\nu}\,, \tag{4.39}$$

where ν is the disc viscosity. On the other hand we can compute the tidal timescale as the ratio between the angular momentum that has to be lose from the satellite to the disc, in order to clean the region $[R_{\rm p}, R_{\rm p}+H]$, and the rate at which angular momentum is exchanged ($T_{\rm tot}$),

$$t_{\rm open} = \frac{\Delta j}{T_{\rm tot}}\,, \tag{4.40}$$

where $\Delta j = \pi\Sigma H^2\sqrt{\mathcal{G}M_{\rm p}R_{\rm p}}$, and $T_{\rm tot}$ has been computed in Eq. 4.10. Therefore, after a little algebra (assuming $b_{\rm min} = 2/3H$) we obtain the gap opening criterion to be (Duffell & MacFadyen 2013),

$$q_{\rm p} \gtrsim \left(\frac{27\pi}{8}\right)^{1/2} \alpha^{1/2} \left(\frac{H}{R_{\rm p}}\right)^{5/2}\,, \tag{4.41}$$

where we used the Shakura & Sunyaev (1973) prescription for ν. It is interesting to note that in this relation we do not have an explicitly dependence on the gas surface density Σ, but in disc where heating due to viscous accretion process is not negligible, H/R varies with Σ. For protoplanetary disc with typical values of $\alpha \simeq 0.01$ and $H/R \simeq 0.1$ a rough estimate gives $q_{\rm p} \gtrsim 7\times10^{-5}$.
Let us briefly summarize other criterions, needed in order to maintain open the gap, once it is formed:

- Syer & Clarke (1995) found a criterion, by requiring that the gap should not be closed by pressure gradients,

$$\frac{t_{\nabla P}}{t_{\rm dyn}} = \frac{\Delta}{c_{\rm s}}\Omega = \frac{\Delta}{H} > 1\,. \tag{4.42}$$

  Indeed, in order to maintain the gap cleared, the planet has to complete its orbit, before the pressure gradient has closed it.

- Moreover we want the planet to be a mere catalyst of angular momentum, i.e. it has not to accrete material from the disc,

$$\Delta > R_H = \left(\frac{q_{\rm p}}{3}\right)^{1/3} R_{\rm p}\,. \tag{4.43}$$

  This relation means that the size of the gap must be greater than the Hill radius.

- Armitage (2013) points out that the opening criterion in Eq. 4.41, has been computed under the assumption that the planet-disc interaction could be treated two-dimensionally. This is valid if $H < R_{\rm H}$, that can be seen also

as another pressure stability requirement. Indeed, it can be shown that any pressure gradient on scales lower than the height of the disc is unstable (Lin & Papaloizou 1993; Malik et al. 2015): it means that density waves induced by the tidal torque could produce shocks that wipe out the material from the planet location, only if the perturber object has a mass greater than three times the thermal mass (Eq. 4.15). Thus, this criterion read as

$$q_{\rm p} > 3\left(\frac{H}{R}\right)^3_{\rm p}\,, \tag{4.44}$$

and it is known as "strong shock limit" or "thermal criterion".

- Previous criteria were based on the assumption that the exchange of angular momentum between the waves and the gas is instantaneous, thus happening in the vicinity of the planet as soon as the wake is generated. We know that spiral waves excited by the planet radially propagate across the gaseous disc, and can affect the structure of the disc as they transfer angular momentum to the disc material. This can happen by damping mechanisms, such as viscosity and/or shocks, leading to a non-local deposition of the tidal torque. The outcome of this non-local process is that the tidal interaction between the gaseous disc and the planet would be weaker at the resonances locations because the angular momentum is carried away by density waves and deposited in a wider region of the disc. Starting from this consideration, Crida et al. (2006) and Crida & Morbidelli (2007) found a criterion, involving the three main parameters of the problem: the mass of the planet, the scale height of the disc and the viscosity. It is based on the definition of a gap as a reduction of 10% of the unperturbed density at the planet's location, and it is given by

$$\frac{3}{4}\frac{H}{R_{\rm p}} + \frac{50\alpha M_\star}{M_{\rm p}}\left(\frac{H}{R_{\rm p}}\right)^2 = \frac{3}{4}\frac{H}{R_{\rm p}} + \frac{50}{q_{\rm p}Re} \lesssim 1\,, \tag{4.45}$$

where in the last equality we introduced the $q_{\rm p}$ planet-to-star mass ratio and the Reynolds number Re (Eq. 2.24).

- Li et al. (2009) and Yu et al. (2010) proposed a criterion (the "intertial limit") taking into account the planet migration. The gap opening rate must be faster than the migration rate across its own horseshoe region. Assuming a power law profile for the unperturbed gas density $\Sigma \propto R^{-p}$, Ward (1997) obtained

$$q_{\rm p} \gtrsim (q_{\rm p})_{\rm migr} \sim \frac{7}{8}p^2\frac{H}{R_{\rm p}}\left(\frac{\pi H^2\Sigma\left(R_{\rm p}\right)}{M_\star}\right)\,. \tag{4.46}$$

It can be derived that planets satisfying the strong shock criterion will automatically satisfy the "intertial limit" criterion.

We note that in all these criterion, depending on the value of the assumed $\Delta_{\rm min} = \max(|R-R_{\rm p}|, 2H/3, R_{\rm H})$ (see Eq. 4.14), the power-law scaling can slightly change.

4.3.1 Gap shape

Another interesting aspect to consider when studying the gap opening process, is the shape of the density profile that the gap would assume once formed, in particular its depth and width. As derived above for the gap opening criteria, one of the most used approach is to balance the local expression of the tidal torque exerted by the satellite on the disc with the local viscous torque. But, as briefly mentioned in the previous Section, this is based on the assumption that the waves excited by the planet are damped in the proximity of the planet, and that they consequently convey angular momentum in a region close to it. This means that the "excitation torque", i.e. the torque exciting the density waves, corresponds to the effective rate of angular momentum transfer from the satellite to the disc (Varnière et al. 2004). It can be said, that in this model, the wave damping is a local process. The issue comes from the possibility that the waves can actually travel within the disc before transferring all the angular momentum, and this is also linked to the physical mechanism behind the angular momentum exchange. If this non-local aspect of the process is considered, the "deposition torque" (also referred to as "pressure torque", Crida et al. 2006; Duffell 2015) is not the same of the "excitation torque".

Generally, we refer to two effective formulae to estimate the gap depth and width. The depth of the gap, expressed as the minimum of the density profile $\Sigma_{\rm gap}$, can be effectively estimated as (Kanagawa et al. 2018)

$$\frac{\Sigma_{\rm gap}}{\Sigma_0} \sim \alpha q_{\rm p}^{-2} \left(\frac{H}{R}\right)_{\rm p}^2 \left(\frac{\Delta_{\rm g,min}}{R_{\rm p}}\right)^3 \sim \begin{cases} \alpha q_{\rm p}^{-2} \left(\frac{H}{R}\right)_{\rm p}^5, & \text{for} \quad \Delta_{\rm g,min} = 2H/3 \\ \alpha q_{\rm p}^{-1} \left(\frac{H}{R}\right)_{\rm p}^2, & \text{for} \quad \Delta_{\rm g,min} = R_{\rm H} \end{cases} \tag{4.47}$$

where Σ_0 is the unperturbed surface density, $(H/R)_{\rm p}$ is the disc aspect ratio evaluated at the planet radius $R_{\rm p}$, and $q_{\rm p} = M_{\rm p}/M_\star$. Similar results, as a function of the planet-to-star mass ratio $q_{\rm p}$, local disc aspect ratio $(H/R)_{\rm p}$, and the viscosity parameter have been obtained in numerous investigations (Duffell & MacFadyen 2013; Fung et al. 2014; Kanagawa et al. 2015; Dong & Fung 2017a).

A width estimate instead can be obtained by balancing the two specific torque (viscous and tidal) $\Lambda_\nu = \Lambda_T$, as (Lin & Papaloizou 1979a)

$$\Delta \approx \left[q_{\rm p}^2 \frac{\Omega_{\rm p} R_{\rm p}^2}{\nu}\right]^{1/3} R_{\rm p}\,, \tag{4.48}$$

where we can identify the Reynolds number as defined in Eq. 2.24. This relation tell us that when $\nu \to 0$, the gap size $\Delta \to \infty$, which means that the tidal forces are not balanced by the viscous one, and they influence the disc structure for a big radial extent. Instead, if $\nu \to \infty$, we would have that the gap size $\Delta \to 0$, which means that the tidal forces are balanced at a radius near the planet orbit. We can restate the previous gap opening criterions in terms of this gap size, finding that $\Delta > H$ corresponds to $q_{\rm p}^2 > 1/fRe(H/R)^3$, while $\Delta > R_H$ becomes $q > 1/3fRe$.

4.3.2 Dust gaps

We can wonder if there is a difference between the dust and gas disc reactions to an embedded planet (Paardekooper & Mellema 2004, 2006). In general, we can think that there will be a difference when dust and gas are decoupled, while when they are coupled they will behave almost the same (for all the mechanism explained in Chapter 2). A little bit more in detail, when considering high mass planets, they exert a tidal torque stronger than the local viscous torque and form a gap in the gas. Dust grains therefore drift towards the pressure maxima located at the gap edges, as a result of gas drag (see Sec. 2.3.1). Trapping of dust at the pressure maxima prevents the solids from being accreted onto the planet, resulting in a lack of dust material around the planet. The gap formation process is generally a competition between torques. From this picture, we can identify that depending on the disc component, there are two different competing torques acting in the gap opening process. In a gas disc the competition is between the tidal torque from the planet trying to open a gap, and the viscous torque trying to close it. Instead, being dust a pressureless and inviscid fluid, the competition is between the tidal torque and the aerodynamic drag torque. As a consequence, the criterion for gap opening in dusty disc depends on the grain size of particles as well as on the planet mass (Paardekooper & Mellema 2006). Recently, Dipierro et al. (2016) and Dipierro & Laibe (2017) have studied the gap opening mechanism in the dusty component of the disc, considering both low-mass and high-mass planets. In the first case, no gap is carved in the gas phase, while it is in case of the massive planet. In their study, they conclude that the gap formation in the gas is not a necessary condition for opening a gap also in the dust. This is clearly described by the right panel of Fig. 4.10, where varying the dust-gas coupling (Stokes number, Eq. 2.54) and the planet mass, we can identify regions where the gap is carved in both dust and gas, or regions where only the dust phase is significantly perturbed by the planet. Their second finding is that for a low mass planet, the drag torque resists (assists) the tidal torque outside (inside) the planetary orbit, forming an asymmetric gap around the planet orbit. In this mass range, they also find two analytic criteria for the minimum planet mass required to stop the inflow of dust particles and ensure that drift can not refill the inner regions of the disc in dust. These two criteria represent the necessary and sufficient conditions for dust gap opening, respectively, and the outcome of their derivation is

$$q_{\rm p} \gtrsim \left(\frac{z}{\rm St}\right)^{3/2} \left(\frac{H}{R}\right)^{3}_{\rm p} . \tag{4.49}$$

Specifically, in their simulations (see left panel in Fig. 4.10) they observe that while the 0.05 $M_{\rm J}$ creates an asymmetric depletion of dust at the planet location, the 0.1 $M_{\rm J}$ planet is able to carve a gap in the dust. Finally, for what concern the high mass planet, it creates pressure maxima in the gas, and solid particles are thus prevented from accreting onto the planet. Here, drag assists the tidal torque, leading to the formation of partial or total gaps, which are deeper in the dust phase. Another recent work on this wake is the one of Rosotti et al. (2016), where they investigate the minimum planet mass that produces observable signatures in both infrared scattered light and (sub-)mm continuum images. This results being

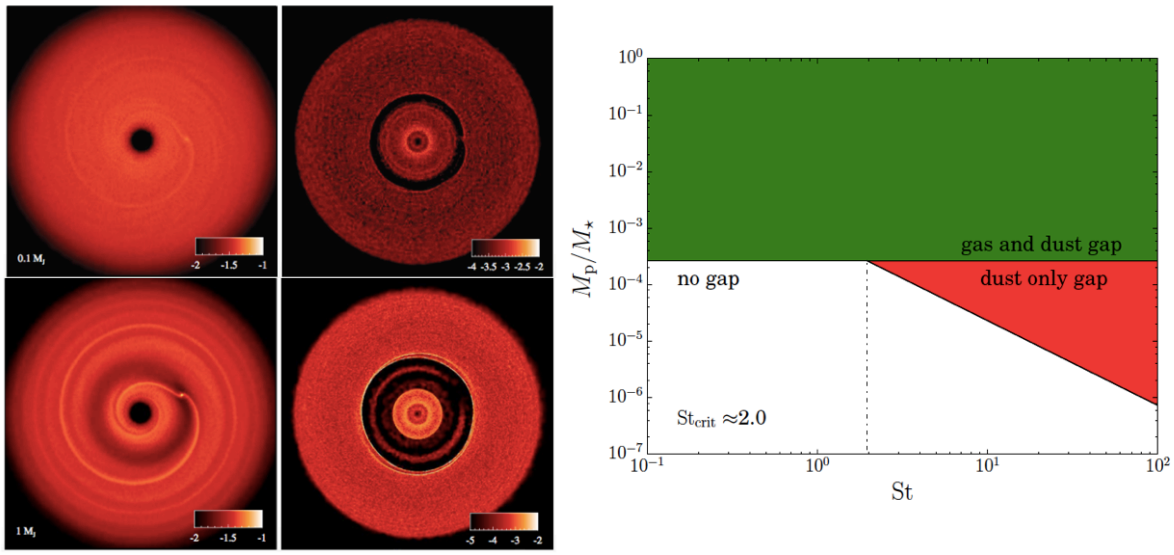

Figure 4.10: Left: the upper row shows a snapshot (gas, left - dust, right) of one simulation performed by Dipierro et al. (2016) with a low-mass planet embedded in a disc. The lower row is the same of the upper one, but for more massive planet. While in the massive case the gap is carved both in dust and gas, in the low-mass case the gas is not significantly perturbed. Right: sufficient condition for dust gap opening from Eq. 4.49, for different Stokes number, as obtained by Dipierro & Laibe (2017). The gap is carved in both phases (green area) or only in the dust (red area), depending on the combination of St-$M_{\rm p}$.

of the order of $\sim 15\,M_{\oplus}$, even if the obtained mass is strongly dependent on the disc temperature and changes slightly with the chosen wavelength. Other studies have also explored the relation between the minimum planet mass necessary to open a gap and other systems properties, such as the stellar properties (Sinclair et al. 2020) or the observed exoplanets population (Lodato et al. 2019). These investigations are interesting since they can give us an indirect estimate of the planet masses expected to open gaps. We also note that dust grains, depending on their Stokes number and thus on their coupling with the gas, can be filtered at the gap edges, and thus partially refill the depleted cavity (Rice et al. 2006b). This mechanism can have some influence on observations, and in particular can bring to cavity showing different sizes in dust and gas, as it has been observed in the protoplanetary disc of HD 135344B (Garufi et al. 2013). Finally, other interesting studies consider the possible effect of the planet migration onto the dust rings at the edge of planet carved gaps (e.g. Meru et al. 2019).

4.4 Coupled evolution for the planet-disc system

In this Chapter we derived that when a planet is embedded in a gaseous disc, orbiting around a central star, in order to describe the disc-binary evolution, one have to consider not only the viscous torque, but also the tidal one.

4.4.1 Disc dynamics

For the disc dynamics, this results in a modified equation for the angular momentum conservation[5], that taking into account also the viscous torque becomes,

$$\frac{\partial}{\partial t}\left(\Sigma R v_\phi\right) + \frac{1}{R}\frac{\partial}{\partial R}\left(\Sigma R v_\phi R v_\mathrm{R}\right) = \frac{1}{2\pi R}\frac{\partial}{\partial R}(G+K)\,, \tag{4.50}$$

where we remember that $G = 2\pi R^3 \nu \Sigma \Omega'$ is the viscous torque, and K is the new tidal torque. Coupled with this equation, we have to solve the continuity equation,

$$\frac{\partial \Sigma}{\partial t} = \frac{1}{R}\frac{\partial}{\partial R}\left(R v_\mathrm{R} \Sigma\right)\,. \tag{4.51}$$

The first step is to express the new torque $K(R)$ in 4.50, in terms of $\Lambda_T(R)$. In particular, we can write $\mathrm{d}K$ as the torque exerted by the planet on a disc annulus of mass $\mathrm{d}M = 2\pi R \Sigma(R) \mathrm{d}R$ between R and $R + \mathrm{d}R$, which leads to

$$\frac{\partial K}{\partial R} = 2\pi R \Lambda_T \Sigma\,. \tag{4.52}$$

Then, by means of Eq. 4.50 and 4.51, we can find the velocity v_R of the gas disc as,

$$v_R = \frac{1}{R\Sigma(R^2\Omega)'}\frac{\partial}{\partial R}\left(\frac{G}{2\pi}+\frac{K}{2\pi}\right) = \tag{4.53}$$

$$= -\frac{3}{\Sigma R^{1/2}}\frac{\partial}{\partial R}\left(R^{1/2}\nu\Sigma\right) + \frac{1}{\pi\sqrt{\mathcal{G}M_\star}}\frac{1}{\Sigma R^{1/2}}\frac{\partial K}{\partial R}\,, \tag{4.54}$$

where we note that the first term in the right-hand side of the equation is the velocity relative to the unperturbed disc $v_0 < 0$ (already derived in Sec. 2.1.1.3), while the second term arises from the planet-disc interaction. Through Eq. 4.52 we can rewrite the radial velocity in a more useful way, as

$$v_R = \begin{cases} v_0 - \left|\frac{2\Lambda_T}{\Omega R}\right|\,, & R < R_\mathrm{p} \\ v_0 - \left|\frac{2\Lambda_T}{\Omega R}\right|\,, & R > R_\mathrm{p}\,, \end{cases} \tag{4.55}$$

which means that for $R < R_p$ the gas is pushed at smaller radii, and viceversa.

Finally we can also write the diffusion equation as,

$$\frac{\partial \Sigma}{\partial t} = \frac{3}{R}\frac{\partial}{\partial R}\left[R^{1/2}\frac{\partial}{\partial R}\left(R^{1/2}\nu\Sigma\right)\right] - \frac{2}{R}\frac{\partial}{\partial R}\left(\frac{\Lambda_T \Sigma}{\Omega}\right)\,, \tag{4.56}$$

where the first is the viscous term, related to a diffusive behavior, and the second one produces a real advection of material.

[5] We stress that we have to modify only the azimuthal component (Eq. 2.20) of the Navier-Stokes equations, because torques act only on angular momentum, with tangential forces.

4.4.2 Binary dinamics

Let us now focus on the binary evolution. Indeed, to properly describe the system evolution we need to consider the angular momentum conservation of the disc and the binary (i.e. the planet and the central star). We know from Eq. 4.9 that, assuming a Keplerian disc, the total torque acting on the binary can be evaluated as

$$\frac{\mathrm{d}J_\mathrm{p}}{\mathrm{d}t} = \int_{R_\mathrm{in}}^{R_\mathrm{out}} \Lambda(R)\Sigma(R)2\pi R\mathrm{d}R = T_\mathrm{tot}\,, \tag{4.57}$$

where $\Lambda(R) = -\Lambda_T$ is the back-reaction of the disc onto the binary. Then, Eq. 4.57 becomes

$$\frac{\mathrm{d}(M_\mathrm{p}\Omega_\mathrm{p}R_\mathrm{p}^2)}{\mathrm{d}t} = \int_{R_\mathrm{in}}^{R_\mathrm{out}} \Lambda_T\Sigma(R)2\pi R\mathrm{d}R\,, \tag{4.58}$$

and developing the time derivative of the angular momentum,

$$\dot{R}_\mathrm{p} = -\frac{4\pi}{M_\mathrm{p}\Omega_\mathrm{p}R_\mathrm{p}}\int_{R_\mathrm{in}}^{R_\mathrm{out}} \Lambda_T\Sigma(R)2\pi R\mathrm{d}R\,. \tag{4.59}$$

We can finally resume that, while the binary opens a gap in the disc, the disc replies (as a back-reaction) with a torque of equal intensity, producing the binary time evolution. Lin & Papaloizou (1986) solved the coupled self-consistent system of equations, composed by Eq. 4.59 and 4.56, through a dimensionless analysis, with the introduction of a set of dimensionless quantities ($x = R/R_0$, $y = R_\mathrm{p}/R_0$, $\Sigma/\Sigma_0 = \sigma$, $\hat{\nu} = \nu/\nu_0$, $\tau = t/t_0$, defined by means of typical scales for the radius R_0, the surface density Σ_0, the viscosity ν_0, and the time $t_0 = R_0^2/\nu$), and by defining the dimensionless specific torque,

$$\lambda = \frac{\Lambda_T}{(\Omega R)^2} = \mathrm{sgn}(R - R_\mathrm{p}) f q_\mathrm{p}^2 \left(\frac{R_\mathrm{p}}{R - R_\mathrm{p}}\right)^4\,, \tag{4.60}$$

as we can find in Lodato et al. (2009). By choosing for the typical scales $R_0 = R_\mathrm{p}(t = 0)$ (i.e. R_0 coincides with the initial radial position of the planet) and $\Sigma_0 = \Sigma(R_0, t = 0)$ (i.e. we evaluate the surface density of the unperturbed disc at the planet radius), and using $\hat{\lambda} = \lambda/q_\mathrm{p}^2$ one can finally write the the two dimensionless equation as,

$$\begin{cases} \dfrac{\mathrm{d}\sigma}{\mathrm{d}t} = \dfrac{3}{x}\dfrac{\partial}{\partial x}\left[x^{1/2}\dfrac{\partial}{\partial x}\left(x^{1/2}\hat{\nu}\sigma\right)\right] - \dfrac{2}{x}A\dfrac{\partial}{\partial x}\left[\hat{\lambda}\sigma x^{1/2}\right] \\ \dfrac{\mathrm{d}y}{\mathrm{d}t} = -y^{1/2}AB\displaystyle\int_{x_\mathrm{in}}^{x_\mathrm{out}} \hat{\lambda}\sigma\mathrm{d}x \end{cases}, \tag{4.61}$$

where the two constant A and B contain the fundamental quantities of the system. They and are defined as,

$$A = \frac{\Omega R^2}{\nu}q_\mathrm{p}^2 \simeq \left(\frac{\Delta}{R}\right)^3 \quad \text{and} \quad B = \frac{4\pi R_0^2\Sigma_0}{M_\mathrm{p}}\,, \tag{4.62}$$

where A represents the gap size we found in Section 4.3, and is a measure of tidal effects respect to the viscosity, telling us that in order to open a gap, the gravitational effect of the satellite, has to overcome the disc pressure and viscosity. On the other hand, B is defined as the ratio between the disc mass and the planet one, and it is the parameter we defined in Section 4.2.3.

Chapter

5

Observations and interpretation of substructures

Crabs substructures on a beach in Queensland (Australia 2019).

In the previous Chapters we described protoplanetary discs, focusing on the gas and dust dynamics and their interplay, on the disc-planet interaction and on a first evolutionary stage of these systems where the disc self-gravity is of paramount importance for the subsequent disc evolution. We have also pointed out that all these aspects that characterise the dynamics and evolution of protoplanetary discs may also be at the origin of the observed substructures, both on a morphological and a kinematical level. Indeed, a wide range of peculiar morphologies has been detected in these systems, going from spiral structures, to rings and gaps, from cavities to

horseshoes. In this Chapter and in the following ones I will draw particular emphasis to the first two kinds of structures, spirals and rings. It is interesting to note that even if we limit our attention to this subgroup, the differences between the various observed systems are enormous. One can encounter discs with one or multiple rings, only in the dust or in both gas and dust; discs with two-armed spirals, or with a larger number of more coiled and less defined arms; discs with spirals in the gas and rings or asymmetric over-densities in the dust. The main "culprits" for the creation of these structures are thought to be planets or instabilities of various kinds. In particular, planets, depending on their mass, are able to dig gaps in the dust and/or gas, and to excite spirals in the gas. It is also thought that the origin of spirals can be found in gravitational instabilities, which are important in massive and young discs, probably still connected to their parental cloud. For what concerns the kinematic "structures" observed in discs, they can be defined generally as deviation from Keplerian rotation. These deviations can appear to be local in both space and velocity, or can interest a larger extent of the disc. Depending on their characteristics, they could be a signpost of gap-carving planets or gravitational instabilities. Observing these structures at high resolution and investigating their origin is therefore crucial for a deeper understanding of the mechanisms that led to the formation of protoplanetary discs and that govern the planet formation process within them.

5.1 Morphological structures

While there are a large number of discs showing substructures, new surveys are revealing that many discs that are considerably smaller at millimeter wavelengths do not show evidence of substructures. The question is whether this apparent smoothness of the discs is real or due to a too low resolution. A possible explanation for the small size of these discs is that the lack of substructures corresponds to a lack of dust traps, making radial drift particularly effective.

In Fig. 5.1 it is shown a schematic representation of observed substructures, with a non-exhaustive collection of the possible formation scenarios. In the next sections we will focus on the description of observations of rings and gaps (panel (b) of Fig. 5.1, see Sec. 5.1.1) and of spirals (panel (c) of Fig. 5.1, see Sec. 5.1.2), together with physical mechanisms that can be related to their formation. The last kind of substructures is described in the panel (a) of Fig. 5.1 and we give here a brief overview. Cavities are often linked to the presence of an inner companion (a star or a massive planet) that progressively depletes the inner region of the disc. The interaction of the two objects can also be linked to the presence of spiral arm that develop at the cavity edge or/and of streams of material connecting the remaining gas in the central region with the disc outside the cavity (see e.g. HD 142527, Price et al. 2018b). Another explanation for the observed cavities is that they formed due to mass-loss driven by a photoevaporative or MHD wind (Alexander et al. 2014; Ercolano & Pascucci 2017). In addition, cavities are sometimes observed in combination with rings just outside the edge of the cavity and vortex (e.g., see Cazzoletti et al. 2018). Indeed, the sharp density contrast at the cavity edge

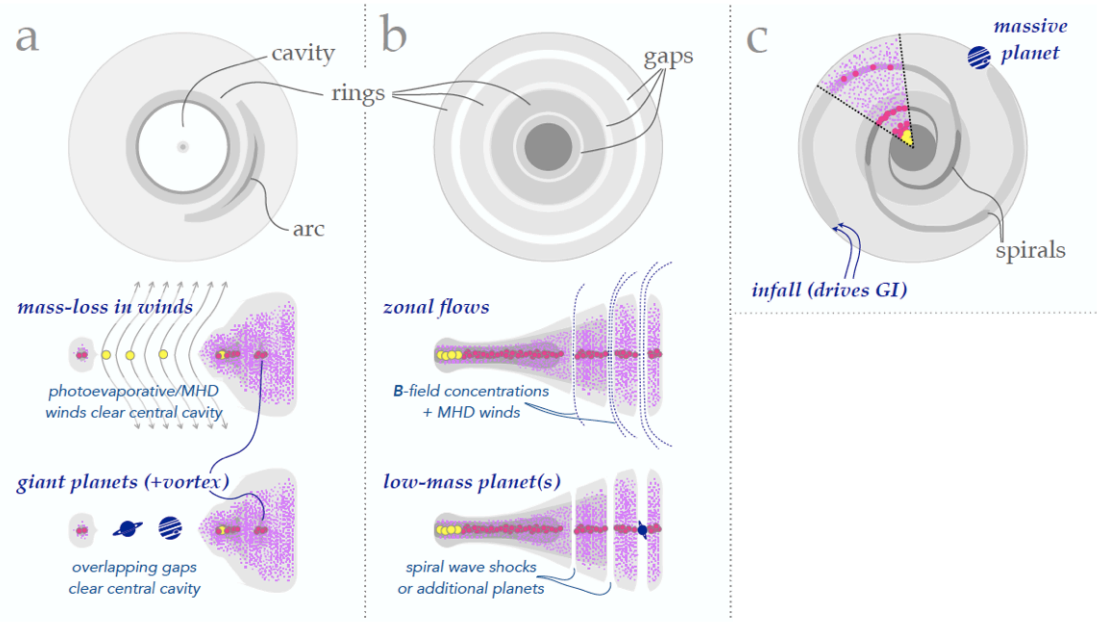

Figure 5.1: Schematic (non exhaustive) representation of substructures observed in protoplanetary discs generated by various physical mechanisms. Panel a): a ring + cavity substructure with an arc feature (upper panel) and some possible mechanisms (e.g., photoevaporation, vortex, giant planets, binary) behind their formation. Panel b): gaps and rings (upper panel) with two formation scenarios (zonal flows and low-mass planets). Panel c): spiral arms that can be generated by a massive planets or by gravitational instabilities. The latter mechanisms can be driven by infall of material from the parental cloud, or by the disc being massive enough to switch on the instabilities. Image taken by Andrews (2020)

can trap particles in a ring and potentially excite vortices or eccentric modes that generate strong azimuthal asymmetries in the pressure structure (Kley & Dirksen 2006; Ataiee et al. 2013; Zhu et al. 2014; Ragusa et al. 2017, 2020). The presence of an inner companion with an inclined orbit, or of a binary can also produce a warp, which is observable as a different illumination of the system (e.g., HD 143006 Marino et al. 2015; Nealon et al. 2018; Facchini et al. 2018a; Benisty et al. 2018; Nealon et al. 2019, 2020a; Aly & Lodato 2020). For a more complete review we refer the reader to Andrews (2020).

5.1.1 Rings and Gaps

Gaps and rings are the most common substructure morphology identified in the millimiter continuum emission by ALMA (e.g., ALMA Partnership et al. 2015a; Long et al. 2018b; Huang et al. 2018c), and also in scattered light (e.g., de Boer et al. 2016; Ginski et al. 2016; van Boekel et al. 2017; Pohl et al. 2017). A system showing rings and gaps structure can be defined as a concentric, nearly axisymmetric pattern of alternating intensity enhancements (rings) and depletions (gaps). In Fig. 5.2, 5.3, 5.3, 5.4, 5.5 I collected (probably not all) systems presenting such substructures at different wavelengths and observed by various telescopes and instruments. Although symmetrical structures such as rings and gaps are very common, there are many differences. For example, when looking at millimeter wavelengths, some systems have a single bright ring at the edge of a central cavity or of a very wide gap (e.g., CIDA 9, IP Tau, HD 135344B, ISO-Oph 2, DoAr 44, WSB 82, RX J1633.9-2442), while others have a series of thin bright rings with more or less wide gaps (e.g., AS 209, GO Tau, CI Tau, DL Tau, DoAr 25, HL Tau, TW Hydrae, Elias 24, HD 163296, HD 143006, GY 91, HD 97048, ISO-Oph 54, ISO-Oph 17, V1094 Scorpii). Some of them present a brighter region along the ring (e.g. HD 143006), or just outside (e.g. HD 135344B). Three of these discs show a ring/gap structure together with spiral arms (see Sec. 5.1.2, Elias 2-27, IM Lup, WaOph 6). In a few cases, bright rings have also been detected in scattered light, by SPHERE (e.g., RX J1615.3-3255, TW Hydrae, HD97048, HD163296, HD 169142). van der Marel et al. (2020) analysed a sample of 16 discs, with the aim of understanding the observed diversity of morphology in this category of substructures. They found that asymmetries correspond to higher Stokes numbers or low gas surface density (see also Veronesi et al. 2019). Several studies have been carried out to find a correlation between the position, width and depth of these gaps/rings and properties of the system (such as the age and luminosity of the star, the presence or absence of cavities within the disc, van der Marel et al. 2019). An example of systems showing rings outside an inner cavity can be found in the sample of transition discs analyzed by Pinilla et al. (2018a).

Rings and gaps-like substructures are usually understood to be the result of disc-companion interaction, but other mechanisms have been studied in recent years, and a final framework to explain the individual observed systems is still missing. This is probably due to the fact that several physical processes are simultaneously at work in shaping the observed systems. In the following sections, I will describe the hypothesis that has been discussed more often so far, and briefly list other mechanisms that may have led to the formation of such structures.

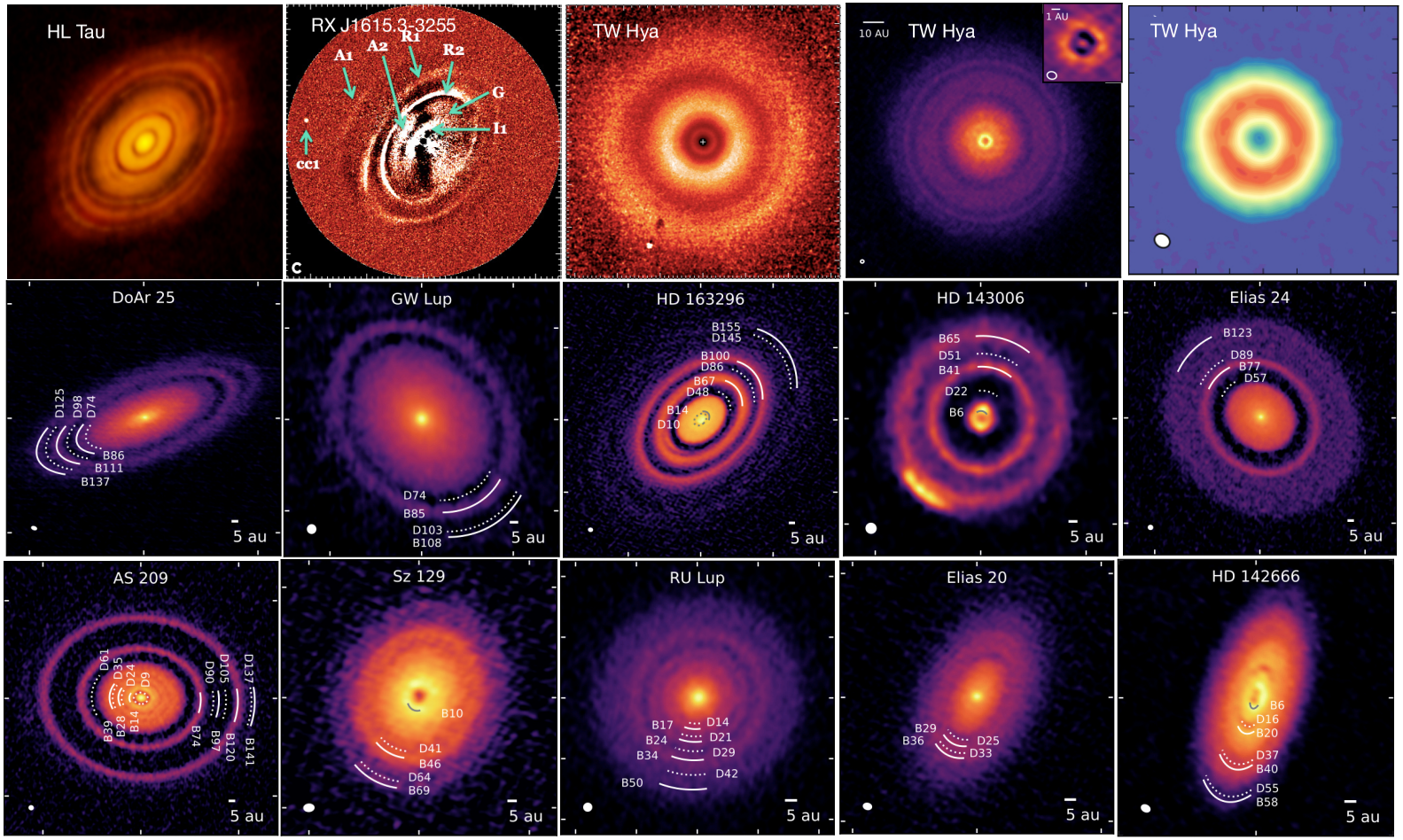

Figure 5.2: Collection of protoplanetary discs showing gaps and rings structures at different wavelengths. From left to right and from top to bottom: HL Tau (ALMA Partnership et al. 2015a), RX J1615.3-3255 (de Boer et al. 2016), TW Hydrae (van Boekel et al. 2017; Andrews et al. 2016; Bergin et al. 2016), DoAr 25, GW Lup, HD 163296 (Isella et al. 2018), HD 143006 (Pérez et al. 2018b), Elias 24 (Huang et al. 2018c), AS 209 (Guzmán et al. 2018), Sz 129, Ru Lup, Elias 20, HD 142666 (Huang et al. 2018c).

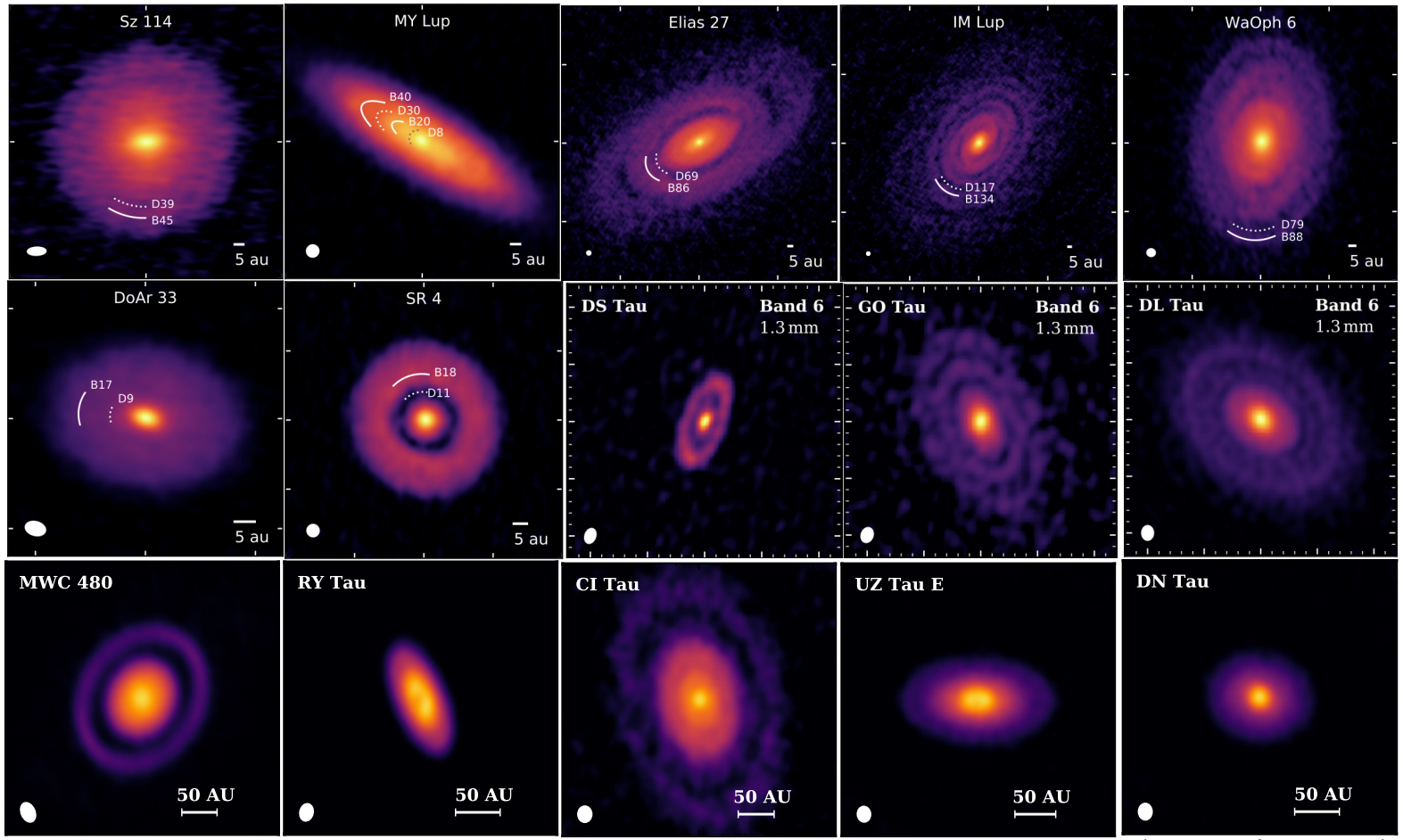

Figure 5.3: Collection of protoplanetary discs showing gaps and rings structures at different wavelengths. From left to right and from top to bottom: Sz 114, MY Lup, Elias 2-27, IM Lup, WaOph 6, DoAr 33, SR 4 (Huang et al. 2018c), DS Tau, GO Tau, DL Tau (Long et al. 2018b, 2020), MWC 480, RY Tau, CI Tau, UZ Tau E, DN Tau (Long et al. 2018b).

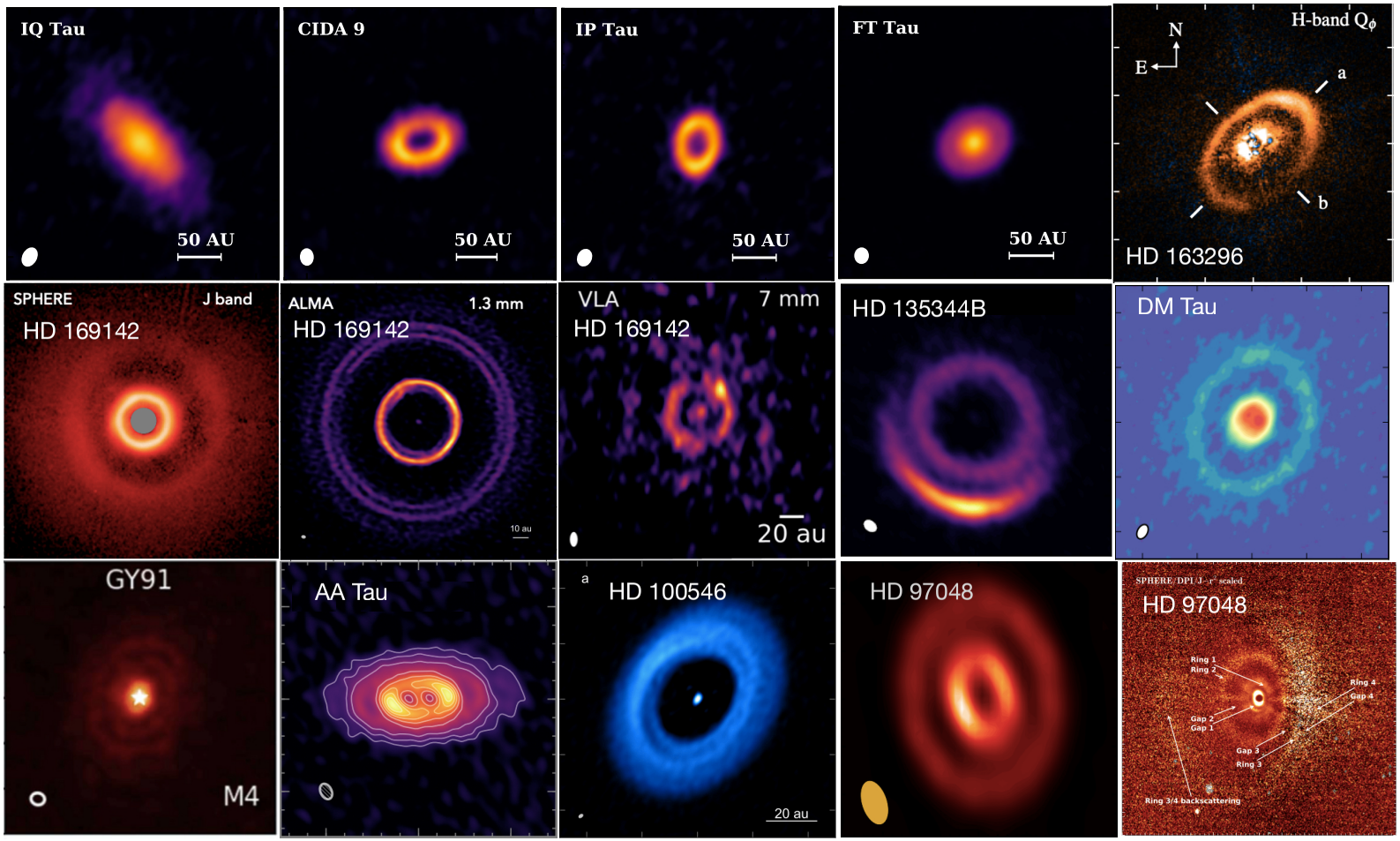

Figure 5.4: Collection of protoplanetary discs showing gaps and rings structures at different wavelengths. From left to right and from top to bottom: IQ Tau, Cida 9, IP Tau, FT Tau (Long et al. 2018b), HD 163296 (Muro-Arena et al. 2018), HD 169142 (Pohl et al. 2017; Pérez et al. 2019; Macías et al. 2017), HD 135344B (Cazzoletti et al. 2018), DM Tau (Bergin et al. 2016), GY91 (Sheehan & Eisner 2018), AA Tau (Loomis et al. 2017), HD 100546 (Pérez et al. 2020), HD 97048 (van der Plas et al. 2017; Ginski et al. 2016).

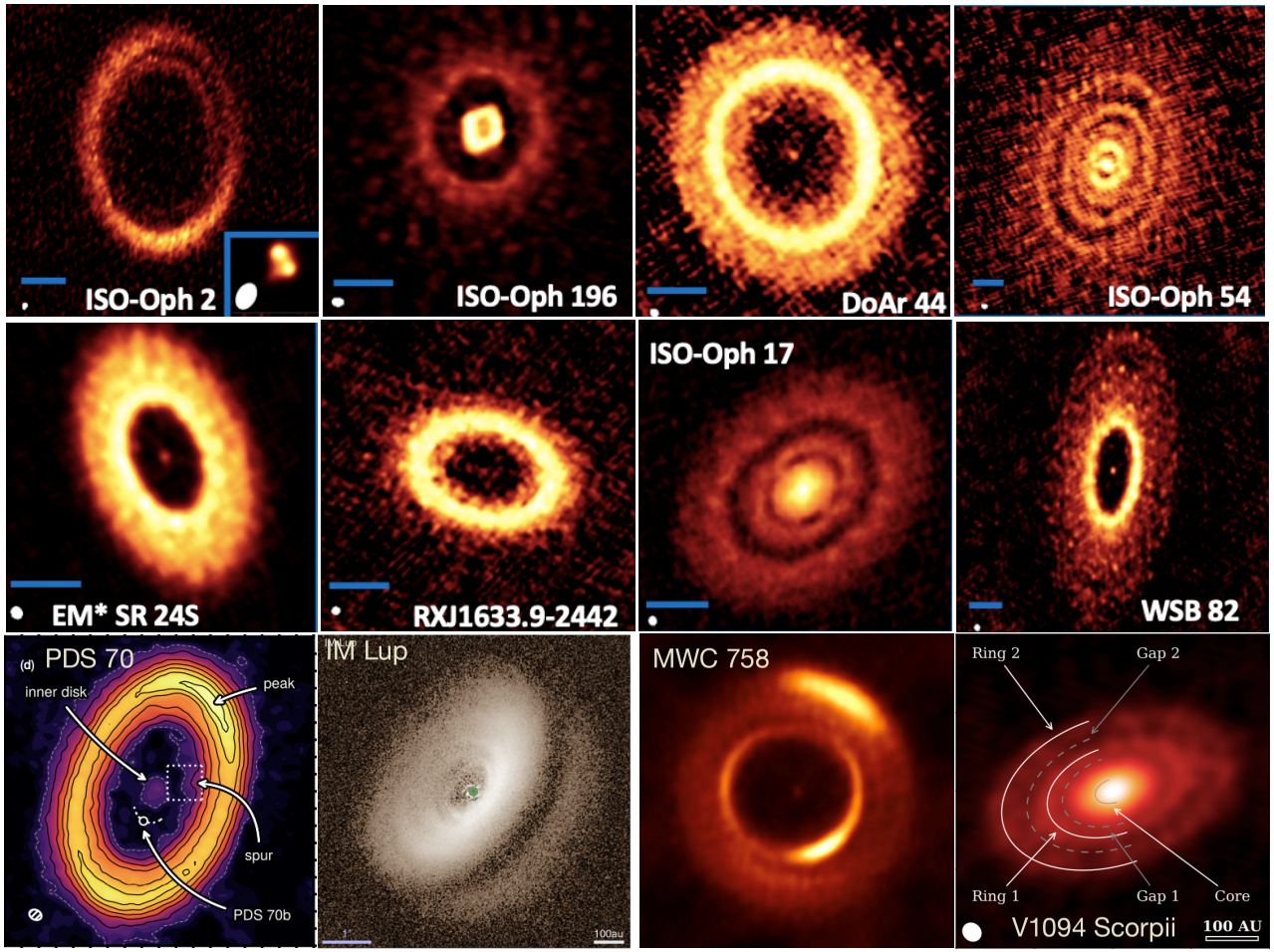

Figure 5.5: Collection of protoplanetary discs showing gaps and rings structures at different wavelengths. From left to right and from top to bottom: ISO-Oph 2, ISO-Oph 196, DoAr 44, ISO-Oph 54, EM* SR 24S, RXJ1633.9-2442, ISO-Oph 17, WSB 82 (Cieza et al. 2021), PDS 70 (Keppler et al. 2019), IM Lup (Avenhaus et al. 2018), MWC 758 (Dong et al. 2018a), V1094 Scorpii (van Terwisga et al. 2018).

5.1.1.1 Gap-carving planets

One of the natural physical mechanisms for explaining these structures is the presence of embedded planets in the disc (Pinilla et al. 2012b; Dipierro et al. 2015b; Rosotti et al. 2016; Fung & Chiang 2016; Clarke et al. 2018; Dipierro et al. 2018a; Facchini et al. 2018b; Liu et al. 2019; Toci et al. 2020b; Veronesi et al. 2020). Indeed, as seen in Chapter 4, one of the outcome of the disc-planet interaction can be under certain circumstances (see Sec. 4.3) the creation of gaps. If the planet is a low-mass one, we expect to see a gap only in the dust (Crida et al. 2006; Rosotti et al. 2016; Dipierro & Laibe 2017), while if the planet is a massive one, it should be able to carve a gap in both dust and gas (Pinilla et al. 2012b; Dipierro et al. 2016; Kanagawa et al. 2015, 2017). Within this assumption, one can use the gap properties, such as its width and depth, in order to infer the planet mass or the disc viscosity. In Sec. 4.3.1 we collect some relations linking the gap properties to the planet mass and disc viscosity. Lodato et al. (2019) use a simple estimate, $\Delta = 5.5\,R_{\rm H}$, based on the relation between the dust gap width Δ and the Hill radius $R_{\rm H}$, with a proportionality constant coming from averaged results of previous hydrodynamical simulations (?Pinilla et al. 2012b; Rosotti et al. 2016; Fung & Chiang 2016; Facchini et al. 2018b), to estimate the planet masses from the rings in the Taurus sample of Long et al. (2018b). They assume that each gap has been carved by one planet, and they also consider the planet evolution (i.e. migration and accretion) for a period between 3 - 5 Myr (see Fig. 5.6). Before considering the system evolution they find that the properties of the analysed sample occupy a different region of the parameter space with respect to the known exo-planet population, currently not accessible through planet finding methods. When considering also the evolution, they interestingly obtain a redistribution of planet properties in the region of cold Jupiters. From a more observational point of view, Asensio-Torres et al. (2021) present a derivation of planet detection limits in a sample of 15 protoplanetary discs showing substructures such as rings and gaps. Under the assumption that one perturber is responsible for the creation of one substructure, they obtain a mass limit range of $0.01-1\ M_{\rm Jup}$ for planets connected to rings and gaps, and a range of $3-10\ M_{\rm Jup}$ for planets inside cavities. The location of this putative population of planets is between $\sim 10-400$ au. They also highlight that there are some systems in which we would be able to detect planets, but in general there is no direct correspondence to any detected population of exoplanets. Another possible approach (in case of single object studies) to infer the mass of the perturber is to perform hydrodynamical and radiative transfer simulations varying the planet mass, and then fitting the obtained synthetic intensity profile with the data. This is the method I used in Veronesi et al. (2020) for the gap observed in the DS Tau disc. For further details see Chapter 7.

The caption of Fig. 5.6 should be corrected as the dashed line connects the properties of planets after 3 or 5 Myr of evolution, not between then final and initial properties

However, as shown in Eq. 4.47 and 4.48, the gap properties depend also on the disc viscosity. Recently, it has been shown that one planet can open multiple gaps, thus creating multiple rings, under specific conditions of low viscosity and temperature (Bae et al. 2017; Dong et al. 2017, 2018b). This has been explained

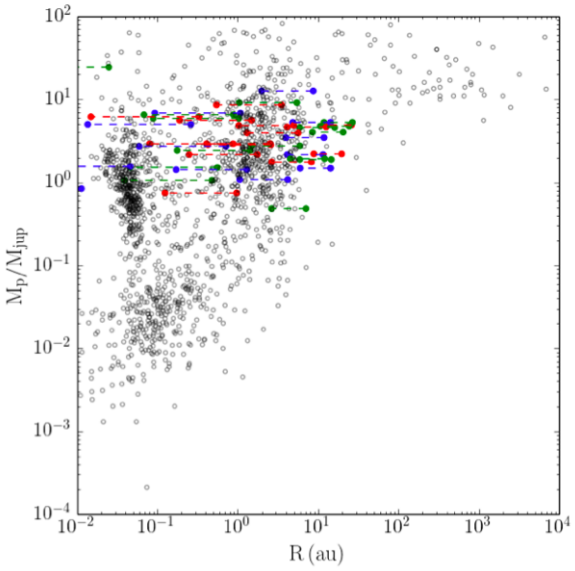

Figure 5.6: The planet mass M_p as a function of the separation from the central star R for the current exoplanets population (empty circles) is compared with planet masses obtained from the sample of Long et al. (2018b) (red points), Zhang et al. (2018) (green points) and Bae et al. (2018) (blue points). The dashed lines connect the planet positions after 3 and 5 Myr of planet evolution (accretion and migration).

to be a result of the complex propagation and dissipation of the multiple spiral density waves excited by the planet in the disc, in particular the secondary and tertiary arms driven by a planet can also open gaps as they steepen into shocks. Bae et al. (2017) also showed that the depths of the secondary/tertiary gaps in surface density grow with time when the disc viscosity is $\alpha \sim 5 \cdot 10^{-5}$, meaning that even low-mass planets (e.g., super-Earth or mini-Neptune-mass) embedded in the disc can open multiple observable gaps, if sufficient time has passed. This low viscosity value appears to be confirmed by new measurements of disc viscosity by Flaherty et al. (2020) that upper limits to the value of $\alpha \lesssim 10^{-3}$ (except in the case of DM Tau). However, a precise measurement of viscosity remains an open issue, not least because insufficient observational evidences have been found. In addition, Miranda & Rafikov (2019b) point out that the approximation of locally isothermal disc used in these latter studies does not provide an accurate description of the density wave dynamics on scales of tens of astronomical units. The outcome is that locally isothermal simulations tend to overestimate the contrast of ring and gap features, and underestimate the masses of planets responsible for the formation of multiple gaps and rings.

Given the large sample of discs showing gaps and rings in the DSHARP survey (Huang et al. 2018c), Zhang et al. (2018) explored the properties of the hypothetic planets responsible for such structures with a grid of 2-dimensional hydrodynamical simulations of dusty gaseous discs with embedded planets. They provide a relationship between the planet mass and the gaseous gap depth/width, and they also discute the sub/super-Keplerian motion across the gap. Also in their computation, they find that with low viscosity a planet is able to carve multiple gaps, and they find a relationship between the position of the secondary gap and the disc scale height (H/R). Their main finding is that the gap becomes deeper with higher planet mass, smaller H/R, and lower α. Also, in a low α disc, when $M_p \geq 3\, M_J$, the gap edge becomes eccentric and the gap depth starts to decrease. Finally they also show that discs with different surface densities and different dust

size distributions have the same gap shape as long as their Stokes numbers for the maximum-size particles (where most of the dust mass is) are the same. This means that their derived relationships can be used in other discs with different surface densities and dust size distributions, but note that Zhang et al. (2018) do not include planet migration in their simulations, nor they include the backreaction of dust drag onto the gas.

Another interesting finding is that several planets may participate in the carving of a single gap or cavity (Zhu et al. 2011). Indeed, in the last years, satellites such as TESS are revealing a plethora of exoplanetary systems composed by many planets (> 2), where at least a couple of them are giants, and astronomers are starting to study the chemical composition of exoplanetary atmospheres, underlining the need to better understand the impact of more than one planet in protoplanetary discs. An example of how deeply a system of planets modify the surrounding material can be found in the modeling of PDS 70 (see Fig. 5.5 and 5, Müller et al. 2018; Keppler et al. 2019) by Bae et al. (2019) and Toci et al. (2020b), where the interaction of two giant planets (that end up locked in resonance) is responsible for the wide gap/cavity creation both in dust and gas [1]. An element confirming the presence of two planets candidates within the cavity of PDS 70 is given by the fact that a mass accretion rate lower than what is typically measured for the observed disc mass is found (Manara et al. 2019b). However, giant planets can also host a ring between them, as found in a modeling of HD 169142, where Toci et al. (2020a) show that it can be possible to form and preserve a dust rings between the orbits of two giant planets for a significant fraction of the disc lifetime. This is explained by the fact that while the dust is initially trapped in the pressure maximum between the two planets, since the gas surface density decreases inside the gas gap, the Stokes number increases to values larger than unity, helping the pressure bump in preserving the dust to migrate, thus preventing the creation of a wider gap.

Other studies have been done focusing in particular on the dust back-reaction (e.g., Kanagawa et al. 2018) and the planet migration. In the latter case, Meru et al. (2019) found that the importance of perturbations in the pressure profile interior and exterior to the planet depends on the particle sizes. For small sizes, a dust enhancement occurs interior to the planet, whereas it is exterior to it for large particles. The transition between these two behaviours happens when the dust drift velocity is comparable to the planet migration velocity. Also, they highlight the difference between results obtained when allowing the planet to migrate or not. Indeed, it is important to consider both migration and accretion in order to recover the correct physical mechanisms behind the formation of the observed substructures.

5.1.1.2 Other physical mechanisms behind gaps

Embedded planets are just one of the proposed mechanisms behind the formation of rings and gaps. Indeed, an interesting point of view related to the gaps/rings-

[1] PDS70 shows a compact (< 5 au) and faint inner ring (Keppler et al. 2019), thus probably the system has a wide gap and not a cavity. Further studies are needed to better characterise the inner region.

planet connection has been highlighted in Riols et al. (2020): "are these rings the result of planet formation (as the planet-induced scenario suggests) or the driver (as envisioned by purely gas-induced)?". In order to answer this question, it is necessary to explore other mechanisms that could have produced such substructures, and to understand what comes first, if the substructures or the planet (e.g., an application of this can be found in Morbidelli 2020). Since other mechanisms are not directly related with the main topic of this Thesis, we will just list some of them. The interested reader can see Andrews (2020) for a review of disc substructures and some of their potential origins. Briefly, gaps and rings can be an outcome of the effects of magnetic fields and wind (e.g., Johansen et al. 2009; Flock et al. 2015; Suriano et al. 2018; Riols & Lesur 2019; Riols et al. 2020), such as the flows induced by magneto-rotational instabilities (Johansen et al. 2009), or can be related to grain growth at condensation fronts (i.e., icelines, e.g. Zhang et al. 2015; van der Marel et al. 2018b). To this regard, in their sample of ringed-discs, Long et al. (2018b) showed the lack of connection between rings and snow-lines, meaning that condensation fronts are unlikely to be a universal mechanism to create gaps and rings. It can also be linked to the presence of dead zones in the disc, where gas accretion is regulated by spatial variations of the ionization level (Flock et al. 2015; Pinilla et al. 2016). Barge et al. (2017) propose that a giant vortex not only captures dust grains with low Stokes number, but can also affect the distribution of larger grains (with St $\sim$ 1), carving a gap associated with a ring composed of incompletely trapped particles. Gap formation can also be the result of secular gravitational instabilities regulated by disc viscosity (Takahashi & Inutsuka 2016), or of large scale instabilities due to variations in the dust-to-gas ratio caused by dust settling (Lorén-Aguilar & Bate 2015a). Also non-ideal MHD effects have been proposed to be at the origin of the disc self-organization in a series of gaps and rings-like structures (Béthune et al. 2017).

5.1.2 Spirals

Another interesting substructure detected in some protoplanetary discs are large-scale spiral patterns. These have mostly been observed in scattered light images, going from pronounced $m = 2$ modes with small brightness asymmetries and a relatively open morphology (e.g., in Fig. 5.7, HD 135344B, Stolker et al. 2016; MWC 758, Benisty et al. 2015; LKHa 330,Uyama et al. 2018) to more intricate, tightly-wrapped, and asymmetric structures (e.g., in Fig. 5.7 and 5.8, HD 142527, Avenhaus et al. 2017; GG Tau, Keppler et al. 2020; AB Aur, Boccaletti et al. 2020; SU Aur, Ginski et al. 2021; HD 100546, Follette et al. 2017). There are only three known examples of discs that exhibit a spiral pattern in the mm continuum, which are Elias 2-27, IM Lup and WaOph 6 (Pérez et al. 2016; Huang et al. 2018b; Paneque-Carreno et al. 2021). All the three discs show a large, symmetric, two-armed spiral arm. While the one in Elias 2-27 appears to have a larger pitch angle (see Eq. 4.25, i.e. the spiral is more open), the other two appear more tightly wound. The three systems are also characterised by a narrow ring, highlighted in Fig. 5.2 (Huang et al. 2018c). While in Elias 2-27 the spiral arms extend throughout much of the disc, also intersecting the gap at $\sim$ 70 au, they appear to be more complex in IM Lup, where they extend halfway radially through the

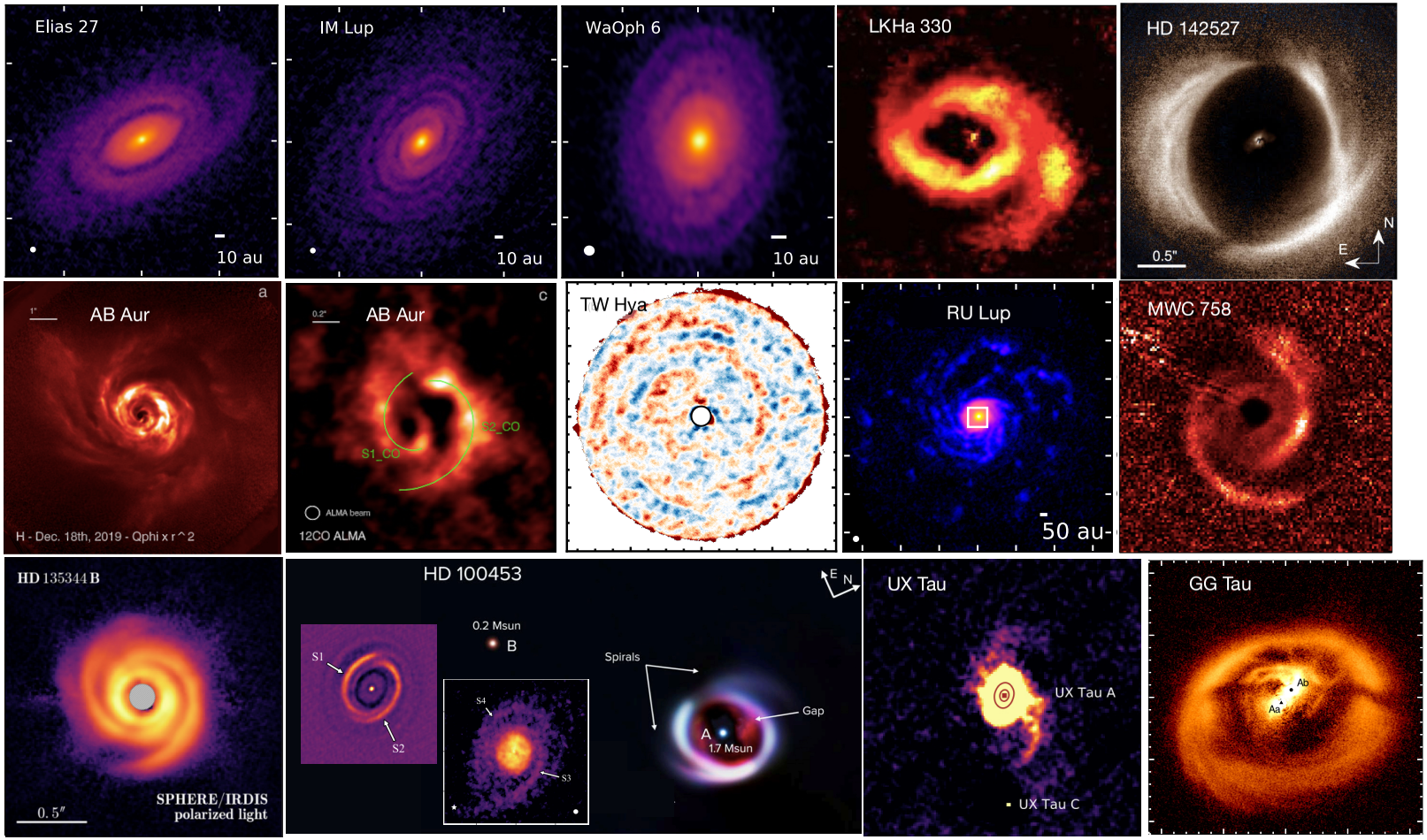

Figure 5.7: Collection of protoplanetary discs showing spiral structures at different wavelengths. From left to right and from top to bottom: Elias 2-27, IM Lup, WaOph 6 (Huang et al. 2018b), LKHa 330 (Uyama et al. 2018), HD 142527 (Avenhaus et al. 2017), AB Aurigae (Boccaletti et al. 2020, Tang et al. 2017), TW Hydrae (Teague et al. 2019b), RU Lup (Huang et al. 2020), MWC 758 (Benisty et al. 2015), HD 135344B (Stolker et al. 2016), HD 100453 (Benisty et al. 2017, Rosotti et al. 2020a), UX Tauri (Ménard et al. 2020), GG Tauri (Keppler et al. 2020).

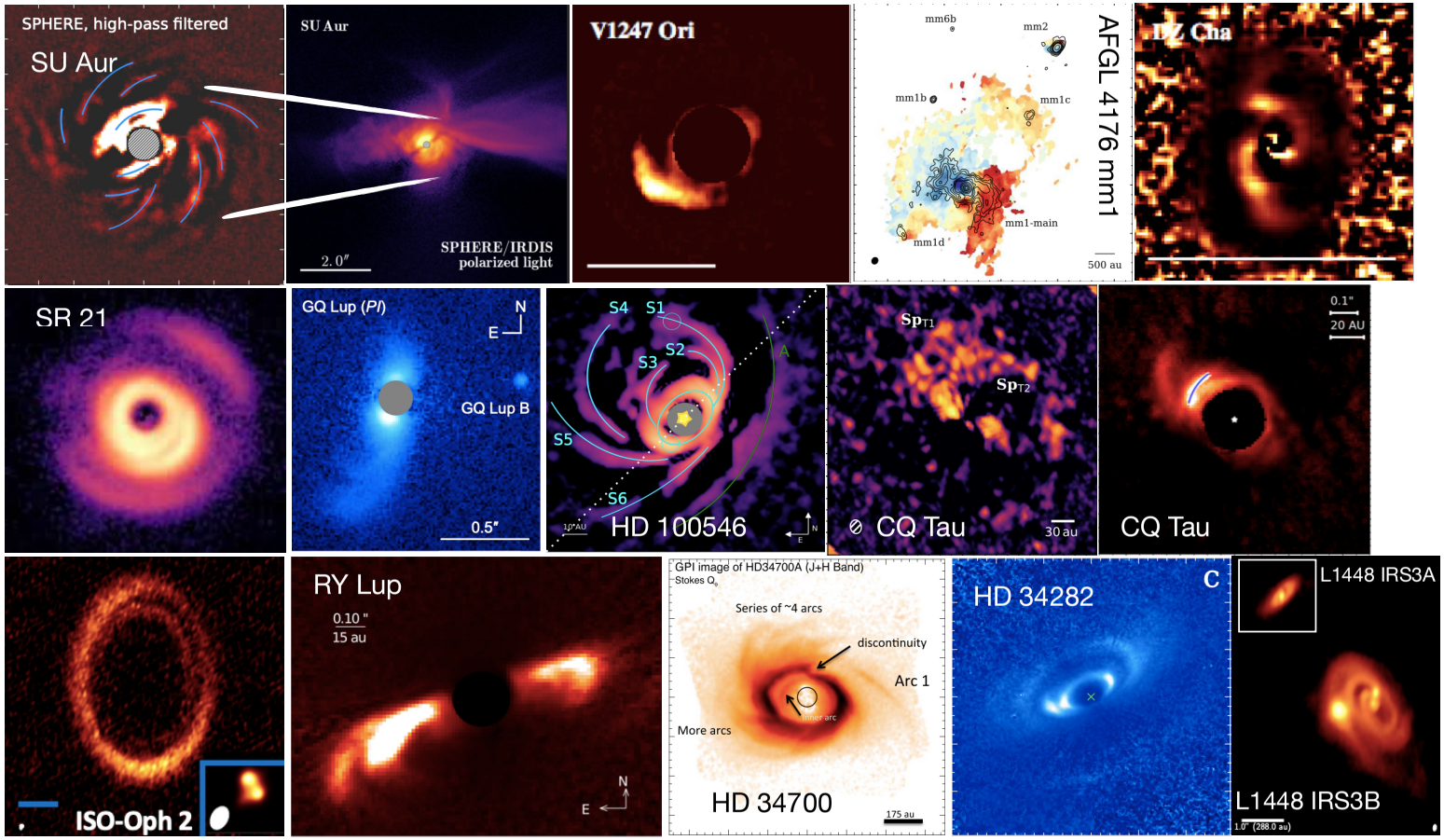

Figure 5.8: Collection of protoplanetary discs showing spiral structures at different wavelengths. From left to right and from top to bottom: zoom of SU Aur and wider field (Ginski et al. 2021), V1247 Ori (Ohta et al. 2016), AFGL 4176 mm1 (Johnston et al. 2020), DZ Chamaeleontis (Canovas et al. 2018), SR 21 (Muro-Arena et al. 2020b), GQ Lup (van Holstein et al. 2021), HD 100546 (Follette et al. 2017), CQ Tau (Wölfer et al. 2020; Uyama et al. 2020), ISO-Oph 2 (Cieza et al. 2021), RY Lup (Langlois et al. 2018), HD 34700 (Monnier et al. 2019), HD 34282 (de Boer et al. 2020), L1448 IRS3B and IRS3A (Reynolds et al. 2021).

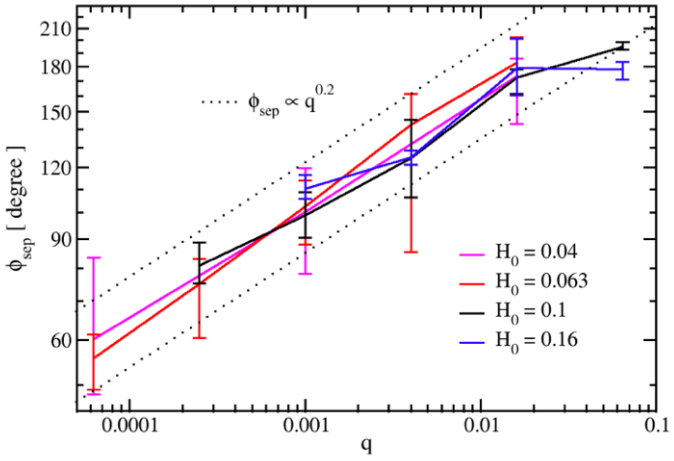

Figure 5.9: Average azimuthal separation $\phi_{\rm sep}$ between the primary and secondary arm, as a function of the planet-to-star mass ratio $q_{\rm p}$ (Fung & Dong 2015).

disc, exhibiting pitch angle variations with radius, and interarm features (Huang et al. 2018b). Spiral structures are observed not only in the dust continuum and scattered light emission, but also they have been detected in spectral line emission, such as in the case of TW Hya (Teague et al. 2019b), RU Lup (Huang et al. 2020), AB Aur (Tang et al. 2012, 2017), HD 100453 (Rosotti et al. 2020a).

Again, as with rings and gaps, there are many mechanisms that can explain the formation of spiral structures. As already discussed in Section 4.1.2 structures with one or more spiral arms can arise from the interaction between the disc and an embedded perturber (star or planet, Dong et al. 2015b, 2016; Price et al. 2018b; Poblete et al. 2020). Also, as described in Section 3.2, if the disc is massive enough ($M_{\rm disc}/M_\star \approx H/R$) spiral structures may arise from the onset of gravitational instabilities in the disc. Among other mechanisms, there are flybys, (i.e. the dynamical interaction of the disc with an external perturber, Cuello et al. 2019, 2020), and the interaction of a vortex with the disc (van der Marel et al. 2016b).

5.1.2.1 Spirals excited by a planet

From Sec. 4.1.2 we know that a planet embedded in a disc can excite spiral arms, where the number of arms m depends especially on the mass of the planet. These features arise from the superposition of multiple modes of azimuthal and radial perturbations in the gravitational potential which constructively and destructively interfere with each other to produce the spiral morphology (Goldreich & Tremaine 1979; Bae & Zhu 2018a; Miranda & Rafikov 2019a). In the linear approximation with $M_{\rm p} \ll M_{\rm th}$ (with $M_{\rm th}$ defined in Eq. 4.15) the excited spiral would have an $m = 1$ arm, while with a mass larger than the thermal mass also modes with $m = 2, 3$ are expected (especially in the region inside the planet orbit). However, as discussed in Sec. 4.1.2, recent studies have found that even in the linear regime more than one spiral arm can be formed. This theoretical background can be used to shed some light on recent observations at sub-mm and infrared wavelengths showing $m = 2$ (or more) spiral structure. In particular, we could be able to constrain some of the planet (e.g., position and mass of the planet) and of the disc (e.g., H/R) properties. The planet mass can be estimated by means of three

different "tracers": the pitch angle, the separation between two arms, and the contrast of the spiral arms (with $m > 1$).

With the assumption that spiral structures can be potential signatures of embedded planets, and that massive planets ($M_{\rm p} > M_{\rm th}$) could excite more than one spiral arms, Fung & Dong (2015) performed two and three-dimensional hydrodynamical simulations obtaining a scaling relation between the azimuthal separation of the primary and secondary arm, $\phi_{\rm sep}$, and the planet-to-star mass ratio $q_{\rm p}$. For companions between Neptune mass and 16 Jupiter masses around a 1 solar mass star, the scaling is given by $\phi_{\rm sep} = 102^{\circ}(q_{\rm p}/0.001)^{0.2}$, while for brown dwarf mass companions is $\phi_{\rm sep} = 180^{\circ}$ (see Fig. 5.9). The interesting and potentially useful aspect of this relation is that it appears to be independent of the disc temperature. Moreover, they also show that for more massive planets, the secondary arm is not seen at larger radii, due to a deep disc gap opened by the planet. A similar result has been obtained by Zhu et al. (2015), where they highlight the fact that more massive planet excite spiral waves with larger pitch angle. They also discuss the vertical motion within the arms, obtaining that while it is negligible in the outer disc, it is not in the inner arms. This results in an increased density perturbation at the disc atmosphere. In a more recent study Bae & Zhu (2018b) have found that the separation between the primary and the secondary spiral arm do actually depends on the disc aspect ratio, and thus on the disc temperature. In particular, they obtain that in the inner disc, the arm-to-arm separation increases more steeply with the planet mass at smaller radii and with smaller $(H/R)_{\rm p}$ values.

By means of 3D global hydro simulations coupled with radiative transfer calculations, Dong et al. (2015c) studied the appearance of density waves induced by giant planets in direct imaging observations at near infrared wavelengths. From their calculations it appears that a 6 $M_{\rm Jup}$ around a 1 $M_{\odot}$ star can produce prominent and detectable spiral arms both interior and exterior to its orbit. In particular, studying the spiral morphology they obtain that the inner arms have a $m = 2$ mode, with pitch angle $i \sim 10 - 15^{\circ}$, and 150% surface brightness enhancement. These properties are consistent with observed spiral arms in HD 135344B (Stolker et al. 2016) and MWC 758 (Benisty et al. 2015). Finally, they also stress that different temperature models (adiabatic vs isothermal) result in density waves contrast weaker in the surface density, but stronger in scattered light images, probably due to a more pronounced vertical structure in the former caused by shock heating. Juhász et al. (2015) found that a relative change of ∼3.5 in the surface density ($\delta\Sigma/\Sigma$) is required for the spirals to be detected with current telescopes in the near-infrared for sources at the distance of typical star-forming regions (140 pc). However, this value is a factor of eight higher than what is seen in hydrodynamic simulations. They also find that a relative change of only 0.2 in pressure scale height is sufficient to create detectable signatures under the same conditions, suggesting that observed spiral arms in protoplanetary discs could be linked to changes in the vertical structure of the disc (e.g. pressure scale height perturbation) instead of surface density perturbations.

A more recent work has investigated the relation between the arm-to-disc brightness contrast and the planet mass. By performing 3D hydrodynamical and radiative transfer simulations, Dong & Fung (2017b) examined the morphology and

contrast of planet-induced arms in discs, finding a power-law relation for the global arm contrast $\delta_{\max}$ (i.e. the ratio of the maximum over azimuthally averaged surface brightness) as a function of planet mass ($M_{\rm p}$) and disc aspect ratio (H/R). In particular, they find that only massive companions with at least multi-Jupiter masses are able to excite bright arms with $\delta_{\max} \geq 2$, as seen in HD 135433B, MWC 758, and LkHα 330.

5.1.2.2 GI spirals

In Sec. 3.2 we described how spiral density waves can be excited by gravitational instabilities in a self-gravitating disc, and how their features (number of spiral arms, pitch angle) are linked to the disc mass. From an observational point of view, the detection of the spiral density waves on a self-gravitating protostellar disc can firstly provide morphological informations in terms of the pitch angle, size and number of the spiral arms. In addition, informations about the intensity of the spiral arms with respect to the inter-arm regions can be obtained by high-resolution observations. This implies that by studying the morphology of the observed spiral and comparing it with results obtained from hydrodynamical simulations, we could in principle be able to put some constraints on the disc mass.

For example, Dipierro et al. (2014) simulated the expected emission at sub-mm wavelengths and produced synthetic ALMA observations of self-gravitating circumstellar discs with different properties in size, mass and inclination. They found that such spiral structures should be detectable by ALMA over a wide range of wavelengths. They also note that even if the original density structure of the disc is characterized by a relatively large number of arms (especially for $q = M_{\rm disc}/M_\star \sim 0.1$), only two spiral arms are visible in the images, because the smaller-sized arms have been washed out by the limited resolution of the observations. Consequently, this effect of resolution should be considered when interpreting observed morphologies. Indeed, at first sight a two-armed spiral is often interpreted as the effect of the interaction between the disc and a companion star or massive planets. By considering this resolution "issue", this could be explained in the context of gravitational instability, even though the underlying disc structure is more complex than a two-armed spiral.

Another interesting aspect is to understand how the detectability of GI-driven spiral arms depends on the temporal evolution of the system. Hall et al. (2019) investigated this, finding hat structures induced by the gravitational instability are detectable when $q \gtrsim 0.25$ and the disc outer radius is < 100 au. The given explanation is that massive discs are characterised by a high accretion rate generated by gravito-turbulence, and they thus experience a significant draining of mass, reaching the detection threshold in $\sim 10^4$ years ($\sim$1% of the typical disc lifetime). They conclude that discs with spiral arms detected in ALMA dust observations, if generated by self-gravity, must either be still receiving infall from the parental cloud to maintain a high q value, or have just emerged from their natal envelope. Some recent observations of protostellar discs show some regions of high cloud contamination together with spiral structures and streams of material on larger scale (e.g., SU Aur Ginski et al. 2021, Elias 2-27 Paneque-Carreno et al.

2021).

Dust trapping and fragmentation in GI spiral If we assume that the observed spiral arms are driven by gravitational instabilities, it is important to make some considerations about how dust trapping and fragmentation could be detectable in observations.

From a numerical point of view, Rice et al. (2004); Rice et al. (2006a) and Clarke & Lodato (2009) showed that solid cores can form rapidly in the outer disc from dust trapped in the spiral structure of a non-fragmenting gravitationally unstable disc. This could be fundamental in the planetesimal formation process. Indeed, this high concentration of dust grains in some regions of the disc enhances their density and collision rate, accelerating the process of grain growth, and thus of planet formation by means of direct gravitational collapse.

Dipierro et al. (2015a) discussed the influence of gravitational instabilities in massive protostellar discs on the dynamics of dust grains, also from an observational perspective (ALMA, Hi-CIAO). Firstly, they find that the pressure inhomogeneities induced by gravitational instabilities produce a non-negligible dynamical effect on centimetre sized particles leading to significant trapping and overdensities in spiral arms. In second place, their obtained spiral structure is detectable by ALMA over a wide range of (sub-)millimetre wavelengths and by HiCIAO in near-infrared scattered light for non-face-on discs located in the ρ Ophiucus star-forming region. They also find spatial spectral index variations across the disc, suggesting that dust trapping produces a migration of large grains that can be investigated through multi-wavelenghts observations in the (sub-)millimetric (see Sec. 5.1.3). Cadman et al. (2020b) studied with a 3D semi-analytical model of self-gravitating discs, including a prescription for dust trapping. They found that a disc requirement to be able to generate spiral structure detectable with ALMA is that the dust opacity budget should be dominated by millimeter- and centimeter-sized grains. In particular, they obtain that also disc with disc-to-star mass ratios as low as 0.10 are able to excite observable spiral arms. If no grain growth has occurred in the system, or if grain growth has overcome the grain fragmentation threshold, it is more difficult to detect these substructures. Finally, they show how to infer information about dust trapping and grain growth with their model, starting from multiwavelength observations of discs and estimates of the opacity spectral index. Applying this model to the Elias 27, WaOph 6, and IM Lup systems, they obtain that gravitational instability is a plausible explanation for the observed substructure in all three discs, if sufficient grain growth has indeed occurred.

Recent observations in the millimeter of the protoplanetary disc orbiting around the massive star AFGL 4176 mm1 (see Fig. 5.8, Johnston et al. 2020) have shown spiral structures, as well as some smaller objects, where at least some of them (mm1c or mm1d) could be interacting with the disc. This hypothesis is strengthened by the detection of gas arcs connecting the main source to the other detected companions. Johnston et al. (2020) also obtain a map of the Toomre parameter $\mathcal{Q}$ across the disc, finding that the disc and spiral arms have already (creating the observed companions) or are likely to fragment in the future, possibly forming other

companions. This picture stresses the fact that both companions and gravitational instabilities play a combined role in creating the observed structure in the AFGL 4176 mm1-main disc. Another system of particular interest is MWC 297 (Vioque et al. 2018; Alonso-Albi et al. 2009; Ubeira-Gabellini et al. 2020). This system is composed by a young (< 1 Myr) massive pre-main sequence star ($M_\star = 17\,M_\odot$) and by a low-mass ($M_\star = 0.1 - 0.5\,M_\odot$) stellar companion, located at ~ 250 au from the central star. In addition, Alonso-Albi et al. (2009) observed the system at millimeter wavelengths with the Very Large Array, modeling the SED using a two-component disc, i.e. an inner ($\sim 7.5 - 43.5$ au) and an outer ($\sim 300 - 450$ au) regions connected by a wide gap. The new discovery of Ubeira-Gabellini et al. (2020) of the low-mass stellar companion described above, and its large separation from a central young high mass (Cadman et al. 2020a) star, supports the hypothesis that the bound object could have formed via gravitational instability. Following the GI origin hypothesis, a numerical counterpart of these systems has been simulated by Meyer et al. (2018, 2019), in order to investigate if circumstellar gaseous clumps and forming multiple systems could be detectable by ALMA. Both spiral arms and gaseous clumps located at a few 100 au from the protostar can be resolved by interferometric ALMA observations at mm wavelengths, under specific observational configurations.

Elias 2-27 Elias 2-27 is a young (0.8 Myr) M0 star (Andrews et al. 2009) in the ρ Ophiucus star-forming region. It hosts a protoplanetary disc that shows a large scale two-armed spiral structure (at 1.25 Huang et al. 2018b, and 1.3 mm Pérez et al. 2016). The most widely accepted hypothesis on their origin is that they derive from gravitational instabilities (Hall et al. 2018; Bae & Zhu 2018b), although also the companion-disc interaction origin cannot be excluded (Meru et al. 2017). This latter hypothesis is suggested also by the observed ring at ~ 70 au in the dust continuum emission (Huang et al. 2018c). In this second case, the massive companion could have been formed through the fragmentation of the unstable disc (see Sec. 3.2.5). On this side, Rowther & Meru (2020) performed three-dimension hydrodynamical simulations to test if planets can survive in self-gravitating protoplanetary discs. They found that both giant and low-mass planets initially migrate inwards very rapidly, but are able to slow down in the inner gravitationally stable regions of the disc without needing to open up a gap. Going back to Elias 2-27, Paneque-Carreno et al. (2021) (to which I contributed substantially) present some new observations of this system at 0.89 and 3.3 mm, showed in the first row of Fig. 5.10, together with the 1.3 mm data. The spiral substructure is detected at all three wavelengths, showing a higher contrast at longer wavelengths. Aiming to test if the gravitational instabilities scenario could have excited the observed spiral arms, Paneque-Carreno et al. (2021) perform Smoothed Particle Hydrodynamics simulations of a gravitationally unstable disc with parameters as those in Elias 2-27 (Pérez et al. 2016), varying the disc-to-star mass ratio. For $q = 0.3$, they obtain a correct spiral morphology at the three different wavelengths. A summary of the obtained results is showed in the middle and bottom rows of Fig. 5.10, where images of the modeled synthetic emission with subtraction of azimuthally averaged intensity profile are shown (middle row), together with the deprojected

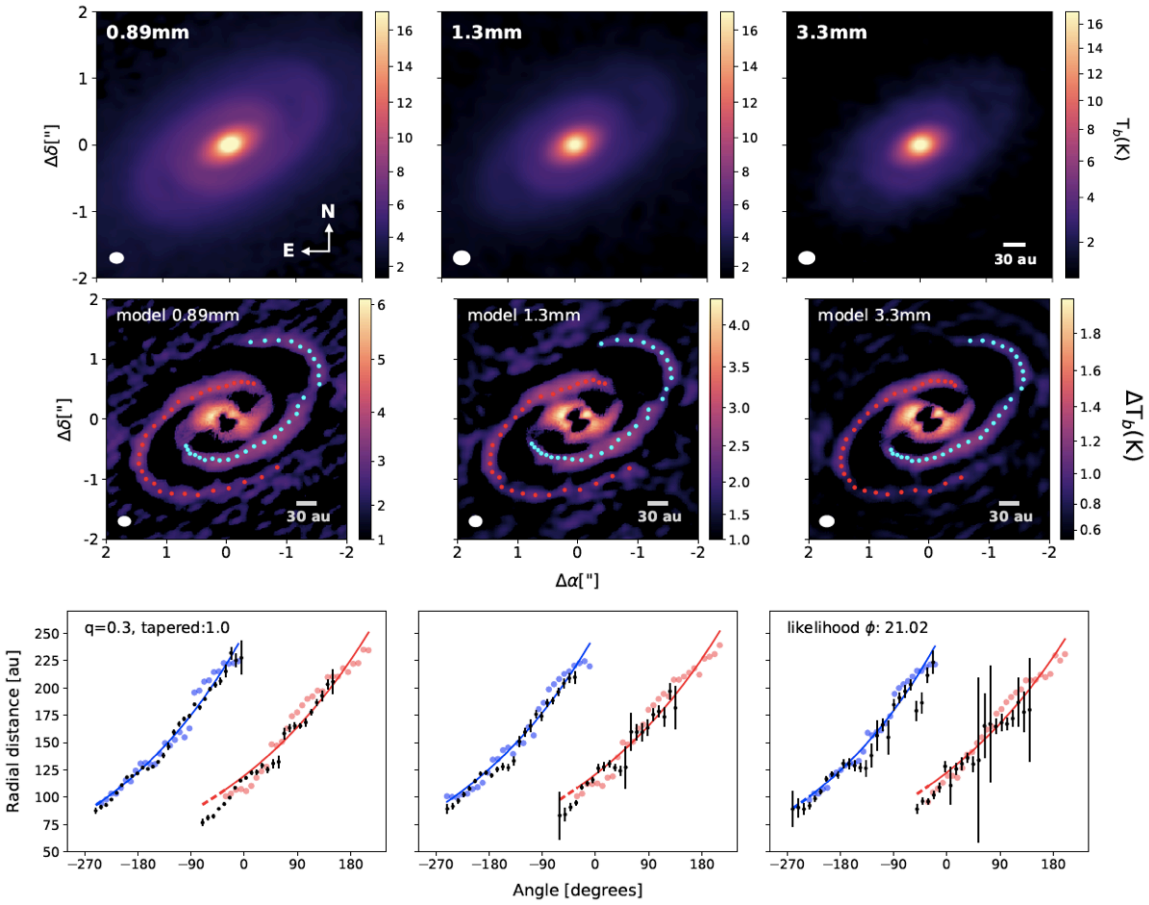

Figure 5.10: Top row: Multi-wavelength observations (0.89,1.33 and 3.3 mm) of the protoplanetary disc Elias 2-27, obtained with ALMA by Pérez et al. (2016) and Paneque-Carreno et al. (2021). In all three wavelengths the $m = 2$ spiral structure is visible. Middle row: images of synthetic emission with subtraction of azimuthally averaged intensity profile (blue and red dots trace the maxima location along the spirals). The simulated model corresponds to an exponentially tapered density profile with index $p = 1$ and disc-to-star mass ratio $q = 0.3$. Bottom row: blue and red dots correspond to the deprojected radial location of the traced spirals in the simulated emission. Colored solid lines show the constant pitch angle logarithmic spiral. Black points are the deprojected radial location of the spirals from the observations with their astrometric error.

radial location of the traced spirals in the simulated emission (red and blue dots in bottom row). The constant pitch angle logarithmic spiral is shown in solid colored lines, while black points are the deprojected radial location of the spirals from the observations (upper row). We note that the assumed disc mass in the simulation of Paneque-Carreno et al. (2021) is consistent with the estimate made by Cadman et al. (2020b) ($q \sim 0.27$), but it is not with the dynamical disc mass estimate obtained by Veronesi et al. (2021). We refer the reader to Chapter 8 for a detailed analysis and discussion about this last result. In addition, Paneque-Carreno et al. (2021) also present kinematic data for different CO-isotopologues that reveal some intriguing peculiarities, which we will describe in more detail in Section 5.2. Regarding the morphology of the detected spiral arms, Paneque-Carreno et al. (2021) show that they are well fitted by a logarithmic spiral with constant pitch angle, with $i \sim 12.9° - 13.3°$, respectively for the West and East side of the disc. A similar result, with slightly smaller value for i was obtained by Bae & Zhu (2018b) ($i \sim 7°$) starting from the data by Pérez et al. (2016), and by slightly larger i Huang et al. (2018b) with $i \sim 15.7° - 16.4°$. A possible explanation to these different values could be found in beam smearing effects, and could also be due to the different resolution of the used datasets in the three works described here. However, it is worth noting that GI-driven spiral arms have shown a constant pitch angle in numerous numerical simulations, unlike planet-driven spiral arms (Zhu et al. 2015; Bae & Zhu 2018b).

5.1.2.3 Differences between spirals generated by planets or by GI

As discussed above, multiple studies have been done in order to understand the origin of spiral structure observed in protoplanetary disc. The question arises as to whether there are any properties of the spirals that are different in the two cases.

It has been shown that since the planet-induced spirals are launched from the planet location, they have a very steep pitch angle that becomes shallower as it propagates further away from the planet. This results in spirals generated from planets having a range of pitch angles between 0° and 20°, depending on the location away from the planet (see Fig. 5.11), but not varying significantly with time (Zhu et al. 2015; Bae & Zhu 2018a). Instead, spirals excited by gravitational instabilities may vary with time, but have a generally consistent pitch angle over the range of the disc for any given time (see dashed horizontal line in the right panel of Fig. 5.11).[2] A possibility to explain the constant pitch angle, in the assumption of planet-driven spiral arms, is to assume a steeper temperature gradient. In the right panel of Fig. 5.11 there are the expected pitch angles for different temperature profile. It can be noted that the steeper the disc temperature gradient is, the more slowly the pitch angle varies in the inner disc. However, if it is the temperature gradient alone, the planet should be located at very large distance to give a constant pitch angle (grey dashed line, for the specific fit of the spiral waves in Elias 2-27, Bae & Zhu 2018b) for its inner spiral arms.

[2]Generally, planet-driven spirals are fitted with an Archimedean spiral with pitch angle varying with radius $r = r_0 + b\theta$, while GI-driven spirals are fitted with a logarithmic spiral $r = r_0 \exp(b\theta)$, with constant pitch angle over their radial extent.

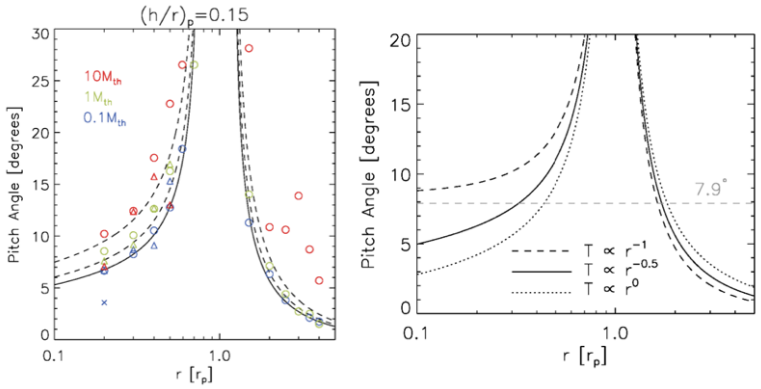

Figure 5.11: Left panel: pitch angle as a function of the radius, for the (circle) primary, (triangle) secondary, and (cross) tertiary arm, with (blue) 0.1 $M_{\rm th}$, (green) 1 $M_{\rm th}$, and (red) 10 $M_{\rm th}$ planets (where $M_{\rm th}$ is the thermal mass). The black solid lines represent the prediction from linear theory. Right panel: pitch angle of a spiral arm predicted by the linear wave theory, for three different temperature profile ($T \propto R^{-1}$, dashed; $T \propto R^{-0.5}$, solid; $T \propto R^{-0}$, dotted). The horizontal line indicates a constant pitch angle as observed in GI-driven spiral simulations and observations. The specific value corresponds to the spirals observed in Elias 2-27 (Bae & Zhu 2018b; Pérez et al. 2016). In both panel the disc aspect ratio has been assumed to be $(H/R)_{\rm p} = 0.15$. Both images are taken from Bae & Zhu (2018b)

Moreover, from simulations, it has been showed that planet-driven spiral structure can show up to $m = 3$ modes, while spiral generated by GI are characterised by $m \propto 1/q$ modes (Lodato & Rice 2004; Cossins et al. 2009a; Dong et al. 2015c), where $q = M_{\rm disc}/M_{\star}$. Thus, for low disc-to-star mass ratio we do expect to observe a large number of spiral arms (e.g., $m \sim 10$ for $q \sim 0.1$). However, Dipierro et al. (2014) show that, even if the density structure has an intrinsic $m > 2$ spiral, smaller-scale arms can be washed out by the limited resolution of the instrument, leaving only the lowest m modes in ALMA dust continuum observations. This could make the distinction between the planet-driven or GI-driven origin more difficult.

Another difference between the two morphology is that while the spiral generated by the planet-disc interaction is expected to have a pattern frequency $\Omega_{\rm p}$ that is the same of the planet velocity, i.e. a Keplerian velocity (Ogilvie & Lubow 2002), the GI-driven spiral arm is characterised by a pattern frequency defined by $\Omega_{\rm p} - \Omega(R) = \text{const}$ (Binney & Tremaine 1987; Bertin 2000). Closely linked to this property, Sturm et al. (2020) show that for a planet-driven spiral wave, the amplitude of the dust spiral decreases with Stokes number (St) and starts to fade out at a typical St > 0.1 as the dust becomes decoupled from the gas. Contrary, in the case of spirals generated by GI, where dust can be trapped (Rice et al. 2004; Rice et al. 2006a; Booth & Clarke 2016), and the consequent dust spiral amplitude increases with Stokes number.

5.1.2.4 Other physical mechanisms behind the formation of spirals

As before, other mechanisms are found to explain the observed spiral structures. In particular, if instead of an embedded planet, we consider the interaction between the disc and an inner binary (i.e. central star + companion), we can obtain multiple features, such as an inner cavity with some residual material (i.e. inner disc), streams connecting the inner disc with the outer part, spirals launching at the edge of the cavity. Three interesting systems showing these features are GG Tau (Keppler et al. 2020), HD 142527 (Avenhaus et al. 2017), and AB Aur (Boccaletti et al. 2020).

Another possible interpretation of spiral structure is that the whole protoplanetary disc has interacted with an external perturber, in a so called "fly-by". Cuello et al. (2019) and Cuello et al. (2020) explore this in a series of hydrodynamical simulations of gaseous dusty protoplanetary discs, interacting with a stellar perturber on a parabolic orbit, lying in a plane inclined with respect to the disc midplane. They find that flybys induce evolving (persisting) spiral structure in both gas and dust, and that the remnant discs are truncated and warped. Applications of this general model to observations can be found, e.g., in UX Tau (Ménard et al. 2020), AS 205 (Kurtovic et al. 2018), V1647 Ori (Principe et al. 2018), RW Aur (Rodriguez et al. 2018), HV and DO Tau (Winter et al. 2018b).

It could also happen that the outer stellar perturber is in a bound orbit, such as in the case of HD 100453 (Chen et al. 2006; Collins et al. 2009; Benisty et al. 2017; Wagner et al. 2018; van der Plas et al. 2019; Rosotti et al. 2020a). This system has been widely studied (Dong et al. 2016) and recentely it has been modeled also by Gonzalez et al. (2020). In particular they compare their SPH simulations results to the high-resolution ALMA ^{12}CO data, findind that the best agreement is obtained for an orbit with eccentricity $e = 0.32$ and semi-major axis $a = 207$ au, inclined by 61° relative to the disc plane. The large misalignment between the disc and orbit planes is compatible with the tidal evolution of a circumprimary disc in an eccentric, unequal-mass binary star. It has to be noted that this probably is not the only mechanism shaping the morphology of this system. Indeed, there are shadows observed in the scattered light image, and an inner cavity, where the presence of a misaligned inner disc has been inferred. The origin of this cavity and of the misalignment between inner and outer disc has been recently investigated by Nealon et al. (2020b), who propose a 5 $M_{\rm J}$ planet at $15 - 20$ au as responsible for the disc structure and kinematics.

A different mechanism is the one proposed for the spiral structures observed in SU Aur Ginski et al. (2021), who suggest that SU Aur is undergoing late infall of material from the cloud onto the disc. Indeed, this kind of spiral structure can be excited as a consequence of instability triggered by infalling material (Moeckel & Throop 2009; Lesur et al. 2015; Bae et al. 2015; Kuffmeier et al. 2018; Dullemond et al. 2019). If this explanation is confirmed, these new observations are of particular interest, since they would be the demonstration that late accretion events can still occur in the class II phase, significantly affecting the evolution of circumstellar discs. The spiral arms in SU Aur appear to be similar to those observed in AB Aur (Boccaletti et al. 2020), but also to those detected in HD 34700 (Monnier et al. 2019), GG Tau (Keppler et al. 2020), and HD 142527 (Avenhaus et al. 2017).

However, it is still not understood if the mechanism behind their formation is the same. Indeed, GG Tau A (Keppler et al. 2020) system is indeed a binary, that could thus be responsible for the spiral morphology (itself a member of a higher order multiple). Also in the case of HD 142527, Price et al. (2018b) obtain that all the observed features (cavity, spirals, shadows, fast radial flows, gap-crossing filaments and horseshoe) can be explained with the interaction between the disc and the observed binary companion (Biller et al. 2012; Lacour et al. 2016). We note that Poblete et al. (2020) point out that the inner spiral structure in the disc around AB Aur could also be caused by a stellar binary, and this idea is also explored by Calcino et al. (2020) in order to reproduce the spiral structures, shadows, cavity and twist in the kinematics observed in MWC 758 (Benisty et al. 2015; Boehler et al. 2018).

Finally, when discussing the origin of spiral structures as possibly related to the GI, it is interesting to note that the need for other physical mechanisms could also be suggested by the comparison between the exoplanet population detected with SPHERE and the planetary population synthesis models obtained by combining core accretion and gravitational instability (Vigan et al. 2020). More specifically, these models work for FGK stars, but not for AB and M stars.

5.1.3 The importance of multiwavelength observations

When observations at different wavelengths are obtained for the same system, we can infer interesting information, e.g. regarding dust trapping, or the intensity of the dust-gas coupling (Stokes number). The latter, given the dependence of the Stokes number on the surface density of the gas disc (see Eq. 2.54), can in principle also give us some local (or global, depending on the observed substructures) constraints on the disc mass. Indeed, if the same substructure is detected at different wavelengths (e.g., millimeter continuum emission and scattered light), this could mean that the dust and the gas are strongly coupled (St$\ll 1$) indicating a high disc surface density. In Chapter 6, I apply this idea by varying the Stokes number in a disc with two embedded planets. When looking at the system in scattered light, I obtain spiral arms (as expected from the disc-planet interaction theory, see Sec. 4.1.2). Instead, when observing the disc with ALMA, I find that for low Stokes number it could be possible to detect spirals due to a strong coupling with the small grains, while with increasing the Stokes number the structures become more symmetric (see Chapter 6).

In Fig. 5.4 I show the protoplanetary disc HD 169142, which has been observed at three different wavelengths, in scattered light (μm) with SPHERE (Pohl et al. 2017), with ALMA at 1.3 mm (Pérez et al. 2019) and with VLA at 7 mm (Macías et al. 2017). Also other bands in the millimeter continuum can be found in the literature (e.g., 1.3 mm with different resolution in Fedele et al. 2017, 3.1 and 0.89 mm in Macías et al. 2019). This disc shows rings at all wavelengths. Being HD 169142 quite an old disc, this is consistent with the idea that the St is high enough that both mm and μm-sized grains are strongly coupled to the gas, displaying similar structures. Carney et al. (2018) also detected CO data, showing a ring structure. It would be interesting to observe this system at a higher resolution, to check if there could be some hints of a tightly wound spiral structure. However,

if the observed gaps have been carved by planets and if the planet is massive enough, we do expect (at a first approximation) to see gaps also in the gas. A similar case is the one of TW Hydrae, for which the 1.6 μm (SPHERE) and the 870 μm (ALMA) observations are shown in Fig. 5.2. This is a more peculiar source, since Teague et al. (2019b) detected spiral structures in the velocity and temperature structure of CO J = 3 - 2 (Huang et al. 2018a). Mentiplay et al. (2019) model this system with embedded super-Earths, reproducing correctly the dust gaps observed at 24 au and 41 au by ALMA. Their model also produces a prominent spiral arm in the scattered light image, while there are only hints of this structure in the data (van Boekel et al. 2017). However, Bae et al. (2021), based on the morphology and magnitude of the perturbation, propose that the tightly wound spirals observed in the CO temperature structure of TW Hya could be driven by a (sub-)Jovian-mass planet at 90 au. They also specify that the spiral seems to be originated by the planet through buoyancy resonances, whose excitation depends on the thermal relaxation timescale of the gas. An intriguing source is also the protoplanetary disc HD 135344 B (also known as SAO 206462), that shows a two-spiral arms structure in the micrometric dust (see Fig. 5.7) and an inner ring with an outer asymmetric overdense region in the ALMA continuum (see Fig. 5.4, Cazzoletti et al. 2018), which appears to be the continuation of the southern spiral arm. Different models have been proposed in order to reproduce the observed substructures, such as an embedded massive planet (Dong et al. 2015b; Veronesi et al. 2019), or an inner planet to reproduce the inner cavity observed by ALMA and a vortex as responsible for the observed spiral structure (van der Marel et al. 2016b). We remark a similarity between HD 135344B and MWC 758. Indeed, this system is characterised by two spiral arms in scattered light (see Fig. 5.7, Benisty et al. 2015) and by an inner ring with two overdense clumps in the ALMA continuum (Dong et al. 2018a), which appear to be co-located with the spiral arms. Another source showing different substructures at mm and μm wavelengths is IM Lup (Huang et al. 2018b; Avenhaus et al. 2018). While an $m = 2$ spiral arm has been detected in the ALMA continuum, the scattered light image shows a series of narrow rings and gaps. However, Avenhaus et al. (2018) cautiously affirm that these substructures are hard to classify as either rings or a tightly wound spiral.

Another interesting aspect of observing the same system at multiple wavelengths it that it allows us to analyse the dust distribution within the disc and test if dust trapping is happening at the substructures location. Indeed, a variation in the spectral index α provides information about the grain size in discs (Testi et al. 2014). Obtaining a $\alpha \approx 2$ can be a sign of dust trapping, while generally a value of $3.5 - 4$ is expected (as in the ISM, Draine 2006; Ricci et al. 2010). An application of this analysis can be found in Paneque-Carreno et al. (2021). Indeed, having obtained data at three different wavelengths for Elias 2-27, they also test if grain growth and dust trapping are happening at the spiral arm location. They obtain that the spectral index values from 1.3 mm and 3.3 mm indicate the presence of large grains in the outer disc, while the 0.89 mm emission appears to have a very low flux. This can be explained if the interested regions have high optical depth and high albedo in the presence of dust scattering. This results in a lower limit

estimate for the disc mass. Long et al. (2020) compared two wavelengths for three discs of their survey (Long et al. 2018b, 2019), DS Tau (see also Veronesi et al. 2020), GO Tau and DL Tau. The marginally resolved ring in DS Tau shows a possibly narrower ring at the longer wavelength, an observational feature expected from efficient dust trapping. The spectral index α has an increasing trend outward and exhibits local minima that correspond to the peaks of dust rings, with low optical depth, indicative of actual changes in grain properties (i.e. dust growth) across the discs.

To conclude, we are still far from a deep comprehension of the mechanisms that are at the origin of these substructures, and the fact that different morphologies are present simultaneously in a same disc, both at different wavelengths but also in the same tracer, can be the signpost of multiple mechanisms operating simultaneously, with different processes manifesting more clearly in tracers of the gas or the solids.

5.2 Kinematic structures: planets or GI footprints

In the previous section we gave a fairly in-depth narration from a morphological point of view, of two particular types of substructures observed in discs, rings/gaps and spirals. We presented a collection of discs showing one of these structures, or even both, at different wavelengths (mm dust continuum, with ALMA; scattered light with VLT-SPHERE or other adaptive optic instruments; CO-isotopologues, with ALMA), or all in one. We have depicted the physical mechanisms behind the formation of these structures, and in particular the most important in the context of this Thesis, tidal disc-planet interaction and gravitational instabilities. We can therefore summarise that generally, these substructures are either an evidence of unseen companions (stellar or planetary) hiding within the disc and leaving as footprint spirals or gaps/rings, or they can be an indicator of a disc massive enough to develop gravitational instabilities in the shape of spiral arms. The latter case can be also associated to system where infall from the parental cloud is still happening at larger scale. However, the information that can be extracted from these substructures and that we have described in the previous section is a fraction of the mine of data they harbour. It is only in the last two or three years that, also thanks to the high resolution that can now be achieved in ALMA observations, we have been digging deeper into this mine, looking in particular for kinematical features linked to the observed substructures. In this section, we will introduce some of the surprising new discoveries in this field that will allow us to increase our understanding of the physical mechanisms that shape the evolution of these systems, thus also determining the characteristics of the observed population of exoplanets. We will focus in particular on the so called "kinks" (Pinte et al. 2019), or more in general on deviation from the Keplerian velocity localised both in space and velocity, and on deviation from Keplerian rotation on a larger scale (e.g., "wiggles", Hall et al. 2020). We will also anticipate that disc kinematics can be used to derive an estimate of the mass of the disc (see Chapter 8), independent of the issues related to the chemistry of CO-isotopologues (described in Sec. 1.2.1) or of the dust measurements.

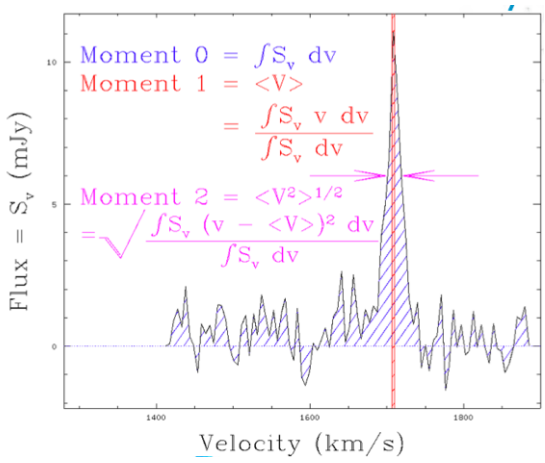

Figure 5.12: Graphic representation of moment 0, moment 1 and moment 2, obtained from Eqs. 5.1, 5.2, 5.3.

5.2.1 A small compendium about moment maps

We give here a brief description of the kinematical data we are going to present and discuss. These data are obtained as a spectral line 3D data cube (with the three dimensions given by RA, Dec, Velocity or Frequency), from which multiple information can be extracted, such as moment 0, moment 1 and moment 2 maps and channel velocity maps. In other words, we can think to a data cube as a series of multiple channels, each showing the emission integrated over a narrow frequency or velocity range. It is possible to collapse the cube into a moment image by taking a linear combination of the individual planes. In particular, by taking a 1-D slice along the velocity axis, one can obtain a line profile that may show changes in line shape, width and depth as a function of the position. Channel maps are instead 2-D slices along the velocity axis showing how the spatial distribution of the line emission changes with frequency/velocity (i.e. dynamical information). Then, by integrating along the velocity axis, moment maps can be obtained. Different moments are especially useful, such as

- the total intensity (Moment 0), giving information about the integrated flux,

$$\text{Moment } 0 = \int S_v dv\,; \tag{5.1}$$

- the intensity-weighted velocity (Moment 1), giving information about the mean velocity in the system,

$$\text{Moment } 1 = \langle V \rangle = \frac{\int S_v v dv}{\int S_v dv}\,; \tag{5.2}$$

- the intensity-weighted velocity dispersion (Moment 2), giving information about velocity dispersion,

$$\text{Moment } 2 = \left\langle V^2 \right\rangle^{1/2} = \sqrt{\frac{\int S_v (v - \langle V \rangle)^2 dv}{\int S_v dv}}\,, \tag{5.3}$$

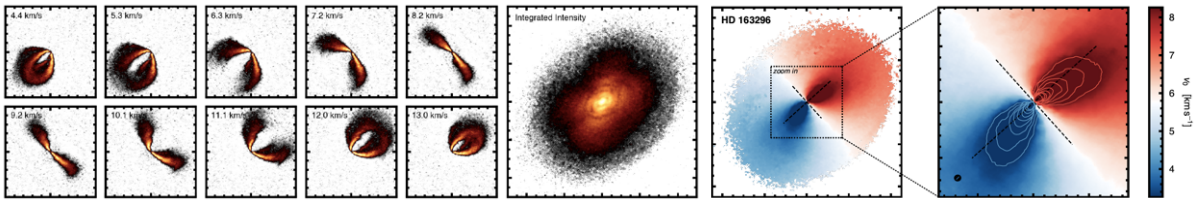

Figure 5.13: First five columns: example of channels of ^{12}CO emission in the disc around HD 163296, with an integrated intensity map (zeroth moment) in the center (Andrews et al., 2018; Isella et al., 2019). To the right, moment 1 maps with a zoom-in of the center with line contours indicating the high velocity lobes which bend away from the disc major axis, plotted with dashed lines, due to the elevated emission surface (a "flat" disc would be perfectly symmetric about the major axis of the disc). This effect is amplified by the inclination of the disc. Images taken from Disk Dynamics Collaboration et al. (2020).

where S_ν is the observed flux. See Fig. 5.12 for a graphic representation. In Fig. 5.13 we show an example of different velocity channels of ^{12}CO emission in the disc around HD 163296, the integrated intensity map (zeroth moment) in the center and moment 1 maps to the right (images taken from Disk Dynamics Collaboration et al. 2020). It is interesting to note that in the assumption of Keplerian motion within the disc, the emission is observed in a characteristic "butterfly" pattern, coming from the projected rotation of the disc,

$$v_0(r, \phi) = v_\phi(r) \sin(i) \cos(\phi) + v_{\rm LSR}\,, \tag{5.4}$$

where i is the inclination of the disc, $i = 0°$ being face-on and $i = 90°$ edge-on, r the disc radius, being the azimuthal angle measured from the red-shifted major axis of the disc, and $v_{\rm LSR}$ being the systemic velocity of the star. If the projected velocities are not purely Keplerian, but there are also radial and vertical components, Eq. 5.4 can be modified to include them in a superposition of the three components ($v_{\rm rad} = v_r \sin(i) \sin(\phi)$; $v_{\rm vert} = v_z \cos(i)$). This is possible (under the assumption of an azimuthally symmetric velocity distribution) since the three components have a different dependence on the azimuthal angle (Teague et al. 2019b).

5.2.1.1 Retrieving the disc geometry and rotation curve

Studying the gas kinematics through these maps (channel maps and moment 1 map) is crucial since they allow us to to measure basic geometrical properties of the disc, such as the disc center, inclination, position angle, and, with some assumptions, also the dynamical mass of the central star. With higher resolution observations it is also possible to resolve the 3D structure of the disc for the more inclined sources. Indeed, this is observable as a bending of the dipole lobes away from the semi-major axis (see rightmost panel in Fig. 5.13).

Different methods have been proposed to infer the disc geometry and a radial velocity profile from the observed channel maps (Teague et al. 2018; Pinte et al.

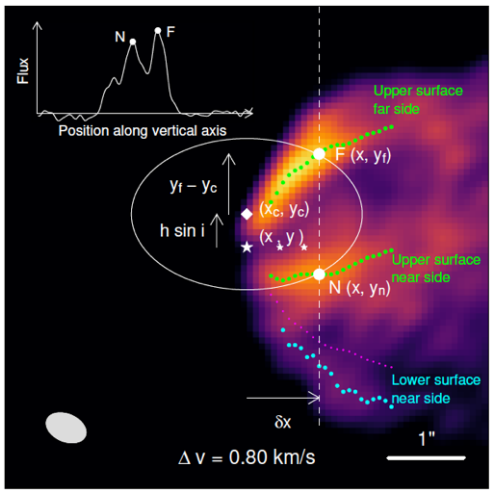

Figure 5.14: Schematic representation of the geometrical method developed by Pinte et al. (2018a) to measure the disc height and velocity. The semi-major axis of the disc has been placed on the horizontal axis. The dashed and dotted green and cyan line represent the upper far and near side and the lower near side, respectively. N and F indicates two maxima on the near and far sides of the disc upper surface, chosen for a given offset δx along the disc major axis. They belong to the same inclined circular orbit (white ellipse), whose centre is marked by a diamond.

2018a; Casassus & Pérez 2019). Here, we will focus mainly on the method developed by Pinte et al. (2018a) to infer the height of the CO emission layer, and then the velocity profile. In principle, for a given channel maps, the line emission is concentrated along the isovelocity curve, defined as the set of points where the projected velocity of the emitting surface is constant. Thus, one can consider that the emission originating from the upper and lower surfaces (i.e. above and below the midplane as seen from the observer), and from the near and far sides of these surfaces, is well separated. By locating the emission in each channel map, it is possible to directly reconstruct, via simple geometrical arguments, the position and velocity of each of the CO layers.

The method is schematically illustrated in Fig. 5.14. After having placed the x-axis of the disc coordinate system aligned with the disc major axis, the star position $(x_\star, y_\star)$ is determined from the peak of the continuum map. The gas is assumed to have a Keplerian rotation at any point in the disc, thanks to the fact that it is vertically pressure supported (gas particles rotate with circular orbit parallel to disc midplane, radial or vertical motion are neglected). The radius and height of the considered gas orbit are r and h. At this point, it is chosen an offset $\delta x = x - x_\star$ along the semi-major axis, and at this location, two points on the same orbits are obtained from the intersection of a vertical line and the isovelocity curve of the upper disc surface (near and far side). It has to be noted that, thanks to the previous assumptions, the two points happens to be at the same distance from the star and at the same altitude.[3] However, the emission is not punctual, but it forms a narrow band around the isovelocity curve, because of line broadening and of finite spatial and spectral resolution. Therefore, the

[3]Within this assumption the emitting layer is assumed to have a cone-like structure, this means that the height of the emitting layer should be symmetric with respect to the disc major axis. If this assumption is not met, the height obtained with this method should be treated with care.

estimate of the position of the emission layer is done by choosing its maximum, and denoting with y_n and y_f the ordinates of the two points on the near and far side. The coordinates of the centre of the projected circular orbit passing through these two point are $(x_\mathrm{c}, y_\mathrm{c})$, with $x_\mathrm{c} = x_\star$ and $y_\mathrm{c} = (y_\mathrm{f} + y_\mathrm{n})/2$. Every point on this ellipse satisfies $(x - x_\star)^2 + ((y - y_\mathrm{c})/\cos i)^2 = r^2$, where the orbital radius r is the length of the semi-major axis of the ellipse and i the disc inclination. Considering the point on the far side of the disc surface, we can for example derive the orbital radius as,

$$r = \sqrt{(x - x_\star)^2 + \left(\frac{y_\mathrm{f} - y_\mathrm{c}}{\cos i}\right)^2}\,. \tag{5.5}$$

The height of the orbit h can be derived by noting that the offset between the centre of the orbit and the star is $h \sin i$:

$$h = \frac{y_\mathrm{c} - y_\star}{\sin i} \tag{5.6}$$

By repeating the procedure for each x (green points) and each velocity channel, a full mapping of the CO upper surface can be obtained.

Having obtained the correct geometry for the system, and knowing the projected radial velocity (Eq. 5.4), with $\cos(\phi) = (x - x_\star)/2$, we can also derive the gas rotation around the central star at each point as,

$$v = (v_\mathrm{obs} - v_\mathrm{syst})\,\frac{r}{(x - x_\star)\sin i}\,. \tag{5.7}$$

Then, to understand the retrieved gas kinematics, one could subtract a Keplerian model, or a model keeping into account the pressure correction and the disc self-gravity (Rosenfeld et al. 2013).

5.2.2 Kinematic planetary signatures: kinks and doppler flips

So far, only few planets have been observed by direct imaging (Keppler et al. 2018; Wagner et al. 2019), mainly because of their faint emission (Brittain et al. 2020). Moreover, in discs where possible planets are still shrouded in gas, this and other methods used so far in exoplanet detection are even more ineffective. For this reason, and also for a disc extinction issue (see e.g. Sanchis et al. 2020), alternative methods must be pursued, one of which is based on the kinematics of the gas in which the planet itself is embedded. In the previous section we mentioned that in absence of perturbations to the star gravitational potential, one would expect to observe the canonical "butterfly" pattern produced by Keplerian motion, with modulation induced by radial pressure gradient (i.e. the gas velocity is slightly sub-Keplerian). The novelty comes from the fact that recently deviations from the Keplerian velocity, localised both in space and velocity, have been observed in some discs molecular line emission, and these deviations often coincide with substructures observed in the millimetre. Hence the idea that the origin of both may be common, and may be found in perturbations induced by the interaction of a planet with the surrounding disc material, specifically by the wake generated by the tidal interaction. A visual representation is given in Fig. 5.15, where it is

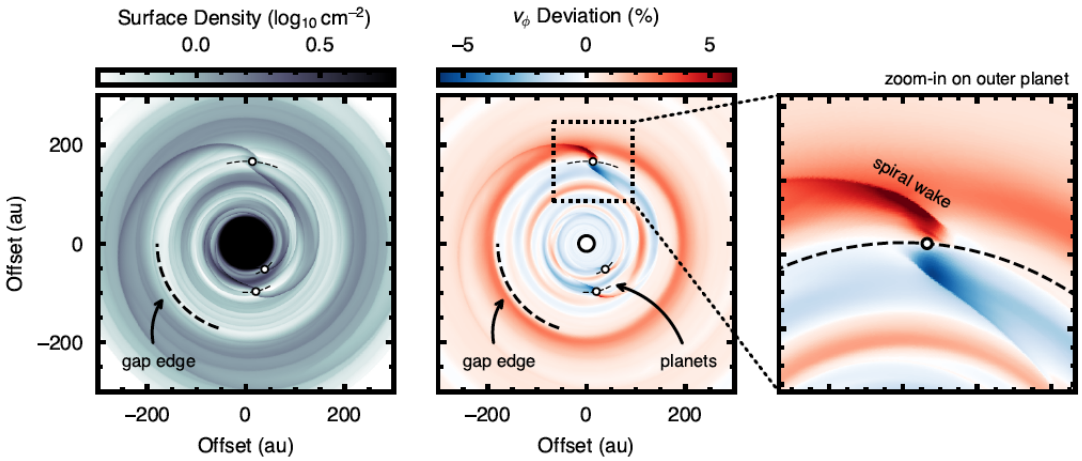

Figure 5.15: 3D hydrodynamical simulation of a disc with three gap-carving planets, illustrating how a planet would influence the gas density structure (left panel) and the velocity structure, showed in terms of velocity perturbations with respect to the background rotation velocity in the central and right panels. Image taken from Disk Dynamics Collaboration et al. (2020).

shown the expected deviations both in density and velocity for hydrodynamical simulation of a disc with three embedded planets. One of the possible outcome of the planet-disc interaction, as described in Sec. 4.1.2 and 4.3, is a gap, visible in the surface density profile, and the excitation of spiral wakes. At the location of the gap edge a deviation from the background velocity is visible, produced by the sharp radial gradients in the gas pressure. However, a stronger deviation is visible at the location of the planet, and specifically along the spiral wakes. It should be noted that in addition to changes in the azimuthal velocity v_ϕ, the spiral waves will induce significant radial and vertical velocities, as the gas is driven away from the embedded planet (Pinte et al. 2019). These can reach deviations of up to 10% (Pérez et al. 2018a; Pinte et al. 2018b; Teague et al. 2018; Zhang et al. 2018).

In the central and right panels of Fig. 5.16 we show a velocity channel map ($v = 1$ km/s) and its opposite ($v = -1$ km/s) of the HD 163296 disc (Pinte et al. 2018b), where a zoom-in has been done on the velocity perturbation. The white dashed line indicates the expected iso-velocity contour for an unperturbed Keplerian disc, while the white dotted line show the detected iso-velocity contour (tracing the emission peak) as it deviates from the Keplerian one. It can be noted that this deviation is not visible in the channel with the opposite velocity. Indeed, it is important to stress that this kinematical feature is seen locally both in space and velocity. This feature, named "kink" has been found for the first time by Pinte et al. (2018b) in the HD 163296 disc, at a distance of $\sim$ 260 au, outside from gaps detected in the millimeter emission.

As further confirmation of a connection between substructures and embedded protoplanets, Teague et al. (2018) by using a slightly different method to retrieve the gas rotation curve, obtained two other detections of velocity perturbation in

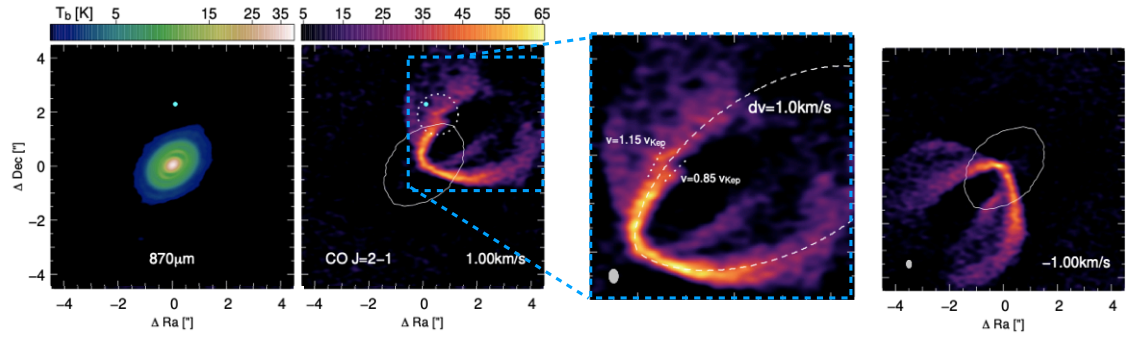

Figure 5.16: Left panel: ALMA dust continuum emission of the protoplanetary disc HD 163296. Central and right panels: channel map of ^{12}CO line emission at +1 and -1 km s^{-1} from the systemic velocity (central and rightmost), with a zoom-in on the channel map (+1 km s^{-1}) showing the velocity perturbation (i.e. "kink"). The solid white line indicates the 5σ level of the continuum dust emission. The white dashed line indicates the expected iso-velocity contour for an unperturbed Keplerian disc in the selected channel, while the white dotted line show the detected iso-velocity contour (tracing the emission peak) as it deviates from the Keplerian one. The potential planet location is marked by a cyan dot, assuming it is located in the midplane.

the same system. Their result is shown in the right panel of Fig. 5.17, together with a schematic illustration showing the connection of a local gas pressure minimum (top, corresponding to a gap) and the induced velocity perturbations on the rotation curve (bottom). Specifically, the obtained rotation curves exhibits evidence of substantial deviations from Keplerian rotation caused by local perturbations in the radial pressure gradient, probably induced by gaps carved in the gas surface density by Jupiter-mass planets. By performing hydrodynamical simulations of the system, they obtain good agreement with the gas rotation profile when the disc is perturbed by two Jupiter mass planets at 83 au and 137 au.

Another hint of a planetary origin behind the observed velocity perturbation has been given by Teague et al. (2019a). They derive the radial profiles of the three velocity components of gas in the upper disc layer of HD 163296, traced by ^{12}CO molecular emission, showing significant flows from the disc surface towards the disc midplane. The location of these flows coincide with the radial location of the gaps detected from ALMA, and possibly carved by embedded planets (see left panel of Fig. 5.18.). Teague et al. (2019a) also stress that the detected flows resemble meridional flows, which are a feature predicted to be linked at early stages of planet formation (Szulágyi et al. 2014; Morbidelli et al. 2014; Fung & Chiang 2016; Dong et al. 2019), illustrated in the left panel of Fig. 5.18.

After this first detection, other deviations from the Keplerian velocity have been observed or hypothesised in other protoplanetary disc (Teague et al. 2018, 2019a; Pinte et al. 2019; Casassus & Pérez 2019; Pinte et al. 2020). Importantly, a perturbation in velocity is often found at the same location of gaps or structures (at millimeter wavelenght) potentially related to the interaction of the disc with the planet. Numerical studies and observations have investigated the possibility to

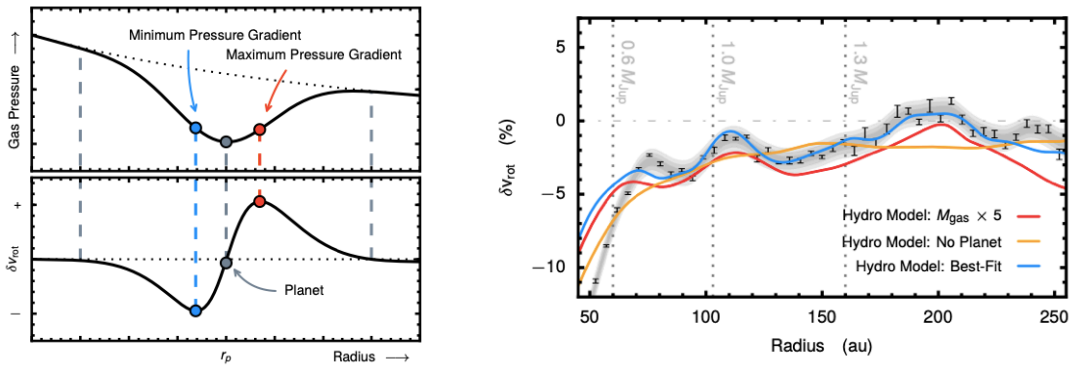

Figure 5.17: Left panel: schematic illustration showing the connection between a local gas pressure minimum (top) and the induced velocity perturbations on the rotation curve (bottom). Right panel: $\delta v_{\rm rot} = (v_{\rm rot} - v_{\rm kep})/v_{\rm kep}$ (deviation from Keplerian rotation) as a function of the radial distance from the star, where a comparison between simulations (three colored lines) and observations is shown. Images taken from Teague et al. (2018).

observe such perturbations, both from a chemical and kinematical point of view (Ayliffe & Bate 2009; Cleeves et al. 2015; Ober et al. 2015; Pérez et al. 2018a; Rabago & Zhu 2021), wondering if they could also be linked to the presence of circumplanetary disc (Perez et al. 2015b). In Fig. 5.19 we collect some of these detections. The first row shows the kink detection by Pinte et al. (2019) in the protoplanetary disc HD 97048. Unlike the previous one, which was positioned outside the observed continuous emission, this one is inside one of the gaps, further confirming the hypothesis that its origin is linked to the presence of a planet. While the velocity perturbation is seen in the channel velocity map at $\Delta v = 0.96$ km/s, it is not in the opposite channel. In the cartoon it is showed a schematic picture of the system, with its characteristic cone structure with a lower and upper CO surface. Pinte et al. (2019) also performe a series of hydrodynamical and radiative transfer simulations varying the planet mass and the Stokes number (to keep into account that with different coupling also the gap shape could change), and they reproduce the observed gap and kink detection with a planet of $2 - 3\,M_{\rm J}$. The second and third rows collect results obtained for the protoplanetary disc HD 100546 by Casassus & Pérez (2019) and Pérez et al. (2020). Their 1.3 mm observation reveals a complex ring structure, where there are hints of an inner spiral arm. Instead, the ^{12}CO channel maps are characterised by wiggles or kinks that deviate from Keplerian velocity particularly over the continuum ring. They associate the most prominent wiggle to the footprint of a massive planet of at least 5 $M_{\rm J}$, predicted from previous hydrodynamical simulation (Pérez et al. 2018a). However, Pérez et al. (2020) stress the fact that this kinematic feature does not lie within a gap (carved as expected from the disc-planet interaction), but it is located near a ridge within the ring. Casassus & Pérez (2019) show that generally, if a perturber is present and is interacting with the surrounding gas, the non-Keplerian velocity along the planetary wakes should undergo an abrupt sign

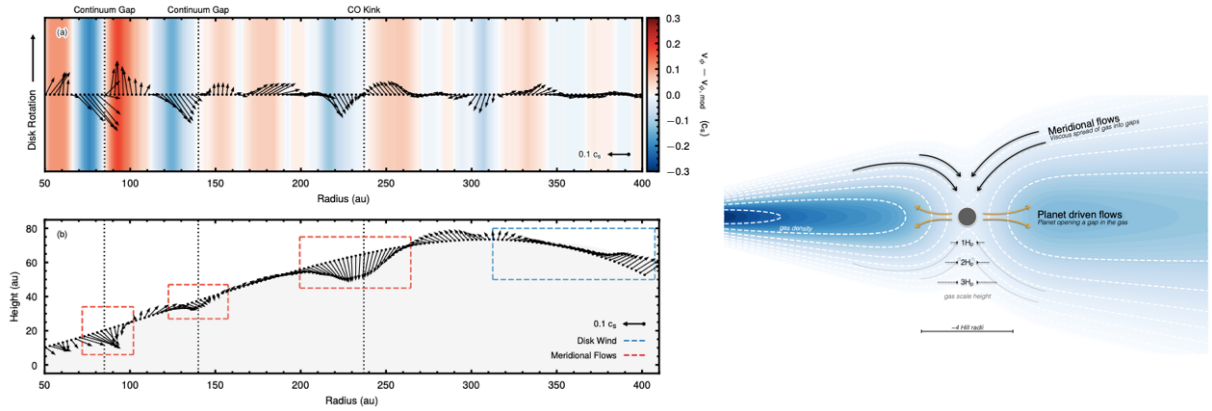

Figure 5.18: Left panel: 3D velocity and height structure in the (R, ϕ) and (R, z) plane, respectively. In the upper panel, vectors in the positive and negative y direction indicate faster or slower-rotating material, while the x direction shows the radial flows. The colour shows the magnitude of the rotation vector. In the lower panel, the three locations of meridional flows are highlighted with red boxes, while the blue one corresponds to a possible wind outflow. The dotted vertical lines mark the location of the gaps detected in the dust continuum emission, and the location of the velocity perturbation traced in CO emission (kink by Pinte et al. 2018b). Right panel: schematic cartoon explaining the meridional flows mechanism observed at the gap location, and associate with early stages of planet formation. Images taken from Teague et al. (2019a).

reversal across the protoplanet (positive residual following the outer trailing arm, negative residual tracing the inner leading spiral arm), and after the subtraction of the disc rotation curve, the location of the planet should be identifiable as a Doppler-flip in velocity centroid maps.[4] Indeed, they detect a Doppler-flip in HD 100546, which is coincident with the previously discovered wiggle. To explain the origin of these perturbations and their peculiar location, not inside a gap, but within a ring showing an intricate morphology, they suggest a complex dynamical scenario, maybe including pebble accretion onto the protoplanet.

It is worth noting that having gas kinematics data allow us to perform numerical studies varying the crucial properties of the system (e.g., planet and disc mass, Stokes number) in order to reproduce the observations. From this comparison, we could be able to put more constraints on the planet mass (Pinte et al. 2019). In Chapter 7 I present a modeling, where I vary the planet and the disc mass, performed for the disc around the DS Tau star, showing a gap of $\sim$ 30 au. I also make a prediction for the hypothetical planet mass that would be detectable as a kink in the channel velocity maps (Veronesi et al. 2020). On an analytical perspective the kink feature has been recently studied by Bollati et al. (2021).

[4] A velocity centroid map is defined by $v_\circ(\vec{x}) = \langle vI \rangle = \int dv v I_v / \int I_v dv$, where $I_v(x)$ are the molecular line channel maps as a function of line-of-sight velocity v.

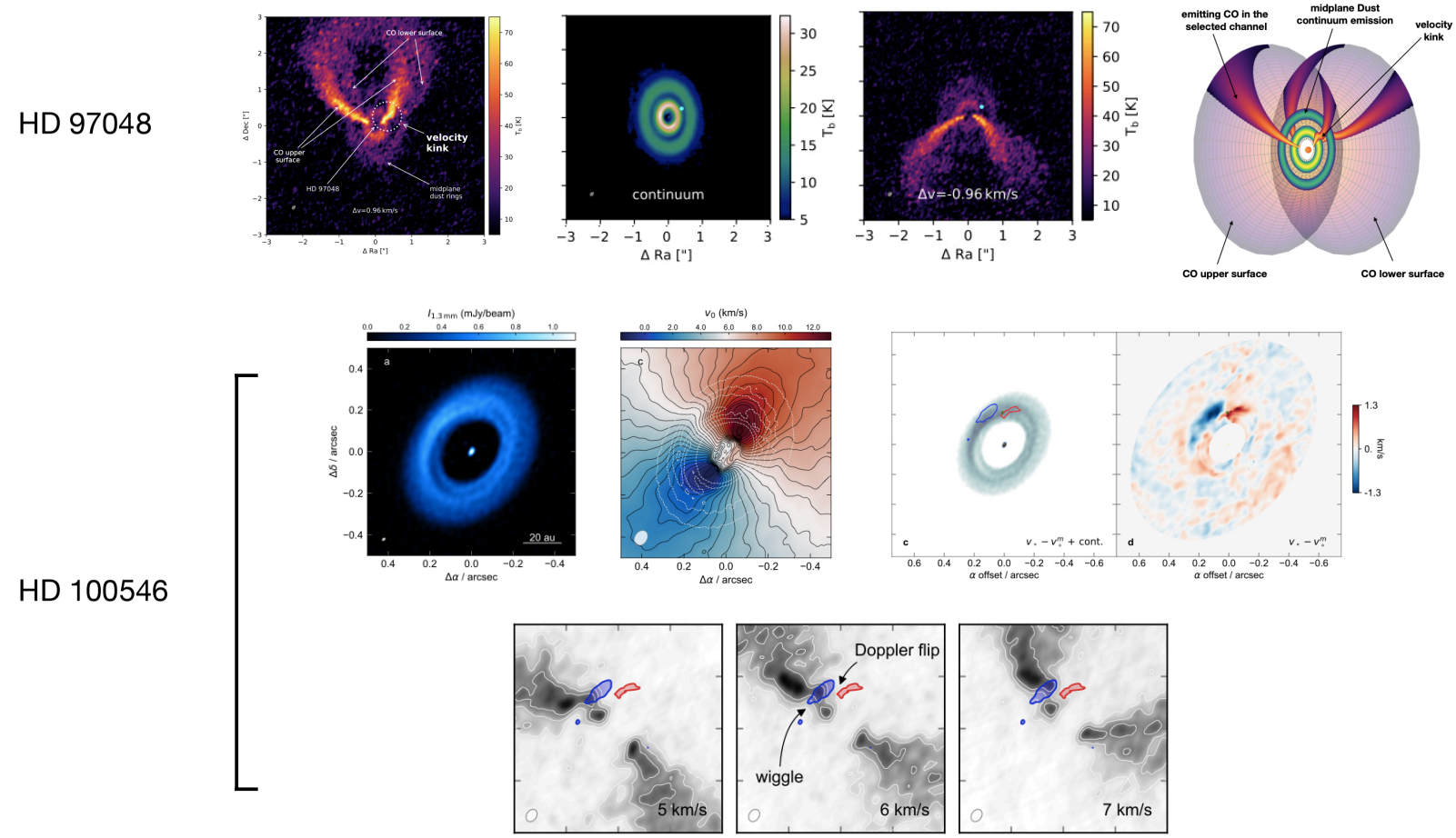

Figure 5.19: Collections of recent detections in CO molecular emission line of deviation from the Keplerian rotation. *First row*: detection of a kink colocated with a gap in the dust continuum emission, in the HD 97048 protoplanetary disc (Pinte et al. 2019). From left to right: superposition of the continuum and the channel velocity map corresponding to the detected perturbation in the isovelocity contour ($\Delta v = 0.96$ km/s). ALMA image of the same system at 885 μm. Channel velocity opposite to the one where the kink is detected ($\Delta v = -0.96$ km/s). Schematic cartoon showing the continuum, the disc cone structure (the CO upper and lower surface), and the velocity kink. Images taken from (Pinte et al. 2019). *Second row*, from left to right: ALMA continuum image of the protoplanetary disc HD 100546 and moment 1 map, where velocity perturbations at the location of the annuli are detected (Pérez et al. 2020). Continuum where the Doppler flip has been marked, and deviation from Keplerian motion map, where is visible the Doppler flip (Casassus & Pérez 2019). *Third row*: channel velocity maps where it is shown the location of the previously detected Doppler flip (Pérez et al. 2020).

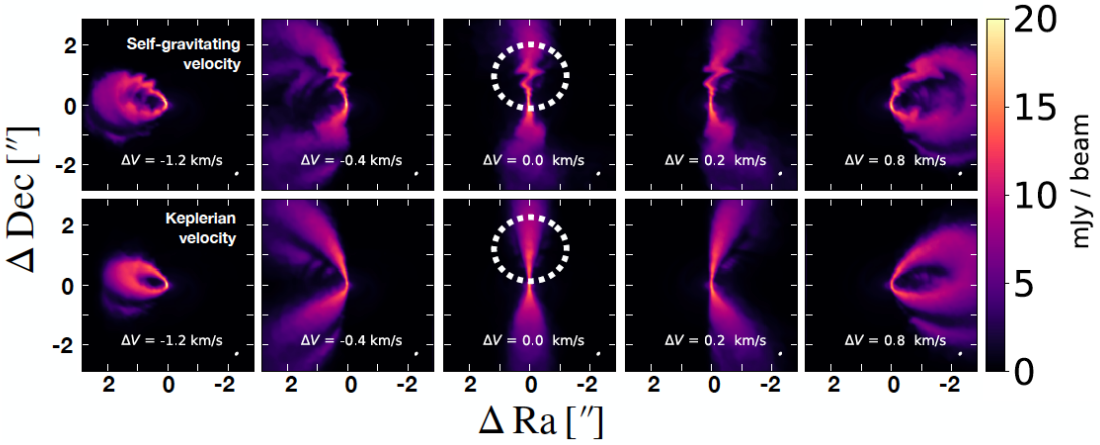

Figure 5.20: Simulated (hydro + radiative transfer postprocess) molecular line emission (^{13}CO $J = 3 \rightarrow 2$ transition) in a disc that has developed gravitational instabilities. The upper row shows the self-gravitating velocity structure, while the bottom row corresponds to a purely Keplerian model. The GI wiggle is circled in the top central velocity channel, but it is visible at all deviations from the systemic velocity. Instead, it does not appear in the Keplerian model. Image taken from Hall et al. (2020).

5.2.3 "GI Wiggles"

Hall et al. (2020) investigate the dynamical effect of GI on the gas disc, traceable with molecular line emission, aiming to introduce new diagnostic tools to identify GI unstable discs with gas observations. They perform hydrodynamical and radiative transfer simulations of a protoplanetary disc with both dust and gas, with a disc-to-star mass ratio of 0.5. Fig. 5.20 (upper row) shows the obtained velocity channel maps, when assuming a distance from the observer of 140 pc and an inclination of 30°, a turbulent velocity of 0.05 km/s, a spectral resolution of 0.03 km/s, and a beam of size $0.11'' - 0.07''$ with a position angle of $-38°$, matching recent ALMA observation that were able to detect a planet-induced kink (Pinte et al. 2019). The bottom row of Fig. 5.20 shows a purely Keplerian model. While in the self-gravitating disc the wiggle is well visible, it is not in the Keplerian model. We note that while for the planet-induced kink the velocity perturbation was localised both in space and velocity, in this case the wiggle appears to be visible in all the velocity channels and on a large disc radial and azimuthal extent. In Fig. 5.21 a comparison is shown between the observed velocity relative to the Keplerian rotation $v_{\rm obs} - v_{\rm obs}^{\rm kep}$, the surface density map and the central velocity channel map. In all the three panels it is also marked the line where $v_{\rm obs} - v_{\rm obs}^{\rm kep} = 0$. The first panel shows interlocking, "finger-like" structure between $[0'', 0'']$ and $[0'', 1.5'']$. These finger-like structure is pushing extra emission into adjacent channels at a given velocity, causing the GI wiggle (right panel). In the central panel it can be seen from where the perturbation comes: faster emission relative to Keplerian is colocated with the density peak of spiral arm, while slower emission is linked to the inter-arm region. This interlocking, "finger-like"

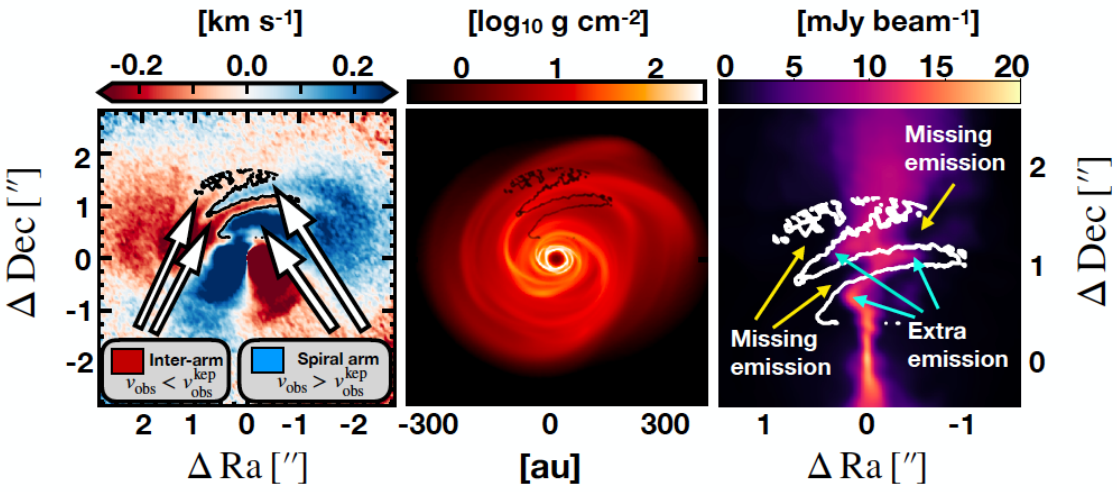

Figure 5.21: In the three panels is shown the link between the underlying structure and the observed emission. Left panel: observed velocity relative to Keplerian rotation. Center panel: surface density map. Faster emission relative to Keplerian comes from the density peak of spiral arm. Slower emission is from inter-arm region. Right panel: zoomed in velocity centroid (top center Figure 2) showing how this affects observed emission. In all the three panels the line $v_{\rm obs} - v^{\rm obs}_{\rm kep} = 0$ is drawn in black (first two), and white (last one). Image taken from Hall et al. (2020).

structure is possible because the spiral induces a radial perturbation. Indeed, the wiggle is present also in the central channel (where in the Keplerian case it is not) because $v_{\rm r} \neq 0$. Hall et al. (2020) also discuss the behaviour of the three different velocity components $(v_{\rm r}, v_\phi, v_{\rm z})$, highlighting that GI discs differ significantly from Keplerian rotation. In particular, they show that the strongest perturbations contributing to the GI wiggle are the ones in $v_{\rm r}$, being visible throughout the azimuthal and radial disc extent. From these considerations, it can be said that velocity perturbations induced by gravitational instabilities should be clearly detectable with current ALMA capabilities.

Observationally, Paneque-Carreno et al. (2021) present not only data relative to two new millimeter wavelengths for the Elias 2-27 disc (see Sec. 5.1.2.2), but also study the kinematics of the disc with ^{13}CO and C^{18}O ALMA observations in the J =3-2 transition. In Fig. 5.22 some of the results presented in Paneque-Carreno et al. (2021) are collected. In particular, the first row shows the moment 0 and moment 1 maps for the ^{13}CO and C^{18}O isotopologues. In the moment 0 map, the continuum spirals, the semi major and minor axes and a gap detected in the C^{18}O gas emission are highlighted. From both the moment 0 and moment 1 maps it is visible that there in an asymmetry between the East (E) and West (W) side of the disc. The East side appears to have a larger extent with respect to the West side, and to be more cloud-absorbed in the ^{13}CO data. The bottom row of Fig. 5.22 shows some selected velocity channel maps for both isotopologues (Paneque-Carreno et al. 2021). The previously described structures are marked with white lines. The blue line traces the expected isovelocity curve in each chan-

nel, following the geometry of the top emission layer constrained with the method described in Sec. 5.2.1.1. The velocity channel maps reveal strong perturbations, which seems to be colocated with the spiral arms in the dust continuum emission. These perturbations are marked with a green and yellow arrows mark the outer and inner perturbation, respectively. By looking at kinematics with a zoom-out they also detect large-scale emission surrounding the disc. Moreover, Paneque-Carreno et al. (2021) also derive the disc height and rotation curve with the method develop by Pinte et al. (2018a), and they fit the obtained velocity curve with a Keplerian mode, getting a value for the star mass $M_\star = 0.46 - 0.5\,M_\odot$. However, when subtracting the Keplerian model to the rotation curve, their fit results is characterised by residuals (sub- and super-Keplerian velocities) throughout the whole radial extent, with a predominance of super-Keplerian velocities at larger radii. This can be an hint of the disc self-gravity being important in this system (see next Section and Chapter 8). Finally, given the highly perturbed gas structure, the spiral structures in the millimeter that are well reproduced by a self-gravitating disc modeling, the large scale emission, and the asymmetry between the two side, they propose infall-triggered gravitational instabilities as origin for the observed spiral structure and for the other peculiarities described above.

5.3 Rotation curve

High spectral and angular resolution line emission can also be used to detect large-scale, coherent deviations from Keplerianity in the rotation curve of the disc, and thus obtain a measure of the azimuthally averaged gravitational field, possibly measuring dynamically the disc mass. This method is widely used in the galactic field, but it has been proposed and used in the context of accretion discs around AGN by Bertin & Lodato (1999) and especially in Lodato & Bertin (2003), for the disc in the NGC 1068 galactic nucleus. In this Thesis, in Chapter 8, we present an application of this model to the protoplanetary disc around Elias 2-27. Potentially, this method can be applied to other discs already showing hints of spiral structures and/or evidences for a high disc-to-star mass ratio, such as IM Lup and WaOph 6 from the DSHARP sample, and RU Lup (Ansdell et al. 2018; Huang et al. 2020).

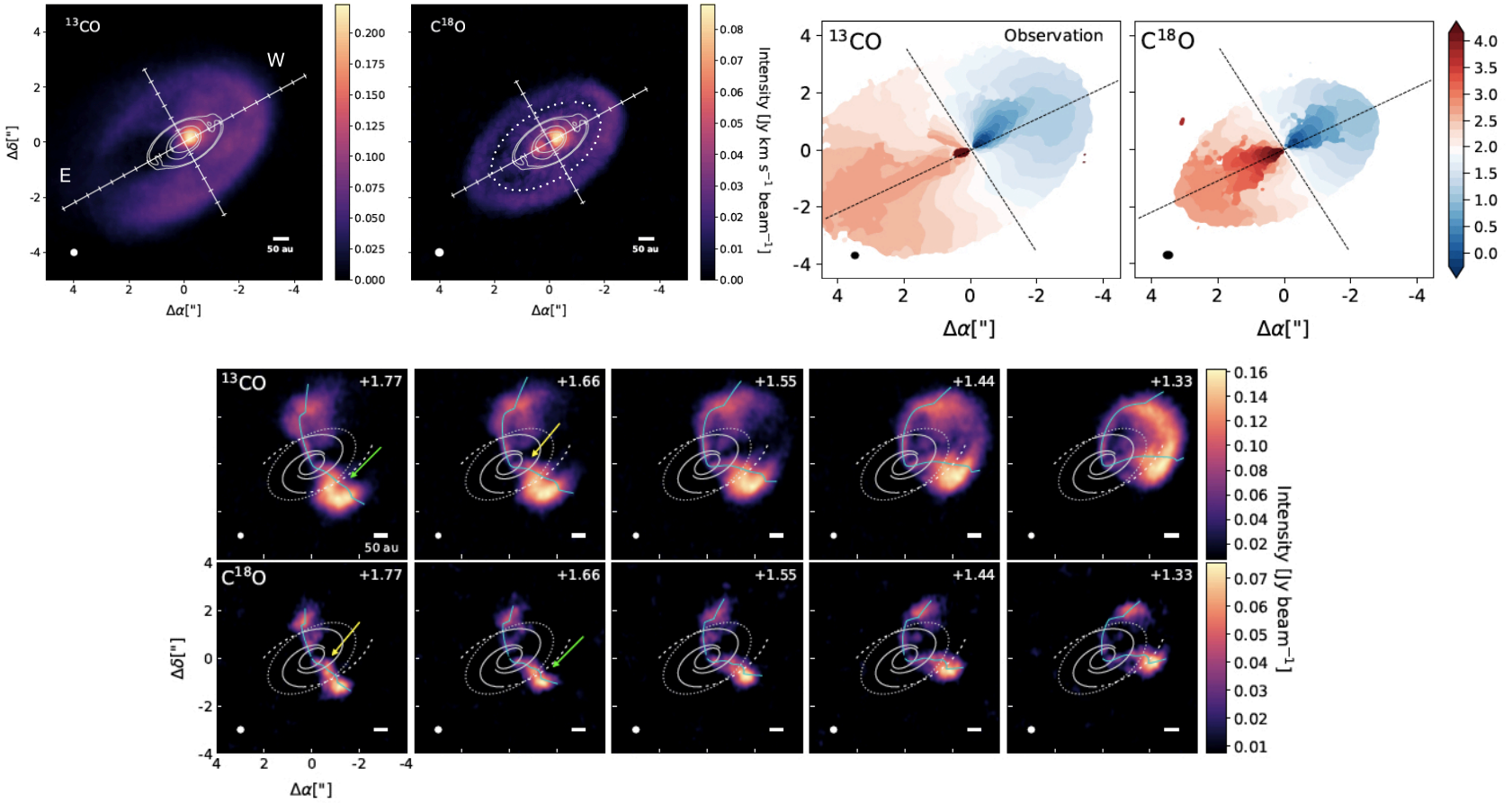

Figure 5.22: *First row, first two columns*: Integrated emission (moment 0) maps for ^{13}CO (left) and C^{18}O (right) gas emission. White contours line relative to the 0.89 mm continuum emission are overlaid on top, while the white grid marks the minor and major axis of the disc. In the C^{18}O moment 0 map it is also overlaid the gap detected in the gas by Paneque-Carreno et al. (2021). *First row, last two columns*: integrated emission velocity map (moment 1) for ^{13}CO (first panel) and C^{18}O (second panel). *Second row*: selected velocity channels of ^{13}CO (top) and C^{18}O (bottom). White continuous line shows the dust features: inner gap at 69 au and the spirals as traced from the 0.89 continuum emission. Dotted white line traces the C^{18}O gas gap location at 241 au. Blue curve traces the expected isovelocity curve of each channel, following the constrained emission layer geometry of the top layer. Green arrows mark the outer perturbation, yellow arrows mark the inner perturbation. Images taken and readapted from Paneque-Carreno et al. (2021).

Part III

Constraining disc dynamics from observations of substructures

Substructures created by leaves shadows (January 2021).

Chapter 6

Multiwavelength observations of protoplanetary discs as a proxy for the gas disc mass

Based on the paper by ***Benedetta Veronesi****, Giuseppe Lodato, Giovanni Dipierro, Enrico Ragusa, Cassandra Hall & Daniel J. Price (2019), "Multiwavelength observations of protoplanetary discs as a proxy for the gas disc mass", Monthly Notices of the Royal Astronomical Society, 489, 3758*

The exceptional imaging capabilities of new instruments such as the Spectro-Polarimetric High-contrast Exoplanet REsearch (SPHERE) imager at the Very Large Telescope and observatories like the Atacama Large Millimeter Array (ALMA) offer exciting new possibilities to explore the dynamics of the two main components of protoplanetary discs: gas and dust. High-resolution observations at a wide range of wavelengths have revealed disc substructures. These substructures are common, as a result of ubiquitous processes in disc evolution (Garufi et al. 2018). Importantly, the morphology of these substructures may differ in scattered light (μm) observations compared to dust thermal emission at $\sim$mm wavelengths (e.g. Follette et al. 2013; Casassus 2016; van Boekel et al. 2016; Hendler et al. 2017; Pinilla et al. 2018b; Dong et al. 2018a). While scattered light observations at near-infrared (NIR) wavelengths trace dust particles with sizes of up to a few microns in the disc surface layers (i.e. the scattering surface), continuum emission at (sub)-millimetre wavelengths provides one of the most direct constraints on the spatial distribution of millimeter-sized dust grains in the discs midplane. Therefore, the different morphology of disc substructures at different wavelengths may be due to the different dynamics of small and large dust grains, making the combination of scattered light (with, e.g., SPHERE) and continuum thermal observations (with, e.g. ALMA) a powerful tool to explore the gas and dust dynamics in protoplanetary discs.

For example, the structures of the disc around HD135344B are different in scattered light observations (Maire et al. 2017) with respect to the dust continuum (Cazzoletti et al. 2018). While in the first case we detect a two armed spiral structure, in the second one we observe an inner ring and an asymmetric structure. It is also interesting to note that by looking at the dust continuum at different wavelengths this asymmetry can be described as part of a ring (in Band 3 and Band 4, see Cazzoletti et al. 2018) or as an horseshoe (in Band 9 and Band 7). Assuming that these structures are generated by a planet (though it has been argued that they could have been originated by other mechanisms, like vortices, e.g. van der Marel et al. 2016c), we know that gas and dust respond differently to the presence of a massive, Jupiter-like planet, with a distinctive spiral structure in the gas (and the small dust tightly coupled to it) (e.g. Dong et al. 2015a), but a more axisymmetric ring-like structure in large dust grains (e.g. Ayliffe et al. 2012; Dong et al. 2015b; Dipierro et al. 2015b; Price et al. 2018b).

The morphology of structures observed at different wavelengths depends on the interaction between the dust and gas. The motion of dust particles is affected by the interaction with the gas with an efficiency that depends on the degree of aerodynamical coupling. This is quantified by the Stokes number, St, the ratio of the drag stopping time t_s and the dynamical time in the disc, i.e. (e.g. Weidenschilling 1977)

$$\mathrm{St} \equiv t_\mathrm{s}\Omega_\mathrm{k} = \sqrt{\frac{\pi}{8}}\frac{a\rho_\mathrm{d}\Omega_\mathrm{k}}{\rho_\mathrm{gas}c_\mathrm{s}} = \frac{\pi}{2}\frac{a\rho_\mathrm{d}}{\Sigma_\mathrm{gas}}\exp\left(\frac{z^2}{2H_\mathrm{g}^2}\right), \tag{6.1}$$

where Ω_k is the Keplerian angular velocity, ρ_d is the internal dust density, z is the vertical coordinate, a is the size of dust grains, Σ_gas is the gas surface density, H_g is the disc scale height assuming vertical hydrostatic equilibrium, i.e. $H_\mathrm{g} = c_\mathrm{s}/\Omega_\mathrm{k}$ where c_s is the sound speed. The above equation is valid for small dust-to-gas mass ratio, isothermal equation of state and in the Epstein drag regime (Epstein 1924), which is the relevant regime of dust-gas coupling up to millimeter-centimetre dust grains for typical disc parameters (Garaud et al. 2004). Strongly coupled and weakly coupled dust is defined by having $\mathrm{St} \ll 1$ and $\mathrm{St} \gg 1$, respectively. Moreover, as we can see from Eq. 6.1, the coupling between dust and gas decreases with increasing vertical distance from the midplane. For this reason, 3D simulations of dust and gas are necessary in order to study the dynamics of the disc and to understand if this different degree of coupling can be detected by SPHERE (tracing grains at $z \approx 2-3$ scale heights) and by ALMA (tracing grains at $z \sim 0$). The Stokes number depends on an elusive yet fundamental disc property — the gas surface density Σ_gas, and thus the total gas disc mass.

The total gas disc mass, M_gas, determines how much mass is available for the formation of giant planets and for the accretion of gas atmosphere around rocky planets. At the same time, it also determines the likelihood of gravitational instability, which may induce disc fragmentation and enhanced angular momentum transport (Kratter & Lodato 2016). Correlations of the disc mass with either the stellar mass (Natta et al. 2000; Andrews et al. 2013, 2018a) or the mass accretion rate (Mulders et al. 2017a; Lodato et al. 2017) can provide important constraints on disc evolution.

The dust mass is relatively easy to measure, starting from optically thin observations at millimetre wavelengths, provided that we have adequate information on the dust opacity and thus on the level of dust growth (Bergin & Williams 2018). However, also in this case there is a lot of uncertainty, due to the optical depth estimate of the dust at (sub-)mm wavelengths. Woitke et al. (2016) discuss this in terms of the uncertainties we have in the dust grain size and composition (see their Fig.3, respectively roughly half and one order of magnitude). For decades, the total disc mass has been obtained from the dust mass simply by assuming a gas-to-dust ratio of 100, typical of the interstellar medium (Mathis et al. 1977). Whether this is applicable to the dense environments of protoplanetary discs is not yet understood (e.g. Bate & Lorén-Aguilar 2017). Moreover, recent observations of protoplanetary discs have found a discrepancy between dust and gas disc sizes (e.g. Ansdell et al. 2016, 2018), that can be explained by the dynamical effect of the dust radial drift (Birnstiel & Andrews 2014). The different dynamics between the two phases inevitably create regions of enhanced or reduced dust-to-gas ratio with respect to its ISM value.

Direct gas tracers are more difficult. The main component in the gas is the H_2 molecule, which lacks a permanent electric dipole and so does not emit significantly. A proxy for the gas mass is provided by observations of CO in its various isotopologues (such as ^{13}CO and C^{18}O), although it is not clear whether these measurements are a reliable estimate of the gas disc mass (Williams & Best 2014; Bergin & Williams 2018). This is due to the fact that the conversion of the observed CO mass into total gas mass is not well understood. For example, the above mentioned correlations between disc mass and either stellar mass or accretion rates are much stronger when one uses dust rather than CO as a proxy for the disc mass (Manara et al. 2016b). Typically, CO observations result in very low disc masses compared to dust estimates (Pascucci et al. 2016; Ansdell et al. 2016; Miotello et al. 2017; Long et al. 2017), which might indicate substantial carbon depletion in the disc, photodissociation in the upper layers, freeze-out at the disc midplane or in general other isotope-selective processes (Miotello et al. 2016). Measurements of the HD line in the far infrared (Bergin et al. 2013) have proved even more controversial, suggesting very high gas masses (but see Trapman et al. 2017). Importantly, Manara et al. (2018) found that not only for the gas mass estimate, but also for the dust mass the picture is not trivial. Indeed, they found that measurements of dust mass of protoplanetary discs in $\sim 1-3$ Myr old regions are lower than the core masses in exo-planets and planetary systems.

In this paper, we propose a method to infer the gas surface density co-located with the continuum and scattered light emissions of protoplanetary discs showing evidence of planet-induced substructures. We base our analysis on the difference in morphology of disc substructures imaged in NIR scattered light and (sub-)mm continuum observations. By combining 3D numerical simulations of a suite of dusty protoplanetary disc models hosting embedded protoplanets with 3D Monte Carlo radiative transfer simulations, we analyse the different observational predictions of disc substructures imaged by SPHERE and ALMA. The main aim is to find an empirical method to link the different morphology of disc substructures at different wavelengths with the gas surface density. This paper is organised as

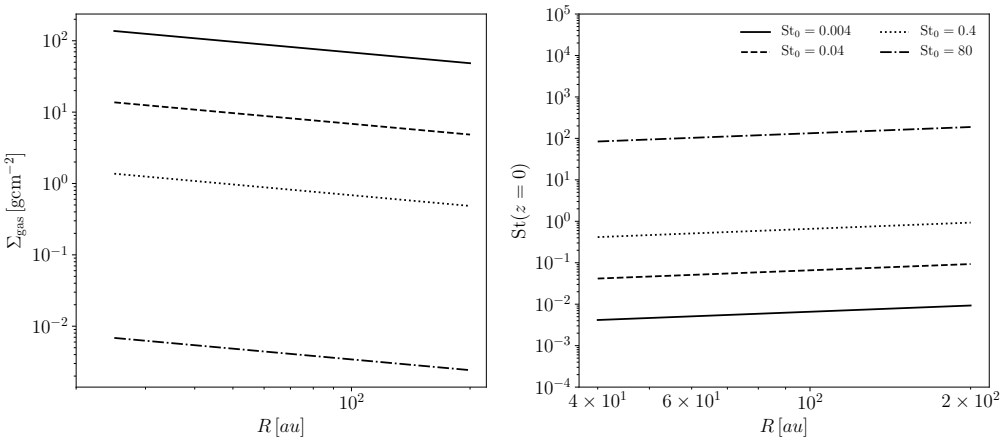

Figure 6.1: Gas surface density (left) and midplane Stokes number (right) in our simulations as a function of radius for different midplane Stokes number (at the inner dust radius) $\mathrm{St}_0 \approx 4 \cdot [10^{-3}, 10^{-2}, 10^{-1}, 20]$

follows: in Section 6.1 we describe our numerical method and simulation setup. In Section 6.2 we describe the results of the numerical simulations and show a set of synthetic SPHERE and ALMA images of disc model. Finally, in Section 6.3 we discuss the implications of our results for the estimate of the gas surface density in protoplanetary discs and draw our conclusions in Section 6.4.

6.1 Methods

6.1.1 Dust and gas numerical simulations

We perform a suite of 3D Smoothed Particle Hydrodynamics (SPH) simulations of dusty protoplanetary discs, using the PHANTOM code developed by Price et al. (2018a). Depending on the level of aerodynamical coupling between the gas and dust, we adopt the one fluid (for St$<$ 1, Price & Laibe 2015; Ballabio et al. 2018) or the two fluid (St$>$ 1, Laibe & Price 2012a,b) methods to simulate the dynamics of dust grains. The one-fluid algorithm is based on the terminal velocity approximation (e.g. Youdin & Goodman 2005). In all our simulations, we include the dust back-reaction, but do not include self-gravity.

6.1.2 Disc models

We pick as a test object HD135344B (also known as SAO 206462), a young stellar object hosting a dusty protoplanetary disc showing a prominent two-armed spiral structure in the near-IR scattered light emission (Stolker et al. 2016; Maire et al. 2017) and an inner ring plus a large horseshoe feature at (sub-)mm wavelengths (van der Marel et al. 2016c; Cazzoletti et al. 2018). HD135344B is also known to be part of a visual binary, but due to the wide separation between the two objects ($21''$, i.e. $\simeq$ 3280 au, Mason et al. 2001) it is unlikely that the disc structure we see

Parameters	Value
$M_\star\,[M_\odot]$	1.7
$R_{\rm in,g}\,[{\rm au}]$	25
$R_{\rm in,d}\,[{\rm au}]$	40
$R_{\rm out,g} = R_{\rm out,d}\,[{\rm au}]$	200
$(H/R_{\rm in})_{\rm g}$	$0.04, 0.06, 0.08$
$M_{\rm dust}\,[M_\odot]$	$5.2 \cdot 10^{-4}$
${\rm St}_0$ (approx)	$4 \cdot [10^{-3}, 10^{-2}, 10^{-1}, 20]$
$\rho_{\rm d}\,[{\rm g\,cm^{-3}}]$	3
p	0.5
q	0.35
$\alpha_{\rm SS}$	0.007
$M_{\rm IP}\,[M_{\rm j}]$	3
$R_{\rm IP}\,[{\rm au}]$	35
$M_{\rm OP}\,[M_{\rm j}]$	5
$R_{\rm OP}\,[{\rm au}]$	145

Table 6.1: Model parameters. ${\rm St}_0$ is the midplane Stokes number at the dust inner radius $R_{\rm in,d}$, $R_{\rm in,g}$ is the gas inner radius. p is the power-law index of the gas surface density profile defined in Eq. 6.2, q is the power-law index of the sound speed radial profile (see Eq. 6.3) and $\alpha_{\rm ss}$ is the effective Shakura & Sunyaev (1973) viscosity. $M_{\rm IP,OP}$ and $R_{\rm IP,OP}$ are the mass of the inner and outer planets and their radial position in the disc.

is originated from the interaction with the companion. This motivates the choice of the parameters for the initial disc conditions in our SPH simulations (outlined in Table 6.1), although we note that the aim of our study is more generally valid to different configurations of planet-disc interaction.

In order to pursue this aim, in our hydrodynamical simulations, rather than changing directly the gas density, we change the Stokes number to obtain a corresponding variation of the gas mass: for example, since St is inversely proportional to the gas density (Eq. 6.1), an increase in St by a factor of 10 is equivalent to a decrease in $\Sigma_{\rm gas}$ by the same factor. This is needed because we want to compare disc morphologies independently of other evolutionary effects that might be affected by the gas mass, such as planetary migration and accretion (e.g. Kley & Nelson 2012; D'Angelo & Lubow 2008). Once the Stokes number and the dust properties (i.e. fluffiness, porosity, composition) are known, it is always possible to go back to the gas mass that has generated that given gas and dust coupling and the resulting system dynamics.

6.1.2.1 Gas and dust

The system consists of a central star of mass $M_\star = 1.7\,M_\odot$ surrounded by a gas disc extending from $R_{\rm in,g} = 25$ au to $R_{\rm out,g} = 200$ au and modelled as a set of 10^6 SPH particles. The initial gas surface density profiles are assumed to be power

laws (Fung & Dong 2015), i.e.

$$\Sigma_{\rm gas}(R) = \Sigma_{\rm in} \left(\frac{R}{R_{\rm in,g}} \right)^{-p}, \tag{6.2}$$

where $\Sigma_{\rm in}$ is a normalization constant at the inner radius and $p = 0.5$. We adopt a locally isothermal equation of state $P = c_{\rm s}^2 \rho_{\rm g}$, with

$$c_{\rm s} = c_{\rm s,in} \left(\frac{R}{R_{\rm in,g}} \right)^{-q}, \tag{6.3}$$

where $c_{\rm s,in}$ is the sound speed at the inner disc radius and $\rho_{\rm g}$ is the gas volume density. We assume $q = 0.35$ (Andrews et al. 2011; Carmona et al. 2014) as the power-law index of the sound speed radial profile. The disc is vertically extended by assuming a Gaussian profile for the volume density and ensuring vertical hydrostatic equilibrium

$$\frac{H_{\rm g}}{R} = \frac{c_{\rm s}}{v_{\rm k}} = \left(\frac{H}{R_{\rm in}} \right)_{\rm g} \left(\frac{R}{R_{\rm in,g}} \right)^{1/2-q}, \tag{6.4}$$

where $v_{\rm k}$ is the Keplerian velocity and $(H_{\rm g}/R)_{\rm in}$ is the aspect ratio at the reference radius $R_{\rm in}$. In our study, we vary the aspect ratio $(H/R_{\rm in})_{\rm g}$ in the range $[0.04, 0.06, 0.08]$ (Stolker et al. 2016). We model viscous gas discs with an effective Shakura & Sunyaev (1973) viscosity $\alpha_{\rm SS} \approx 0.007$, implemented through the artificial viscosity formalism in SPH (Lodato & Price 2010a).

Given the different cavity radius in gas and dust observed in HD135344B disc (Garufi et al. 2013; van der Marel et al. 2015), we consider a dust disc extending from $R_{\rm in,d} = 40$ au to $R_{\rm out,d} = 200$ au. We use the same functional form of the initial surface density as for the gas (Eq. 6.2), assuming a dust mass of $M_{\rm dust} = 5.2 \cdot 10^{-4}\, M_{\odot}$. The dust-to-gas is initially assumed constant for the whole disc extent, so that the dust has the same vertical structure of the gas. After a few orbits of the outer planet, the dust has settled down forming a layer with thickness $H_{\rm d} = H_{\rm g} \sqrt{\alpha_{\rm ss}/({\rm St} + \alpha_{\rm ss})}$ (Fromang & Nelson 2009).

6.1.2.2 Treating different degrees of coupling

As already outlined, the aerodynamical coupling between the dust and gas phase is related to the grain size and the disc gas mass (see Eq. 6.1), i.e.

$${\rm St}_0 \propto \frac{\pi}{2} \frac{a \rho_{\rm d}}{\Sigma_{\rm gas}} \propto \frac{a}{M_{\rm gas}}. \tag{6.5}$$

where $M_{\rm gas}$ is the gas disc mass. We have run simulations with initial values of the midplane Stokes number ($\rm St_0$) in the range $\sim 4 \cdot [10^{-3}, 10^{-2}, 10^{-1}, 20]$ at the inner dust radius $R_{\rm in,d} = 40$ au, assuming an intrinsic grain density $\rho_{\rm d} = 3\,{\rm g\,cm^{-3}}$. In the left panel of Fig. 6.1 gas surface densities relative to the four choices of Stokes number are displayed, as a function of the disc radius. We note that the Stokes number range used in our models was chosen in order to span a wide range of dust-gas coupling. It is clear that the lower Stokes number of this model is unphysical

because it corresponds to a very high disc mass that will lead to the development of gravitational instabilities. However, the same study is still relevant for smaller grains and lower intrinsic grain density, which would provide smaller and more physical gas masses for the same degree of coupling. In the right panel of Fig. 6.1 we show the initial value of the midplane ($z = 0$) Stokes number as a function of radius. Each line represents a different gas mass. The solid, dashed and dotted lines ($\mathrm{St}_0 \sim 4 \cdot [10^{-3}, 10^{-2}, 10^{-1}]$) refer to simulations performed with the one-fluid method, while the dot-dashed line ($\mathrm{St}_0 \sim 80$) refers to a two-fluid simulation.

Note that, once the dust is decoupled from the gas ($\mathrm{St} \gg 1$), the dust dynamics depends very little on St, so our results for the largest value of St are in general applicable also for moderate St.

6.1.2.3 Properties of the embedded planets

In each disc model we embed two planets at radial distances from the central star of $R_{\mathrm{IP}} = 35$ au and $R_{\mathrm{OP}} = 145$ au, respectively. We model the planets and the central star as sink particles. The sinks are free to migrate and are able to accrete gas and dust (Bate et al. 1995). Depending on the planetary mass and local disc structure, a planet can excite multiple spiral arms (Miranda & Rafikov 2019a). Generally, planets with masses larger than a threshold, i.e.

$$M_{\mathrm{p}} \gtrsim M_{\mathrm{th}} \equiv \left(\frac{H_{\mathrm{g}}}{R}\right)^3_{\mathrm{p}} M_{\star}, \tag{6.6}$$

are expected to excite two spiral arms interior to their orbit, while the tidal interaction with planets with $M_p \ll M_{\mathrm{th}}$ give rise to a spiral structure with only one arm. In both cases, the pitch angle of the spiral arms are expected to be proportional to the local aspect ratio $(H/R)_{\mathrm{p}}$ (Rafikov 2002; Zhu et al. 2015; Miranda & Rafikov 2019a). The mass M_{th} is defined as the planet mass at which the Hill radius of the planet (Eq. 6.7 below) is equal to the thickness of the disc $H(R_{\mathrm{p}})$ at the planet position R_{p}. The planet masses in our disc models are chosen to be equal to $M_{\mathrm{IP}} = 3\,M_{\mathrm{j}}$ and $M_{\mathrm{OP}} = 5\,M_{\mathrm{j}}$, where M_{j} indicates the Jupiter mass. With this parameter choice, we get an inner cavity and a two armed spiral feature. These masses correspond to $\simeq [23, 7, 3]\,M_{\mathrm{th}}$ and $\simeq [20, 6, 2.5] M_{\mathrm{th}}$ respectively, for $(H/R_{\mathrm{in}})_{\mathrm{g}} = [0.04, 0.06, 0.08]$. The accretion radius of each planet is chosen to be half the minimum between the Hill radius,

$$R_{\mathrm{H}} = \left(\frac{1}{3}\frac{M_{\mathrm{p}}}{M_{\star}}\right)^{1/3} R_{\mathrm{p}}, \tag{6.7}$$

and the disc height at the planet position $H(R_{\mathrm{p}})$,

$$R_{\mathrm{acc,p}} = 0.5 \min(R_{\mathrm{H}}, H_{\mathrm{g}}(R_{\mathrm{p}})). \tag{6.8}$$

In this way, we are able to accurately reproduce the spiral arms excited by the planets embedded in the disc, with reasonable computational efforts. Also, since different values of $(H/R_{\mathrm{in}})_{\mathrm{g}}$ correspond to different values of gas density at the disc midplane, this will result in a slightly different planetary migration and accretion (e.g. D'Angelo & Lubow 2008; Baruteau et al. 2014).

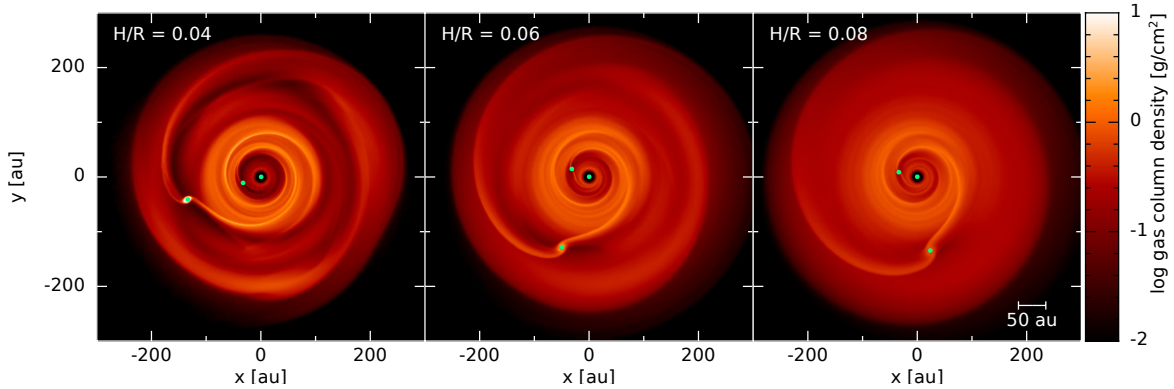

Figure 6.2: Gas surface density maps of our set of hydrodynamic simulations. From left to right are shown the results related to disc models with different aspect ratio $(H/R_{\rm in})_{\rm g} = [0.04, 0.06, 0.08]$ at the gas inner disc radius $R_{\rm in} = 25$ au.

6.1.3 Radiative transfer and synthetic observations

We compute synthetic observations of our disc models by performing 3D radiative transfer simulations, by means of the RADMC-3D code (Dullemond et al. 2012), starting from the results of the hydrodynamical simulations. Our goal is to compute the synthetic ALMA Band 6 (1.3 mm) and SPHERE Band H (1.65 μm) observations.

The main inputs for the radiative transfer modelling are the dust density structure of large and small grains, a model for the dust opacities and the source of luminosity. We compute the dust opacities using the DIANA OpacityTool code[1] developed by Woitke et al. (2016), adopting the dust model from Min et al. (2016). We choose two ranges of grain sizes in order to sample both the small ($0.1 \lesssim a \lesssim 10\mu m$) and the large (0.1mm $\lesssim a \lesssim$ 1cm) dust population and to study scattered light and continuum images. While the large dust ($\sim$ 1 mm) is directly available from the simulation, we assume that the small ($\sim 1\,\mu$m) dust density is simply proportional to the gas density (since it is expected to be tightly coupled to the gas for any gas mass), $\Sigma_{\rm sd}(R) = f\Sigma_{\rm gas}(R)$. This factor f is chosen so as to have a total small dust mass of $M_{\rm sd} \simeq 1.6 \cdot 10^{-5} M_{\odot}$, which corresponds to a ISM-like grain size distribution ($dn/da \propto a^{-3.5}$), if the large dust mass is $M_{\rm ld} \simeq 5 \cdot 10^{-4} M_{\odot}$.

The expected emission maps at 1.65 μm and 1.3 mm are computed via ray-tracing using 10^9 photon packages, assuming that the disc is face-on. The source of radiation is assumed to be the central star, located at the centre of the coordinate system, with $M_{\star} = 1.7 M_{\odot}$, $T_{\rm eff} = 6810$ K and $R_{\star} = 1.4 R_{\odot}$. We assume the disc to be located in Ophiuchus star-forming region (d ~156 pc). In order to simulate the effect of a coronograph in scattered light observations, we mask a circular region of diameter $\sim$ 0.15" around the central star. This corresponds to the coronograph diameter used in the most common service NIR configuration for

[1] https://dianaproject.wp.st-andrews.ac.uk

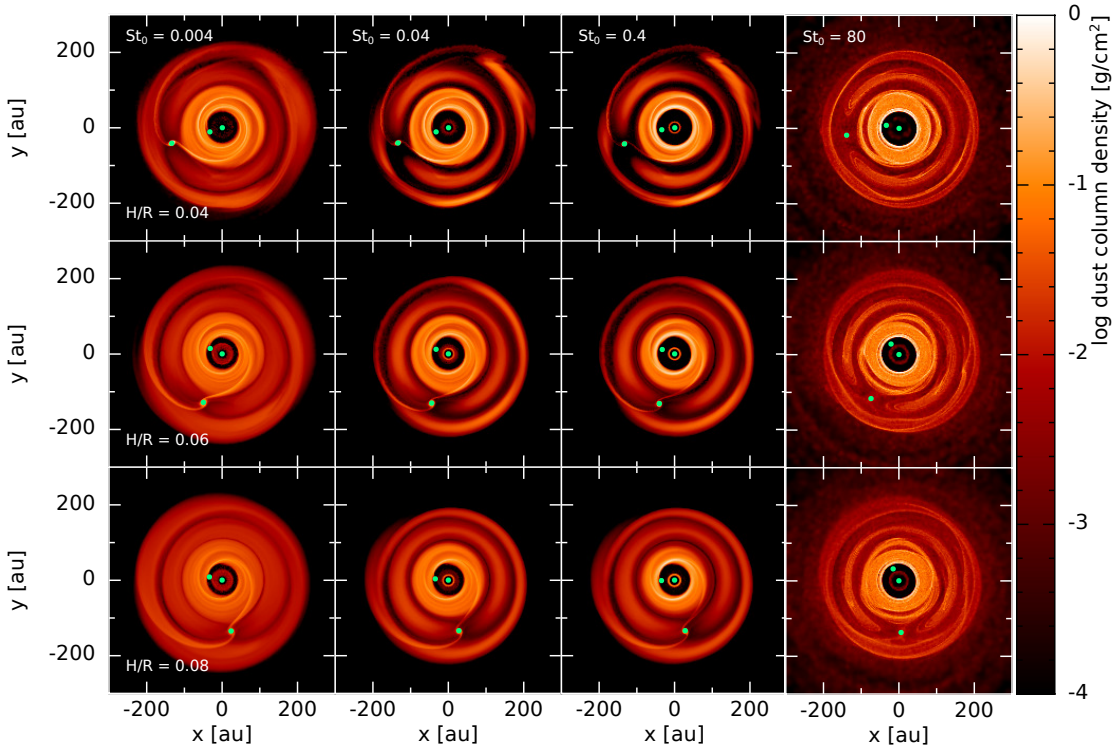

Figure 6.3: Dust surface density maps of our set of hydrodynamic simulations with (from top to bottom) different disc aspect ratio $(H/R_{\rm in})_{\rm g} = [0.04, 0.06, 0.08]$ at the gas inner disc radius $R_{\rm in,g} = 25$ au, and (from left to right) different initial midplane Stokes number $\mathrm{St}_0 \simeq 4 \cdot [10^{-3}, 10^{-2}, 10^{-1}, 20]$ at the dust inner disc radius $R_{\rm in,d} = 40$ au.

the IRDIS instrument[2].

The full-resolution images at 1.3 mm directly produced by RADMC-3D are used as input sky models to simulate realistic ALMA observations using the Common Astronomy Software Application (CASA) ALMA simulator (version 4.5.3, McMullin et al. 2007). We take into account the thermal noise from the receivers and the atmosphere (Pardo et al. 2002) and assume a perfect calibration of the visibility measurements. We assumed Cycle 6 ALMA capabilities adopting an antenna configuration alma.cycle6.6 that provides a beam of 0.1 × 0.08 arcsec ($\sim 16 \times 13$ au at 156 pc), adopting a transit duration of 300 minutes. However, in order to remove possible external asymmetries and to be able to study only non axi-symmetric structures due to the dynamic of the system, we manually changed the beam to a circular one with a dimension of 0.09 × 0.09 arcsec. The SPHERE images are computed by convolving the full-resolution scattered light image in H-band produced by RADMC-3D with a circular Gaussian point spread function with a full width half maximum (FWHM) of 0.037", taken as a good approximation to the angular resolution achieved by SPHERE.

6.2 Results

6.2.1 Disc morphologies as a function of the Stokes number

Figure 6.2 shows the gas surface density maps of our disc models with the three aspect ratio (from left to right) $(H/R_{\rm in})_{\rm g} = [0.04, 0.06, 0.08]$ after ~ 10 orbits of the outer planet (at the initial planet location $R_{\rm OP} = 145$ au) and 80 orbits of the inner planet (initial location $R_{\rm IP} = 35$ au). Due to the different locations and masses of the embedded planets, the resulting spiral structures induced by planet-disc interactions is dominated by the outer planet, while the inner one is responsible for carving the cavity. As already mentioned in Sect. 6.1.2.3, the spiral features interior to the orbit of the outer planet are characterized by two spiral arms with a pitch angles that increases with increasing $(H/R_{\rm in})_{\rm g}$. At the same time, the arms become less sharp, since the intensity of the spiral structures depends on the planet mass and on the disc aspect ratio (eq. 16 in Miranda & Rafikov 2019a). The density colour scale is in arbitrary units and the gas densities for the various choices of disc mass can be obtained by a suitable rescaling.

Fig. 6.3 shows the dust surface density maps of our models. Here the different rows represent different disc aspect ratio $(H/R_{\rm in})_{\rm g} = 0.04, 0.06, 0.08$, while each column represents a specific Stokes number at the disc midplane ($\mathrm{St}_0 = 4 \cdot [10^{-3}, 10^{-2}, 10^{-1}, 20]$ at the reference radius $R_{\rm in,d}$ for the initial conditions). All the snapshot of Fig. 6.3 are taken at the same time, so the different position of the planets are due to a slightly different migration rate for the various disc aspect ratios. If we look at the last column of Fig. 6.3, $\mathrm{St}_0 = 80$, some elliptical asymmetries are visible. These are caused by the fact that if the dust is decoupled from the gas, eccentricity pumping at the mean motion resonances (i.e. 1:2, 2:1, 2:3 and 3:2, which are respectively 0.6, 1.6, 0.76 and 1.3 times the planet radius

[2]Table 45 in https://www.eso.org/sci/facilities/paranal/instruments/sphere/doc/VLT-MAN-SPH-14690-0430_v96.pdf

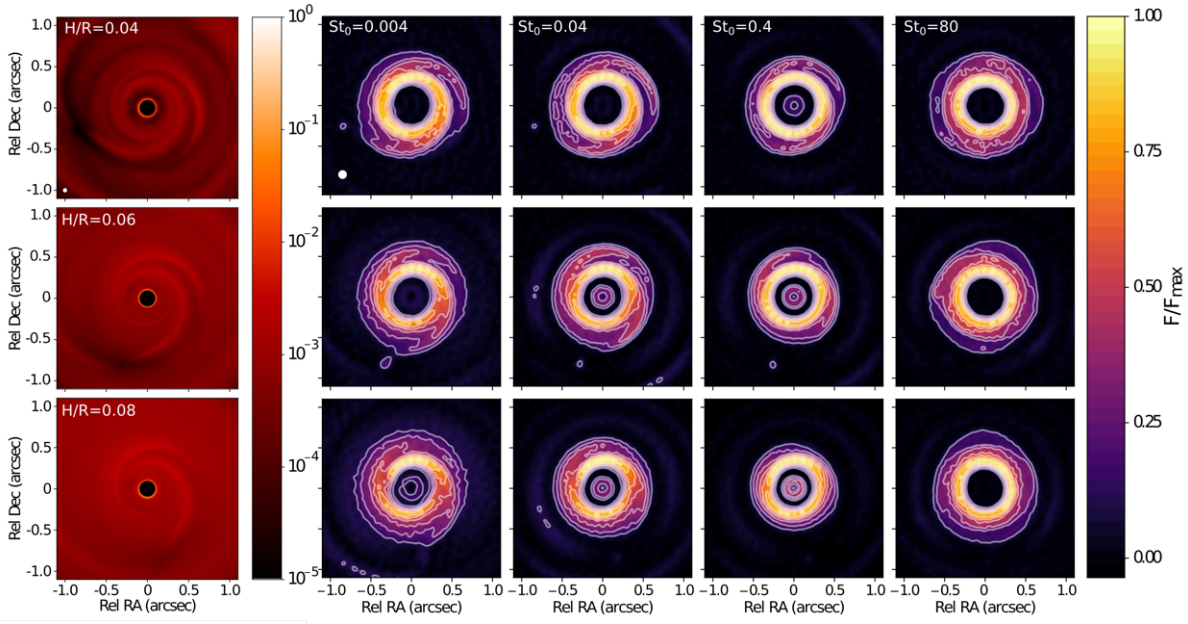

Figure 6.4: Synthetic SPHERE and ALMA observations of disc models with different disc aspect ratio $(H/R_{\rm in})_{\rm g} = [0.04, 0.06, 0.08]$, respectively from top to bottom. First column: SPHERE synthetic observations obtained by rescaling the gas surface density into micron-sized dust grains. From the second to the fifth columns are shown the ALMA synthetic images for different Stokes number $\mathrm{St}_0 = 4 \cdot [10^{-3}, 10^{-2}, 10^{-1}, 20]$. In the ALMA images contours are $5, 10, 15, 20, 25, 30, 35, 40, 45, 50, 55, 60$ times the rms noise ($2.5 \cdot 10^{-2}$ mJ) at 230 GHz. Both the ALMA and SPHERE images have been renormalized to the maximum value of the flux. The SPHERE images have a logarithmic flux scale.

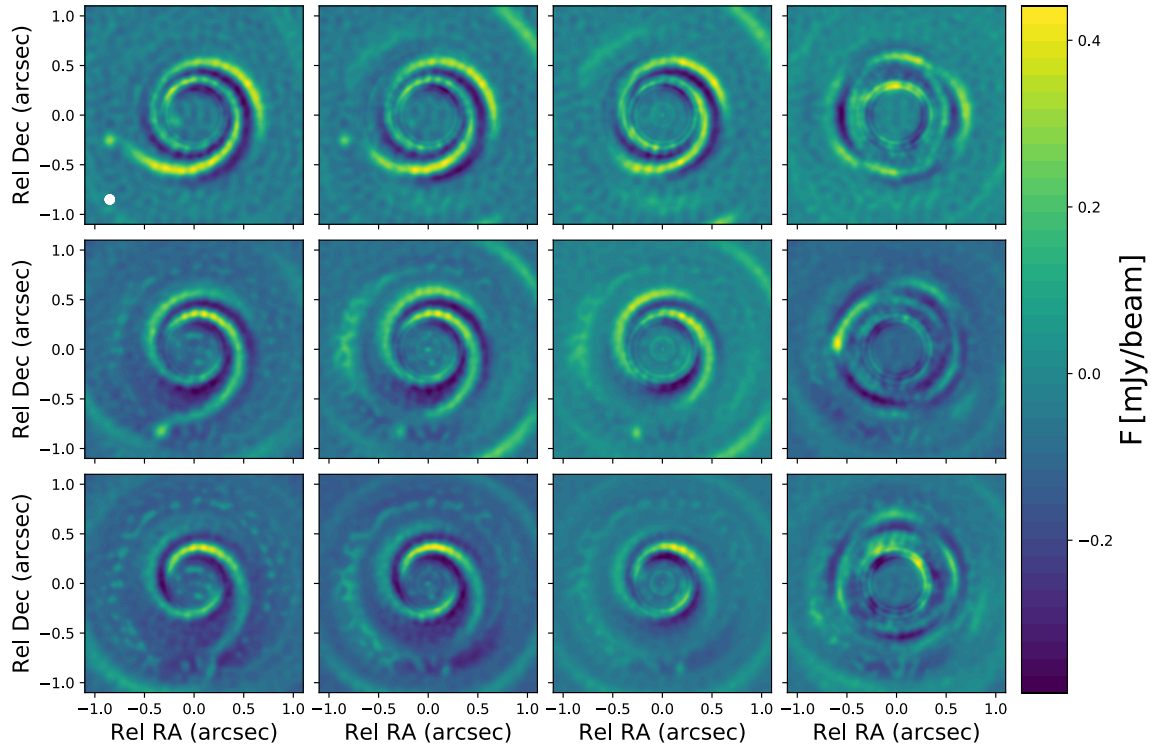

Figure 6.5: Residuals of the synthetic ALMA observations shown in Fig. 6.4, for $(H/R_{\rm in})_{\rm g} = 0.04, 0.06, 0.08$ (top to bottom) and for different Stokes number $\mathrm{St}_0 = 4 \cdot [10^{-3}, 10^{-2}, 10^{-1}, 20]$ (left to right). To obtain these residuals we divide the disc in 22 annuli from 0.02 to 1.0 arcsec. Then, we subtract from the intensity of each annulus the respective mean intensity.

R_p) can arise (Zhu et al. 2014). The inner resonances (1:2 and 2:3) in our case are at $\simeq 87$ au and $\simeq 110$ au, that correspond with the elliptical shape visible in the dust with $\mathrm{St}_0 = 80$.

6.2.2 Simulated images

When the dust and the gas are coupled (i.e. for high gas mass) we expect to detect spiral structures, both in the dust continuum and in the scattered light emission, while when they are decoupled (i.e. lower gas mass) the disc will be characterized by a more axi-symmetric structure at mm-wavelengths (e.g. rings or horseshoes). Fig. 6.4 shows the synthetic images obtained as described in Section 6.1.3 for the SPHERE and ALMA observations. In the first column there are the scattered light SPHERE images (micron-sized grains). The dust continuum ALMA images (tracers of millimetric grains distribution) are presented for different Stokes parameters ($\mathrm{St}_0 = 4 \cdot [10^{-3}, 10^{-2}, 10^{-1}, 20]$ at the midplane in the initial condition) from the second to the fifth columns. Different disc aspect ratio $(H/R_{\rm in})_{\rm g} = 0.04, 0.06, 0.08$ are shown from the top to the bottom row.

As expected all SPHERE images show a spiral feature, since we obtained them by rescaling the gas by a factor that takes into account the amount of micron-sized

dust in the disc. By doing in this way, the dynamics of the micron-sized grains are assumed to follow the gas, producing the characteristic spirals we see. The ALMA images with $\mathrm{St}_0 = 4 \cdot 10^{-3}$ (for all the disc aspect ratio), also display two spiral arms as visible also in the SPHERE image. Indeed, in this case the dust is strongly coupled to the gas. However, increasing the Stokes number (i.e. decreasing the gas disc mass) the dust and gas become progressively less coupled: the non axi-symmetric sub-structures become gradually more symmetric and circular. As an example, if we consider the ALMA image with $\mathrm{St}_0 = 80$ and we compare it with the $\mathrm{St}_0 = 4 \cdot 10^{-3}$ image, a ring-like structure instead of the two-armed spiral is observed. From $\mathrm{St}_0 = 4 \cdot 10^{-3}$ to $\mathrm{St}_0 = 0.4$ the disc also becomes more compact since radial dust drift becomes more effective (Weidenschilling 1977). This effect has been also discussed by Powell et al. (2019). At $\mathrm{St}_0 = 80$ the disc retains its original radius due to the strong decoupling between dust and gas.

If we look at different disc aspect ratios, while the spiral structures are well defined in a disc with $(H/R_{\mathrm{in}})_{\mathrm{g}} = 0.04$, they become less evident in a disc with $(H/R_{\mathrm{in}})_{\mathrm{g}} = 0.08$ also for low Stokes number. In fact, when the disc is thinner, since the interaction between the planet and the disc is stronger, the gap carved by the planet is deeper and the resulting spiral is brighter with respect to the background (see Fig. 1 in Fung & Dong 2015). We highlight that increasing the aspect ratio the spiral arms become less wound up. This is visible especially for the case with initial $\mathrm{St}_0 = 0.4$.

6.3 Discussion

6.3.1 Spiral or ring? An analysis of substructure (a)symmetries

In Fig. 6.4 we have shown the ALMA synthetic images for different gas masses, corresponding to different Stokes number. However, since the dynamic range of the image is large, in order to enhance the fainter non axi-symmetric features, we compute the residuals of each image. First, we divide the disc in 22 annuli from 0.02 to 1.0 arcsec. The chosen radial width $\Delta R = 0.045''$ corresponds to the beam radius, and has been chosen as a fair compromise between the resolution of our images and the need of thin annuli. Then, in each annulus j, we subtract from the pixel intensity $I_{\mathrm{pix,j}}$ the flux mean value $\overline{I_{\mathrm{ann,j}}}$, as

$$\overline{I_{\mathrm{pix,j}}} = I_{\mathrm{pix,j}} - \overline{I_{\mathrm{ann,j}}}\,. \tag{6.9}$$

The result is shown in Fig. 6.5, where the Stokes number increases from left to right and the disc aspect ratio increases from the top to the bottom. In this figure the more axi-symmetric component has been removed, and the spirals, if present, are clearly visible. As already evinced from Fig. 6.4, the disc with low Stokes number and smaller aspect ratio H/R are characterized by spirals. Increasing the Stokes number the spirals become more tightly wound and also smaller, until they disappear in the disc with the higher Stokes number. However, for St_0=80 the residual images appear to be less symmetric than expected. This could be due to the fact that in the surface density map were already present some asymmetries (eccentricity pumping, e.g. Zhu et al. 2014), and by computing the residuals we are enhancing them.

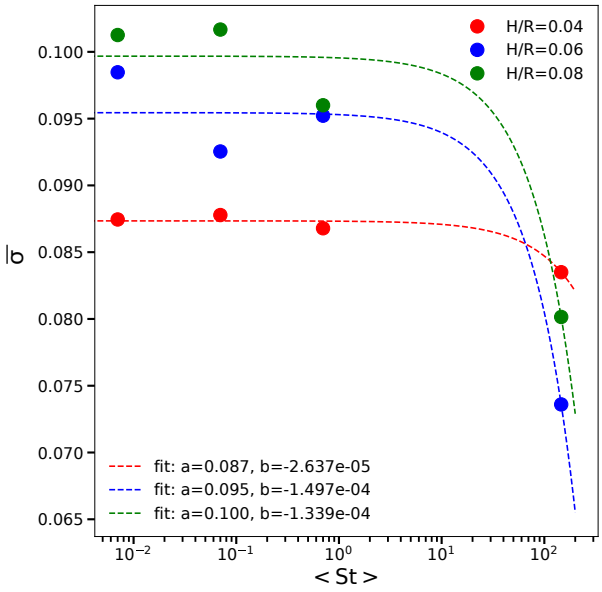

Figure 6.6: Weighted average of the standard deviation for the whole disc, as defined in Eq. 6.10, as a function of the Stokes number (in log scale) for different disc aspect ratio $(H/R_{\rm in})_{\rm g} = [0.04, 0.06, 0.08]$ (red, blue and green points-lines respectively). The weight is the square mean intensity computed in the 22 annuli between 0.02 and 1.0 arcsec. The dashed lines represent the fit of the data with first order polynomials.

We now apply a more quantitative method in order to relate the morphologies (i.e. asymmetries or symmetries) of the residuals images (Fig. 6.5) to the gas disc mass. We compute for each image of Fig. 6.4 the standard deviation of the intensity for each annulus. The flux in each pixels, I_i, has been normalized to the maximum value for each images, $I_i = I_i/\max(I)$. Then, we compute the weighted average of the standard deviation for the whole disc, where the weight is the square mean intensity of each annulus,

$$\overline{\sigma} = \frac{\sum_{j=1}^{N_{\rm ann}} \sigma_j \overline{I_j}^2}{\sum_{j=1}^{N_{\rm ann}} \overline{I_j}^2} \,. \tag{6.10}$$

In this equation, σ_j is the standard deviation and $\overline{I_j}$ is the mean flux, in each annulus. In Figure 6.6 we show the weighted average standard deviation as a function of the Stokes number, where the points represent the value computed from the residuals of the simulated images (red for $(H/R_{\rm in})_{\rm g} = 0.04$, blue for $(H/R_{\rm in})_{\rm g} = 0.06$ and green for $(H/R_{\rm in})_{\rm g} = 0.08$), while the dashed lines are the first order polynomial fit of the data points. Combining this result with Fig. 6.4, it is interesting to note that the general trend of structures becoming more symmetric with increasing Stokes number is visible also through the standard deviation of the intensity. In addition, by increasing the disc aspect ratio, the standard deviation of the flux intensity increases slightly.

Table 6.2: Sources name, age of the disc, dust disc mass and disc morphologies for the protoplanetary discs discussed in Sec 6.3.2.

Source name (a)	t [Myr] (b)	$M_{\rm d,disc}$ [$M_\odot$] (c)	Ref. (Age, $M_{\rm d,disc}$) (d)	Morphologies (e)
HD135344B	8	$[1-4]\cdot10^{-4}$	[Grady et al. (2009) - Cazzoletti et al. (2018)]	A=horseshoes+ring; S=spirals [1]
TWHya	10	$[2-6]\cdot10^{-4}$	[Weinberger et al. (2013) - Calvet et al. (2002); Thi et al. (2010)]	A,S= rings [2]
MWC758	3.5^{+2}_{-2}	$2\cdot10^{-4}$	[Meeus et al. (2012) - Boehler et al. (2018)]	A=ring+spiral/clumps; S=spirals [3]
HD97048	3	$7\cdot10^{-4}$	[Lagage et al. (2006) - van der Plas et al. (2017)]	A,S= rings [4]
AB Aurigae	4.	$7.5\cdot10^{-5}$	[DeWarf et al. (2003) - Lin et al. (2006)]	A=rings,spirals;S=spirals [5]
PDS70	5.4	$3\cdot10^{-5}$	[Müller et al. (2018) - Keppler et al. (2018)]	A=rings;S=rings [6]
IMLup	0.5	$3\cdot10^{-6}$	[Alcalá et al. (2017) - Avenhaus et al. (2018)]	A=spirals;S=rings [7]
HD169142	6^{+6}_{-3}	10^{-4}	[Grady et al. (2007) - Fedele et al. (2017)]	A=rings;S=rings [8]
HD 143006	$11.9^{+3.7}_{-5.8}$	$0.39\cdot10^{-4}$	[Garufi et al. (2018) - Natta et al. (2004)]	A=rings;S=rings, clump [9]

Notes: a) Source name; (b) Disc age; (c) dust disc mass; (d) references for the disc age and for the dust disc mass; (e) disc morphologies observed in the continuum, with ALMA (A) and in scattered light, with SPHERE-VLT/Subaru-HiCIAO (S).
Continuum/scattered light discs morphologies references: [1] Cazzoletti et al. (2018); Maire et al. (2017), [2] van Boekel et al. (2017); Andrews et al. (2016), [3] Boehler et al. (2018); Benisty et al. (2015), [4] van der Plas et al. (2017); Ginski et al. (2016), [5] Hashimoto et al. (2011), [6] Long et al. (2018a); Keppler et al. (2018), [7] Huang et al. (2018c); Avenhaus et al. (2018),[8] Fedele et al. (2017); Pohl et al. (2017),[9] Pérez et al. (2018b); Benisty et al. (2018)

6.3.2 An application to observed morphologies in protoplanetary discs

The main result of our work is that disc substructures due to planet-disc interaction should be characterized by rings or ring-like structures, rather than spirals, if the Stokes number of millimetre-emitting grains ($a_{\max} = \lambda/2\pi$, e.g. Kataoka et al. 2015) is larger than ~ 0.4. Provided that the properties of the dust (fluffiness, porosity, intrinsic grain density and size) are known, we can infer the gas surface density, which corresponds to $\Sigma_{\rm gas} \lesssim 0.4 {\rm g/cm}^2$ (using Eq. 6.5 and assuming $\rho_d = 3 {\rm gcm}^{-3}$), and hence to a disc mass of the order of $\approx 1.4 \cdot 10^{-3} M_\odot$ for structures located at ≈ 100 au or to $\approx 5 \cdot 10^{-3} M_\odot$ for structures located at 200 au (indeed note, for example, that Dipierro et al. 2015a have used a mass of $2 \cdot 10^{-4} M_\odot$ within 120 au to reproduce the system of rings in HL Tau). What implications does this have, when one takes into account the observed disc structures? First of all, we note that the majority of substructures observed with ALMA at high resolution are in the form of rings (Huang et al. 2018c; Long et al. 2018b), which would then point to a prevalence of low mass discs. Note, however, that dust rings may be produced by mechanisms other than planet-disc interaction, so that the mere detection of rings in the mm continuum does not in itself imply the presence of a planet. A stronger indication for planet-disc interaction is present in those cases where, in addition to structure in the mm continuum, one also observe a substructure, such as a spiral, in scattered light images. We thus list in Table 2 all the known discs that have shown substructures both in scattered light and in mm continuum images, indicating for each of them what kind of structure is observed. From this small sample of discs, it is clear that in order to build a wider picture of disc evolution and to unravel the gas disc mass problem, the observation of a wider zoo of protoplanetary discs at different wavelengths is crucial (Haworth et al. 2016). However, we can extract interesting clues from the discussion of some of these systems.

In some cases, such as HD135344B and MWC758, we indeed observe a spiral structure in scattered light and rings or circular structures in the mm continuum, indicating that the disc mass in these system should be relatively low. In particular, for the case of HD135344B, which was the initial motivation of our study, we confirm that the observed spiral structure in scattered light can be ascribed to the presence of two massive planets, with a mass of a few Jupiter masses. ALMA images of HD135344B show a circular structure, but rather than full rings, a horseshoe is observed (Cazzoletti et al. 2018), which might indicate the presence of a vortex (van der Marel et al. 2016c), that we cannot reproduce in our images because the viscosity that we assume is too large for vortex production. In MWC758 we do see hints of spiral structures: a southern arm in the continuum emission (optically thin, traces disc midplane) and two of them in the ^{13}CO J=3-2 peak emission lines (optically thick, traces variation of the disc temperature), almost in the same location of the ones observed in the scattered light (see Boehler et al. 2018; Dong et al. 2018a). The small offset in the radial location of the southern spiral observed in the continuum is probably due to the vertical propagation of the spiral (i.e. they bend over toward the star), or to a nonzero inclination so that the "NIR/surface spiral" and "ALMA/midplane spiral" are projected to dif-

ferent locations on the plane of the sky. The origin of the spiral observed in the continuum could be found in the trapping of millimeter-sized dust particles. Two clumps in correspondence of the two NIR spirals are also observed, and they are explained as possible Rossby wave instability (Boehler et al. 2018). Also Dong et al. (2018a) hypothesized that their radial widths is related to emitting particles having Stokes numbers smaller than unity. This could be due to a locally high gas surface density.

TW Hya, HD143006 and HD169142 are three old ($t \geq 6 - 12$ Myr, Weinberger et al. 2013; Grady et al. 2007; Garufi et al. 2018) protoplanetary discs with symmetric structures imaged both in the ALMA and in the SPHERE data (van Boekel et al. 2017; Andrews et al. 2016; Fedele et al. 2017; Pohl et al. 2017). They all are evolved systems, where the gas has almost all been dissipated leaving a disc with a low gas-to-dust ratio (Williams & Cieza 2011). This low surface gas density implies a high Stokes number not only for the millimetre grains, but also for the micron-sized dust, producing the observed structures in the SPHERE images. For this to happen, the gas disc mass should be smaller than $10^{-4} M_{\odot}$. The case of TW Hya is particularly controversial. While its age would be in line with a very small gas mass, HD line observations by Bergin et al. (2013) would instead point to a much higher gas mass (i.e. $M_{\rm gas} > 0.06\, M_{\odot}$). Note that recently Powell et al. (2019) have performed an analysis similar in spirit to our own, in that they try and weigh the gas mass by estimating the different degrees of dust-gas coupling comparing multi-wavelength images. However, rather than using the effect of dust coupling on sub-structures, as we do, they observe its effect on the dust disc size, whereby dust with a larger St is expected to drift at a faster rate and produce a smaller disc (an effect that we also see in our simulations). By using this method, they generally conclude that the proto-planetary discs that they have analysed are relatively massive (close to gravitational instability). In particular, for TW Hya, they estimate a mass of 0.11 $M_{\odot}$, in line with the HD measurements. However, this beg the question of how, with such a high disc mass, a regular system of rings is observed in the ALMA continuum. Mentiplay et al. (2019) have recently modeled TW Hya using PHANTOM and a gas mass $\lesssim 10^{-2} M_{\odot}$ and indeed find that the scattered light images of their best model do show a spiral structure. To produce rings also in scattered light would require a very low disc mass $\lesssim 10^{-5} M_{\odot}$, well below the minimum of $3 \cdot 10^{-4} M_{\odot}$ inferred from CS measurements by Teague et al. 2018.

Another interesting case is IM Lup, for which a tightly wound spiral structure is observed with ALMA (Huang et al. 2018b), while in scattered light the structure could be described both as multiple rings (Avenhaus et al. 2018) or as another tightly wound spiral. Despite a very low amount of dust (Avenhaus et al. 2018), this is thought to be one of the largest disc with a radial extent of $\approx$ 950 au, measured from CO data, and a gas mass of $0.17 M_{\odot}$ (Pinte et al. 2018a)[3]. This would be consistent with a spiral induced by planet disc interaction in a massive disc with small H/R (in order for the spiral to be tight). However, note that in

[3] Ansdell et al. (2018) found a gas mass of $10^{-2}\, M_{\odot}$, which is lower than the one given by Pinte et al. (2018a). This discrepancy highlights the fact that we still have a large uncertainty on the gas mass measurements.

this parameter range, the disc would be also prone to gravitational instability, which may be responsible for the observed spiral.

6.3.3 Caveats

Our calculations consider only $\simeq 10$ orbits of the outer planets, due to computational resources. However, it is worth highlighting that the relation we found between the observed substructures and the disc Stokes number is time-dependent: in more evolved systems the gas has already been partially dissipated, involving lower Stokes number and more symmetric structures. Also, the gap carving process is determined by the viscous timescale and for lower Stokes number it requires a large number of orbits. This means that while the transition between spirals and more axisymmetric structures in the continuum is general, the threshold between the two regimes may be different with longer timescale simulations (i.e. $\mathrm{St}_0 < 0.4$).

From an observational point of view, to be able to distinguish between spiral and ring in scattered light one needs large pitch angle spiral, such the one in HD135344B or MWC758, unlike the one observed in TW Hya.

Moreover, it is important to note that in a single protoplanetary disc we can have regions with high and low Stokes number, resulting in a locally different coupling and so in different substructures. This can be due to both a lower/higher surface density regions (along the radial/vertical direction) and to different grain size populations in the same disc. In the first scenario, this is the result of the disc-planet interaction, with the formation of gaps and/or cavity (Dipierro et al. 2016; Ragusa et al. 2017), and of photo-evaporative process (Alexander et al. 2014), while in the second one this is the result of the process of grain growth and settling (Testi et al. 2014). For this reason, in order to obtain a more accurate study of the system, one should consider a single model with a wide range of dust grains sizes (Hutchison et al. 2018; Dipierro et al. 2018c). This is now possible with the new MULTIGRAIN utility that has been developed in the PHANTOM code.

6.4 Conclusions

One of the most crucial, unsolved, questions in the field of planet formation is "how massive are protoplanetary discs?" (Bergin & Williams 2018). Indeed, the gas mass affects how planets form and what is the origin of the substructures we observe in protoplanetary discs. In this paper we explore if there is a relationship between the observed morphologies (spirals, gaps, rings) and the gas mass. We have performed 3D dust and gas Smoothed Particle Hydrodynamics and radiative transfer simulations of protoplanetary discs with embedded planets, exploring different aerodynamical coupling between millimetre dust grains and gas and different aspect ratios.

The basic result of our work is that, as a result of planet-disc interaction, spiral structure observed in scattered light images would be observed as a circular, ring-like configuration in ALMA continuum emission for Stokes number close to unity or larger, corresponding to gas surface density $\lesssim 0.4\mathrm{g/cm}^2$. The observed prevalence of ring-like structures in ALMA images would thus imply that discs are generally less massive than $\approx 10^{-3}\,M_\odot$. Powell et al. (2019) use a method similar to ours

to estimate the gas disc mass but use the dust radial extent rather than the dust morphology to estimate the Stokes number. By using their method, they obtain an opposite result, in that most of the disc that they have considered would instead result in very massive discs, often close to gravitational stability. Further work is needed to resolve this discrepancy.

Chapter

7

On the gap of the DS Tau protoplanetary disc

Based on the paper by ***Benedetta Veronesi****, Enrico Ragusa, Giuseppe Lodato, Hossam Aly, Christophe Pinte, Daniel J. Price, Feng Long, Gregory J. Herczeg & Valentin Christiaens (2020), "Is the gap in the DS Tau disc hiding a planet?", Monthly Notices of the Royal Astronomical Society, 495, 1913*

Recent observations with the Atacama Large Millimeter Array (ALMA) and the SPHERE instrument on the Very Large Telescope (VLT) have revealed protoplanetary discs characterized by sub-structures in their thermal and scattered light emission, including inner holes (e.g. Dutrey et al. 2008; Brown et al. 2009; Andrews et al. 2011), gaps, rings (e.g. ALMA Partnership et al. 2015b; Hendler et al. 2018; Fedele et al. 2018; Dipierro et al. 2018a), and non-axisymmetric features such as horseshoes (e.g. Isella et al. 2013; Zhang et al. 2014; van der Marel et al. 2016c; Canovas et al. 2016; Fedele et al. 2017; Pinilla et al. 2017; van der Marel et al. 2018a; Casassus et al. 2018; Long et al. 2018b; Liu et al. 2018a), spirals (e.g. Muto et al. 2012b; Grady et al. 2013; Garufi et al. 2013; Benisty et al. 2015; Pérez et al. 2016; Stolker et al. 2016; Benisty et al. 2017) and shadows (e.g. Garufi et al. 2014; Avenhaus et al. 2014; Benisty et al. 2017; Avenhaus et al. 2017).

The most common substructure in recent ALMA surveys are rings and gaps (e.g Long et al. 2018b; Zhang et al. 2018 and Bae et al. 2018). Possible explanations include dust condensation at the snowlines (e.g. Zhang et al. 2015), dead zones (e.g. Flock et al. 2015) and the presence of planets embedded in the disc (e.g. Dipierro et al. 2015a, 2018a; Bae et al. 2017; Dong & Fung 2017a; Rosotti et al. 2016). In this work we focus in particular on the planets hypothesis.

Significant information can be extracted from the morphology of gaps. The size and shape of the gap is thought to constraint the mass of the carving planet (Kanagawa et al. 2015; Dong & Fung 2017a; Dipierro & Laibe 2017), while its

position inside the disc and its mass can tell us something about the migration history of the planet inside the disc. Planet masses inferred from gap widths are uncertain. First, the time evolution and initial conditions of the disc may lead to different gap shapes and therefore inferred mass for the gap-carving planet. Second, as pointed out also by Pinte et al. (2019) the gap width alone cannot uniquely constrain the planet mass because changes in the grain density (i.e. the Stokes number) can produce the same gap width with a different planet mass. For these reasons, estimates for planet masses should combine gap widths with other diagnostics.

Recent studies (Pinte et al. 2018b; Teague et al. 2018; Pinte et al. 2019; Casassus & Pérez 2019; Pinte et al. 2020) inferred the location and mass of some planets from the gas kinematics of the discs they were embedded in. Specifically, these studies search in different ways for velocity deviations (localised in both space and velocity) from the unperturbed Keplerian flow of the disc, induced by the presence of a planet, known as "kinks" and "Doppler flips". These revealed giant planets in HD163216 and HD97048.

Here, we study the protoplanetary disc orbiting around DS Tau, an M-type star ($0.83 M_{\odot}$, Lodato et al. 2019) in the Taurus star-forming region located at a distance of 159 pc (Gaia Collaboration et al. 2018). It has been observed in ALMA Cycle 4 program (ID: 2016.1.01164.S; PI: Herczeg) in Band 6 at 1.33 mm, at high-spatial resolution ($\sim 0.12''$, corresponding to ~ 16 au). This disc shows the widest gap (see Fig. 7.1, Long et al. 2018b) of the Taurus survey with a width[1] of 27 au centered at ≈ 33 au (i.e. $\sim 0.2''$). Assuming the planetary hypothesis for the origin of this gap, Lodato et al. (2019) estimated that a planet mass of $5.6 M_{\rm J}$ could have carved the gap, under the assumption that for low viscosity discs the gap width scales with the planet Hill radius as $\Delta = k R_{\rm H}$ (Dodson-Robinson & Salyk 2011; Pinilla et al. 2012b; Rosotti et al. 2016; Fung & Chiang 2016; Facchini et al. 2018b). Lodato et al. (2019) assumed a proportionality constant $k = 5.5$ derived from averaging hydrodynamical simulations results (Clarke et al. 2018; Liu et al. 2018a).

In this paper, we present a follow-up study by modeling the continuum emission of the protoplanetary disc orbiting around DS Tau, focusing on the gap observed in the Taurus survey and assuming its origin is due to a planet. By combining 3D hydrodynamical simulations of a suite of dusty protoplanetary disc models hosting one embedded protoplanet with 3D Monte Carlo radiative transfer simulations, we study the gap shape of DS Tau and also analyse the different observational predictions for a planet kink detectable in the gas kinematics. Here, we have chosen to explore the simplest model that can explain the formation of the gap, that is a single planet on a circular, non-inclined orbit, following Occam's razor. Other scenarios could be equally plausible but generally involve a larger number of free parameters. Among these, we might consider: a multiple planet system, a planet on an eccentric (Muley et al. 2019) or inclined orbit, a lower disc viscosity combined with a sub-Neptune mass planet (Dong et al. 2017, 2018a). Moreover, a higher resolution image could turn the observed broad disc ring into multiple narrow rings (e.g. HD 169142: Fedele et al. 2017 vs Pérez et al. 2019), something

[1] the gap width has been defined as the full width half maximum.

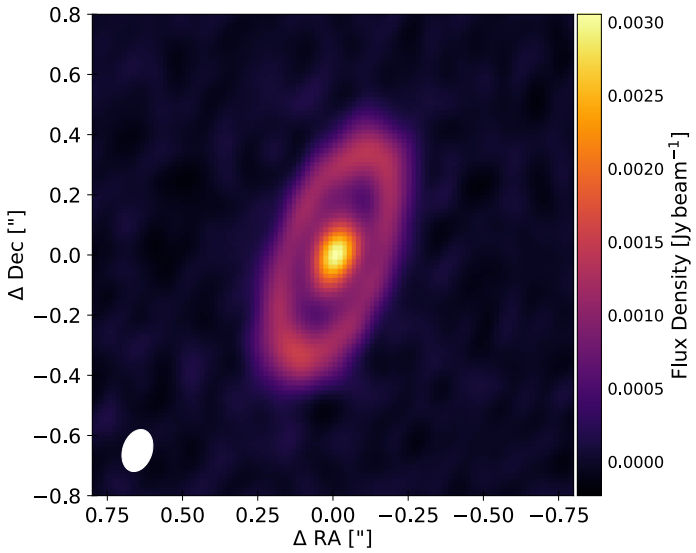

Figure 7.1: ALMA observation at 1.3 mm of the system DS Tau, with a beam size of $0.14'' \times 0.1''$ wide (image readapted from (Long et al. 2018b)).

that at present we cannot exclude but neither explore.

This paper is organised as follows: in Section 7.1 we describe our numerical method and simulation setup. In Section 7.2 we describe the results of the numerical simulations and the fitting procedure we use to find our best model. In Section 7.3 we discuss our modeling results for the continuum images and we analyse our kink prediction. We finally draw our conclusions in Section 7.4.

7.1 Methods

7.1.1 Dust and gas numerical simulations

We perform a suite of 3D Smoothed Particle Hydrodynamics (SPH) simulations of dusty protoplanetary discs, using the code PHANTOM (Price et al. 2018a). We adopt the multigrain (Hutchison et al. 2018) one fluid (for St<1, Price & Laibe 2015; Ballabio et al. 2018) method to simulate the dynamics and evolution of dust grains. In this algorithm, SPH particles representing gas and dust are evolved using a set of governing equations describing the gas-dust mixture (Laibe & Price 2014a). A dust fraction scalar is carried by the particles and is updated according to an evolution equation. This model is only suited for modelling small dust grains (St<1) since the formalism lacks the ability to represent large grains velocity dispersion. Moreover, the formalism employs the 'terminal velocity approximation' (e.g. Youdin & Goodman 2005) which greatly simplifies the governing equations and alleviates the need to temporally resolve the dust stopping time, significantly speeding up the computation. Back-reaction from the dust on to the gas is automatically included in this approach. In all our simulations we do not take into account the fluid self-gravity.

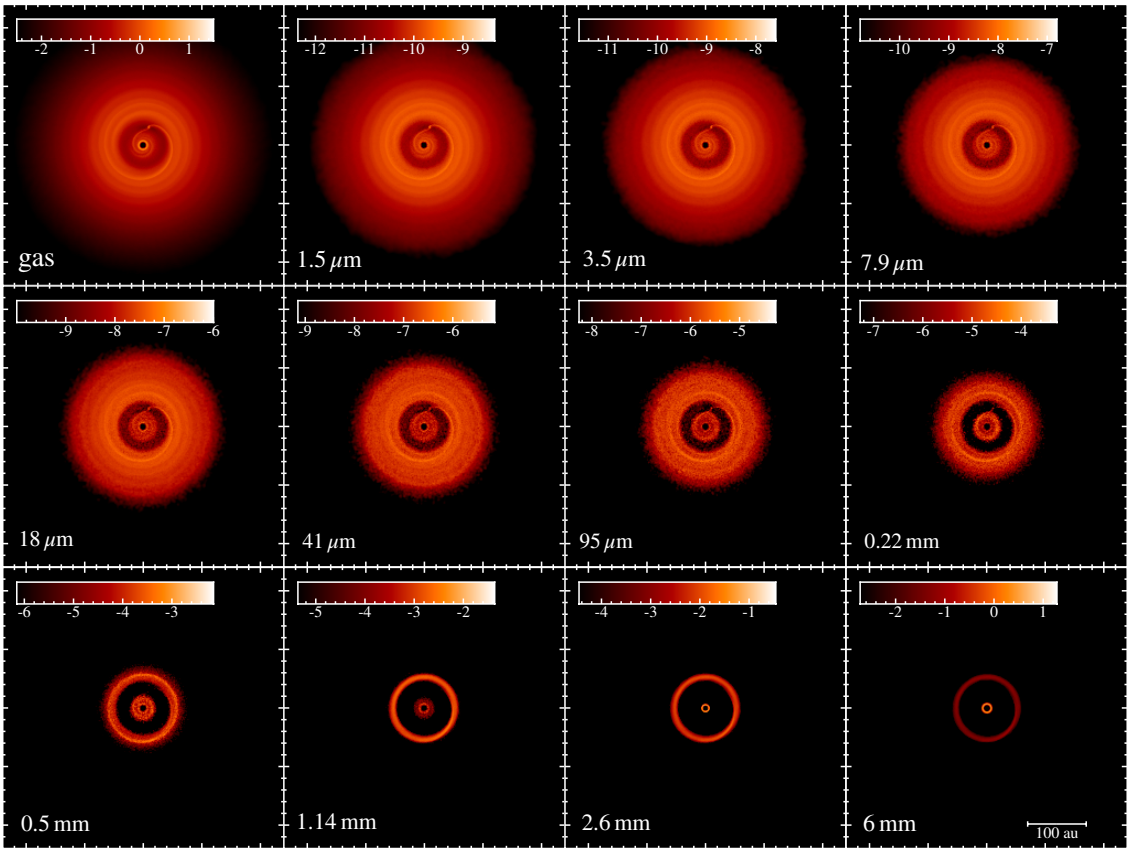

Figure 7.2: Rendered images of gas (first panel) and dust surface density (in units of g cm^{-2} on a logarithmic scale) of the $M_{\rm p,0} = 2\,M_{\rm Jup}$ hydrodynamic simulation after ≈140 orbits of the embedded planet at $R_{\rm p,0} = 34.5$ au. The dust density is presented for the 11 grain sizes simulated in our model (see Table 7.1).

7.1.2 Disc models

The parameter choice for our models is motivated by the observations of Long et al. (2018b) (see Table 7.1).

7.1.2.1 Gas and dust

The system consists of a central star of mass $M_\star = 0.83\,M_\odot$ (Lodato et al. 2019) surrounded by a gas and dust disc extending from $R_{\rm in} = 10$ au to $R_{\rm out} = 100$ au and modelled as a set of 10^6 SPH particles. The initial gas surface density profile is assumed to be a power law with an exponential taper at large radii, i.e.,

$$\Sigma_{\rm g}(r) = \Sigma_{\rm c} \left(\frac{r}{R_{\rm c}}\right)^{-p} \exp\left[-\left(\frac{r}{R_{\rm c}}\right)^{2-p}\right], \tag{7.1}$$

where $\Sigma_{\rm c}$ is a normalization constant, chosen in order to match the total disc mass, $R_c = 70$ au is the radius of the exponential taper and $p = 1$. We adopt a locally

Parameters	Value
$M_\star\,[M_\odot]$	0.83
$T_{\rm eff}$ [K]	3800
d [pc]	159
$i\,[^\circ]$	65
$R_{\rm in}$ [au]	10
$R_{\rm out}$ [au]	100
$R_{\rm c}$ [au]	70
p	1.
q	0.25
$\alpha_{\rm SS}$	0.005
$H/R_{\rm in}$	0.06
$M_{\rm dust}\,[M_\odot]$	$4.8 \cdot 10^{-5}$
$M_{\rm gas}\,[M_\odot]$	$4.8 \cdot 10^{-3}$
$a_{\rm d}$ [cm]	$[a_{\rm min} = 1.5 \cdot 10^{-4}, a_{\rm max} = 0.6, N = 11]$
$\rho_{\rm d}\,[{\rm g\,cm^{-3}}]$	1
$M_{\rm P}\,[M_{\rm j}]$	$1, 2, 2.5, 3, 5$
$R_{\rm P}$ [au]	34.5

Table 7.1: Model parameters. $M_\star$ is the star mass as in Lodato et al. (2019). $T_{\rm eff}$ is the effective temperature we use in our radiative transfer model, assuming the star to be radiating isotropically with a Kurucz spectrum at 3750 K. The disc is located in the Taurus star-forming region at a distance d (Gaia Collaboration et al. 2018) with an inclination i (Long et al. 2018b). $R_{\rm in}$ and $R_{\rm out}$ are the initial condition for the disc inner and outer radius. R_c and p are respectively the radius of the exponential taper and the power-law index of the gas surface density profile defined in Eq. 7.1. q is the power-law index of the sound speed radial profile (see Eq. 7.2) and $\alpha_{\rm ss}$ is the effective Shakura & Sunyaev (1973) viscosity. $H/R_{\rm in}$ is the disc aspect ratio at the inner radius. $M_{\rm dust}$ and $M_{\rm gas}$ are the dust and gas disc initial mass. In our model we have $N = 11$ dust grains a_d, logaritmically spaced between $a_{\rm min}$ and $a_{\rm max}$, with intrinsic grain density ρ_d. $M_{\rm p}$ and $R_{\rm p}$ are the mass and the radial position in the disc of the planet.

isothermal equation of state $P = c_s^2 \rho_g$, with

$$c_s = c_{s,in} \left(\frac{R}{R_{in}} \right)^{-q}, \tag{7.2}$$

where $c_{s,in}$ is the sound speed at the inner disc radius and ρ_g is the gas volume density. We assume $q = 0.25$ as the power-law index of the sound speed radial profile. The disc is vertically extended by assuming a Gaussian profile for the volume density and ensuring vertical hydrostatic equilibrium

$$\frac{H}{R} = \frac{c_s}{v_k} = \frac{H}{R_{in}} \left(\frac{R}{R_{in}} \right)^{1/2-q}, \tag{7.3}$$

where v_k is the Keplerian velocity and $H/R_{in} = 0.06$ is the aspect ratio at the reference radius R_{in}. We model the angular momentum transport throughout the disc using the SPH artificial viscosity (Price et al. 2018a, see Sec. 2.6) with $\alpha_{AV} = 0.3$, which results in a Shakura & Sunyaev (1973) viscous parameter $\alpha_{SS} \approx 0.005$.

For the dust we use the same functional form of the initial surface density as for the gas (Eq. 7.1), assuming a dust mass of $M_{dust} = 4.8 \cdot 10^{-5}\, M_\odot$. In our SPH simulations the disc mass is fixed, while to fit the continuum emission we rescale it (i.e. the dust mass) as a free parameter (this is possible since the back-reaction is negligible). The dust-to-gas ratio is initially assumed constant for the whole disc extent (dust/gas = 0.01), so that the dust has the same vertical structure as the gas. After a few orbits of the planet, the dust settles down forming a layer with thickness (Dubrulle et al. 1995; Fromang & Nelson 2009)

$$H_d = H_g \sqrt{\alpha_{ss}/(St + \alpha_{ss})} \tag{7.4}$$

where α_{ss} is the Shakura & Sunyaev (1973) viscous parameter, H_g and H_d are respectively the gas and dust disc height, St is the Stokes number (i.e. $St = t_s \Omega_k$, Weidenschilling 1977).

We perform simulations with the multigrain one-fluid method considering 11 grain sizes logarithmically spaced in a range between 1.5 μm and 6 mm with a grain size distribution $dn/da \propto a^{-3.5}$. In this multi-grain method, the dust and gas evolve simultaneously, allowing us to take into account the back-reaction of the dust on the gas, and to simulate different levels of coupling between the two disc components. We note that the back-reaction in our models is in principle negligible for an initial dust-to-gas ratio equal to 0.01. Additionally, even if we consider a later stage in the evolution of our system, the maximum dust-to-gas ratio is still ~ 0.1. In Fig. 7.2 we show for illustrative purposes the gas (first panel) and the 11 grains dust surface density maps of the disc model with $M_{p,0} = 2\, M_{Jup}$, after ≈ 140 orbits of the planet (at the initial planet location $R_p = 34.5$ au). Increasing the grain size (from top to bottom) leads to increases in the width and depth of the gap carved by the planet. Moreover, for larger dust grains the dust disc extent is smaller because of radial drift.

7.1.2.2 Properties of the embedded planets

In each disc model we embed one planet with an initial mass of $M_p = [1, 2, 2.5, 3, 5]\, M_j$ at a radial distance from the central star of $R_p = 34.5$ au slightly more distant

than the 33 au centroid of the gap to account for some migration. The planet orbit is assumed to be initially circular and coplanar. We model the planet and the central star as sink particles, free to migrate and which are able to accrete gas and dust (Bate et al. 1995). The accretion radius of each planet is chosen to be one quarter of the Hill radius. Lodato et al. (2019) estimated a planet mass equal to $M_{\rm p} = 5.6\,M_{\rm Jup}$ in order to open a gap as wide as the one observed in DS Tau by Long et al. (2018b).

We have also attempted to simulate planets with $M_{\rm p} > 5\,M_{\rm Jup}$ (Lodato et al. 2019), but we do not discuss them, since upon an initial analysis the radial flux profile we obtain in these cases is too different with respect to the observations. Moreover, the planet mass derived from the gap width gives an upper limit estimate.

7.1.3 Radiative transfer and synthetic observations

We compute synthetic observations of our disc models by performing 3D radiative transfer simulations, by means of the MCFOST code (Pinte et al. 2006, 2009), starting from the results of the hydrodynamical simulations. Our goal is to compute the dust continuum for Band 6 (1.3 mm, Long et al. 2018b) and Band 3 (2.9 mm, Long et al. 2020) and the CO, ^{13}CO and C^{18}O isotopologue channel maps.

The main inputs for the radiative transfer modelling are the gas and dust density structure, a model for the dust opacities and the source of luminosity. We used a Voronoi tesselation where each MCFOST cell corresponds to a SPH particle. We adopted the DIANA dust model for the dust opacity (Woitke et al. 2016; Min et al. 2016), assuming a fixed dust mixture composed of 70% silicate, 30% amorphous carbonaceous. Note that the shape and the width of a gap carved by a fixed planet mass might change for different opacity values and different Stokes number (e.g. for different grain porosity, fluffiness or shape, see Pinte et al. 2019).

The expected emission maps at 1.3 mm and 2.9 mm are computed via ray-tracing, and using 10^8 photon packets to sample the radiation field, assuming a disc inclination of $i = 65°$ (Long et al. 2018b). We use a passively heated model, where the source of radiation is assumed to be the central star, located at the centre of the coordinate system, with parameters described in Table 7.1. The full-resolution images at 1.3 mm directly produced by MCFOST is then convolved with the same Gaussian beam of the observations reported in Long et al. (2018b), 0.14 $\times$ 0.1 arcsec ($\sim 22\times16$ au at 159 pc). In order to compute the CO, ^{13}CO and C^{18}O isotopologue channel maps in the J=2-1 transitions we perform radiative transfer simulations, assuming $T_{\rm gas} = T_{\rm dust}$ and that the emission is at LTE. We include in our simulations freeze-out where $T < 20$ K and photo-dissociation induced by UV radiation. We consider a velocity resolution of $0.2\,{\rm kms}^{-1}$. We then convolve the obtained channel maps with a 40 mas beam (~ 6.5 au at the source distance).

7.2 Results

Our main goal is to reproduce the ALMA continuum image at 1.3 mm observed by Long et al. (2018b), as shown in Fig. 7.1. For a more accurate analysis we focus

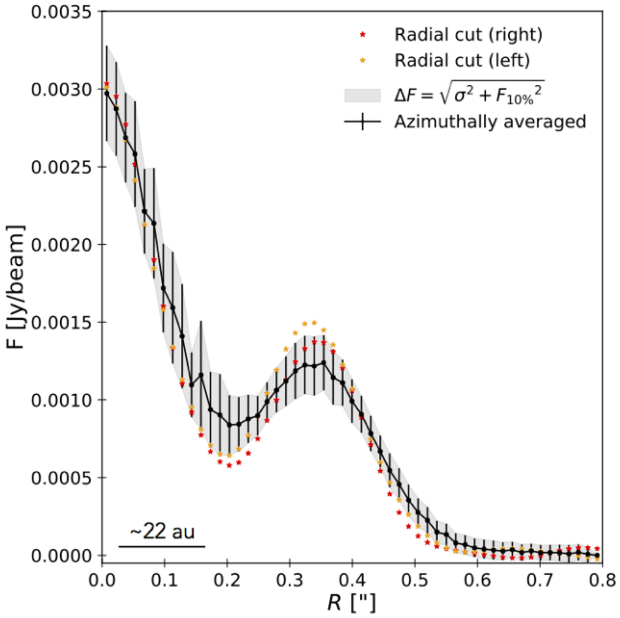

Figure 7.3: Radial flux intensity profile for the ALMA continuum image at 1.3 mm (see Fig. 7.1). In black we show the azimuthally averaged profile while in red and orange the radial cut along the disc major axis. The error is obtained as the root mean square of σ and the 10% of the flux value $F_{10\%} = 0.1 \times F(R)$. In the left corner is reported the projected beam size along the disc major axis $0.14''$.

on the radial intensity profile along the disc major axis (i.e. radial cut). Fig. 7.3 shows both the azimuthally averaged radial intensity profile (black lines) and the radial cut (red and orange markers). We also compute the errors by considering the quadratic sum of the standard deviation σ and of the 10% of the flux at each radii (Long et al. 2018b). The standard deviation with respect to the azimuthally averaged radial profile has been computed by deprojecting the disc on a planar surface and binning it into 40 annuli (to match the beam resolution).

7.2.1 Fitting the radial profiles

For a better comparison between our models and observations, and in order to reproduce the correct gap shape, we study the radial intensity profile along the disc major axis. Fig. 7.4 shows the radial intensity profile for the disc described in Sec 7.1.2.1 with a dust disc mass of $4.8 \cdot 10^{-5}\, M_{\rm Jup}$ and an initial planet mass in the range $M_{\rm p,0} = [1, 2, 2.5, 3, 5]\, M_{\rm Jup}$. As mentioned in Sec. 7.1.2.2, we excluded from our analysis systems with a planet mass $> 5\, M_{\rm Jup}$, since their gap shape was too different with respect to the data (as one can already notice in the radial flux intensity profile obtained with $M_{\rm p,0} = 5\, M_{\rm Jup}$, see Fig. 7.4). Lines with different colours describe the time evolution of the system (increasing from blue, $N_{\rm orb} = 50$, to dark red, $N_{\rm orb} = 250$) while the data are presented as black star markers. The better match between the models and the observations is found for the $M_{\rm p,0} = 2\, M_{\rm Jup}$ case, but the flux needs to be rescaled by a constant factor. In

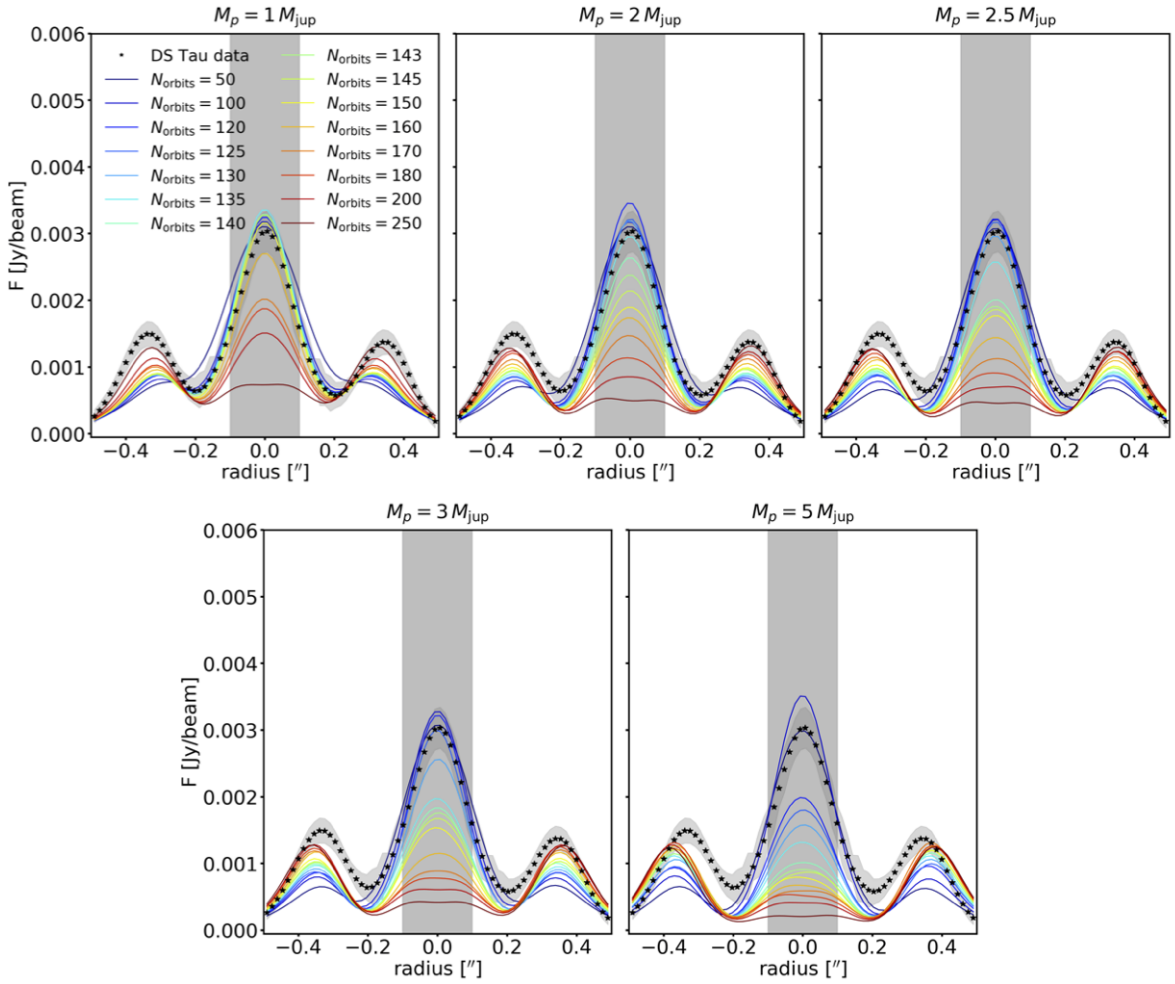

Figure 7.4: Radial flux intensity profile along the disc major axis for the models with initial planet masses $M_{\rm p,0} = [1, 2, 2.5, 3, 5]\,M_{\rm Jup}$ (from left to right) and for a dust disc mass of $M_{\rm dust} = 4.8 \cdot 10^{-5}\,M_{\rm Jup}$. Different line colours represent the time evolution of the system in terms of planet orbits from 50 (dark blue line) to 250 (dark red line). The grey shaded area $R < 0.1$" corresponds to the region we excluded from the fitting procedure described in Sec. 7.2.1.1.

order to fit both the $M_{\rm p}$, the time evolution of the system, the dust disc mass (i.e. the flux intensity), we performed MCFOST simulations considering values of gas-to-dust between 10 and 150 for all the orbit snapshots collected in Fig. 7.4 (keeping the gas mass constant at $M_{\rm gas} = 0.0048$). It is important to highlight that, since the dust-to-gas ratio in our simulation is always $\ll 1$ and so the back-reaction of the dust onto the gas is negligible, it is possible to rescale $M_{\rm dust}$, without affecting the disc dynamics.

As the system evolves, the shape of the intensity profiles shows a similar behaviour for all planet masses. After an annular gap is opened, the inner disc is progressively depleted, both in gas and dust. This is due to a combination of factors. Firstly, the tidal torques produced by the planet reduce the mass accretion rate into the inner portion of the disc (c.f. Ragusa et al. 2016). Secondly, large dust grains are trapped at the pressure maximum and are thus filtered out from the inner regions (Rice et al. 2006b). Thirdly, there is some spurious evacuation of material from the inner disc, since as the surface density of the gas is reduced, we lose resolution, increasing the SPH artificial viscosity, which in turn speeds up the cavity depletion. Moreover, the increased pressure gradient at the inner boundary accelerates the radial drift in the inner regions. The depletion observed in the inner disc in our models could be explained also by the fact that in our simulation we are not considering dust growth, so we might be neglecting an opacity contribution from larger grains. Finally, we note that by increasing the planet mass, the position of the ring outside the gap moves outward, and that as the system evolves, the planet accretes gas from the disc, so its mass grows with time.

In order to find the best fit model to the data, we thus perform a χ^2 fit assuming as free parameters the planet mass, the scale factor for the dust density and the planet number of orbits. For this last parameter we stop at 170 orbits. After this time, especially for higher planet masses, the inner disc becomes optically thin due to the partially artificial draining of the inner disc. We show the result as a function of the disc dust mass in panels [A,B,C,D,E] of Fig. 7.5, corresponding to different initial planet masses in the range $M_{\rm p,0} = [1, 2, 2.5, 3, 5]\, M_{\rm Jup}$. Different line colours represents different planet orbits in our simulations, from 50 (dark blue line) to 250 (dark red line). We then proceed as follows: for each planet mass we consider the best matching model in terms of minimum χ^2 for the various choices of dust mass and number of orbits. We then compare the best models for different planet masses. In the bottom-right panel of Fig. 7.5 we plot the minimum χ^2 obtained for each planet mass, as a function of the instantaneous planet mass, both with (black markers) and without (red markers, see Sec. 7.2.1.1) the inner region $R < 0.1''$. Grey (and red) arrows connect the value of the current mass with its initial value. The best fitting model corresponds to the case with an initial planet mass $M_{\rm p,0} = 2 M_{\rm Jup}$, which corresponds to $3.5 \pm 1\ M_{\rm Jup}$. We estimated the mass uncertainty via bootstrapping the data. In this way we computed the χ^2 on 10000 new samples taken from the measured data set itself.

Lodato et al. (2019) estimate a planet mass of the order of 5.6 $M_{\rm Jup}$, assuming that the gap width was $\sim 5.5 R_{\rm Hill}$. Our best fitting model yields a smaller value, which results in a gap width $\Delta / R_{\rm Hill} = 7.3$, which is slightly higher compared to the value obtained by Lodato et al. (2019).

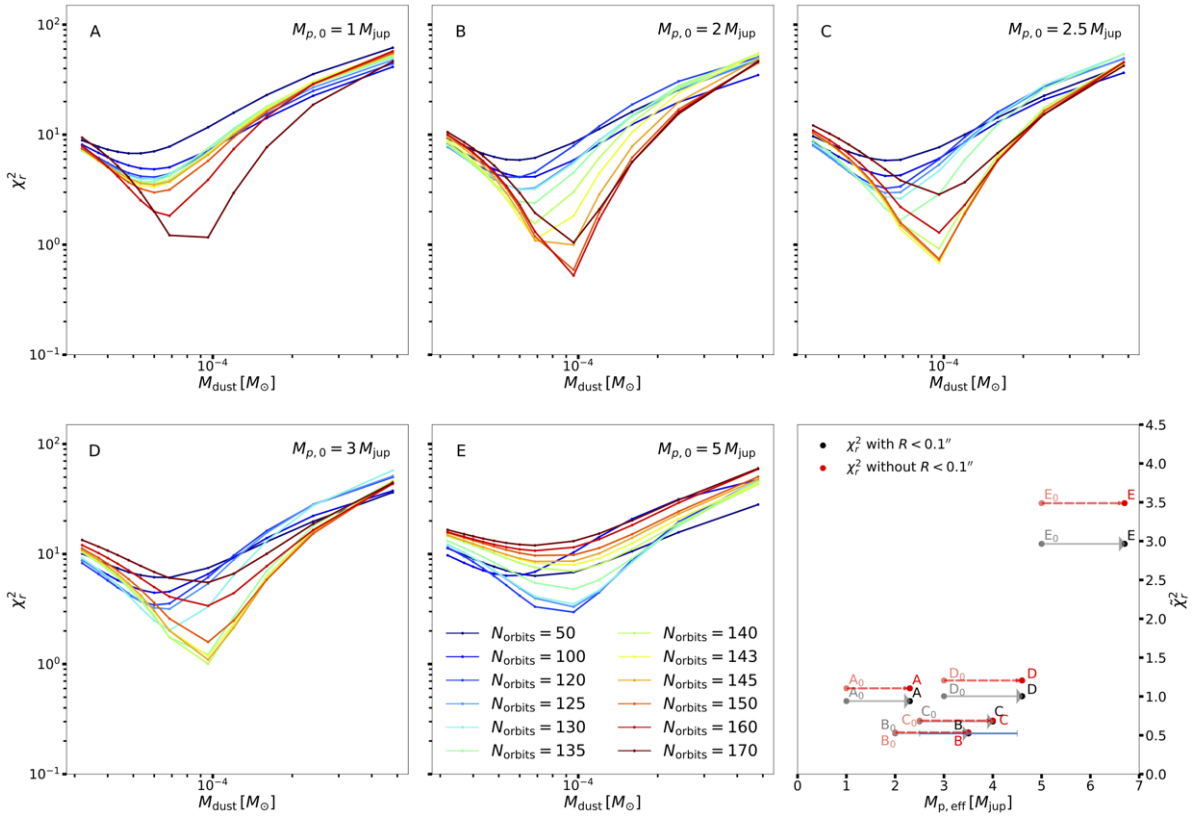

Figure 7.5: Reduced chi squared χ^2_r as a function of the disc dust mass (A,B,C,D,E panels). In each panel we show results obtained for our models with initial planet masses $M_{p,0} = 1, 2, 2.5, 3, 5\,M_{Jup}$, while different colours correspond to the time evolution in our models, from $N_{orb} = 50$ (dark blue line) to $N_{orb} = 170$ (dark red line). Minimum reduced chi squared $\tilde{\chi_r}^2 = \min(\chi^2_r)$ (bottom-right panel) from [A,B,C,D,E] panels, as a function of the planet mass in unit of Jupiter masses. The black markers represent the results obtained considering the disc extent $-0.5'' < R < 0.5''$, while the red ones represent results obtained excluding the inner region $-0.1'' < R < 0.1''$. The letters with the $_0$ subscript represent the initial planet mass values, and are connected to the final ones by grey arrows. The value of the planet mass that minimise the $\tilde{\chi_r}^2$ is $M_p = 3.5 \pm 1\,M_{Jup}$. The error has been obtained via bootstrapping the data.

7.2.1.1 Fitting procedure excluding $R < 0.1$"

Due to the possible numerical effects that accelerate the formation of a cavity (discussed in Sec. 7.2.1), and in order to check the robustness of our result, we repeat the fit procedure described in the previous section excluding the flux inside a radius $R < 0.1$" (grey band in Fig. 7.4). This allows us to evaluate the exact portion of the disc which contains the gap and the outer ring, avoiding the possible contamination with regions that could have an evolution influenced by numerical effects. Indeed, we do expect physically to see an inner depletion due to radial drift, on larger timescales with respect to the number of orbits in our models. The results obtained are presented by red markers in the bottom-right panel of Fig. 7.5. We recover for the planet mass the same value found in Sec. 7.2. We also note that the minimum reduced χ^2 for the $M_{p,0} = 1, 3, 5\, M_{\rm Jup}$ cases is slightly higher than found previously.

7.3 Discussion

7.3.1 Dust continuum

In this Section we discuss our results starting from the dust continuum synthetic images at both 1.3 and 2.9 mm wavelengths obtained with MCFOST.

7.3.1.1 ALMA synthetic images and gap shape

The result we obtain from our χ^2 test show that a planet with a mass of $3.5\, M_{\rm Jup} \pm 1$ is the best fit in order to reproduce the gap shape. The quoted uncertainty clearly refers to the specific model that we assume and additional systematic uncertainty arises if one considers extra degrees of freedom (e.g. multiple planets, orbit eccentricity and inclination, lower viscosity). Moreover, having kept as free parameters the dust disc mass and the evolution time of our system, we also obtain that the disc should have a gas-to-dust ratio of 50 with a dust mass of $9.6 \cdot 10^{-5}\, M_\odot$ (similar to what we have fixed in our SPH simulations).

Concerning the time evolution of the system, the best outcome for our modeling is reached in different time for different planet masses. This is to be expected, since more massive planets carve their gaps faster compared to smaller ones. We also note that by the end of our simulations the system has not reached a steady state configuration. However, it is important to remember that in reality such a quasi steady-state condition does not exist: the disc and planet secularly evolve due to planet migration and accretion processes (note that, often, modeling efforts *assume* that the planet does not migrate nor accrete, and that is why they are able to reach a quasi-steady state: this is not the approach that we have adopted here). What is important is that the number of orbits in our models is enough to avoid transients on a short time scale and that the initial conditions have washed out. This is certainly achieved in our case, as we evolve the simulation for $\gtrsim 100$ orbits.

Fig. 7.6 shows the comparison between the data and our modeling for the DS Tau disc for both 1.3 (first row) and 2.9 (second row) mm wavelengths. Left

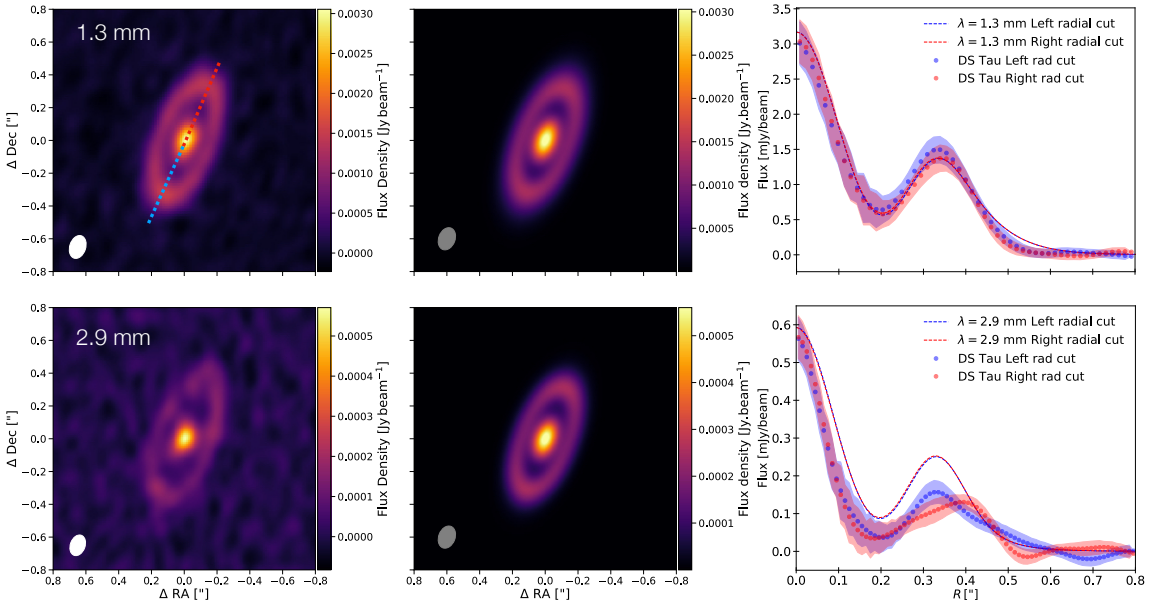

Figure 7.6: *First row*: ALMA observation (left panel) and continuum mock image (center panel) of the DS Tau disc at 1.3 mm. The synthetic image has been computed for our best fit model ($M_{\rm p} = 3.5\,M_{\rm Jup}$ and $M_{\rm dust} = 9.6 \cdot 10^{-5}\,M_{\odot}$). The Gaussian beam we take to convolve the full resolution image has been chosen to reproduce the observations reported by Long et al. (2018b) and Long et al. (2020), respectively $0.14'' \times 0.1''$ and $0.13'' \times 0.09''$. In the 1.3 mm image we highlight in blue the left side of the major axis and in red the right side. Right panel shows the comparison between the left (blue) - right (red) side of the radial cut along the disc major axis for the data (dot marker) and the modeling (dashed line). *Second row*: Same as first row but for the 2.9 mm continuum image. ALMA images have been readapted from Long et al. (2018b) and Long et al. (2020).

panels show the ALMA continuum images from Long et al. (2018b) for the 1.3 mm wavelength and from Long et al. (2020) for the 2.9 mm one. Center panels show the synthetic images, that have been computed for our best fit model (performed on the 1.3 mm case) parameters: $M_{\rm p} = 3.5\,M_{\rm Jup}$, $M_{\rm dust} = 9.6 \cdot 10^{-5}\,M_{\odot}$ and $t = 145$ orbits (discussed in Sec. 7.2.1). The right panels of Fig. 7.6 compare radial cuts of the flux intensity profile along the disc major axis obtained from the synthetic image at 1.3 and 2.9 mm (top and bottom center panel of Fig. 7.6) with the ALMA data (top and bottom left panel). The left (blue) and right (red) side of the radial cut correspond to the left and right side of the disc major axis. Dot markers represent the data, while the models are in dashed lines.

By looking at the synthetic images, the gap shape and the flux of the observation are recovered in our models at 1.3 mm and 2.9 mm. We note that in both cases we end up with a slightly higher peak flux with respect to the observation. An interesting point is that by looking at the real ALMA image at 1.3 mm the ring has a brighter spot in the lower part. This can be due to an inclination effect, though this feature is missing in our model. Also, if we consider the 2.9 mm comparison, the data show an asymmetry in the ring that seems to be more elongated in the right-end side of the major axis. This feature is also not recovered in our model.

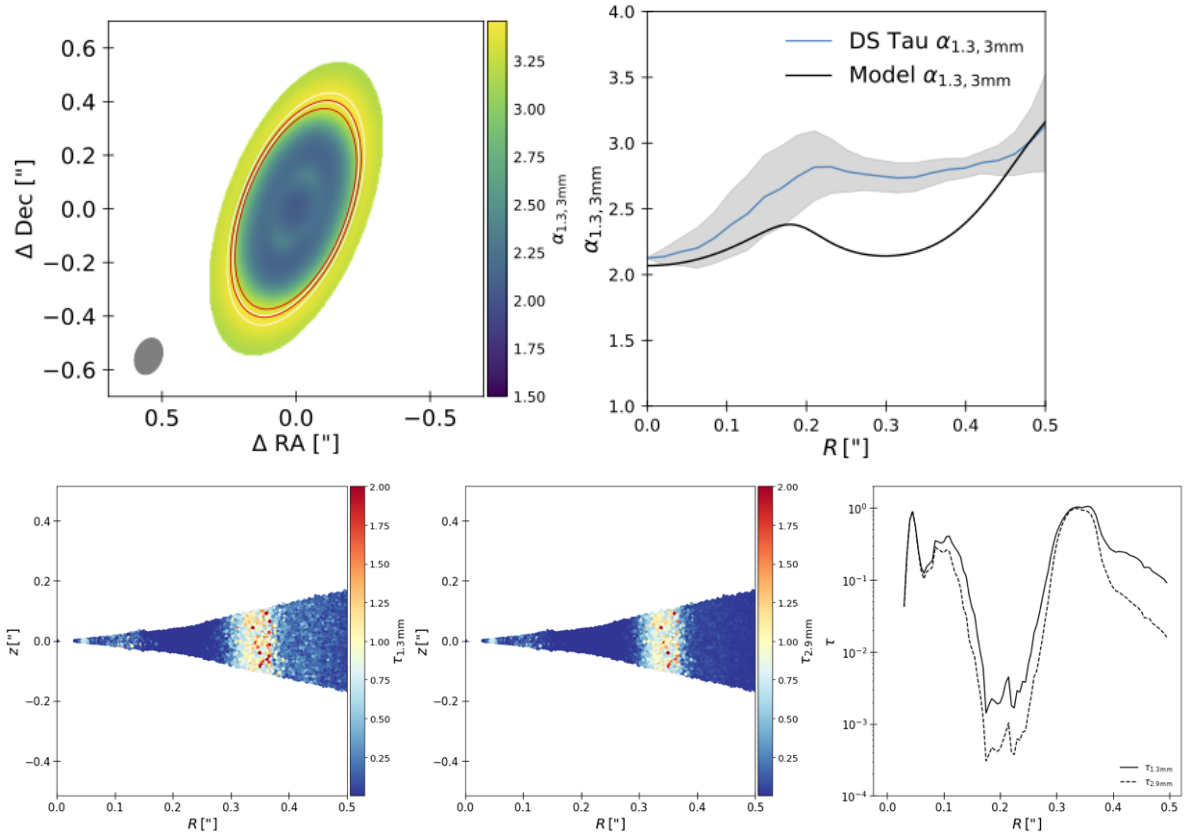

Figure 7.7: *First row.* Map (left panel) and radial cut along disc major axis (right panel) of the spectral index $\alpha_{1.3,2.9mm}$. Red and white contour lines in the left panel indicate the approximate size of the disc in the 1.3 (white line) and 2.9 (red line) mm images. Central panel shows the spectral index α obtained by Long et al. (2020). *Second row.* Left and central panels: vertical section of the optical depth as a function of the radius at 1.3 mm and 2.9 mm, respectively. Right panel: azimuthal and vertical average of the optical depth as a function of radius. The solid line represents τ at 1.3 mm while the dashed line at 2.9 mm. The disc appears to be generally optically thin, but approaches $\tau = 1$ in the ring.

By a comparison of the synthetic images obtained for the two wavelengths, the 2.9 mm one seems more compact with respect to the other one due to radial drift (see also Fig. 7.2). We will discuss in Sec. 7.3.1.2 what we can learn from this modeling regarding the dust distribution inside the disc.

The peak of our radial profiles at both wavelengths is slightly higher with respect to the data. This can be due to different dust opacity or to the fact that in our fitting procedure we excluded the flux contribution from a region with radius $R < 0.1''$. If we consider the 1.3 mm case, for which we have reduced χ^2 fitting process, the gap shape of our model reproduces the one of the data. Instead, for the 2.9 mm case, we note that the model flux is higher by a factor of 0.7 with respect to the data for the entire disc extent.

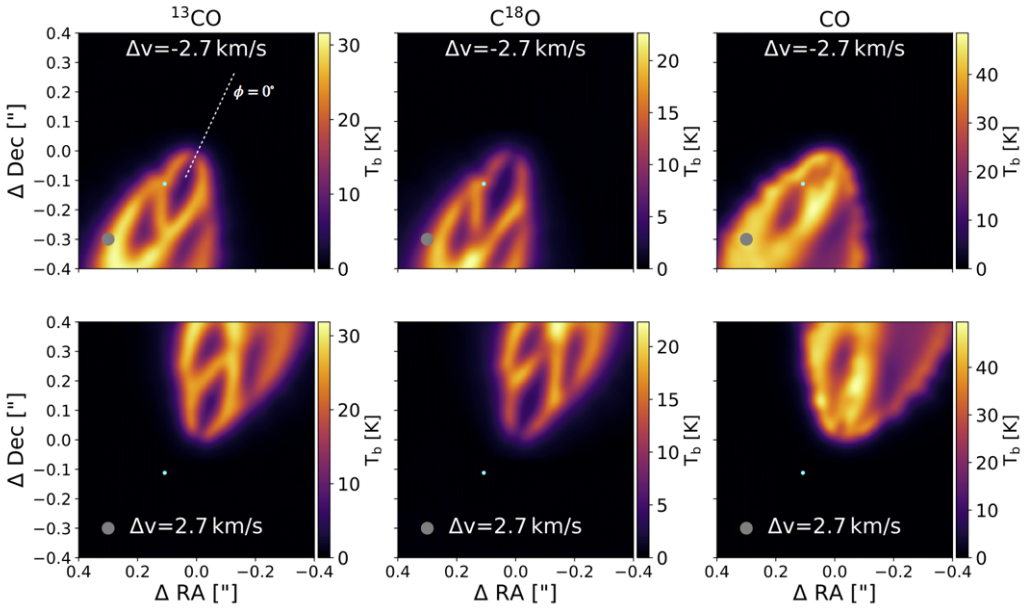

Figure 7.8: Synthetic ^{13}CO, C^{18}O and CO ALMA channel maps (J=2-1 transitions) for our best model with $M_p = 3.5\,M_{Jup}$ (cyan dot). The disc inclination is $i = 65°$ (Long et al. 2018b), the images have been convolved with a 40 mas Gaussian beam. The azimuthal planet position is $\phi = 225°$ with respect to the reference case ($\phi = 0°$, dashed white line). We notice that the kink produced by the planet is detectable at -2.7 km/s with a velocity resolution of $0.2\,\mathrm{kms}^{-1}$.

7.3.1.2 Dust trapping?

Having multiwavelength data for the same system allows to analyse the dust distribution inside the disc. In particular, a change in the spectral index α provides information about the grain size in discs (Testi et al. 2014). When dust trapping occurs, α is expected to be ≈ 2, which is smaller than the value tipically found in the ISM, $\alpha_{ISM} \simeq 3.5{-}4.0$ (Draine 2006; Ricci et al. 2010). Our simulations do produce dust traps (see Fig. 7.2), such that larger grains collect in narrower rings. We can thus test whether such traps also show up as a change in the spectral index.

Since we obtained both the 1.3 and 2.9 mm synthetic images, we compute the spectral index $\alpha_{1.3,2.9mm}$

$$\alpha_{\nu_1,\nu_2} = \frac{\log(\nu_2 F_{\nu_2}) - \log(\nu_1 F_{\nu_1})}{\log \nu_2 - \log \nu_1}\,, \tag{7.5}$$

with $\nu_1 = 1.3$ mm and $\nu_2 = 2.9$ mm. In Fig. 7.7 we show the resulting spectral index, both as a map (left panel) and as a radial cut along the disc major axis (central panel) in comparison with the $\alpha_{1.3,2.9mm}$ radial profile (blue line) found by Long et al. (2020). We note that at $\simeq 0.3''$ we have a spectral index $\alpha_{1.3,2.9mm} \simeq 2$. This can be due to two different reasons: there could be dust trapping in the ring region, or the disc may be optically thick. Thus, we compute with MCFOST the disc optical depth τ_ν, where in each cell τ_ν is computed from the center of the cell

to $z = +\infty$ (and $-\infty$). Then, for each Voronoi cell of the model we sum the optical depth towards the $+z$ and the $-z$ direction. The results are displayed in the lower row of Fig. 7.7. In the first two panels we show the vertical cut of the map of the optical depth for each cell. In these plots SPH noise is visible, so we also compute the azimuthal and vertical average of the optical depth within concentric annuli. The results of the azimuthally and vertically averaged optical depths are shown in the right panel of Fig. 7.7, with a solid line for 1.3 mm and a dashed line for 2.9 mm. While the disc appears to be generally optically thin, the ring is marginally optically thick. Thus, we cannot draw any firm conclusion on the origin of the spectral slope. Comparing our results with the one presented in Long et al. (2020), the shape of the spectral index radial profile is similar between the model and the data. Indeed, we qualitatively reproduce the features observed in the data: a local minimum and maximum, with an increase in spectral index at larger radius. The actual value of the spectral index is different between the two cases. This can be due to dust grain properties (maximum grain size, dust composition, morphology) in our model not in agreement with the real conditions of DS Tau. This results in different spectral index and different opacity in the optically thin case. Moreover, we point out that considering higher levels of porosity and fluffyness for the dust produces differences in the spectral index profile with respect to the compact case (Kataoka et al. 2014).

However, this observed decreasing of α could also be motivated if we consider the presence of larger grains near the ring region. In general, a more precise estimate of the optical thickness of the disc is necessary in order to confirm it.

7.3.2 Is it possible to detect the planet from gas kinematics?

The ubiquity of rings and gaps in recent observations of proto-planetary discs poses one important question: if all these structures have been formed by embedded planets, why are we not able to observe them, apart from few cases such as PDS 70 (Keppler et al. 2018; Isella et al. 2019; Mesa et al. 2019)? A possible way of answering this question and understanding what is the correct origin scenarios for these structures is to study the kinematics of these systems, in particular looking for kinks.

Assuming that the observed gap is due to a planet with a mass of $M_{\rm p} = 3.5\,M_{\rm Jup}$ (see Sec 7.2.1), we check if it can be detected via "kinks" in the gas channel maps. Therefore, we study the kinematics to determine whether the observational capabilities of ALMA would allow us to detect such a planet at such a distance ($\approx$ 30 au) from the central star. For our purpose we choose a channel velocity resolution of 0.5 km/s and an angular resolution of 40 mas. Fig. 7.8 shows the computed channel maps for the three CO-isotopologue, for two different channels, with Δv equals to -2.70 and 2.70 km/s from the systemic velocity. We assure the planet is at an azimuthal position of $\phi = 225°$ with respect to the reference case (dashed white line). The planet position is plotted in cyan. We note that a kink at the planet location is visible in the $\Delta v = -2.7$ km/s channel but not in the symmetrical one at $\Delta v = 2.7$ km/s.

In Fig. 7.9, we collect channels from -4.10 to -1.30 km/s and from 1.30 to 4.10 km/s. The kink appears localised both in space and in velocity in channels

from -3.5 to -1.9 km/s. It is necessary to highlight that there are other similar features, e.g. in channels from 2.10 to 2.70 km/s, which could actually be due to the inside borders of the gap. As a first analysis, the main difference between the two features is that for the planet-induced kink there is an asymmetry between the left and right side of the disc, while for the geometric feature the deviation is symmetric.

To check what is the threshold needed in (spatial and velocity) resolution to be able to observe it, we perform a further analysis, varying the azimuthal angle, the angular and the velocity resolution. We also performed a test in order to determine what is the minimum mass detectable in this system according to our models ($M_{\rm p,fin} = 2.3\,M_{\rm Jup}$), at a distance of ≈ 30 au from the star.

7.3.2.1 Minimum detectable planet mass test: $M_{\rm p} = 2.3\,M_{\rm Jup}$

We present here the channel maps computed for a planet with a mass of $2.3\,M_{\rm Jup}$. We perform this test to check what is the minimum planet mass detectable by ALMA at the distance of ≈ 30 au from the star, according to our models. As reference case, we use the best observational parameters we found in Sec. 7.3.2: an angular resolution of 40 mas, an azimuthal planet position of $\phi = 225°$ and a velocity resolution of $v_{\rm res} = 0.2{\rm kms}^{-1}$. Fig. 7.10 shows the three CO-isotopologue channel map (CO left column,^{13}CO center column ,C^{18}O right column), for two different channels, with Δv equals to -2.7 (top row) and 2.7 (bottom row) km/s from the systemic velocity. The channel maps we recover for this planet are very similar to the one presented in Sec. 7.3.2. The kink should be detectable also in this case in the channel with $\Delta v = -2.7$ km/s.

7.3.2.2 Changing the azimuthal angle

To be able to judge the robustness of our prediction of a velocity kink feature shown in Sec. 7.3.2, we need to investigate the dependence of this feature on the azimuthal position of the planet, the velocity resolution, and the beam size. Fig. 7.11 shows the channel maps for the C^{18}O isotopologue (as best case), varying the azimuthal planet position ($\phi = 65°, 90°, 265°, 315°$ from left to right). For each azimuthal position, the first row shows the channel in which the planet kink is detectable at different Δv with respect to the systemic one, while the second one is its symmetrical one. Taking into account also the channel maps obtained with $\phi = 225°$ in Fig. 7.8, we highlight that the kink feature changes for different planet azimuth. Also it appears more detectable for the 225°, 265° and 315° cases. It is interesting to note that when the planet is closer to the disc minor axis ($\phi = 90°$ or $\phi = 265°$) the kink appears to be visible in a channel and in its symmetrical one.

7.3.2.3 Changing the angular resolution

We also computed channel maps for different beam size and channel velocity resolution, keeping the planet azimuth fixed at $\phi = 225$. Fig. 7.12 shows the results obtained with beam size of $30, 40, 50, 70$ mas. The velocity resolution is 0.2 km/s. Reaching a beam resolution of both 30,40 mas would allow to clearly detect the

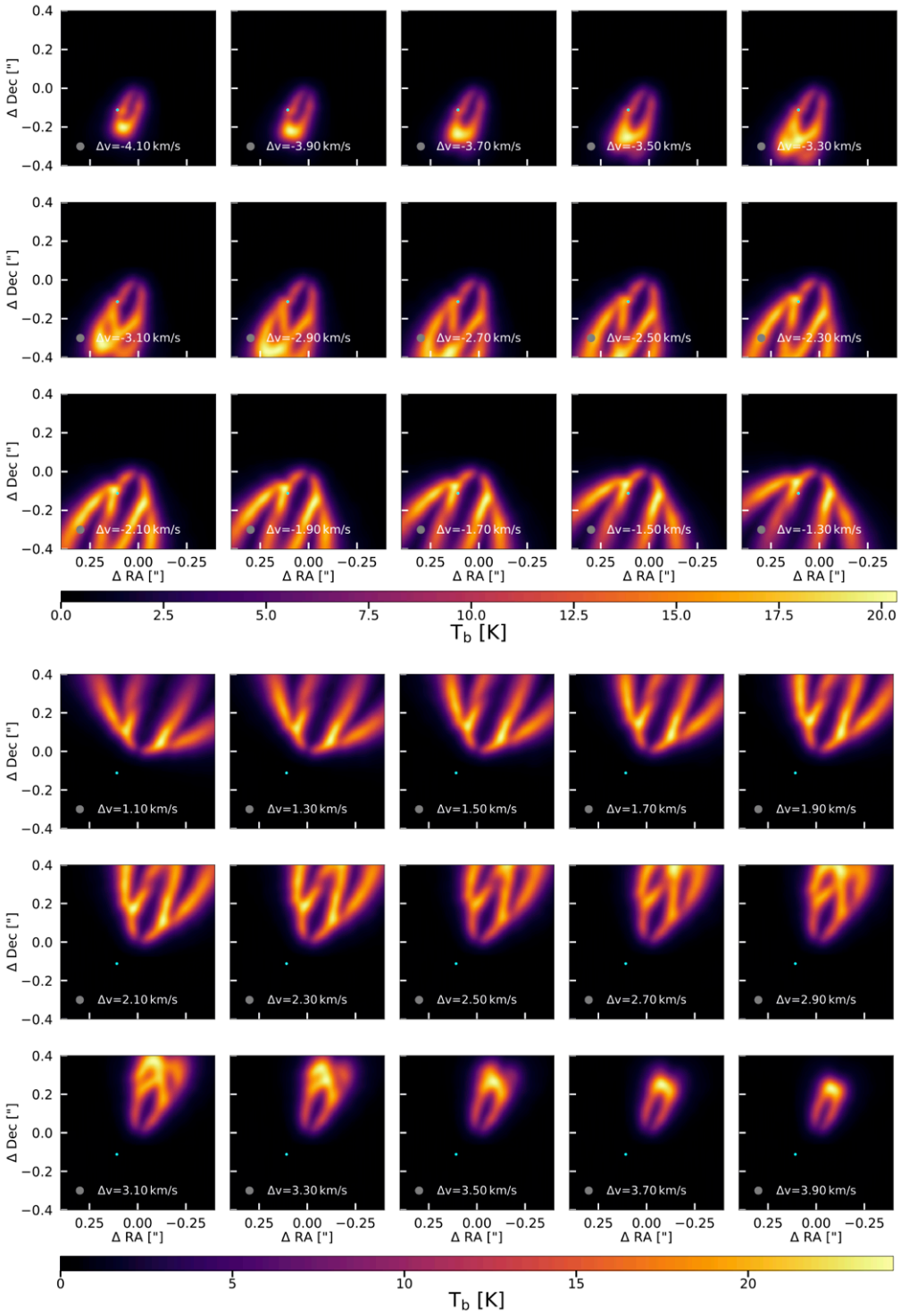

Figure 7.9: Channel maps for $C^{18}O$ isotopologue with a velocty resolution of 0.2 km/s, from -4.10 to -1.30 km/s, and from 1.30 to 4.10 km/s. The azimuthal position of the planet is $\phi = 225°$. The beam resolution is 40 mas.

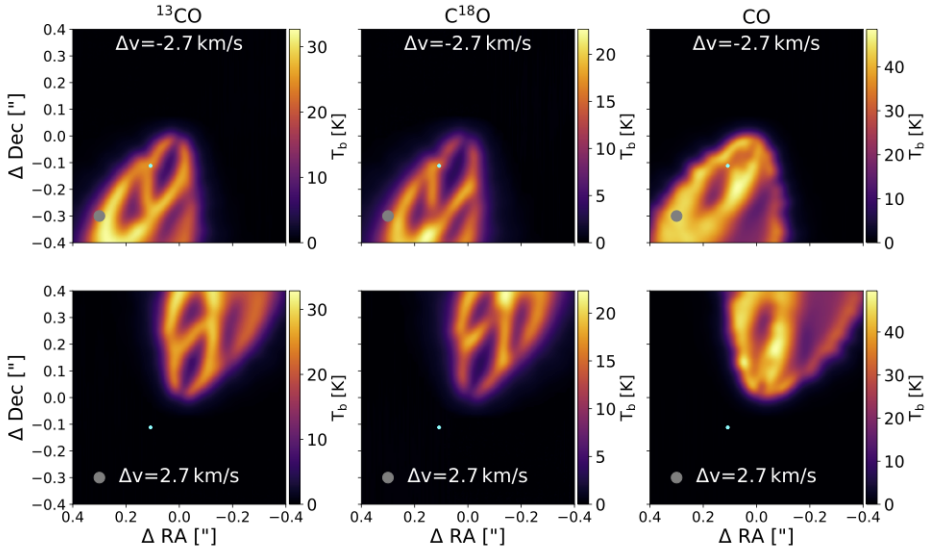

Figure 7.10: Channel maps obtained for a planet with mass $M_\mathrm{p} = 2.3\,M_\mathrm{Jup}$. Columns show the ^{13}CO (left column), C^{18}O (center column), CO (right column) isotopologue channel maps with a velocity resolution of 0.2 km/s, $\phi = 225°$ and with a beam resolution of 40 mas. The velocity channel of the first row is the one in which the kink is visible ($\Delta v = -2.7$ km/s), while the second row shows its opposite ($\Delta v = 2.7$ km/s).

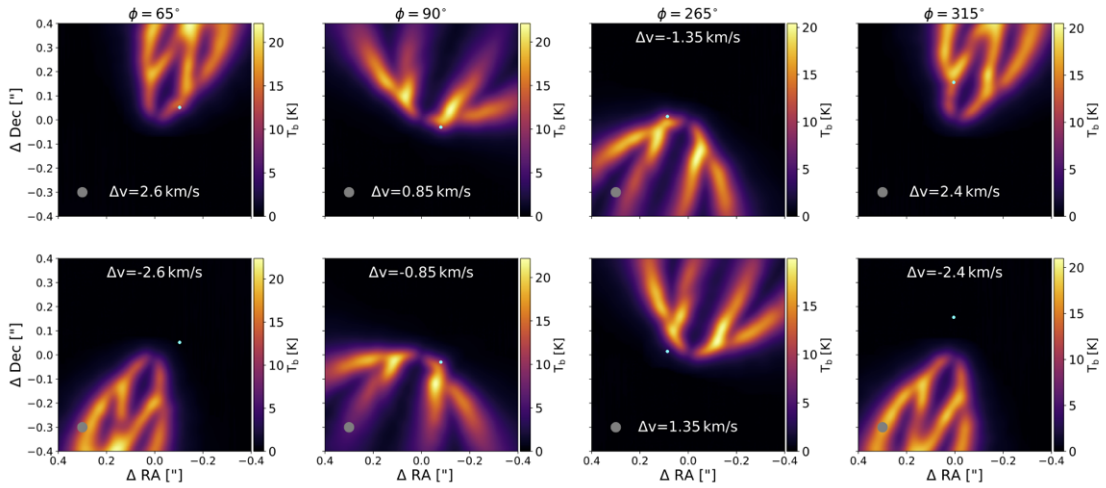

Figure 7.11: Synthetic C^{18}O ALMA channel maps (J=2-1 transitions) for our best model with $M_\mathrm{p} = 3.5\,M_\mathrm{Jup}$ (cyan dot). With respect to Fig. 7.8 we changed the planet azimuthal position, $\phi = [65°, 90°, 265°, 315°]$ (from left to right).

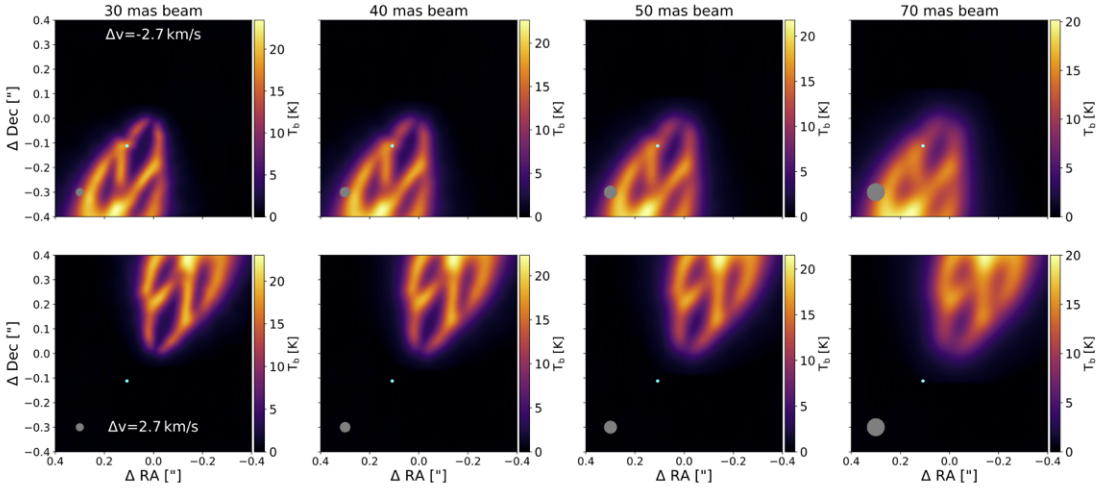

Figure 7.12: Channel maps for $C^{18}O$ isotopologue with a velocity resolution of 0.2 km/s and a beam size of [30,40,50,70] mas (from left to right). The azimuthal position of the planet is $\phi = 225°$.

kink at the planet location, while at 50 mas it is barely visible and at 70 mas it is not detectable.

7.3.2.4 Changing the velocity resolution

Fig. 7.13 shows channel maps obtained by changing the channel velocity resolution in the range [0.1,0.2,0.3,0.5] km/s (from left to right). We kept the planet fixed at an azimuthal location of $\phi = 225°$. The beam size is set to 40 mas. The kink feature is detectable with all the velocity resolutions.

To summarise, with this more detailed analysis in which we vary both the beam and velocity resolution we found that a planet kink in this system would be detectable using a beam of [30,40] mas (barely visible with 50 mas), and velocity resolution between 0.1 and 0.5 km/s. A more detailed study about the probability of detecting or not a planet depending on its azimuthal position would be necessary. Moreover, also if a kink is not detectable, having access to gas kinematics data could be useful to map the height of the two side of the CO-isotopologue layer in the disc and check if there are some discrepancies due to the presence of a planet (Pinte et al. 2018b).

7.4 Conclusions

In this paper we modeled the gap shape observed by Long et al. (2018b) and Long et al. (2020) around the DS Tau star. Assuming that a planet has carved the gap, we performed 3D dust and gas Smoothed Particle Hydrodynamics and radiative transfer simulations of protoplanetary discs with one embedded planet, considering different values for the planet mass.By comparing the simulated dust gap/ring morphology with observations, we derive a best-fit planet mass and compare the

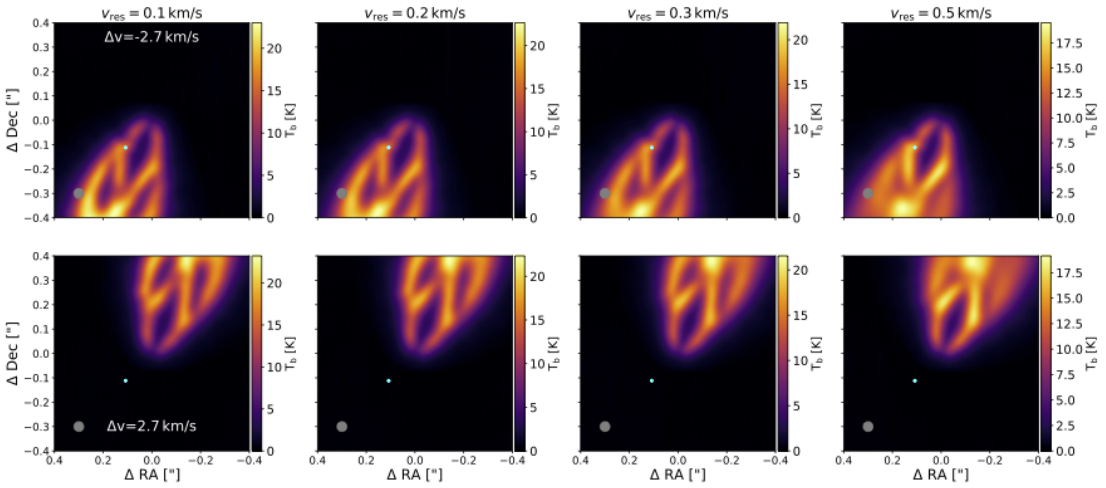

Figure 7.13: Channel maps for $C^{18}O$ isotopologue with a velocity resolution of 0.1, 0.2, 0.3 and 0.5 km/s (from left to right). The azimuthal position of the planet is $\phi = 225°$. The beam resolution is 40 mas.

result with simple analytical calculations (Lodato et al. 2019). We also studied the gas kinematics in order to check if a kink produced by the embedded planet would be visible in the channel maps.

The basic result of our modeling is that the planet we expect to be responsible for the gap observed in DS Tau should have a mass of $M_p = 3.5 \pm 1\, M_{Jup}$. We recall that this confidence interval should be interpreted in the light of the chosen one-planet model. For future developments, it would be interesting to gradually add other degrees of freedom in order to explore other formation scenarios. To reach this result, we performed a χ^2 test comparing the major axis radial profile of the data with the ones obtained by the different planet mass models. To match the correct flux, we also performed different radiative transfer models varying the gas-to-dust ratio from our initial reference case (i.e. 100) in order to take into account different dust disc masses. The outcome of this fitting procedure is that the dust mass required to produce the observed ALMA images is of $9.6 \cdot 10^{-5}\, M_\odot$. Another interesting point to be noted is that in order to recover the correct gap shape, it is necessary to study the system in its time evolution. Indeed, as time increases, the inner disc is gradually depleted, paving the way for a cavity to originate at a later stage (see Sec. 7.2.1 for a discussion about possible numerical effects that might affect the dust depletion in the inner disc).

Starting from this result, we then computed the CO, ^{13}CO and $C^{18}O$ isotopologue channel maps. We found that a planet with 3.5 Jupiter masses, with a channel width of 0.3/0.5 km/s and a beam size of 70 mas, would be barely detectable in the gas kinematics through the kink feature. Instead, by assuming a slightly higher (0.2 km/s) velocity resolution, and by choosing a slightly smaller (i.e. 40 or 50 mas) beam size the kink appears to be visible. Moreover, we showed that changing the azimuthal position of the planet results in different kink signatures.

Chapter

8

A dynamical mass estimate for Elias 2-27

Based on the paper by ***Benedetta Veronesi*** *et al., (2021) "A dynamical measurement of the protoplanetary disc mass in Elias 2-27", AstroPhysical Journal Letter, accepted for publication*

Protoplanetary discs form in the chaotic environment of molecular cloud cores and in their early stages they are massive enough to have a non negligible effect on the evolution of the overall system. The disc self-gravity may influence the disc dynamics through the propagation of density waves that lead to the formation of prominent structures in the form of one or more spiral arms. These morphologies have been detected by ALMA and VLT-SPHERE in both Class 0/I and Class II systems, and they are usually assumed to be originated by embedded companions (e.g. HD135344B, Veronesi et al. 2019, MWC 758, Calcino et al. 2020) or by self-gravity (e.g. Elias 2-27, Pérez et al. 2016; Huang et al. 2018b). In the second case, density waves are thought to provide a non negligible contribution to the angular momentum transport and may have a crucial role in the formation of planetesimals through dust trapping at the location of the spirals and the following direct fragmentation of spiral overdensities into bound objects (Rice et al. 2004; Rice et al. 2006a; Kratter & Lodato 2016). Being able to give an estimate of the disc mass is the first step in order to put other pieces in the puzzle of planet formation and to understand the origin of the observed spirals (van der Marel et al. 2020; Veronesi et al. 2019; Bergin & Williams 2018). But how can we determine the mass of these systems?

First, dust masses are typically inferred using the optically thin approximation at millimeter wavelengths. It is worth noting that, although it may be trivial, this estimate still carries a high level of uncertainty, due to the assumed optical depth of the dust at (sub-)mm wavelengths (e.g. the dust opacity and the level of

dust growth, Bergin & Williams 2018). Once the dust mass is known, one needs to convert this into a total disc mass by assuming some gas/dust ratio, which is generally assumed to be equal to 100 (Draine 2003), although this number is highly uncertain (see e.g. Macias et al. 2021). On the other hand, it is more difficult to quantify the disc mass from direct gas tracers. A common procedure is to use CO observations in its various isotopologues (such as ^{13}CO and C^{18}O) as a proxy for the gas mass. But since the conversion of the observed CO mass into total gas mass is not well understood (Williams & Best 2014; Bergin & Williams 2018), this is not straightforward. Another issue adding complexity to the problem is that the properties of different molecules also vary spatially and temporally, depending on the models (Ilee et al. 2017; Quénard et al. 2018). Indeed, estimates derived from CO observations result in very low disc masses compared to dust estimates (Pascucci et al. 2016; Ansdell et al. 2016; Miotello et al. 2017; Long et al. 2017). Miotello et al. (2016) associated this trend with multiple possible processes: carbon depletion in the disc (Favre et al. 2013; Bosman et al. 2018; Cleeves et al. 2018), photodissociation in the upper layers, freeze-out at the disc midplane or in general other isotope-selective processes. Another aspect that should be considered comes from far-IR HD lines (Bergin et al. 2013; Trapman et al. 2017) observations, suggesting that the gas-to-dust ratio measurement is affected by the fact that the emitting regions of various gas tracers differ from each other and in turn differ from the regions where the dust is observed.

We can also estimate the total disc mass in a dynamical way, by using the disc rotation curve, and detecting deviations from the expected Keplerian curve. This method has been widely used with galaxies (Barbieri et al. 2005) and sometimes it has been used to estimate also the mass of AGN discs (Lodato & Bertin 2003). Usually protoplanetary discs are assumed to be Keplerian, since typically the stellar mass dominates over the disc mass, and their rotation curve can be sufficiently well described by the stellar contribution alone. Instead, when the disc contribution is significant, we could be able to fit the observed rotation curve and to give an independent disc mass estimate (Bertin & Lodato 1999). For relatively massive discs, this dynamical estimate is now possible since we have access to a large amount of gas kinematic data with high (angular and velocity) resolution and high sensitivity. From these data, we can infer the geometry of the disc and recover the height and the velocity of the emitting gas layer (Pinte et al. 2018a).

One of the most interesting observed spiral structures is the one hosted by the protoplanetary disc orbiting around Elias 2-27. Elias 2-27 is a young 0.8 Myr M0 star (Andrews et al. 2009) located at a distance of ∼115 pc (Gaia Collaboration et al. 2018) in the Ophiucus star-forming region (Luhman & Rieke 1999). The surrounding disc is unusually large and massive, with a disc-to-star mass ratio of ∼ 0.3 (Andrews et al. 2009; Pérez et al. 2016), as estimated by converting dust mass into total disc mass with the usual gas/dust ratio of 100. ALMA observations of this system detected two large-scale spiral arms (Pérez et al. 2016), which have been confirmed in the DSHARP survey at higher resolution (Andrews et al. 2018a). Together with these spiral arms, a 14 au wide, inner gap, located at 69 au from the star (Huang et al. 2018c,b) has been observed. Recent studies have confirmed that a possible origin for the spiral arms is the development of

gravitational instabilities (Meru et al. 2017; Hall et al. 2018; Forgan et al. 2018; Bae & Zhu 2018b; Hall et al. 2020; Paneque-Carreno et al. 2021). However, this physical mechanism does not explain the origin of the dust gap, which could have been carved by a companion of $\sim$0.1 $M_{\rm Jup}$ as constrained from hydrodynamical simulations by Zhang et al. (2018). Moreover, localized deviations from Keplerian motions at the location of this dust gap have been found recently, reinforcing the hypothesis of a planetary-mass companion (Pinte et al. 2020). Yet, it has been shown that a low-mass inner companion would be able to explain the gap but not the origin of the observed spiral arms (Meru et al. 2017). With this background in mind, we decided to take a closer look at the rotation curve of this system in order to provide a dynamical mass estimate of the disc independent of dust-CO measurements and to test the viability of gravitational instabilities as the origin of the observed grand-design spiral structure.

In this paper we study the rotation curve of the protoplanetary disc orbiting around Elias 2-27 by comparing two competing models: a Keplerian disc model and a self-gravitating disc model (Bertin & Lodato 1999; Lodato & Bertin 2003). The gravitational field has been computed by solving the Poisson equation including the central point-like object and the disc contribution (Bertin & Lodato 1999). We fit the two models to the rotation curve obtained in Paneque-Carreno et al. (2021) (following the method proposed by Pinte et al. 2018a to derive the height of the CO emitting layer) from the gas CO observations.

8.1 The rotation curve of a protoplanetary disc

where $M_\star$ is the mass of the central object, Φ_σ is the disc contribution to the gravitational potential and where we also consider the pressure gradient (under the assumption of a barotropic disc). However, we expect the contribution of the pressure gradient to the rotation curve to be negligible when compared to the disc self-gravity contribution. Indeed, for a marginally stable self-gravitating disc the disc contribution is of the order of H/R, while the pressure term is $O(H^2/R^2)$, where H is the pressure scale height (Kratter & Lodato 2016). To compute the pressure gradient we consider a disc temperature profile $T(R) \propto R^{-q}$, with $q = 0.5$ (with $T = 25$ K at $R = 60$ au, corresponding to a disc aspect ratio at this location of $H/R = 0.11$, Pérez et al. 2016). We consider two models for the rotation curve of the disc orbiting around Elias 2-27: a Keplerian disc model and a self-gravitating disc model. Usually the Keplerian model is considered when $M_{\rm disc} \ll M_\star$, since in this case the contribution of the disc to the gravitational field is negligible (Pringle 1981). The Keplerian model has also been used by Paneque-Carreno et al. (2021) to estimate the stellar mass.

In polar cylindrical coordinates, the radial gravitational field generated by the disc can be written as:

$$\frac{\partial \Phi_\sigma}{\partial R}(R,z) = \frac{\mathcal{G}}{R}\int_0^\infty \left[K(k) - \frac{1}{4}\left(\frac{k^2}{1-k^2}\right)\times\left(\frac{R'}{R} - \frac{R}{R'} + \frac{z^2}{RR'}\right)E(k)\right]\sqrt{\frac{R'}{R}}k\sigma\left(R'\right)dR' \tag{8.1}$$

where $E(k)$ and $K(k)$ are complete elliptic integrals of the first kind, and $k^2 = 4RR'/[(R+R')^2+z^2]$ (see Gradshteyn & Ryzhik 1980). Bertin & Lodato (1999)

computed the field $\mathrm{d}\Phi_\sigma/\mathrm{d}R$ in the equatorial plane by taking the limit $z \to 0$. Instead, we are interested in computing the rotation curve for the gas at a given height. The vertical position $z(R)$ has been determined by Paneque-Carreno et al. (2021), tracing the emitting layers of the CO-isotopologues channel maps with the method outlined in Pinte et al. (2018a), and has been parameterized as:

$$z(R) = z_0 \left(\frac{R}{R_0}\right)^{\psi} + z_1 \left(\frac{R}{R_0}\right)^{\varphi} , \tag{8.2}$$

where z_0, z_1, ϕ, ψ are fitting parameters reported in Table 2 of Paneque-Carreno et al. (2021) and R_0 is equal to 115.88 au. Note that a major finding of Paneque-Carreno et al. (2021) is that the West and East side of the disc show an asymmetry in the height of the gas layer, so the fitting parameters differ for the two sides of the disc. **Furthermore,** the two isotopologues considered (^{13}CO and C^{18}O) **trace different vertical layers of the disc, and thus, will have distinct fitting parameters**. We also take into account the vertical position of the gas $z(R)$ when computing the Keplerian gravitational field in Eq. **??**, as

$$\Omega^2_{\mathrm{Kep}} = \frac{\mathcal{G}M_\star}{(R^2 + z(R)^2)^{3/2}} , \tag{8.3}$$

where $z(R)$ is defined in Eq. 8.2. The total disc surface density profile has been chosen after Pérez et al. (2016) and Andrews et al. (2009) as,

$$\Sigma(R) = \Sigma_c \left(\frac{R}{R_c}\right)^{-p} \exp\left[-\left(\frac{R}{R_c}\right)^{2-p}\right] , \tag{8.4}$$

where Σ_c is a normalisation constant assumed to be a free parameter of the model, while $R_c = 200$ au is the truncation radius and the power-law index is fixed at $p = 1$. We choose these values for the parameters to match the ones that were parametrized by Pérez et al. (2016) and Paneque-Carreno et al. (2021).

8.2 Results

Rather than performing a complete analysis of the channel maps, as done in Paneque-Carreno et al. (2021), we here take their constraints for the rotation curve and directly fit such rotation curve with two analytical competing models, the self-gravitating (see Eqs. **??** and 8.1) and the Keplerian one (see Eq. 8.3), using an MCMC algorithm as implemented in EMCEE (Foreman-Mackey et al. 2013). We choose 300 walkers and 3500 steps (where the convergence has already been reached at ∼2500 steps). We also compare the data with a simple power-law fit, given by

$$f(R) = p_1 \cdot R^{-p_2} \tag{8.5}$$

where p_1 is a normalisation constant and p_2 the power-law slope. An exponent $p_2 = 0.5$ would point to a Keplerian disc, while $p_2 < 0.5$ to the presence of a self-gravitating disc. Instead, an exponent $p_2 > 0.5$ could be suggesting a warp or the presence of chaotic accretion from the cloud (at large scale). In the analysis

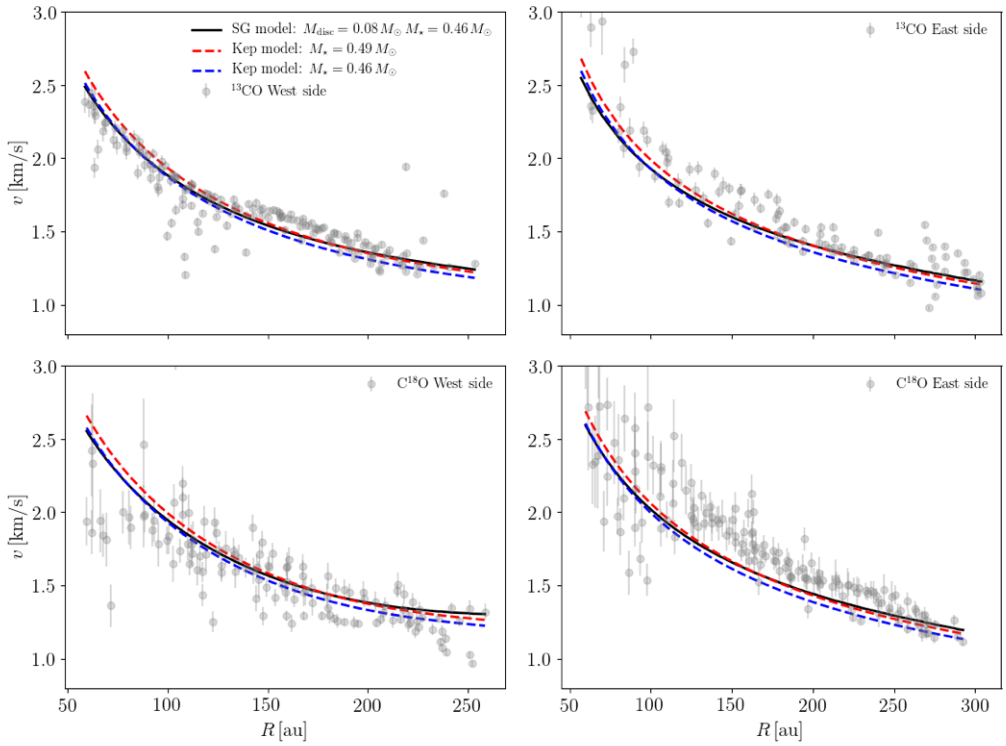

Figure 8.1: Rotation curve for the ^{13}CO and C^{18}O isotopologues for different models. The fitting procedure has been done simultaneously for the East (right column) and West (left column) side velocity data (plotted as grey markers), and for the two CO-isotopologues (top: ^{13}CO; bottom: C^{18}O). The black solid line corresponds to the self-gravitating fit, the red dashed line to the Keplerian fit and the blue dashed one to the Keplerian curve obtained with the star mass from the SG fit.

presented below, we do not fit the data points in the inner 60 au, since this region is strongly affected by the observed dust gap (Huang et al. 2018c; Paneque-Carreno et al. 2021), and shows noisier data. However, we have also performed the fit also including this region, obtaining results similar to those showed in the following Sections.

A detailed description of the velocity data used here can be found in Paneque-Carreno et al. (2021), along with the procedure used to obtain the height of the CO emitting layer, and we refer the reader to that paper for details. Here we just point out that, due to their higher signal-to-noise, the error bars are much lower for the ^{13}CO data than for the C^{18}O data. Also note that we do not radially bin the data points obtained by Paneque-Carreno et al. (2021) and that different velocity points related to the same radius arise from different azimuthal angles, highlighting the intrinsic non-axisymmetry of the disc. Still, our fitting model is by construction axisymmetric, since we are interested in the overall gravitational field of the disc, and we thus expect some non-negligible residuals to our fitting procedure due to this.

8.2.1 Combined fit

In Fig. 8.1 we show the results obtained with the Keplerian (see Eq. 8.3, red and blue dashed lines) and self-gravitating (see Eqs. **??** and 8.1, black solid lines) models, when simultaneously fitting all the data points (but considering the height profiles separately) for both CO isotopologues and for both sides of the disc, shown in separate panels for clarity, with the East and West side of the disc on the right and left columns, respectively, and the two CO-isotopologues (top: ^{13}CO; bottom: C^{18}O). The red line corresponds to the Keplerian best fit model, the blue line shows the rotation curve for a Keplerian disc where the star mass has been fixed to the one found with the self-gravitating best fit. The values obtained for the fit parameters are reported in the third column of Table 8.1. The East data points, especially for the C^{18}O, tend to lie above the best fit curves, since in this combined fit the model naturally tends to reproduce the lower uncertainty ^{13}CO data. If we first look at the power-law model, once we leave the freedom of a general power-law index, the best-fit value of the exponent p_2 is smaller than 0.5 ($p_2 = 0.43 \pm 0.03$), by more than 2σ. This already suggests that the data are better reproduced by a self-gravitating model. In such a model, the disc mass obtained from the combined fit is $M_{\rm disc} = 0.08 \pm 0.04\,M_\odot$ with a star mass $M_\star = 0.46 \pm 0.03\,M_\odot$. Note that we obtain a non-zero measurement of the disc mass too within $\sim 2\sigma$ uncertainties. Instead, in the Keplerian case, the star mass is $M_\star = 0.49 \pm 0.01\,M_\odot$. For both models, the stellar mass is in agreement with previous estimates (Paneque-Carreno et al. 2021).

	^{13}CO	C^{18}O	Combined fit
Keplerian fit			
$M_\star\,[M_\odot]$	$0.50^{+0.01}_{-0.01}$	$0.46^{+0.03}_{-0.03}$	$0.49^{+0.01}_{-0.01}$
Self-gravitating fit			
$M_\star\,[M_\odot]$	$0.45^{+0.03}_{-0.03}$	$0.43^{+0.05}_{-0.07}$	$0.46^{+0.03}_{-0.03}$
$M_{\rm disc}\,[M_\odot]$	$0.1^{+0.05}_{-0.04}$	$0.08^{+0.08}_{-0.05}$	$0.08^{+0.04}_{-0.04}$
$\lambda = \Delta(\chi^2_{\rm red})$	2.16	-0.19	1.38
Power-law fit			
p_1	$13.46^{+2.39}_{-2.07}$	$25.31^{+14.67}_{-9.39}$	$13.95^{+2.39}_{-2.06}$
p_2	$0.43^{+0.03}_{-0.03}$	$0.54^{+0.09}_{-0.1}$	$0.43^{+0.03}_{-0.03}$

Table 8.1: Parameter obtained with a Keplerian, self-gravitating and power-law model for each CO-isotopologues (first two columns) and for a combined fit (both sides and both CO-isotopologues, third column). We also show the reduced χ^2 difference between the Keplerian and self-gravitating fit, as $\lambda = \Delta(\chi^2_{\rm red})$.

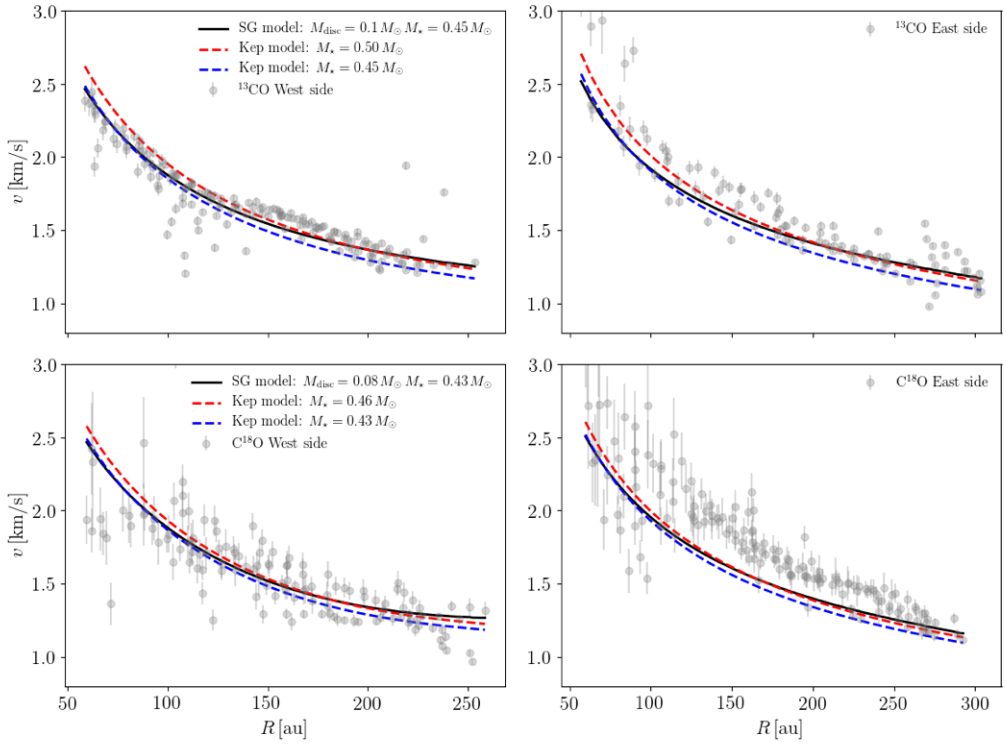

Figure 8.2: Rotation curve for the ^{13}CO and C^{18}O isotopologues for different models. The fitting procedure has been done simultaneously for the East (right column) and West (left column) side velocity data (plotted as grey markers). The black solid line corresponds to the self-gravitating fit, the red dashed line to the Keplerian fit and the blue dashed one to the Keplerian curve obtained with the star mass from the SG fit.

8.2.2 Individual isotopologues fit

We also performed a fit separately for the two CO isotopologues. The result is shown in Fig. 8.2, where the upper and lower panels correspond to the West (left panel) and East (right panel) side of the ^{13}CO and C^{18}O isotopologue, respectively. The parameters obtained from the best-fit models are shown in the first two columns of Table 8.1. Also in this case, we start by looking at the power-law model. For the ^{13}CO data, the best-fit value of the exponent p_2 is again smaller than 0.5 ($p_2 = 0.43 \pm 0.03$), meaning that the self-gravitating model should be preferred to reproduce the data. In contrast, for the C^{18}O the best-fit power-law index is $p_2 = 0.54^{+0.09}_{-0.1}$, where the value of 0.5 is inside the uncertainties, meaning that a purely Keplerian model is consistent with the ^{18}CO data, given the larger uncertainty in the velocity points in this case. We also note that the obtained value > 0.5 could suggest the presence of a warp or chaotic accretion from the cloud. By considering the results for the ^{13}CO, best fitted by a self-gravitating model, the disc mass is $M_{\rm disc} = 0.1^{+0.05}_{-0.04}\,M_\odot$, with a stellar mass of $M_\star = 0.45 \pm 0.03\,M_\odot$.

8.3 Discussion

Having performed fits for the self-gravitating and the Keplerian model, we now compare which one is a better fit to the data. To do so, we compute the reduced χ-square ($\chi^2_{\rm red}$) for each model and each CO-isotopologue. We then compute the likelihood ratio λ, defined as the difference between the Keplerian and self-gravitating minimum reduced χ-square:

$$\lambda = (\chi^2_{\rm red})_{\rm min,Kep} - (\chi^2_{\rm red})_{\rm min,SG}\,. \tag{8.6}$$

For Gaussian, independent measurements, this function is distributed like a χ^2 with n degrees of freedom, where n is the number of new parameters in the more general case ($n = 1$), with the hypothesis that the less general model is correct (i.e. the Keplerian model). The computed values are presented in Table 8.1. We obtain $\lambda \simeq 2.16$ for the ^{13}CO fit, and 1.38 for the combined fit, which means that the Keplerian model is rejected with respect to the self-gravitating one. If we consider only the C^{18}O data, instead, the likelihood ratio tends to slightly prefer a simple Keplerian model (see Table 8.1). This means that in this case the two models are indistinguishable, possibly because the errors are larger with respect to the ^{13}CO case.

In summary, the best fitting model for the combined set of data, including both available CO isotopologues is a non-Keplerian one, with a disc mass $M_{\rm disc} = 0.08 \pm 0.04\,M_\odot$, and a star mass $M_\star = 0.46 \pm 0.03\,M_\odot$. Considering only the ^{13}CO data (that are of better quality with respect to the C^{18}O ones), we obtain a disc mass of $M_{\rm disc} = 0.1^{+0.05}_{-0.04}\,M_\odot$ and a star mass $M_\star = 0.45 \pm 0.03\,M_\odot$. In both cases, we obtain a non-zero disc mass within 2σ. Instead, the C^{18}O alone might be compatible with a purely Keplerian rotation curve, even though the self-gravitating fit returns a non-zero disc mass to within 1σ uncertainty, $M_{\rm disc} = 0.08^{+0.08}_{-0.05}\,M_\odot$ and a star mass of $0.43^{+0.05}_{-0.07}\,M_\odot$.

Thus, assuming a total disc mass equal to $0.08 - 0.1\ M_\odot$ (and a star mass of $0.46 - 0.45\ M_\odot$) as obtained from the fits above, we get a disc-to-star mass ratio

of $\sim 0.17 - 0.22$. Gravitational instabilities arise when the disc-to-star mass ratio becomes of the order of the disc aspect ratio H/R, which is typically of the order of ≈ 0.1 for protostellar discs. The disc mass we derive from the rotation curve is thus in the correct range to produce gravitational instabilities and thus the spiral structure observed. In particular, the observed two-armed grand-design structure is strongly suggestive of an internal origin due to gravitational instabilities. We note that from the relation between the disc-to-star mass ratio and the number of spiral arms $M_{\rm disc}/M_\star \propto 1/m$ (Lodato & Rice 2004; Cossins et al. 2009a; Dong et al. 2015c) the obtained disc mass would point to high m modes, while just two spiral arms are observed through ALMA. However, Dipierro et al. (2014) have demonstrated that, even if the density structure has an intrinsic $m > 2$ spiral, smaller-scale arms can be washed out by the limited resolution of the instrument, leaving only the lowest m modes in ALMA dust continuum observations. The disc mass obtained in this work is consistent with those used in the hydrodynamical simulations that reproduce the observed spirals, as performed by Paneque-Carreno et al. (2021), where they employ a disc-to-star mass ratio in the range of q = 0.1-0.3, and in the simulations of Cadman et al. (2020b), with a slightly larger q = 0.27 value.

Having obtained a dynamical estimate of the total disc mass, and assuming a dust disc mass of $10^{-3}\,M_\odot$ (Paneque-Carreno et al. 2021; Pérez et al. 2016), we can put interesting constraints on the gas-to-dust, that turns out to be of the order of $\approx 80 - 100$ (for the combined fit and the ^{13}CO isotopologue), which in the first case corresponds to a factor ~ 1.2 smaller than the usually assumed value of 100. Note that the so obtained gas-to-dust ratio estimate extremely depends on the dust mass derivation and thus it should be considered with care. For this derivation we assumed a dust mass of $10^{-3}\,M_\odot$, but Paneque-Carreno et al. (2021) showed that the disc being optically thick with a low spectral index, scattering could be important leading to a dust mass estimate up to 2 times larger than previously considered.

As a further analysis of the results obtained in the combined fit, we show in Fig. 8.3 the residuals for both disc sides (left: West; right: East) and the CO-isotopologues (blue: ^{13}CO; red: C^{18}O). In particular, the points are the difference between the velocity data and a Keplerian model where the star mass $M_{\star,\rm sg}$ has been obtained through the self-gravitating model. The dashed line is the difference between the self-gravitating model and the Keplerian velocity with the stellar mass $M_{\star,\rm sg}$. From these results it appears that especially the residuals for the West side in the ^{13}CO do require a significant disc contribution to the gravitational potential. Indeed, the data residuals present an increasing trend, following the disc contribution model, in particular for the West side. Instead, for the C^{18}O there is still some large scatter in both directions. This aspect is particularly interesting, indeed, Paneque-Carreno et al. (2021) find that there is an important asymmetry between the East and West side data (see their Discussion section). The main characteristic of this asymmetry is that the West side is more compact and brighter than the East side, which is more extended and cloud-contaminated. The rotation curve on the East side then should be considered with care, since the disc can be contaminated by chaotic accretion from the cloud. This infall of material could in

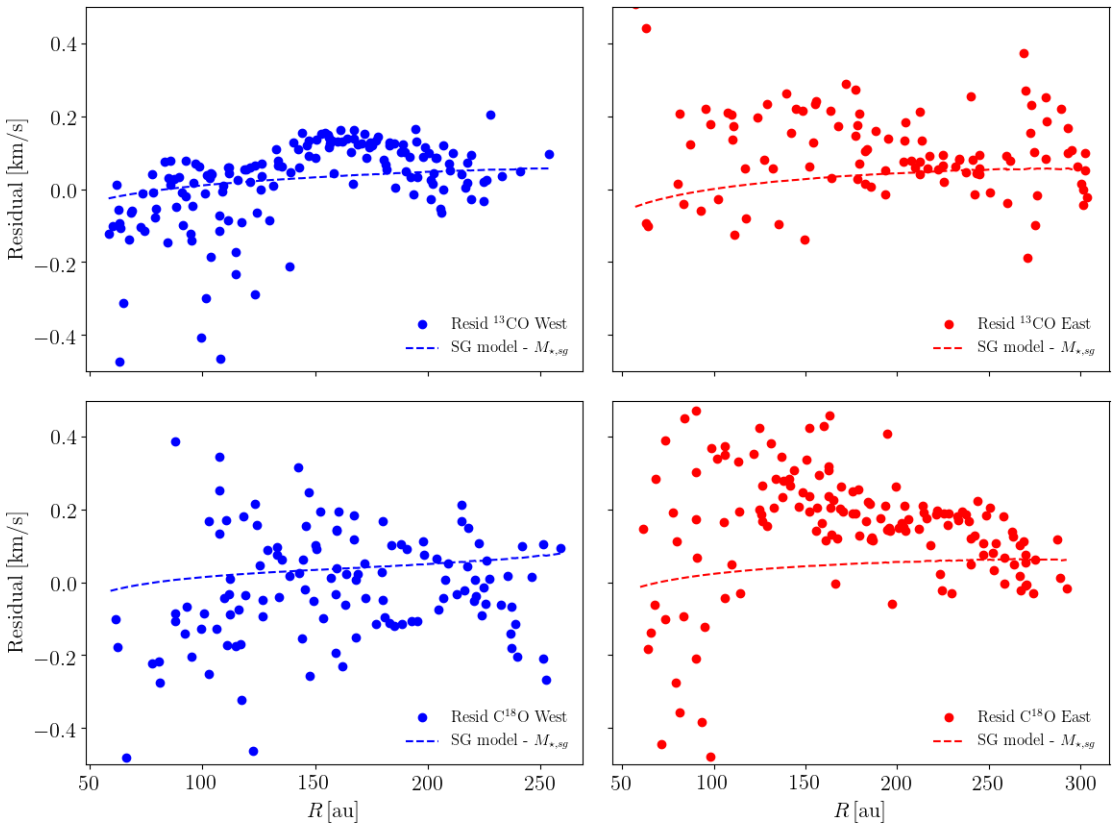

Figure 8.3: Residuals obtained for the combined fit. The top panels show residual for the ^{13}CO (blue points and dashed line), while the bottom ones for the C^{18}O (red points and dashed line). The left panels correspond to the West side, while the right one to the East side. Points represent the difference between the velocity data and a Keplerian model where the star mass $M_{\star,\mathrm{sg}}$ has been obtained through the self-gravitating model. The dashed line is the difference between the self-gravitating model and the above mentioned stellar contribution, $M_{\star,\mathrm{sg}}$.

principle change the centrifugal balance, increasing the complexity of the system. For this reason, we decided to repeat the fit procedure for the West side only. The obtained results are described in Appendix 8.8. We obtain an even stronger indication in favor of a self-gravitating fit, with the Keplerian fit rejected with 80% confidence for the combined fit and with 97% confidence considering the ^{13}CO data only. The resulting disc mass in this case is $M_{\mathrm{disc}} = 0.16 \pm 0.06\, M_{\odot}$ with a stellar mass $M_{\star} = 0.41 \pm 0.04\, M_{\odot}$, and thus in a disc-to-star mass ratio of ~ 0.40.

Finally, it has to be noted that small scale gas turbulence could contribute to deviations from keplerian motion, but this generally amounts to no more than $0.1 c_{\mathrm{s}} \sim 20$ m/s (Flaherty et al. 2020), being thus smaller than the observed deviation (the disc contribution is $\sim 50 - 100$ m/s, see Fig. 8.3).

8.4 Conclusions

In this paper we have looked for deviations from Keplerian rotation in the disc orbiting around the Elias 2-27 system, providing for the first time a dynamical measurement of the total mass of a planet forming disc, by fitting its rotation curve as derived from CO emission with a model including both the stellar and the disc contribution to the gravitational field. We performed three different fit procedures, that is, a combined fit considering both disc sides and both CO-isotopologues, an individual fit to the data points for the separate isotopologues, and a third fit considering only the less cloud-contaminated West side of the disc; the last case is described in Appendix C. The outcome of these analysis is that the ^{13}CO isotopologues data, and in particular the West side of the disc, are better reproduced by a self-gravitating disc model rather than a pure Keplerian one. The same is true also considering both isotopologues, although with smaller confidence, with a resulting disc mass of $M_{\rm disc} = 0.08 \pm 0.04\,M_{\odot}$ and a stellar mass $M_{\star} = 0.46 \pm 0.03\,M_{\odot}$ (where the stellar mass is compatible with previous estimates). We point out that we obtain a non-zero measure of the disc mass within 2σ uncertainty, both in the combined fit and in the fit for the ^{13}CO isotopologue alone. Assuming these values for the disc and star mass, and assuming a dust disc mass of $10^{-3}\,M_{\odot}$ (Paneque-Carreno et al. 2021; Pérez et al. 2016), we obtain a disc-to-star mass ratio of $\simeq 0.17$ and a gas-to-dust ratio of $\simeq 80$. These results highlight the fact that Elias 2-27 should be considered as a self-gravitating disc, reinforcing the internal gravitational instability interpretation for the observed spiral structures. This result is more evident when fitting for the ^{13}CO data on the West side of the disc, that are less contaminated by the cloud contamination and possible infall (Paneque-Carreno et al. 2021) for which we obtain a disc-to-star mass ratio of ~ 0.40, with a disc mass of $0.16\,M_{\odot}$ and a star mass of $0.41\,M_{\odot}$. We point out that the lower confidence level obtained in the combined isotopologues fit is due to the relatively lower quality of the C^{18}O data, which can be improved in future observations.

Finally, we remark that this method to estimate the disc mass can be applied to other protoplanetary discs (such as, for example, IM Lup and WaOph 6 from the DSHARP sample, Huang et al. 2018b, and RU Lup, Huang et al. 2020, that also show a prominent spiral structure), aiming to give better constraints (independent of CO or dust to H_2 conversion) on the disc mass. Such measurement can also be used to calibrate the conversion factors between dust and total mass, at least for these systems.

8.5 Supplementary material

In this section we present material that originally was in the Appendix of Veronesi et al. (2021).

8.6 Corner plot results for the combined fit

Fig. 8.4 collects the corner plots of the MCMC procedure for the Keplerian (left), self-gravitating (disc+star, centre) and power-law (right) fit of the CO isotopologues velocity data for the combined fit. The fit results correspond to those discussed in Sec. 8.2.1. The final masses and errors are computed from the median value, 16th and 84th percentile uncertainties derived from the posteriors.

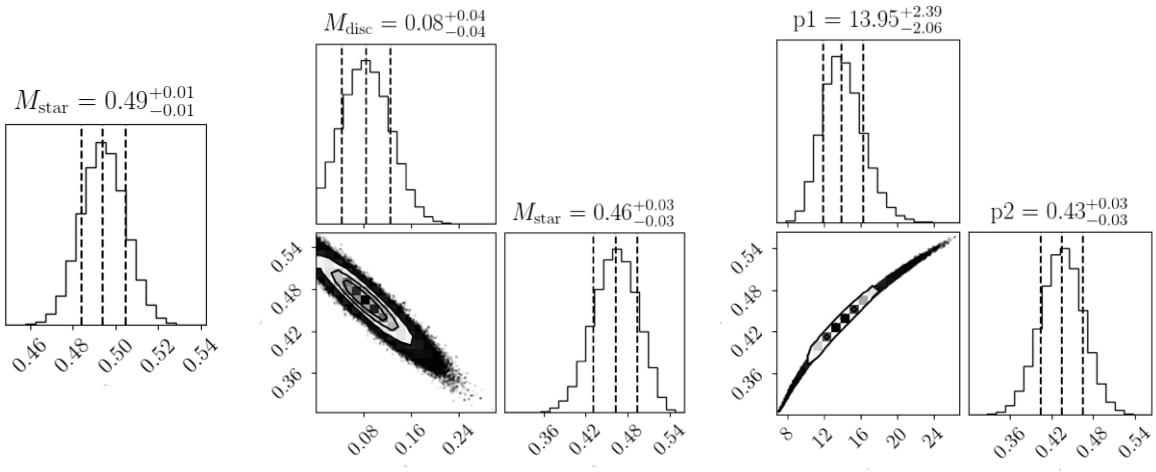

Figure 8.4: Probability distribution and corner plots obtained with the Keplerian (left), disc+star (centre) and power law (right) model for the total fit, where the East and West sides, and the ^{13}CO and C^{18}O data have been fitted simultaneously.

8.7 Corner plot results for the individual isotopologues fit

Fig. 8.5 collects the corner plots of the MCMC procedure for the Keplerian (left panels), self-gravitating (disc+star, central panels) and power-law (right panels) fit of the CO isotopologues velocity data (upper panels: ^{13}CO; lower panels: C^{18}O), fitted separately. The fit results correspond to those discussed in Sec. 8.2.2. The final masses and errors are computed from the median value, 16th and 84th percentile uncertainties derived from the posteriors.

8.8 West side fit

In Fig. 8.6 we show results where the fit has been done only for the West side, which is less contaminated by the infalling cloud. As in Sec. 8.2, the models we choose are a self-gravitating model (black solid lines), a Keplerian one (red dashed line), and a simple power-law model (see Eq. 8.5). As before, the blue dashed line represent the Keplerian rotation curve with the star mass fixed to the value obtained with the self-gravitating fit. The top panels collect results obtained

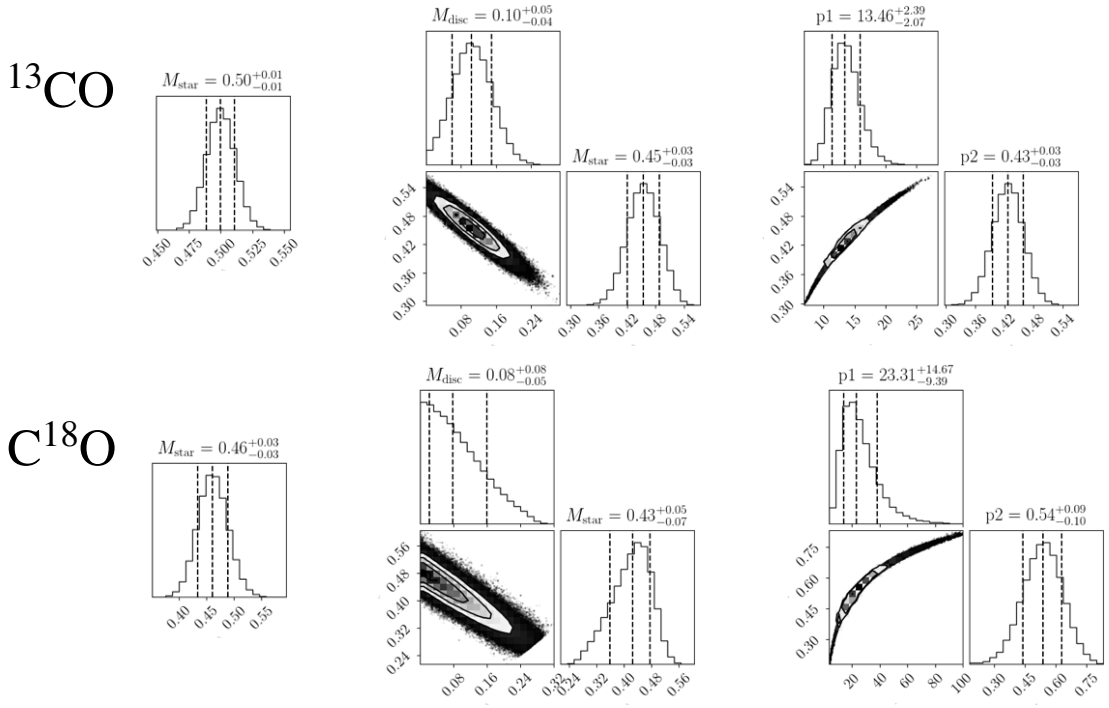

Figure 8.5: Probability distribution and corner plots for different models (from left to right: Keplerian, disc+star,power law model) for the ^{13}CO (upper panels) and C^{18}O (lower panels) isotopologues.

for the combined fit, while the bottom panels show results when fitting separately the two CO-isotopologues. In Table 8.2 we report the obtained parameter values for each model, each CO-isotopologues (first two columns), and for the combined fit (fitting simultaneously the CO-isotopologues data, third column).

The resulting disc mass in the combined fit is $M_{\rm disc} = 0.1^{+0.06}_{-0.05}\,M_{\odot}$, with a stellar mass of $M_{\star} = 0.44 \pm 0.04\,M_{\odot}$. The obtained likelihood ratio $\lambda = \Delta\chi^2 \sim 1.6$ implies a rejection of the Keplerian model.This values would provide a disc-to-star mass ratio of 0.22, meaning that the disc mass is in the right range to give rise to gravitational instabilities. Also when considering the CO-isotopologues separately, this behaviour is seen for the ^{13}CO. In this case, the expected disc mass is $M_{\rm disc} = 0.16 \pm 0.06\,M_{\odot}$, the stellar mass $M_{\star} = 0.41 \pm 0.04\,M_{\odot}$ and $\lambda = \Delta\chi^2 \sim 4.6$, implying also in this case a rejection of the Keplerian model. These values correspond to a disc-to-star mass ratio of 0.39.

For the combined (both CO- isotopologues) West fit, we collect in Fig. 8.7 the residuals. The difference between the self-gravitating model and the star contribution to the gravitational potential (as obtained with the self-gravitating model) shows that the disc contribution fits well the data residual (data - Keplerian mass), especially for the ^{13}CO isotopologue.

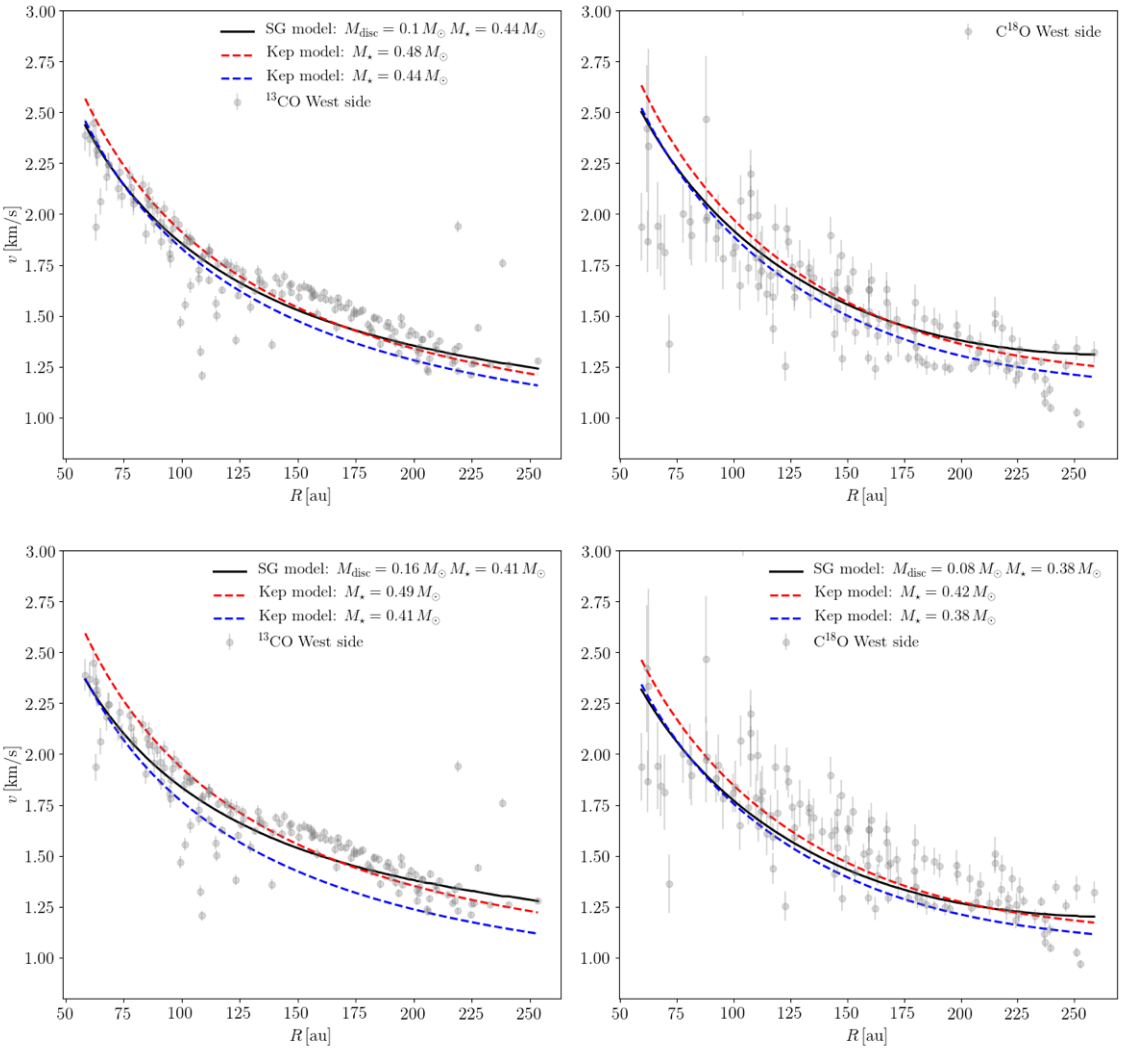

Figure 8.6: Top panels: rotation curve for the ^{13}CO (left) and C^{18}O (right) isotopologues for different models. In this case the fitting procedure has been performed considering only the West side of the disc. The black solid line corresponds to the self-gravitating fit and the red and blue dashed lines to the Keplerian fit and to the Keplerian curve obtained with the star mass from the SG fit, respectively. Grey markers represent the velocity data. Bottom panels: same as above, but with a fit performed separately for the two CO-isotopologues.

8.8.1 Corner plot results

Fig. 8.8 collects the probability distribution and corner plots obtained with the Keplerian (left), self-gravitating (disc+star, centre) and power-law (right) fit of the CO isotopologues velocity data, when fitting the West side, simultaneously for the ^{13}CO and C^{18}O isotopologues. Fig. 8.9 shows the same results but for a fit where the two CO-isotopologues (top: ^{13}CO; bottom: C^{18}O) have been fitted separately.

The fit results correspond to those discussed in Sec. 8.8. The final masses and

	^{13}CO	C^{18}O	Combined fit
Keplerian fit			
$M_\star\,[M_\odot]$	$0.49^{0.01}_{-0.01}$	$0.42^{0.03}_{-0.03}$	$0.48^{+0.01}_{-0.01}$
Self-gravitating fit			
$M_\star\,[M_\odot]$	$0.41^{+0.04}_{-0.04}$	$0.38^{+0.06}_{-0.07}$	$0.44^{+0.04}_{-0.04}$
$M_{\rm disc}\,[M_\odot]$	$0.16^{+0.06}_{-0.06}$	$0.08^{+0.08}_{-0.06}$	$0.1^{+0.06}_{-0.05}$
$\lambda = \Delta(\chi^2_{\rm red})$	4.57	-0.51	1.58
Power-law fit			
p_1	$12.66^{+3.47}_{-2.75}$	$27.49^{+23.67}_{-13.33}$	$14.07^{+3.53}_{-2.85}$
p_2	$0.42^{+0.05}_{-0.05}$	$0.58^{+0.12}_{-0.13}$	$0.44^{+0.04}_{-0.04}$

Table 8.2: System parameters obtained with a Keplerian, self-gravitating and power-law models for the West side disc fit. The first two columns collect results for a fit when considering separately the two CO-isotopologues, the third one when considering them simultaneously. We also show the reduced χ^2 difference between the Keplerian and self-gravitating fit, as $\lambda = \Delta(\chi^2_{\rm red})$.

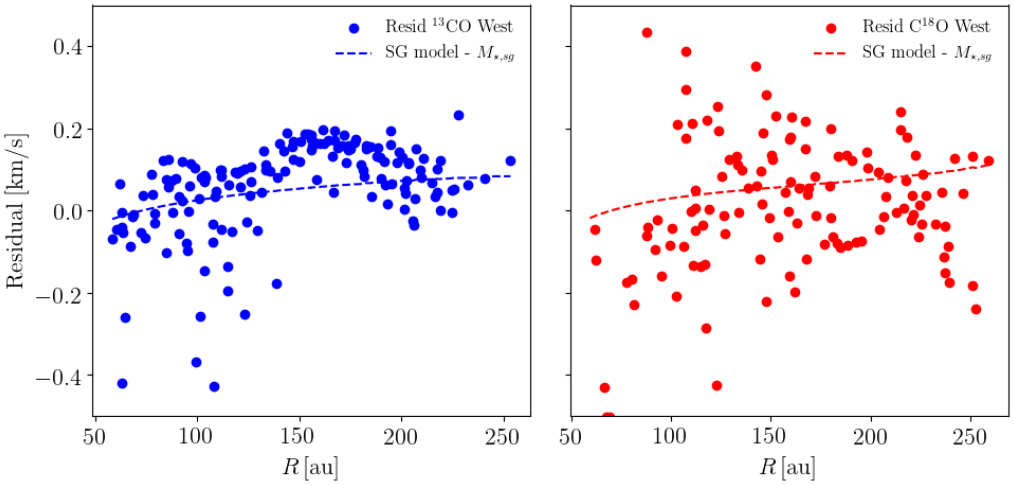

Figure 8.7: Residuals obtained for the West side fit, when considering simultaneously the two CO-isotopologues. The left panel shows residual for the ^{13}CO (blue markers and dashed line), while the right one for the C^{18}O (red markers and dashed line). Markers represent the difference between the velocity data and a Keplerian model where the star mass $M_{\star,\rm sg}$ has been obtained through the self-gravitating model. The dashed line is the difference between the self-gravitating model and the above mentioned star contribution, $M_{\star,\rm sg}$.

errors are computed from the median value, 16th and 84th percentile uncertainties derived from the posteriors.

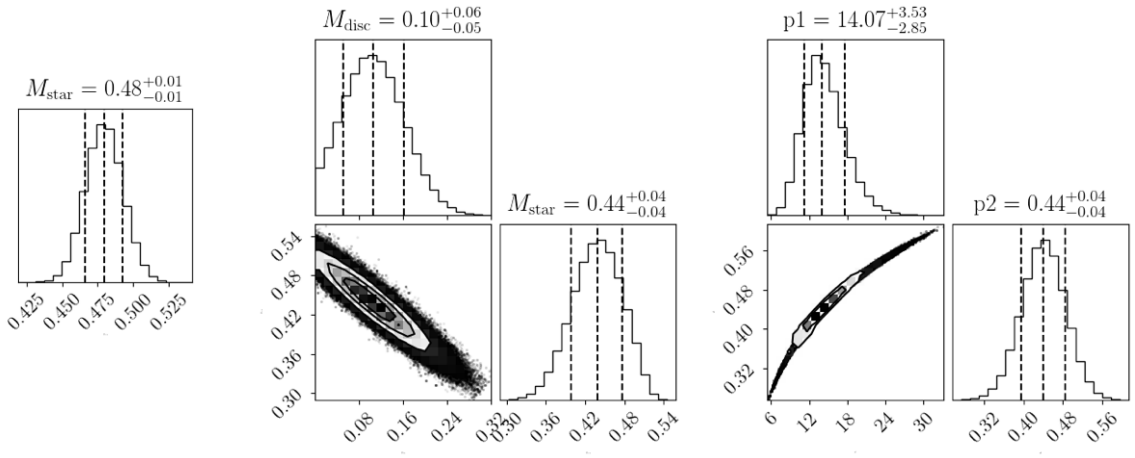

Figure 8.8: Probability distribution and corner plots obtained with the Keplerian (left), disc+star (centre) and power law (right) model for the West side, where the ^{13}CO and C^{18}O data have been fitted simultaneously.

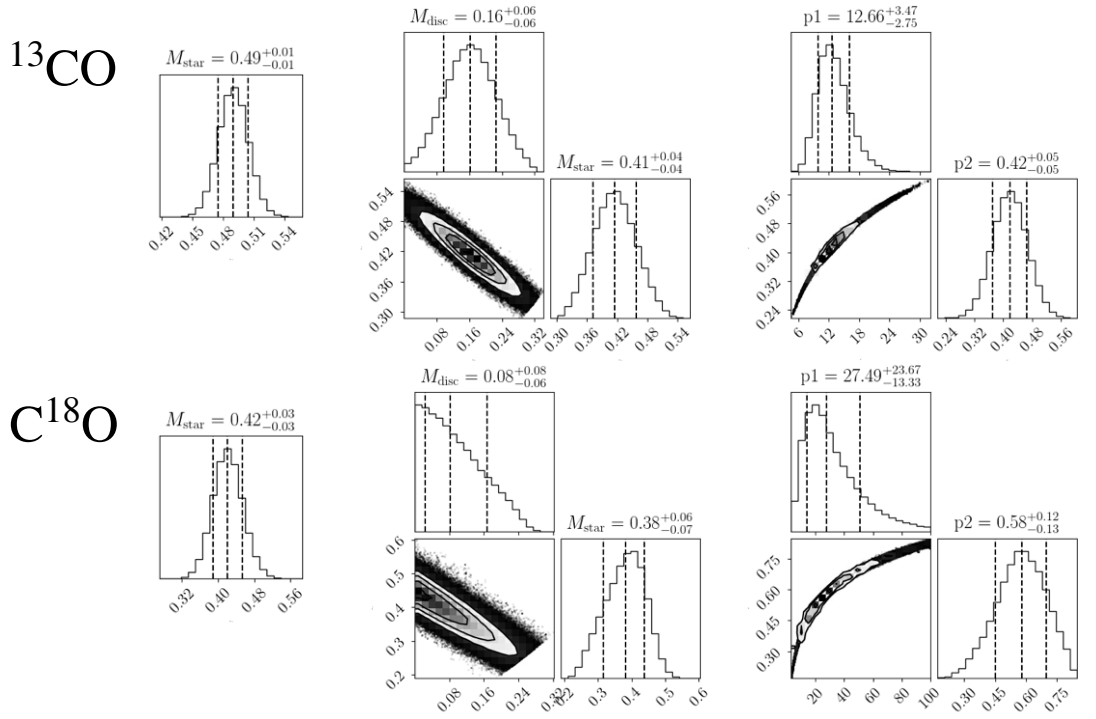

Figure 8.9: Probability distribution and corner plots obtained with the Keplerian (left), disc+star (centre) and power law (right) model for the West side, where the ^{13}CO (upper panels) and C^{18}O (lower panels) data have been fitted separately.

Conclusions

Looking back at what has been picked up. Preparing to fly elsewhere (Cavaglia, Piemonte 2018).

In this Thesis I have investigated how the observed morphology and kinematics of planet-forming discs can be used to probe dynamical processes occurring within them, such as the development of gravitational instabilities and the tidal interaction between the gas and young planets that are embedded in the disc. A brief overview regarding the formation process of these discs and their main properties is given in Chapter 1. The relevance and necessity of this work arises from the vast

number of high resolution and high sensitivity observations that telescopes such as ALMA in the millimetre range, or SPHERE-VLT in the infrared, have been collecting in recent years. Only a few years ago the astrophysical community was astonished and surprised to discover the first image collected by ALMA of the disc orbiting HL Tau. Nowadays, ALMA has shown that substructures are ubiquitous in disks, when observed with sufficient angular resolution and sensitivity. Among them, we can identify simple structures, formed by rings and gaps, with or without a central cavity, and more complex structures, with spirals and asymmetric overdensities. Considering a protoplanetary disc, sometimes the substructures are observed at a specific wavelength, thus characterising a specific type of dust or gas emission (e.g., small or large dust grains), other times they are visible (with more or less similarities) at different wavelengths. Given the complexity and the wide range of detected structures, it is natural to wonder what their origin might be, whether there is a common origin, or whether different physical mechanisms are at work in shaping the systems we observe. Some of the possible mechanisms that regulate the formation and evolution of these systems are described in Chapter 2, 3, and 4 of this Thesis. In Chapter 2 I give an overview of gas and dust dynamics in protoplanetary discs. In Chapter 3 I describe a specific class of protoplanetary discs that are thought to be typical of the early stages of their evolution. In these systems, the mass of the disc is crucial and affects the gravitational potential. Under certain circumstances, the disc self-gravity is therefore responsible for the onset of gravitational instabilities, whose manifestation are spiral density waves. In Chapter 4, assuming that there is a perturber embedded in the disc (star/planet), I describe the tidal interaction between these two actors. In particular, I discuss the conditions necessary for a gap to open, and how spiral structures can also be associated to this interaction.

In the last two years ALMA has also started to collect high-resolution molecular line emission. This has revealed the presence of some peculiar kinematic structures, in particular in the form of deviations from the Keplerian velocity, usually assumed to be, to a first approximation, the velocity of the disc. These appear to be spatially and velocity localised, and have sometimes been seen to coincide with structures in the millimeter dust continuum emission. This has raised the possibility that there might be a common origin. In addition, recent studies have shown that these velocity perturbations could be the signature of planets still embedded in the gas, but which have carved a gap in the dust. Peculiar features in the gas kinematics have also been observed and numerically investigated in (possibly) self-gravitating discs (e.g. Elias 2-27). In Chapter 5 I provide a broad overview of structures observed at morphological and kinematic level in recent years, building links between the observational and theoretical aspects, and underlining that both are needed to shed light on the still obscure issues in the field of planet formation.

Indeed, even if we have improved and deepened our knowledge of these systems, some issues remain unsolved. In fact, although many of the observed structures can be explained by planet-disc interaction, or by gravitational instabilities, on the one hand the (still forming) planets directly detected in these discs are very few, mainly due to the gas in which they are embedded, which hides them from our view. Secondly, for a disc to develop gravitational instabilities it must be

massive, in particular $M_{\rm disc}/M_\star \approx H/R$. A fundamental uncertainty here arises precisely from the fact that, so far, it has not been possible to give a firm estimate of the mass of the discs, since what is usually obtained by the methods described in Chapter 1, that use tracers such as the dust flux or the CO emission, is a lower estimate.

That is why it is of paramount importance to find other features or signatures, from a morphological or kinematical point of view, that will allow us to discover which mechanisms are responsible for the observed structures. If the "culprit" is the disc-planet interaction, that will allow us to find the signature of the planet, and to possibly give an estimate of the planet mass. At the same time, we need new methods to estimate the mass of the discs, without running into the issues of conversion between CO-isotopologue and gas, or the ignorance that still surrounds the interaction between dust and gas, specifically their ratio. This can also be achieved "digging into the mine" of gas kinematics.

The work carried out in this thesis therefore fits into this context. In Chapter 6, 7 and 8 I present the original results obtained in the course of this thesis. Looking back at my findings, I can identify two underlying questions:

- **How massive are protoplanetary discs?** This is one of the most crucial, unsolved, questions in the field of planet formation. Indeed, the gas mass affects how planets form and what is the origin of the substructures we observe in protoplanetary discs. Focusing in particular on spirals and rings, assuming that such substructures are due to embedded protoplanets, I explored if there is a relationship between the observed morphologies in dust continuum and scattered light, and the gas mass (see Chapter 6). I combined hydrodynamical modelling with radiative transfer simulations (PHANTOM + RADMC-3D) of dusty gaseous protoplanetary discs with embedded protoplanets. In these simulations, I vary the Stokes parameter, which is a function of the generally unknown local gas density. Indeed, it is well known that the dynamics of the dust is affected by the gas (and viceversa under certain conditions), resulting in different substructures depending on the strength of the dust-gas coupling. Usually, small dust grains, characterised by a $\mathrm{St} \ll 1$, are stuck to the gas, thus showing spirals. Instead, larger grains, decouple, showing progressively more axisymmetric (ring-like) substructure as decoupling increases with grain size or with the inverse of the gas disc mass. My main finding is that simultaneous modelling of scattered light and dust continuum emission is able to constrain the Stokes number, and, if the dust properties are known, this can constrains the gas surface density, $\Sigma_{\rm gas}$, at the location of the structure.

- The same ultimate goal of measuring the disc mass is the aim of Chapter 8. Here, I consider a specific protoplanetary disc, Elias 2-27. ALMA observations at multiple wavelengths have revealed a two armed large scale spiral structure (Pérez et al. 2016; Paneque-Carreno et al. 2021). Considering also the young age of the star and the disc-to-star mass ratio estimated in previous works (both from the dust continuum emission in Pérez et al. 2016, from dust trapping consideration in Cadman et al. 2020b and from hydrodynamical modeling in Paneque-Carreno et al. 2021), this system can be a perfect

laboratory to investigate the role of self-gravity in the early phases of star formation. The idea it to obtain a dynamical estimate of the disc mass of Elias 2-27 in order to confirm the GI origin of the spirals. To do that, I model the rotation curve obtained by CO data of Elias 2-27 (Paneque-Carreno et al. 2021) with a theoretical rotation curve including both the disc and the star contribution to the gravitational potential (Bertin & Lodato 1999). I compare this model with a purely Keplerian one and with a simple power-law function. I find that (especially for the ^{13}CO isotopologue, in the West side of the disc) the rotation curve is better described by considering both the star and the disc contribution. Therefore, the dynamical estimate of the disc mass is $0.06^{+0.04}_{-0.03}\,M_{\odot}$ and the star mass is $0.45 \pm 0.03\,M_{\odot}$, the latter being comparable with previous estimates. From these values, we derive that the disc is 13% of the star mass, meaning that it could be prone to gravitational instabilities. This result has a twofold outcome: it would strongly support the hypothesis that the two spiral arms observed in Elias 2-27 are generated by gravitational instabilities, and it lays the foundations for the application of this method (independent of CO or dust to H_2 conversion) to other potentially self-gravitating systems.

- **Does DS Tau host a massive planet, possibly detectable from kinematics?** This protoplanetary disc shows a wide gap followed by a bright ring. Lodato et al. (2019) estimated that a planet could be the responsible for the carved gap, and that its mass should be approximately $5.6\,M_{\rm jup}$. In Chapter 7, I present hydrodynamical (PHANTOM) and radiative transfer (MCFOST) simulations with different planet and disc masses, performed in order to reproduce the dust continuum observed at 1.3 and 2.9 mm (Long et al. 2018b, 2020). To find the parameters that better reproduce the observed structure, I fit the shape of the radial intensity profile along the disc major axis varying the planet mass, the dust disc mass, and the evolution time of the system. I obtain that, if the planetary origin is assumed in order to explain the observed dust/ring structure, the embedded planet should have a mass $M_{\rm p} = 3.5\,M_{\rm Jup}$. Assuming this value for the planet mass, I also compute the expected signature of the planet in the gas kinematics, as traced by CO emission. I find that such a velocity perturbation, in the form of a "kink" in the channel maps, could be detected by ALMA with a velocity resolution between $0.2 - 0.5$ kms^1 and a beam size between 30 and 50 mas.

In Chapter 5 I also presented two works in which I was involved in a prominent role:

- Hall et al. (2020): the main result of this work is that the spirals excited by GI in self-gravitating disc leave a kinematical signature in the molecular line emission, which differs from the planet "kink" signature. We perform hydrodynamical (PHANTOM) and radiative transfer (MCFOST) simulations of a self-gravitating disc showing spiral structure. While in the planetary case the velocity deviation is localised both in space and velocity, the "GI-wiggles" are visible in all velocity channels and on a large disc radial and azimuthal extent. With reasonable parameters (e.g., disc inclination, PA,

distance from the observer, beam size) these features should be detected by the current ALMA capabilities.

- Paneque-Carreno et al. (2021) present new ALMA observations at multiple wavelengths of the protoplanetary disc Elias 2-27, showing two large-scale spiral arms. We perform hydrodynamical (PHANTOM) and radiative transfer (MCFOST) simulations varying the disc mass (specifically, the gas-to-dust ratio) and the disc surface density radial profile, obtaining that the better agreement between observations and the simulations is achieved with a disc-to-star mass ratio of $q \sim 0.3$. We also present ^{13}CO and C^{18}O molecular line emission (the same data used by myself in Chapter 8). The main findings of the gas kinematics analysis are that there is an evident asymmetry between the East and the West side of the disc, being the East side more radially extended and more cloud-absorbed, and that deviations from the Keplerian velocity are detected in the velocity channel maps. Moreover, they also see some large-scale emission, that could be linked to infall of material from the cloud onto the disc. All this evidence points towards the possibility that the disc is self-gravitating.

8.9 Future developments

Starting from the work I performed in this Thesis, I identified some issues that it would be interested to address in future projects:

- First of all, as a follow up to Veronesi et al. (2019), there would be some improvements to be made. In fact, in this work, some limitations were due to the short duration of the simulations and to the fact that the hydrodynamic simulations performed contained only one dust species each. We know that in discs, there is usually a distribution of grains of different sizes, which can affect the general evolution of the system. In particular, it would be interesting to study the time evolution of the structures and of the coupling between dust and gas. Moreover, we know that as the system evolves the dust-to-gas ratio increases, reaching a value around ~ 1 within the gaps. This is not compatible with the one-fluid approximation (St$\ll 1$) used in the hydrodynamical simulations. A possible solution is to use an hybrid algorithm, allowing to exchange between the one-fluid and the two-fluid scheme, depending on the value of the Stokes number and of the dust-to-gas ratio. This algorithm is now implemented in PHANTOM, and it should be tested.

- Secondly, a generalisation of the work done in Veronesi et al. (2020) could be the creation of a catalogue investigating the conditions of detectability of a planet-induced "kink", both from a dynamical and observational point of view. Some studies have already been done connecting the kink velocity to some properties of the system (e.g., Rabago & Zhu 2021), but it could be interested to make a more comprehensive study. The parameters of interest could be the dust-to-gas ratio, the planet mass (Bollati et al. 2021), the

disc aspect ratio (and thus the temperature profile) and the disc viscosity. Observationally, one could vary the position angle, the inclination of the disc and the azimuthal angle of the planet. Moreover, it would be interesting to study the time evolution of the "kink" feature.

- Regarding Veronesi et al. (2021), a direct follow up is to apply the method used to estimate dynamically the disc mass to other protoplanetary discs, potentially self-gravitating. Some promising candidates are IM Lup and WaOph 6 from the DSHARP sample, and RU Lup (Ansdell et al. 2018; Huang et al. 2020), all showing a prominent spiral structure. It would be interesting also to look at disc with no substructures, but with an estimated high disc-to-star mass ratio. By estimating the disc mass in a way which is independent of assumptions related to the abundances of the different gas species, we could also give an estimate of the disc dust-to-gas ratio. In Chapter 8 I use velocity data obtained by Paneque-Carreno et al. (2021) following the method developed by Pinte et al. (2018a), but we know that other techniques have been proposed (e.g., Teague et al. 2018), giving a measure of the rotation curves of CO isotopologue emission to sub-percent precision relative to the Keplerian rotation. Re-do our fitting procedure with velocity data obtained with a different procedure can strengthen our result. Finally, in our modeling we include the star and disc gravitational potential, but to properly compute the disc rotation curve also pressure gradients should be taken into account. Since the pressure contribution causes the gas to move with a slightly sub-Keplerian velocity, we expect that in order to re-establish a good agreement with the data, the disc contribution must increase.

On a more general level, but still with a link to the work carried out in this Thesis, I have identified two interesting topics towards which future research could be addressed. The first one is related to dust dynamics in the presence of gas kinematic signatures. Indeed, as described in Chapter 5, in a few cases these velocity perturbations have been detected (almost) co-located with substructures in the dust continuum emission, such as gaps and rings (e.g., HD 97048 and HD 163296), probably originated by a planet. In one case, this feature has been observed near a ridge within a ring (HD 100546). It would be interesting to study if, in the presence of gap and ring structure, the dust could be trapped in the planet-driven wake. Generally, without a gap, this would not be possible since a planet induced spiral moves at the same angular velocity as the planet throughout the disc, thus the spiral crossing is short (compared to the orbital time-scale) and there is no particle trapping. However, if a pressure maximum is already present, the outcome could change leading to a specific signature in the dust.

A final direction in which I think it is important to push our research is on a more general level, related to the way in which we usually model these systems. What we do is in fact to perform hydrodynamic simulations by evolving an already "formed" disc, within which we can add embedded planets, or where we can "switch-on" the disc self-gravity. The disc can be composed by gas and dust, where these two components can be evolved simultaneously, or where we can wait for the system to "thermalize" in the gas, and then add the dust. What we do know, however, is that

these discs form in molecular clouds, which are extremely chaotic environments, and that the infall of material from the cloud to the disc can continue even after the disc has formed (Bate et al. 2010; Bate 2011, 2018; Maury et al. 2019; Tobin et al. 2020). In addition, several discs may interact with each other, or there may be a disc around multiple systems of stars. With this picture in mind, I think that it would be crucial to better understand what are the initial conditions of the systems we study through hydrodynamical simulations. This would allow us to start from initial conditions that are more physical, and closer to reality, and thus perhaps help us to explain aspects of the planet formation process that are still nebulous at present. One way of doing this would be to start with large-scale simulations, such as those performed and analysed by (Bate 2018), and then from the obtained results, zoom-in and study the evolution of protoplanetary discs, with or without embedded planets. It would even be interesting to see whether from self-gravitating systems, such as discs are expected to be in their early stages of life, could form future protoplanets, by including dust growth algorithms in the modelling (e.g., Lombart & Laibe 2020).

Appendices

Appendix

A Derivation of the self-gravity disc gravitational potential

In this Appendix we go through the derivation of the disc self-gravity contribution to the gravitational potential, as presented in Lodato (1998); Bertin & Lodato (1999). We consider a distribution of matter infinitesimally thin and axisymmetric, where (R, θ) are the radial and angolar coordinates. $\Sigma(R)$ is the surface disc density radial profile. The disc gravitational potential associated to this matter distribution and computed on the equatorial plane can be written as

$$\Phi(R) = -2\mathcal{G} \int_0^\pi d\theta \int_0^\infty \frac{\Sigma(R')R'dR'}{(R^2 + R'^2 - 2RR'\cos\theta)^{1/2}} \,. \tag{A.0.1}$$

The argument of the square root can be rewritten as $(R + R' \left[1 - k^2 \cos^2(\theta/2)\right])$ where

$$k^2 = \frac{4RR'}{(R + R')} \leq 1 \,. \tag{A.0.2}$$

We can now rewrite the potential

$$\Phi(R) = -2\mathcal{G} \int_0^\infty \frac{\Sigma(R')R'dR'}{(R + R')} \int_0^\pi d\theta \frac{1}{\sqrt{1 - k^2\cos^2(\theta/2)}} = -4\mathcal{G} \int_0^\infty K(k) \frac{\Sigma(R')R'dR'}{(R + R')} \,, \tag{A.0.3}$$

where

$$K(k) = \int_0^{\pi/2} \frac{dx}{\sqrt{1 - k^2\cos^2 x}} \tag{A.0.4}$$

is a complete elliptic integral of the first type (see Gradshteyn & Ryzhik 1980). Lastly, we can define

$$K^{(0)}(R, R') = \frac{1}{\pi}\sqrt{\frac{R'}{R}} k K(k) \tag{A.0.5}$$

and thus rewrite Eq. A.0.3 as

$$\Phi(R) = -2\pi\mathcal{G} \int_0^\infty K^{(0)}(R, R')\Sigma(R')dR' \,. \tag{A.0.6}$$

The elliptic integral in the above equation diverges for $k \to 1$, which in terms of the radial coordinate corresponds to $R' \to R$. We highlight that this kind of divergence is typical of infinitesimally thin disc. Actually, since protostellar discs have a finite thickness, this divergence disappears. Indeed, in Chapter 8 we compute the self-gravity disc contribution to the rotation curve at a finite distance from the midplane, z. In any case, this divergence is logarithmic and thus integrable. Indeed, for $k \to 1$ we have that

$$K(k) \to \ln\left(\frac{4}{\sqrt{1-k^2}}\right) = -\ln\left(\frac{|R-R'|}{4(R+R')}\right) \tag{A.0.7}$$

(Abramowitz & Stegun 1972). To avoid this divergence could be useful to compute the potential at a finite vertical distance $z \neq 0$ from the midplane with cylindrical coordinates (R, θ, z). The potential is still given by Eq. A.0.6 where we rewrite k as

$$k^2 = \frac{4RR'}{(R+R')^2 + z^2} \tag{A.0.8}$$

(Binney & Tremaine 1987). Then, to compute the gravitational field we have to derive Eq. A.0.6 with respect to R. The outcome is given by

$$\frac{\partial \Phi}{\partial R}(R,z) = \frac{\mathcal{G}}{R}\int_0^\infty \left[kK - 2R\frac{d(kK)}{dk}\frac{\partial k}{\partial R}\right]\Sigma(R')\sqrt{\frac{R'}{R}}dR' \,. \tag{A.0.9}$$

This equation can be rewritten by considering a property of elliptic integral for which

$$\frac{d(kK)}{dk} = \frac{E(k)}{1-k^2} \,, \tag{A.0.10}$$

where $E(k)$ is another complete elliptic integral defined as

$$E(k) = \int_0^{\pi/2} dx \sqrt{1 - k^2 \cos^2 x} \,, \tag{A.0.11}$$

and the radial derivative of k is given by

$$2R\frac{\partial k}{\partial R} = \frac{k^3}{4}\left(\frac{R'}{R} - \frac{R}{R'} + \frac{z^2}{RR'}\right) \,. \tag{A.0.12}$$

Putting Eqs. A.0.9, A.0.10 and A.0.12 we finally get the disc contribution to the gravitational potential as,

$$\frac{\partial \Phi_{\rm disc}}{\partial R}(R,z) = \frac{\mathcal{G}}{R}\int_0^\infty \left[K(k) - \frac{1}{4}\left(\frac{k^2}{1-k^2}\right)\left(\frac{R'}{R} - \frac{R}{R'} + \frac{z}{RR'}\right)E(k)\right]\sqrt{\frac{R'}{R}}k\Sigma\left(R'\right)\mathrm{d}R' \,. \tag{A.0.13}$$

Lodato (1998) and Bertin & Lodato (1999) also compute the gravitational potential in the limit of $z \to 0$, but since in Chapter 8 we use this result with $z \neq 0$, we do not go further in the derivation.

Appendix

B Smoothed Particle Hydrodynamics

As we stress during this work, in order to achieve a complete understanding of the new astonishing observations we are collecting, it is necessary a theoretical approach match with numerical simulations. Indeed they allow us to study the evolution of system that are not reachable directly. In particular, two different approaches can be found in the astrophysical field: grid-based codes and particle-based smoothed particle hydrodynamics (SPH) codes (Lucy 1977; Gingold & Monaghan 1977; Monaghan & Lattanzio 1985; Monaghan 1992). The second ones are born as a numerical approach for non-axisimmetric problems in astrophysics involving fluid dynamics. This is a Lagrangian computational method, particularly interesting because it allows the conservation of linear and angular momentum and of other important physical invariants, which can not be easily guaranteed with grid codes. We stress that the Lagrangian formulation of the fluid equations considers the evolution of the fluid properties for any given fluid element, at positions co-moving with the flow. On the other hand, a second formulation of the hydrodynamic equations is the Eulerian one. In the Eulerian approach, one follows the evolution of the fluid variables at a given point in space. Therefore, Eulerian numerical methods use geometric grids, either fixed or adaptive.

In this Appendix we will briefly describe the main aspect that make SPH be one of the more innovative and powerful code. We refer for an exhaustive reading at Price (2005, 2012a,b).

B.1 "How do I compute a density from a distribution of point-mass particles?"

The fundamental idea of SPH is to define a set of mass-particles, each having a proper mass and position, that store the values of a set of quantities (such

as velocity, density, thermal energy, entropy) in that particular point in space. This means that, rather than discretizing space in small cells as done in grid-based code, we discretize the mass of the fluid particles. The evolution of the quantities in time and space is ruled by a set of partial differential equations obtained starting from a function that "smooth" the discreteness, due to point particles, and interpolate those quantities through space (for this reason SPH does not require a grid to perform spatial derivatives and can be easily applied to non-symmetric systems). The interpolation evaluates quantities for each particle, then the system is made to evolve in time through the use of a temporal integrator. This means that partial differential equations (PDE) reduce to simple ordinary differential equations (ODE) which can be solved with standard ODE integrators. In Fig. B.1 we can see a schematic representation of three different approaches in

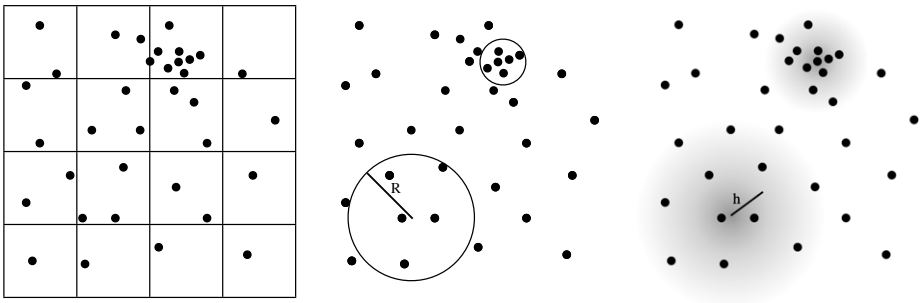

Figure B.1: Computing a continuous density field from a collection of point mass particles. a) In particle-mesh methods (left panel) the density is computed by interpolating the mass to a grid. However, this tends to over/under resolve dense/sparse regions. b) An alternative not requiring a mesh is to construct a local volume around the sampling point, solving the clustering problem by scaling the sample volume according to the local number density of particles. c) This panel shows the approach adopted in SPH, where the density is computed via a weighted sum over neighbouring particles, with the weight decreasing with distance from the sample point according to a scale factor h. Image taken from Price (2012a).

order to compute density, starting from a collection of point mass particles. SPH has its bedrock on the third approach, that consists in setting a local "bubble" around the sampling point, and then computes the density inside it through a weighting function, according to a scale factor h. By doing this, we would take into account that distant particles have a progressively smaller influence in the local estimate, leading to a smoothed density estimate.

B.1.1 Discrete Approximation of a Continuous Field: Interpolation Theory

In order to compute continuum quantities from point particles, we need to develop a mathematical method able to express a continuum function starting from the values it assume at a discrete, but not necessarily ordered (no grid), set of points in space. Each point of this set is a particle that store informations about position, and values assumed by other arbitrary quantities, e.g. density and velocity, in that position. Defining one of this quantities with $f(\mathbf{r})$ (any (scalar) function defined

on a three-dimensional coordinate system $\mathbf{r}$ ranging over a volume V), we can write the trivial identity

$$f(\mathbf{r}) = \int f(\mathbf{r}')\delta(\mathbf{r} - \mathbf{r}')d\mathbf{r}' \,, \tag{B.1.1}$$

where $\delta(\mathbf{r})$ is the Dirac delta function. One can generalize the delta function with a so-called "smoothing kernel" W (with dimensions of inverse volume) with a characteristic scale factor h (known as the "smoothing length"), that determines the rate of fall-off of W, such that

$$\lim_{h\to 0} W(\mathbf{r} - \mathbf{r}', h) = \delta(\mathbf{r} - \mathbf{r}') \,, \tag{B.1.2}$$

giving

$$f(\mathbf{r}) = \int f(\mathbf{r}')W(\mathbf{r} - \mathbf{r}', h)d\mathbf{r}' + O(h^2) \,. \tag{B.1.3}$$

The kernel function is normalized according to the total mass conservation ($\int \rho dV = \sum_{b=1}^{N_{\text{neigh}}} m_b$, where the total mass is given by the summation over the point particles mass) as

$$\int W(\mathbf{r} - \mathbf{r}', h)d\mathbf{r}' = 1 \,. \tag{B.1.4}$$

Finally one has to discretize this continuous field onto a finite set of interpolation points (the particles) by replacing the integral by a summation and the mass element ρdV with the particle mass m, resulting in a new expression for Eq.B.1.1,

$$\begin{aligned} f(\mathbf{r}) &= \int \frac{f(\mathbf{r}')}{\rho(\mathbf{r}')} W(\mathbf{r} - \mathbf{r}', h)\rho(\mathbf{r}')d\mathbf{r}' + O(h^2) \\ &\approx \sum_{b=1}^{N} \frac{m_b}{\rho_b} f(\mathbf{r}_b)W(\mathbf{r} - \mathbf{r}_b, h), \end{aligned} \tag{B.1.5}$$

where now $f(\mathbf{r}_b)$, m_b and $\rho_b = \rho(\mathbf{r}_b)$ are the scalar quantity, mass and density of the b^{th} particle, and b ranges over all particles. This is the basis of all SPH formalisms. In particular, if we estimate the density via Eq.B.1.5 we obtain:

$$\rho(\mathbf{r}) = \sum_{b=1}^{N} m_b W(\mathbf{r} - \mathbf{r}_b, h(\mathbf{r})) \tag{B.1.6}$$

The reader should notice that up to now no assumptions about the continuity of $f(\mathbf{r})$ have been done, however we will see in the next sections that the assumption of continuity and differentiability will be necessary for the development of the equations of motion.

B.1.2 The smoothed prescription: Kernel and length

The next step, in order to obtain a correct density estimate, is to characterize the smoothing kernel, and its length.

The smoothing Kernel In the previous section we described two of its fundamental properties: the normalization to 1 (Eq. B.1.4), and the fact that it must tend to a delta function as the smoothing length h tends to zero (Eq. B.1.2). Other properties are also advantageous:

- it should be positively defined and monotonically decreasing with distance;
- both itself and its derivatives should be continuous;
- it should be isotropic: $W(\mathbf{r}-\mathbf{r}',h) = W(|\mathbf{r}-\mathbf{r}'|,h)$;
- it should be bell-shaped (namely, flat in the centre), so that density estimate is not strongly affected in fluctuations of nearby particles.

An obvious candidate that satisfy most of the previous properties is the Gaussian function:

$$W(\mathbf{r}-\mathbf{r}',h) = \frac{1}{(\sqrt{\pi}h)^d}\exp\left[-\frac{(\mathbf{r}-\mathbf{r}')^2}{h^2}\right], \tag{B.1.7}$$

where d refers to the number of spatial dimensions. A Gaussian kernel presents the disadvantage of being greater than zero for all $r = |\mathbf{r}-\mathbf{r}'|$, requiring interaction with all the particle in the domain. The computational cost of such a kernel therefore scales as $O(N^2)$, where N is the number of particles in the simulation. The use of a compact support function as kernel has some advantages with respect to the gaussian, as it assumes non-zero values on a finite domain, therefore limiting the summation on a well defined list of neighbour particles. For this reason, a common choice in SPH for the kernel are the B-spline functions M_n (Monaghan & Lattanzio 1985), obtained as the Fourier transform of

$$M_n(x,h) = \frac{1}{2\pi}\int_{-\infty}^{\infty}\left[\frac{\sin(kh/2)}{kh/2}\right]^n \cos(x)dk. \tag{B.1.8}$$

These functions give better approximation of the Gaussian function with growing n and have the form of a polynomial of $n-1$ power. Using such a Kernel, means that we are more efficient in evaluating the density, since the computational cost scales like $O(N_{\rm neigh}N)$, but on the other hand we will be more sensitive to small changes in the local distribution (i.e. we have a more noisy density estimate). Of these the most commonly used kernel is that based on cubic splines, given by

$$M_4(q,h) = \frac{\sigma}{h^d}\begin{cases}\frac{1}{4}(2-q)^3 - (1-q)^3 & 0\le q<1\\ \frac{1}{4}(2-q)^3 & 1\le q<2\\ 0 & q\ge 2.\end{cases} \tag{B.1.9}$$

with $q \equiv |\mathbf{r}-\mathbf{r}'|/h$ and $\sigma = [2/3, 10/7\pi, 1/\pi]$ are the normalisation constants respectively for $d = [1,2,3]$ dimensions. Also useful for our purpose is the quintic kernel,

$$M_6(q,h) = \frac{\sigma}{h^d}\begin{cases}(3-q)^5 - 6(2-q)^5 + 15(1-q)^5 & 0\le q<1\\ (3-q)^5 - 6(2-q)^5 & 1\le q<2\\ (3-q)^5 & 2\le 3\\ 0 & q\ge 3.\end{cases} \tag{B.1.10}$$

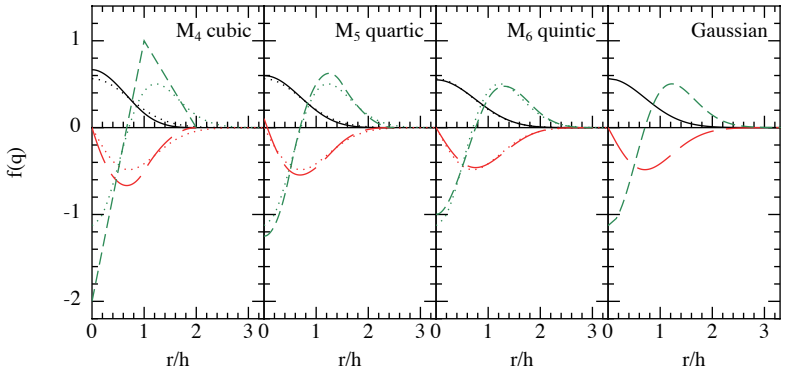

Figure B.2: B-Splines functions (black full line) with their first (long dashed red line) and second derivative (short dashed green line) compared to Gaussian (rightmost panel and dotted line in other). Plot from Price (2012a).

with normalisation $\sigma = [1/120, 7/478\pi, 1/120\pi]$. The higher order polynomials have the advantage of smoother derivatives which, in combination with the increased size of compact support, decreases the sensitivity of the kernel to disorder in the particle distribution.

The smoothing length The choice of the smoothing length h plays a fundamental role in the density estimate, because it turns out to have somehow the meaning of the spatial resolution upon a grid. If we have an arbitrary number of regularly displaced particles, as in a grid code, we could use the same h over the entire set of particles, since the number of "neighbours" (i.e. the number of particles contained in the compact support) would be approximately the same for each particle. Instead, if we drop regularity and consider a random displacement of particles, the use a single h for all the particles will end to affect accuracy, because some particles could have no neighbours at all. So, in order to resolve both dense and sparse regions, a natural choice could be to relate the smoothing length with the local number of particles,

$$h(\mathbf{r}) \propto n(\mathbf{r})^{-1/d}, \quad \text{with } n(\mathbf{r}) = \sum_{b=1}^{N} W(\mathbf{r} - \mathbf{r}_b, h(\mathbf{r})), \tag{B.1.11}$$

where $n(\mathbf{r})$ is the number of particles per unit volume and d is the number of spatial dimensions. Note that, if particles have the same masses, $n(\mathbf{r}) \propto \rho(\mathbf{r})$. The relation between the density and the smoothing length is

$$h_a = \eta \left(\frac{m_a}{\rho_a} \right)^{1/d}, \tag{B.1.12}$$

and we will have to deal with an iterative summation to simultaneously obtain the $\rho(\mathbf{r})$ and $h(\mathbf{r})$ (Springel & Hernquist 2002). The constant η is a free parameter and gives the smoothing length in units of the mean particle spacing. Assuming density constant over the entire kernel radius, we can compute the number of

neighbours as a function of η. In three dimensions

$$N_{\text{neight}} = \frac{4}{3}\pi(\zeta\eta)^3, \tag{B.1.13}$$

where ζ is the compact support radius in units of h (i.e. $\zeta = 2$ for the cubic spline and $\zeta = 3$ for the quintic spline). We highlight that N_{neigh} only characterize the mean neighbour number, and there could be strong fluctuations about this mean, particularly in strong density gradients. For a detailed discussion we strongly recommend the reading of the dedicated section in Price (2012a).

B.2 SPH equations

We now summarize the SPH equations, which coupled to an equation of state for the pressure give the time evolution of the system

$$\rho_a = \sum_{b=1}^{N} m_b W(\mathbf{r}_a - \mathbf{r}_b, h_a) \qquad h_a = \eta\left(\frac{m_a}{\rho_a}\right)^{1/3}, \tag{B.2.1}$$

$$\frac{\mathrm{d}\mathbf{v}_a}{\mathrm{d}t} = -\sum_b m_b \left[\frac{P_a}{\Omega_a\rho_a^2}\frac{\partial W_{ab}(h_a)}{\partial \mathbf{r}_a} + \frac{P_b}{\Omega_b\rho_b^2}\frac{\partial W_{ab}(h_a)}{\partial \mathbf{r}_a}\right], \tag{B.2.2}$$

$$\frac{\mathrm{d}u_a}{\mathrm{d}t} = \frac{P_a}{\Omega_a\rho_a^2}\sum_b m_b(\mathbf{v}_a - \mathbf{v}_b)\cdot\nabla_a W_{ab}(h_a)\,, \tag{B.2.3}$$

where u_a is the internal energy. All the equations above can be derived from a given Lagrangian of the system. Interestingly, it can be demonstrated that Eqs. B.2.1, B.2.2 and B.2.3 are indeed the discrete approximation of hydrodynamics equation of continuity, Euler and energy, respectively.

B.2.1 Conservation properties

One of the strongest point of SPH is exact conservation of constants of motion. Since the equations of motion were derived from the Lagrangian using only the density sum, it is clear that the symmetries in the Lagrangian will be reflected as conservation properties in the equations of motion. In particular, the invariance to translations leads to exact conservation of linear momentum, the invariance to rotation results in a simultaneous exact conservation of angular momentum, the independence of the Hamiltonian of time translates into the energy conservation, and lastly, we will have also entropy conservation, since the equations were derived under a constant entropy constraint. This simultaneous conservation of the main physical quantities is a revolutionary outcome. Particularly, we note that the angular momentum conservation is independent of the geometry, and this allows astrophysicists to study problems with complicated 3D-geometries and dynamics. For a detailed derivation we recommend the reading of the Price (2005, 2012a).

B.3 Dissipative Effects in SPH: artificial and physical viscosity

So far we have assumed a perfectly inviscid, entropy-conserving and therefore dissipationless fluid. While this is an adequate approximation for many incompressible, inviscid and unshocked flows, it presents serious problems when it comes to modeling transonic and supersonic flow regimes, as the conversion of kinetic energy into heat (internal energy) is not correctly captured. The problem occurs because at a shock front, flow properties such as velocity, pressure, density and entropy change very rapidly, on the length-scale of the mean free path of the gas particles. On large scales therefore these changes appear discontinuous. Flow solvers do not resolve the mean free path, and break down due to the apparently singular flow gradients. Therefore, the simulation of shocks is accompanied by unphysical oscillations behind the shock front. In order to resolve shocked flows the majority of SPH codes use a workaround, that consists in broadening the shock across a small number of smoothing lengths. This ensures that the flow gradients do not become infinite, and gives the correct asymptotic behavior away from the shock. This method is implemented by including an artificial dissipative term in the momentum and energy equations that is triggered only in the presence of shocks. One can see that artificial viscosity terms can be translated to a combination of Navier-Stokes bulk and shear viscosity terms. Indeed, it has been known for quite some time (Artymowicz & Lubow 1994) that the artificial terms in SPH can be understood straightforwardly as numerical representations of second derivatives of the velocity. This makes viscosity act also when there is a purely shear flow, as in an accretion disc.

In particular, the standard α parameter of the Shakura-Sunyaev viscosity in the artificial viscosity term provides a shear viscosity, given by

$$\nu_{\rm AV} = \frac{1}{10}\alpha_{\rm AV} c_s h \,, \tag{B.3.1}$$

where the AV notation refers to terms related to artificial viscosity. Since h is the smoothing length, we see that the viscosity is resolution dependent. If one wants to compute the resulting equivalent Shakura-Sunyaev $\alpha_{\rm SS}$ parameter for the shear viscosity, the result is

$$\alpha_{\rm SS} = \frac{1}{10}\alpha_{\rm AV}\frac{h}{H} \,, \tag{B.3.2}$$

where H is the scale-height of the disc. It should be noticed that, as h is inversely proportional to density, physical viscosity grows when density decreases; hence, if a precise treatment of viscosity in low density region is needed, using artificial viscosity to simulate the physical one could result a bad choice.

Lodato & Price (2010a) showed excellent agreement between this relation and the outcome of simulations. Thus, we could simulate the physical viscosity of our discs with the artificial one. Though, in order to keep an uniform value of $\alpha_{\rm SS}$, we would need a ratio h/H constant in the disc. In case of power-law density and sound speed profile, this translates in a relation between the two exponents. Then, once one of the two has been chosen, the other is fixed as a consequence.

B.3.1 Artificial Dissipation Switches

At this point, one has to ensure that artificial viscosity is acting only close to the discontinuities, and that is negligible elsewhere. In attempt to solve these problems, it has been proposed to use "switches" that turn off artificial viscosity where not needed. A switch to reduce the artificial viscosity away from shocks is proposed by Morris & Monaghan (1997). The key idea is to regard the dissipation parameter α as a particle property. For a proper description of these switches we refer to Price (2005). Use of this switch ensures that artificial thermal conductivity is only applied at large gradients in the thermal energy.

Appendix

C A dust mass conservation problem

Based on the paper by Giulia Ballabio, Giovanni Dipierro, ***Benedetta Veronesi****, Giuseppe Lodato, Mark Hutchison, Guillaume Laibe, Daniel J. Price (2018), "Enforcing dust mass conservation in 3D simulations of tightly-coupled grains with the* Phantom *SPH code", Monthly Notices of the Royal Astronomical Society, 477, 2766*

Protoplanetary discs are composed of a mixture of gas and dust. While gas usually dominates the mass, and hence the hydrodynamics of the system, dust is the dominant source of opacity in the bulk of the disc. As a result, the optical appearance of discs is strongly influenced by the dust distribution (Testi et al. 2014; Birnstiel et al. 2016). Recent high-resolution observations of protoplanetary discs have revealed a wealth of asymmetric structures in both gas and dust phases (e.g. Casassus 2016; Boehler et al. 2018). The physical mechanisms driving the formation of these structures are best understood using 3D hydrodynamical simulations that accurately model the coupling between gas and dust for a wide range of grain sizes (Haworth et al. 2016).

Solid particles embedded in a gas fluid are often treated using a continuous fluid description (Garaud et al. 2004). The macroscopic properties of the dust (e.g. density and velocity) are evolved on a set of grid points or particles that represent a volume large enough to be statistically meaningful, but sufficiently small as to ignore variations of the fluid quantities within that volume. In Smoothed Particle Hydrodynamic (SPH) simulations, the dust dynamics can be computed using two different approaches: the two-fluid algorithm described in Laibe & Price (2012a), typically used for large dust grains in weak drag regimes, and the one-fluid algorithm (Price & Laibe 2015) based on the so-called terminal velocity approximation (Youdin & Goodman 2005), which is better suited for simulating dust phases that

are tightly coupled with the gas. In terms of gas-dust modelling, the two-fluid implementation treats the gas and the dust as two separate sets of simulation particles, coupled by a drag force. In contrast, the SPH particles in the one-fluid approach represent the mixture, whose composition is determined by the dust fraction, that is evolved as a local property of the mixture.

Since it is numerically difficult to simulate all of the physical drag regimes that occur in nature with a single algorithm, methods/studies are often distinguished by the degree of coupling between phases, usually quantified by the so-called *Stokes number*: particles with the same Stokes number are aerodynamically identical – regardless of their shape, size, and/or density. The Stokes number is found by comparing the typical dynamical timescale of the system, $t_{\rm dyn}$, to the typical stopping timescale, $t_{\rm s}$, i.e. the time it takes for drag to significantly modify the relative velocity between a single grain and the gas. When the grains size is smaller than the mean free path of the gas (Epstein 1924) – which is generally the case for mm-cm size grains in protoplanetary discs (Garaud et al. 2004) –, the Stokes number is given by (Price & Laibe 2015)

$$\mathrm{St} \equiv \frac{t_{\rm s}}{t_{\rm dyn}} = \sqrt{\frac{\pi\gamma}{8}}\frac{\rho_{\rm int} a \Omega_{\rm k}}{\rho c_{\rm s} l}, \tag{C.0.1}$$

where a is the grain size, $\rho_{\rm int}$ is the intrinsic grain density, $c_{\rm s}$ is the sound speed, γ is the adiabatic index, $\Omega_{\rm k}$ is the Keplerian angular velocity ($\Omega_{\rm k} = t_{\rm dyn}^{-1}$), l is a correction factor for supersonic drag and ρ is the total density.

C.0.1 The one-fluid method

The one-fluid equations can be derived by rewriting the fluid equations for the gas and the dust in the barycentric reference frame of the mixture (Laibe & Price 2014a). In doing so, we substitute out the individual velocities of the gas and dust phases in favour of the new barycentric velocity of the mixture,

$$\mathbf{v} = \frac{\rho_{\rm g}\mathbf{v}_{\rm g} + \rho_{\rm d}\mathbf{v}_{\rm d}}{\rho_{\rm g} + \rho_{\rm d}}, \tag{C.0.2}$$

and the differential velocity between the two phases,

$$\Delta\mathbf{v} = \mathbf{v}_{\rm d} - \mathbf{v}_{\rm g}, \tag{C.0.3}$$

where ρ is the density, $\mathbf{v}$ is the velocity, and the subscripts g and d identify gas and dust quantities, respectively. Similar to the velocities, we replace the gas and dust densities by the total density, $\rho = \rho_{\rm d} + \rho_{\rm g}$, and the dust fraction, $\epsilon \equiv \rho_{\rm d}/\rho$, such that

$$\rho_{\rm g} = (1-\epsilon)\rho, \tag{C.0.4}$$

$$\rho_{\rm d} = \epsilon\rho. \tag{C.0.5}$$

The equations describing the evolution of a dust-gas mixture can be therefore written in the form (Laibe & Price 2014a)

$$\frac{\mathrm{d}\rho}{\mathrm{d}t} = -\rho(\nabla\cdot\mathbf{v}), \tag{C.0.6}$$

$$\frac{\mathrm{d}\epsilon}{\mathrm{d}t} = -\frac{1}{\rho}\nabla\cdot\left[\epsilon(1-\epsilon)\rho\Delta\mathbf{v}\right], \tag{C.0.7}$$

$$\frac{\mathrm{d}\mathbf{v}}{\mathrm{d}t} = -\frac{\nabla P}{\rho} - \frac{1}{\rho}\nabla\cdot\left[\epsilon(1-\epsilon)\rho\Delta\mathbf{v}\Delta\mathbf{v}\right] + \mathbf{f}, \tag{C.0.8}$$

$$\frac{\mathrm{d}\Delta\mathbf{v}}{\mathrm{d}t} = -\frac{\Delta\mathbf{v}}{t_\mathrm{s}} + \frac{\nabla P}{(1-\epsilon)\rho} - (\Delta\mathbf{v}\cdot\nabla)\mathbf{v} + \frac{1}{2}\nabla\cdot\left[(2\epsilon-1)\Delta\mathbf{v}\Delta\mathbf{v}\right], \tag{C.0.9}$$

$$\frac{\mathrm{d}\tilde{u}}{\mathrm{d}t} = -\frac{P}{\rho}\nabla\cdot(\mathbf{v}-\epsilon\Delta\mathbf{v}) + \epsilon(1-\epsilon)\frac{\Delta\mathbf{v}^2}{t_\mathrm{s}}, \tag{C.0.10}$$

where P is the gas pressure and $\mathbf{f}$ represents the external forces acting on both components (e.g. gravity). Moreover, for convenience we have parametrised the thermal energy as $\tilde{u} = u(1-\epsilon)$. The stopping time, t_s, is given by

$$t_\mathrm{s} = \frac{\epsilon(1-\epsilon)\rho}{K}, \tag{C.0.11}$$

where K is the drag coefficient, which regulates the aerodynamical coupling between the two phases (Weidenschilling 1977). The equations of the mixture are closed by the equation of state, such as the adiabatic one, i.e.

$$P = (\gamma-1)\rho\,\tilde{u}. \tag{C.0.12}$$

There are several advantages to using the one-fluid formulation over the two-fluid approach (see Price & Laibe 2015), particularly for small dust grains. For example, since the gas and dust are co-located in the one-fluid approach, it does not require (or can easily circumvent) the prohibitive temporal and spatial resolution requirements at high drag (needed in two-fluid simulations by the interpolation of fluid quantities between different phases, Laibe & Price 2012a). Furthermore, the one-fluid method prevents artificial trapping of dust beneath the resolution length of the gas. Finally, the one-fluid formalism naturally generalises to account for multiple dust species coupled to the same gas phase (Laibe & Price 2014c; Hutchison et al. 2018).

Terminal Velocity Approximation

The fluid equations in the one-fluid formalism can be simplified when the stopping time is small compared to the typical hydrodynamic timescale, i.e. the time required for a sound wave to propagate over a characteristic distance. In the context of SPH, we can write this condition as, $t_\mathrm{s} < h/c_\mathrm{s}$, where h is the local smoothing length of the particles. In this regime, usually referred to as *terminal velocity regime* (Youdin & Goodman 2005), the relative velocity between the two phases rapidly reach a terminal velocity due to the balancing of the drag and pressure forces. As a consequence, the time dependence of the differential velocity between

the gas and the dust can be ignored,

$$\Delta \mathbf{v} = t_{\rm s} \frac{\nabla P}{\rho_{\rm g}} = \frac{t_{\rm s}}{(1-\epsilon)} \frac{\nabla P}{\rho}. \tag{C.0.13}$$

Neglecting terms of second order in $t_{\rm s}$, Eqs. (C.0.6)-(C.0.10) reduce to

$$\frac{{\rm d}\rho}{{\rm d}t} = -\rho(\nabla \cdot \mathbf{v}), \tag{C.0.14}$$

$$\frac{{\rm d}\epsilon}{{\rm d}t} = -\frac{1}{\rho}\nabla \cdot (\epsilon t_{\rm s} \nabla P)\,, \tag{C.0.15}$$

$$\frac{{\rm d}\mathbf{v}}{{\rm d}t} = -\frac{\nabla P}{\rho} + \mathbf{f}, \tag{C.0.16}$$

$$\frac{{\rm d}\tilde{u}}{{\rm d}t} = -\frac{P}{\rho}(\nabla \cdot \mathbf{v}). \tag{C.0.17}$$

Apart from the additional evolution equation for the dust fraction, the equations in the terminal velocity approximation bear striking resemblance to the usual hydrodynamic equations for the gas without the dust. Therefore, the SPH discretisation of the continuity and momentum equations are identical to that of a regular gas-only simulation while the dust fraction and the thermal energy are discretised directly as shown in Eq. 43 in Price & Laibe (2015) and Eq. 55 in Hutchison et al. (2018).

C.0.2 Timestepping

The addition of the diffusion equation for the dust fraction (Eq. C.0.15) leads to an additional constraint on the timestep. Assuming a constant density and an isothermal equation of state, $P = c_{\rm s}^2(1-\epsilon)\rho$, Eq. (C.0.15) can be rewritten as

$$\frac{{\rm d}\epsilon}{{\rm d}t} = \nabla \cdot (\eta_\epsilon \nabla \epsilon)\,, \tag{C.0.18}$$

where $\eta_\epsilon \equiv \epsilon t_{\rm s} c_{\rm s}^2$ is the diffusion coefficient. A new constraint on the timestep is needed when the diffusion coefficient is larger. Indeed, Price & Laibe (2015) provide a stability criterion of the form

$$\Delta t < \Delta t_\epsilon \equiv C_0 \frac{h^2}{\eta_\epsilon} = C_0 \frac{h^2}{\epsilon c_{\rm s}^2\, t_{\rm s}}, \tag{C.0.19}$$

which implies that the timestep needs to be constrained when the stopping time is long – the opposite of the two-fluid case where the timestep is constrained for short stopping times. It is worth remarking that the terminal velocity approximation is only strictly valid when the stopping time is less than the computational timestep. Actually, a more general timestep condition can be derived, taking into account possible gradients in ϵ (see Subsection C.0.3). This is given as:

$$\Delta t < C_0 \frac{h^2}{\epsilon c_{\rm s}^2 t_{\rm s}} \frac{2a}{a^2+b^2}, \tag{C.0.20}$$

where $a = (1 - h^2\nabla^2\epsilon/\epsilon)$ and $b = 2h|\nabla\epsilon|/\epsilon$. It can be easily seen that Eq. (C.0.20) reduces to Eq. (C.0.19) for constant ϵ. This condition is safer than Eq. (C.0.19) in regions of strong gradients of ϵ, but it is more difficult to implement (since it requires an additional loop over the particles to obtain the gradient of ϵ) and can lead to severe timestep restrictions in certain practical applications (see Sect. C.3). As a result, we default back to Eq. (C.0.19) for our timestep control in this work.

C.0.3 Time stepping with gradients of ϵ

For simplicity, we derive the time step condition with non-zero derivatives of the dust fraction in 1D first, from

$$\frac{\mathrm{d}\epsilon}{\mathrm{d}t} = \frac{\partial}{\partial x}\left(\epsilon t_{\mathrm{s}} c_{\mathrm{s}}^2 \frac{\partial \epsilon}{\partial x}\right). \tag{C.0.21}$$

For the first order backward Euler scheme, the linear expansion of Eq. C.0.21 for modes of the form $\epsilon^n = \epsilon_0 + \delta\epsilon^n \mathrm{e}^{ikx}$ provides

$$\delta\epsilon^{n+1} = \delta\epsilon^n \left[1 + \Delta t \left(t_{\mathrm{s}} c_{\mathrm{s}}^2\right)\left(-k^2\epsilon_0 + \frac{\partial^2\epsilon_0}{\partial x^2} + 2ik\frac{\partial \epsilon_0}{\partial x}\right)\right]. \tag{C.0.22}$$

The numerical scheme requires $\left|\delta\epsilon^{n+1}/\delta\epsilon^n\right| < 1$ for stability. With the usual substitution $k \to h^{-1}$, this condition gives

$$|1 - q\,(a + ib)| < 1, \tag{C.0.23}$$

where $q \equiv \Delta t/\left(h^2/\eta_{\epsilon,0}\right)$, $a \equiv 1 - \frac{h^2}{\epsilon_0}\frac{\partial^2\epsilon_0}{\partial x^2}$ and $b \equiv 2\frac{h}{\epsilon_0}\frac{\partial\epsilon_0}{\partial x}$. Hence,

$$(1 - qa)^2 + (qb)^2 < 1. \tag{C.0.24}$$

Expanding the left-hand side of Eq. C.0.24 and dividing by $q > 0$ provides finally

$$q < \frac{2a}{a^2 + b^2}. \tag{C.0.25}$$

Putting a safety constant C_0 in front of the right-hand side of Eq. C.0.25 gives the generic form for the time step condition with gradients of ϵ, which can be generalised in 3D accordingly.

C.1 Enforcing positivity of the dust fraction

The one-fluid approach does not put any constraint on the positivity of the dust fraction. This problem can arise in regions where, for example, particles containing a finite amount of dust are adjacent to pure gas particles (i.e. $\epsilon = 0$). As the particles evolve in time, the infinite gradient in ϵ created at this interface leads the pure gas particles to develop a negative dust fraction. We can avert this problem by parameterising and evolving the dust fraction using a new variable, $s = \sqrt{\epsilon\rho}$. The positivity of the physical variable ϵ is now guaranteed since

$$\epsilon = s^2/\rho. \tag{C.1.1}$$

The corresponding diffusion equation for the new variable s is

$$\begin{aligned}\frac{\mathrm{d}s}{\mathrm{d}t} &= -\frac{1}{2s}\nabla\cdot\left(\frac{s^2}{\rho}t_{\mathrm{s}}\nabla P\right) - \frac{s}{2}\nabla\cdot\mathbf{v} \\ &= -\frac{1}{2}\nabla\cdot\left(\frac{s}{\rho}t_{\mathrm{s}}\nabla P\right) - \frac{t_{\mathrm{s}}}{2\rho}\nabla P\cdot\nabla s - \frac{s}{2}\nabla\cdot\mathbf{v}. \end{aligned} \tag{C.1.2}$$

We note that the first term on the right hand side of Eq. C.1.2 is written so as to prevent an infinite gradient in ϵ when $s \to 0$ (i.e. $\epsilon \to 0$). The usual method for discretising Eq. C.0.14,

$$\rho_a = \sum_b m_b W_{ab}(h_a), \tag{C.1.3}$$

trivially conserves the total mass of the mixture, but does nothing to conserve the mass of each of the components. Formally, mass conservation of the dust and gas also holds as long as the energy equation is modified appropriately Price et al. (2018a), i.e. such that

$$\frac{\mathrm{d}E}{\mathrm{d}t} = \frac{\mathrm{d}}{\mathrm{d}t}\sum_a m_a\left[\frac{1}{2}\mathbf{v}_a^2 + (1-\epsilon_a)u_a\right] = 0, \tag{C.1.4}$$

which, in terms of the new variable s, requires that

$$\sum_a m_a\left[\mathbf{v}_a\frac{\mathrm{d}\mathbf{v}_a}{\mathrm{d}t} + \rho_a^{\mathrm{g}}\frac{\mathrm{d}u_a}{\mathrm{d}t} - u_a\left(\frac{2s_a}{\rho_a}\frac{\mathrm{d}s_a}{\mathrm{d}t} - \frac{s_a^2}{\rho_a^2}\frac{\mathrm{d}\rho_a}{\mathrm{d}t}\right)\right] = 0. \tag{C.1.5}$$

The SPH discretisation for the evolution of s is shown in Eq. 280 of Price et al. (2018a). Although the formulation prevents ϵ from going negative, it does not guarantee that the dust fraction will remain smaller than unity. Numerical artefacts can appear in regions where the gradient of the dust fraction is steep, resulting in a spontaneous increase in dust mass. These artefacts are most severe when $\epsilon \to 0$ or $\epsilon \to 1$ and, at least in some instances, quickly drive the dust fraction to values larger than unity.

C.2 A new implementation

In this section we propose a new parametrization of the dust fraction similar to that used by Price & Laibe (2015), but that enforces the constraint $0 < \epsilon < 1$ by mapping the dust fraction to a function whose co-domain is only defined from $[0, 1]$, thereby preventing ϵ from becoming unphysical. A promising parametrization that meets the above criterion is given by

$$\epsilon = \frac{s^2}{1+s^2} \quad \text{such that} \quad s = \sqrt{\frac{\epsilon}{1-\epsilon}}. \tag{C.2.1}$$

In this new formulation the variable s is then related simply to the ratio of dust to gas densities, $s = \sqrt{\rho_{\mathrm{d}}/\rho_{\mathrm{g}}}$. We calculate the time derivative as

$$\frac{\mathrm{d}s}{\mathrm{d}t} = \frac{1}{2s(1-\epsilon)^2}\frac{\mathrm{d}\epsilon}{\mathrm{d}t}. \tag{C.2.2}$$

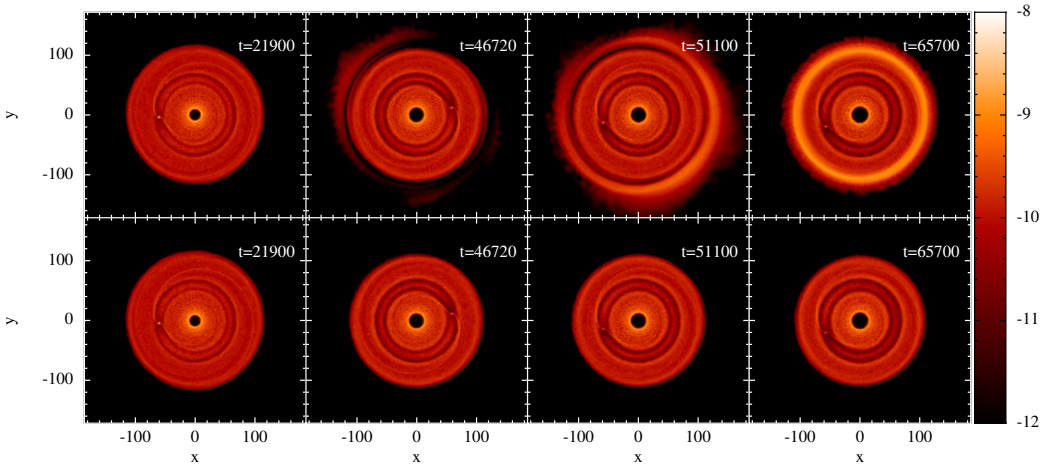

Figure C.1: Rendered images of dust surface density (in code units) at different times during a 3D SPH simulation of a dusty protostellar disc with a radial extent of $R \in [1, 120]$ au and an embedded planet of mass 0.5 M_J at 60 au. The dust surface density profile follows a power law with index $p = 0.5$. We used both the implementations described in Sect. C.1 (upper panels) and Sect. C.2 (lower panels). The gas disc density structure (not shown) is spatially larger than the dusty disc, producing a region in the outer disc with a strong gradient in the dust diffusivity. The evolution of the dust dynamics in these regions is better handled with the new implementation. In particular, the spurious dust rings, that appear at late times with the old formulation and that signal that dust mass is not well conserved, disappear with the new formulation. The temperature profile drops as a power law with $q = -0.7$ and the disc aspect ratio is $H(R_0)/R_0 = 0.025$, at $R_0 = 1$ au. The simulation describes the evolution of a 0.1 millimeter grain population.

Substituting Eq. (C.0.7) and manipulating the term on the right hand side of Eq. (C.2.2), we obtain

$$\frac{\mathrm{d}s}{\mathrm{d}t} = -\frac{1}{2\rho(1-\epsilon)^2}\Big\{\nabla\cdot\big[s(1-\epsilon)t_{\mathrm{s}}\nabla P\big] + (1-\epsilon)t_{\mathrm{s}}\nabla P\cdot\nabla s\Big\}. \tag{C.2.3}$$

The SPH discretisation is implemented in the form

$$\frac{\mathrm{d}s_a}{\mathrm{d}t} = -\frac{1}{2\rho_a\,(1-\epsilon_a)^2}\sum_b\left[\frac{m_b s_b}{\rho_b}\,(D_a+D_b)\,(P_a-P_b)\frac{\overline{F}_{ab}}{|r_{ab}|}\right], \tag{C.2.4}$$

where $D_a \equiv t_{\mathrm{s},a}\,(1-\epsilon_a)$. Like the previous implementation (Sect. C.1), our new expressions conserve linear and angular momentum, energy, and mass — at least up to the accuracy of the timestepping algorithm. Although it is true that the *total* mass is trivially conserved by virtue of Eq. (C.1.3), this attribute is not bequeathed to the individual phases due to their dependence on ϵ, an evolved quantity. This contingency on the time-evolution accuracy of ϵ plays an important role in the discussion that follows.

We implemented the above formalism into the SPH code PHANTOM (Lodato & Price 2010b; Price et al. 2018a) and tested it using PHANTOM's standard nightly test suite (described in Sect. 5.1 of Price et al. 2018a), which includes (among others) the DUSTYWAVE, DUSTYSHOCK, and DUSTYDIFFUSE tests described in Price & Laibe (2015). The new implementation not only passed within the 'acceptable' tolerances set for each test, it outperformed the existing algorithm. As a specific example, when compared with the previous method, the 'derivatives test' (Sect. 5.1.1 of Price et al. 2018a) showed an improvement in the accuracy of the time derivative of ϵ by a factor of five while the total energy conservation improved by a factor of ~ 400.

Next we looked at some typical configurations involving the interaction of an embedded protoplanet with its parent disc. Comparing the two parametrizations discussed in this paper, Fig. C.1 follows the evolution of the dust surface density (initial power law profile with index $p = -0.5$) in a 3D simulation of a dusty protostellar disc with a radial extent of $R \in [1, 120]$ au and an embedded planet of mass 0.5 $\mathrm{M_J}$ located at a distance of 60 au from the central star. The temperature profile drops as a power law with $q = -0.7$ and the disc aspect ratio is $H(R_0)/R_0 = 0.025$, at $R_0 = 1$ au. We embed the planet in order to further investigate diffusivity gradients that arise due to planet-disc interactions. The planet also alters the relative dust fractions in the inner and outer parts of the disc with time. The simulation describes the evolution of a 0.1 millimeter grain population. Particles with a non-negligible dust fraction exhibit Stokes numbers in the range $[0.02, 0.2]$, which safely correspond to stopping times below h/c_{s}.

As time progresses, the viscous and pressure forces in the disc cause the gas to expand radially outward, creating a strong gradient in the dust fraction (and hence diffusivity) at the edge of the dusty disc. Fig. C.1 shows that the numerical artefacts that occurred with the old implementation are removed with the new parametrization. This improved accuracy is thanks to the more accurate time-evolution of ϵ in regions with steep gradients in the dust diffusivity (i.e., at the outer edge of the dusty disc).

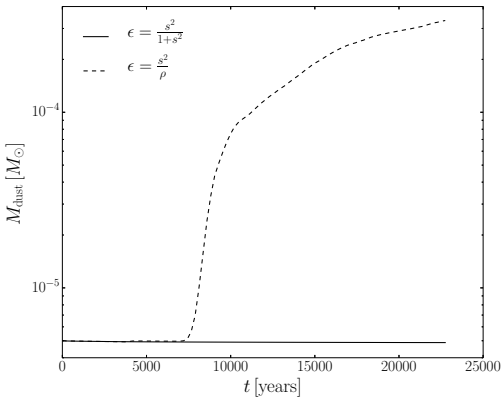

Figure C.2: Time evolution of the total dust mass for the parametrization $\epsilon = s^2/\rho$ described in Sect. C.1 (dashed line) and $\epsilon = s^2/(1+s^2)$ in Sect. C.2 (solid line). Importantly, the dust mass does not increase over time with the new parametrization.

Again comparing the two implementations, Fig. C.2 shows the time evolution of the total dust mass, i.e $\epsilon = s^2/\rho$ (dashed line) and $\epsilon = s^2/(1+s^2)$ (solid line). While with the old implementation the dust mass increases in time (starting from a value of $5 \cdot 10^{-6}\, M_\odot$ and reaching $3 \cdot 10^{-4}\, M_\odot$, after $\sim 2 \cdot 10^4$ years), the new implementation better computes the evolution of the dust density, avoiding most of the numerical artefacts occurring at the edge of the dusty disc due to the strong gradients in the dust fraction. Moreover, our tests show that the computation of the dust fraction and the thermal energy in our new implementation is faster than the $\sqrt{\epsilon\rho}$ parametrization described in Sect. C.1.

C.3 Limiting the stopping time

As mentioned earlier, despite the conservation ensured by the spatial discretisation of the fluid equations, non-conservation may still arise due to timestepping errors. Non-conservation of gas/dust mass are particularly vulnerable in regions of small ϵ where the dust fraction tends to relax the timestep (see Eq. C.0.19). However, since these regions are usually occupied by dust grains with large stopping times, they are the very regions that need a small timestep in order to be accurate. This breakdown of our timestep criterion is most likely due to the violation of the assumptions used to derive Eq. (C.0.19), and in particular to the fact that it was derived neglecting gradents in the dust fraction, as discussed already in Sect. C.1 above. In theory, we should be able to reduce our timestep (by adopting the full timestep condition, Eq. C.0.20, or by reducing C_0) to maintain mass conservation. We have verified that maintaining a 'sufficiently small' timestep for these problematic particles preserves mass conservation for the system, but at the cost of impossibly slow simulations when, e.g., very small amounts of dust get flung out and stranded in the low-density outer disc. Therefore, in practice we seek a more viable option that can circumvent these problem particles while still conserving gas/dust mass for the system. It is rather vexing that such violations most likely occur in 'peripherial' particles that often have little influence on the

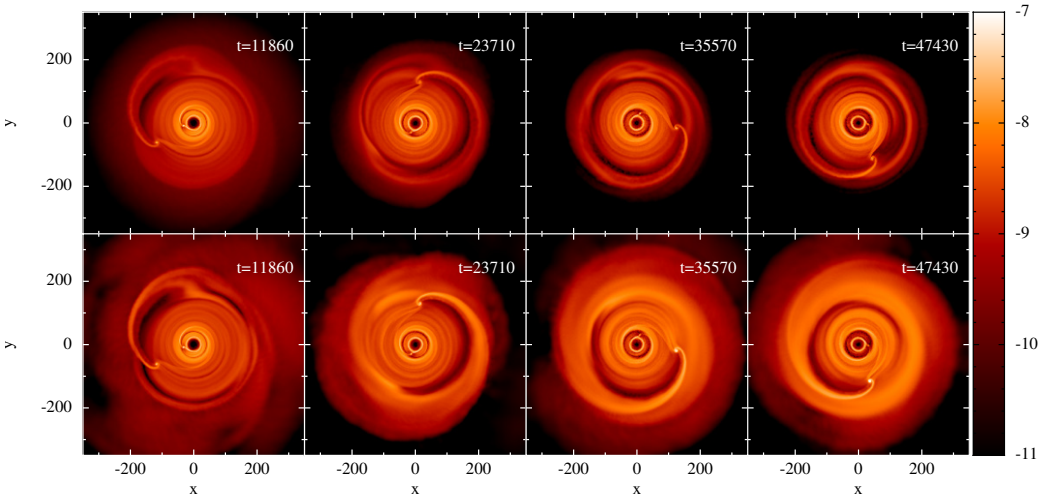

Figure C.3: Rendered images of dust surface density (in code units) at different times using our new $\sqrt{\rho_\mathrm{d}/\rho_\mathrm{g}}$ parametrization, including the limit on the stopping time (top panels) and not (bottom panels). To test the limits of our algorithm, we alter the disc model so that a large fraction of the dust grains in the outer disc have a stopping time larger than h/c_s. We further exacerbate the conditions by placing a massive protoplanet near the outer disc edge to stir up the dust in low density regions. Limiting the stopping time allows mass conservation to hold, even in these extreme conditions. The protoplanetary disc used in this simulation has a radial extent of $r \in [25, 200]$ au, with an aspect ratio, $H(R_0)/R_0 = 0.09$, at $R_0 = 25$ au and a power law temperature profile with index $q = -0.5$. The gaseous disc mass is $0.034\,M_\odot$, with a dust-to-gas ratio of 0.007. The initial gas and dust surface densities are given by a power law (index $p = -1$) with an exponential cut-off at $R_\mathrm{tap} = 70$ au. We considered a dust grain size of 1 mm. Two planets are embedded in the disc at 35 au and 140 au, of $4\,\mathrm{M_J}$ and $6\,\mathrm{M_J}$, respectively.

simulation at large. From experience, numerical artefacts are mostly likely to occur in the upper/outer regions of discs with high aspect ratio, H/R, and low (in absolute value) radial power-law index for the temperature, q. The dust diffusion, i.e. $\epsilon t_\mathrm{s} \nabla P$, in these regions is strong due to the steep gradients in the pressure and for particles with large stopping time.

To prevent the numerical inaccuracies we see when such strong gradients are present in the disc for particles with large stopping time, we propose moderating the rapid dust diffusion for problematic particles by enforcing the following limit on the stopping time

$$\tilde{t}_\mathrm{s} = \min\left(t_\mathrm{s}, h/c_\mathrm{s}\right), \tag{C.3.1}$$

that results in limiting the flux of the mass embodied in large particles. Limiting the flux of dust mass through the stopping time (as opposed to the pressure gradient or the diffusion coefficient as a whole) has the advantage that it is localised strictly to particles that violate the terminal velocity approximation and requires no prior knowledge about the dynamical state of the system.

Fig. C.3 compares the evolution of the dust surface density using our new dust implementation presented in Sect. C.2 (lower panels) and the same implementation, but limiting the stopping time (upper panels). The protoplanetary disc used

in these two simulations has a radial extent of $r \in [25, 200]$ au and it is thicker than the one used in Fig. C.1, with an aspect ratio, $H(R_0)/R_0 = 0.09$, at $R_0 = 25$ au and a temperature profile index $q = -0.5$. The gaseous disc mass is $0.034\,M_\odot$, with a dust-to-gas ratio of 0.007. The initial gas and dust surface densities are given by a power law (index $p = -1$) with an exponential cut-off at $R_{\rm tap} = 70$ au. The dust grain size is 1 mm. In this case, we include two planets at 35 au and 140 au, of $4\,{\rm M_J}$ and $6\,{\rm M_J}$, respectively. The outer planet is deliberately placed so as to fling dust into regions where we know the terminal velocity approximation has difficulty. Importantly, the flux limited simulations conserve the dust mass to machine precision while our other simulations do not. The spurious increase in dust mass in our unmodified simulation takes place in the outer disc where the gradients in the dust diffusivity are large.

It is important to note that by limiting the stopping time we are artificially modifying the Stokes number. Rewriting Eq. C.3.1 in terms of the Stokes number (for discs in vertical hydrostatic equilibrium, i.e. $H = c_{\rm s}/\Omega_{\rm k}$) yields

$$\mathrm{St} < h/H. \tag{C.3.2}$$

Since in typical SPH simulations $h/H < 1$, this new implementation affects the dust density evolution of large dust grains, even with moderately low $\mathrm{St} > h/H$. Since the radial dust velocity increases with St for $\mathrm{St} < 1$ (Nakagawa et al. 1986), limiting the stopping time leads to an underestimate of the radial flux of large grains towards disc regions of high pressure. Consequently, the new-found mass conservation afforded by limiting the flux is not an excuse to apply our method in every situation. In particular, care should be taken when simulating protoplanetary discs with high aspect ratio and low q, where it is more likely to find dust grains with both large and small Stokes number. For these discs, a correct physical description of the system may only be attainable with the full one-fluid approach (Laibe & Price 2014a), hybrid method combining the one- and two-fluid approaches or semi-analytical two-fluid methods (e.g. Lorén-Aguilar & Bate 2014).

In summary, limiting the stopping time conserves dust mass and prevents numerical artefacts from developing in particles in the outer disc where Stokes numbers are large and dust mass is negligible. The evolution of the dust density in these situations can be considered reliable. However, when the stopping time of particles are being limited in the bulk of the disc, where mass fractions are still high, we recommend using a different approach.

C.4 Conclusions

We introduce a new algorithm to compute the dynamics of tightly-coupled dust grains in the context of the one fluid approach described in Laibe & Price (2014a). Our algorithm avoids certain numerical artefacts that arise in the previous formalism (Price & Laibe 2015), rendering our method both faster and more accurate. We do this by

(i) parameterising the dust fraction using the square root of the dust-to-gas ratio, which enforces $\epsilon \in [0, 1]$;

(ii) limiting the stopping time below a value that ensures the validity of the equations of motion in the terminal velocity approximation, i.e. $t_s < h/c_s$.

The latter leaves the numerically-stable, strongly-coupled dust grains untouched, while limiting the amount of dust that can be transferred between weakly-coupled particles that would otherwise violate the assumptions of the one-fluid diffusion approximation. When the flux in these weakly-coupled grains is not constrained, the dust mass can un-physically grow over long times in some regions of the disc, violating mass conservation. We find no adverse effects of limiting the flux of particles with low dust fraction, which are typically found in the upper/outer regions of the disc. However, we caution that the stopping time limiter needs to be used with care, since it can lead to an incorrect computation of the dust dynamics of large decoupled dust grains when the dust fraction is non-negligible. In these situations, we recommend switching to a two-fluid formalism (Laibe & Price 2012a; Lorén-Aguilar & Bate 2014).

Finally, there are realistic scenarios in which a single grain size can be strongly-coupled in one region of the disc and weakly-coupled in another – with a significant dust mass in each region. In this scenario, neither the one-fluid diffusion approximation or the two-fluid method would be adequate, but would require a hybrid scheme that marries the two approaches or, alternatively, the full one-fluid formalism that allows for a wider range in drag regimes (Laibe & Price 2014a,b). Alternatively, implicit or semi-analytic methods have been proposed to simulate tightly-coupled particles in multi-fluid simulations with strong drag regimes (Lorén-Aguilar & Bate 2014; Booth et al. 2015; Lorén-Aguilar & Bate 2015b).

Bibliography

ALMA Partnership et al., 2015a, Astrophysical Journal, 808, L3

ALMA Partnership et al., 2015b, ApJL, 808, L3

Abramowitz M., Stegun I. A., 1972, Handbook of Mathematical Functions

Adams F. C., Shu F. H., 1986, ApJ, 308, 836

Aikawa Y., van Zadelhoff G. J., van Dishoeck E. F., Herbst E., 2002, Astronomy and Astrophysics, 386, 622

Alcalá J. M., et al., 2014, Astronomy and Astrophysics, 561, A2

Alcalá J. M., et al., 2017, Astronomy and Astrophysics, 600, A20

Alexander R., Pascucci I., Andrews S., Armitage P., Cieza L., 2014, in Beuther H., Klessen R. S., Dullemond C. P., Henning T., eds, Protostars and Planets VI. p. 475 (arXiv:1311.1819), doi:10.2458/azu˙uapress˙9780816531240-ch021

Alonso-Albi T., Fuente A., Bachiller R., Neri R., Planesas P., Testi L., Berné O., Joblin C., 2009, Astronomy and Astrophysics, 497, 117

Aly H., Lodato G., 2020, Monthly Notices of the RAS, 492, 3306

André P., 2002, in Bouvier J., Zahn J.-P., eds, EAS Publications Series Vol. 3, EAS Publications Series. pp 1–38, doi:10.1051/eas:2002043

André P., et al., 2010, Astronomy and Astrophysics, 518, L102

Andrews S. M., 2015, Publications of the Astronomical Society of the Pacific, 127, 961

Andrews S. M., 2020, arXiv e-prints, p. arXiv:2001.05007

Andrews S. M., Williams J. P., 2005, ApJ, 631, 1134

Andrews S. M., Williams J. P., 2007a, ApJ, 659, 705

Andrews S. M., Williams J. P., 2007b, Astrophysical Journal, 671, 1800

Andrews S. M., Wilner D. J., Hughes A. M., Qi C., Dullemond C. P., 2009, Astrophysical Journal, 700, 1502

Andrews S. M., Wilner D. J., Hughes A. M., Qi C., Dullemond C. P., 2010, Astrophysical Journal, 723, 1241

Andrews S. M., Wilner D. J., Espaillat C., Hughes A. M., Dullemond C. P., McClure M. K., Qi C., Brown J. M., 2011, Astrophysical Journal, 732, 42

Andrews S. M., Rosenfeld K. A., Kraus A. L., Wilner D. J., 2013, Astrophysical Journal, 771, 129

Andrews S. M., et al., 2016, Astrophysical Journal, Letters to the Editor, 820, L40

Andrews S. M., Terrell M., Tripathi A., Ansdell M., Williams J. P., Wilner D. J., 2018a, preprint, (arXiv:1808.10510)

Andrews S. M., et al., 2018b, Astrophysical Journal, Letters to the Editor, 869, L41

Ansdell M., et al., 2016, Astrophysical Journal, 828, 46

Ansdell M., Williams J. P., Manara C. F., Miotello A., Facchini S., van der Marel N., Testi L., van Dishoeck E. F., 2017, Astronomical Journal, 153, 240

Ansdell M., et al., 2018, preprint, (arXiv:1803.05923)

Armitage P. J., 2007, ArXiv Astrophysics e-prints, 0701485

Armitage P. J., 2013, Astrophysics of Planet Formation

Armitage P. J., 2015, arXiv e-prints, p. arXiv:1509.06382

Armitage P. J., 2018, A Brief Overview of Planet Formation. p. 135, doi:10.1007/978-3-319-55333-7˙135

Armitage P. J., Rice W. K. M., 2005, arXiv e-prints, pp astro–ph/0507492

Artymowicz P., 1993, Astrophysical Journal, 419, 155

Artymowicz P., 2004, in Caroff L., Moon L. J., Backman D., Praton E., eds, Astronomical Society of the Pacific Conference Series Vol. 324, Debris Disks and the Formation of Planets. p. 39

Artymowicz P., Lubow S. H., 1994, ApJ, 421, 651

Asensio-Torres R., et al., 2021, arXiv e-prints, p. arXiv:2103.05377

Ataiee S., Pinilla P., Zsom A., Dullemond C. P., Dominik C., Ghanbari J., 2013, Astronomy and Astrophysics, 553, L3

Auddy S., Lin M.-K., 2020, Astrophysical Journal, 900, 62

Avenhaus H., Quanz S. P., Schmid H. M., Meyer M. R., Garufi A., Wolf S., Dominik C., 2014, Astrophysical Journal, 781, 87

Avenhaus H., et al., 2017, Astronomical Journal, 154, 33

Avenhaus H., et al., 2018, Astrophysical Journal, 863, 44

Ayliffe B. A., Bate M. R., 2009, Monthly Notices of the RAS, 397, 657

Ayliffe B. A., Laibe G., Price D. J., Bate M. R., 2012, Monthly Notices of the RAS, 423, 1450

Bae J., Zhu Z., 2018a, Astrophysical Journal, 859, 118

Bae J., Zhu Z., 2018b, Astrophysical Journal, 859, 119

Bae J., Hartmann L., Zhu Z., 2015, Astrophysical Journal, 805, 15

Bae J., Zhu Z., Hartmann L., 2017, preprint, (arXiv:1706.03066)

Bae J., Pinilla P., Birnstiel T., 2018, Astrophysical Journal, Letters to the Editor,

864, L26
Bae J., et al., 2019, Astrophysical Journal, Letters to the Editor, 884, L41
Bae J., Teague R., Zhu Z., 2021, arXiv e-prints, p. arXiv:2102.03899
Bai X.-N., 2011, Astrophysical Journal, 739, 50
Bai X.-N., Stone J. M., 2010, Astrophysical Journal, 722, 1437
Bai X.-N., Stone J. M., 2011, Astrophysical Journal, 736, 144
Bai X.-N., Stone J. M., 2013, Astrophysical Journal, 769, 76
Balbus S. A., Hawley J. F., 1991, ApJ, 376, 214
Balbus S. A., Hawley J. F., 1998, Reviews of Modern Physics, 70, 1
Balbus S. A., Papaloizou J. C. B., 1999, ApJ, 521, 650
Ballabio G., Dipierro G., Veronesi B., Lodato G., Hutchison M., Laibe G., Price D. J., 2018, Monthly Notices of the RAS, 477, 2766
Ballabio G., Alexander R. D., Clarke C. J., 2020, Monthly Notices of the RAS, 496, 2932
Barbieri C. V., Fraternali F., Oosterloo T., Bertin G., Boomsma R., Sancisi R., 2005, Astronomy and Astrophysics, 439, 947
Barenfeld S. A., Carpenter J. M., Ricci L., Isella A., 2016, Astrophysical Journal, 827, 142
Barge P., Sommeria J., 1995, Astronomy and Astrophysics, 295, L1
Barge P., Ricci L., Carilli C. L., Previn-Ratnasingam R., 2017, Astronomy and Astrophysics, 605, A122
Baruteau C., Meru F., Paardekooper S.-J., 2011, Monthly Notices of the RAS, 416, 1971
Baruteau C., et al., 2014, Protostars and Planets VI, pp 667–689
Baruteau C., Bai X., Mordasini C., Mollière P., 2016, , 205, 77
Basri G., Bertout C., 1989, Astrophysical Journal, 341, 340
Bate M. R., 2011, Monthly Notices of the RAS, 417, 2036
Bate M. R., 2018, Monthly Notices of the RAS, 475, 5618
Bate M. R., Lorén-Aguilar P., 2017, Monthly Notices of the RAS, 465, 1089
Bate M. R., Bonnell I. A., Price N. M., 1995, MNRAS, 277, 362
Bate M. R., Lodato G., Pringle J. E., 2010, MNRAS, 401, 1505
Beckwith S. V. W., Sargent A. I., Chini R. S., Guesten R., 1990, AJ, 99, 924
Beichman C. A., Myers P. C., Emerson J. P., Harris S., Mathieu R., Benson P. J., Jennings R. E., 1986, Astrophysical Journal, 307, 337
Bell K. R., Lin D. N. C., 1994, ApJ, 427, 987
Benisty M., et al., 2015, Astronomy and Astrophysics, 578, L6
Benisty M., et al., 2017, Astronomy and Astrophysics, 597, A42
Benisty M., et al., 2018, Astronomy and Astrophysics, 619, A171
Benítez-Llambay P., Masset F. S., 2016, Astrophysical Journal, Supplement, 223, 11
Bergin E. A., Williams J. P., 2018, arXiv e-prints,
Bergin E. A., et al., 2013, Nature, 493, 644
Bergin E. A., Du F., Cleeves L. I., Blake G. A., Schwarz K., Visser R., Zhang K.,

2016, Astrophysical Journal, 831, 101
Bertin G., 1997, ApJ, 478, L71
Bertin G., 2000, Dynamics of Galaxies. Cambridge University Press, Cambridge
Bertin G., Lin C. C., 1996, Spiral structure in galaxies a density wave theory
Bertin G., Lodato G., 1999, A&A, 350, 694
Bertout C., 1989, Annual Review of Astronomy and Astrophysics, 27, 351
Béthune W., Lesur G., Ferreira J., 2017, Astronomy and Astrophysics, 600, A75
Biller B., et al., 2012, Astrophysical Journal, Letters to the Editor, 753, L38
Binney J., Tremaine S., 1987, Galactic dynamics. Princeton, NJ, Princeton University Press, 1987, 747 p.
Birnstiel T., Andrews S. M., 2014, Astrophysical Journal, 780, 153
Birnstiel T., Dullemond C. P., Brauer F., 2010a, Astronomy and Astrophysics, 513, A79
Birnstiel T., et al., 2010b, Astronomy and Astrophysics, 516, L14
Birnstiel T., Klahr H., Ercolano B., 2012, Astronomy and Astrophysics, 539, A148
Birnstiel T., Fang M., Johansen A., 2016, , 205, 41
Blum J., Wurm G., 2008, Annual Review of Astronomy and Astrophysics, 46, 21
Boccaletti A., et al., 2020, Astronomy and Astrophysics, 637, L5
Boehler Y., et al., 2018, Astrophysical Journal, 853, 162
Bohlin R. C., Savage B. D., Drake J. F., 1978, Astrophysical Journal, 224, 132
Boley A. C., Durisen R. H., Nordlund Å., Lord J., 2007, Astrophysical Journal, 665, 1254
Bollati F., Lodato G., Price D. J., Pinte C., 2021, arXiv e-prints, p. arXiv:2103.00016
Booth R. A., Clarke C. J., 2016, Monthly Notices of the RAS, 458, 2676
Booth R. A., Sijacki D., Clarke C. J., 2015, MNRAS, 452, 3932
Bosman A. D., Walsh C., van Dishoeck E. F., 2018, Astronomy and Astrophysics, 618, A182
Brauer F., Dullemond C. P., Johansen A., Henning T., Klahr H., Natta A., 2007, Astronomy and Astrophysics, 469, 1169
Brauer F., Dullemond C. P., Henning T., 2008, Astronomy and Astrophysics, 480, 859
Brittain S. D., Najita J. R., Dong R., Zhu Z., 2020, Astrophysical Journal, 895, 48
Brown J. M., Blake G. A., Qi C., Dullemond C. P., Wilner D. J., Williams J. P., 2009, Astrophysical Journal, 704, 496
Cadman J., Rice K., Hall C., Haworth T. J., Biller B., 2020a, Monthly Notices of the RAS, 492, 5041
Cadman J., Hall C., Rice K., Harries T. J., Klaassen P. D., 2020b, Monthly Notices of the RAS, 498, 4256
Calcino J., Christiaens V., Price D. J., Pinte C., Davis T. M., van der Marel N., Cuello N., 2020, Monthly Notices of the RAS, 498, 639
Calvet N., D'Alessio P., Hartmann L., Wilner D., Walsh A., Sitko M., 2002,

Astrophysical Journal, 568, 1008
Canovas H., et al., 2016, Monthly Notices of the RAS, 458, L29
Canovas H., et al., 2018, Astronomy and Astrophysics, 610, A13
Carballido A., Fromang S., Papaloizou J., 2006, Monthly Notices of the RAS, 373, 1633
Carmona A., et al., 2008, Astronomy and Astrophysics, 477, 839
Carmona A., et al., 2014, Astronomy and Astrophysics, 567, A51
Carney M. T., et al., 2018, Astronomy and Astrophysics, 614, A106
Carrasco-González C., Rodríguez L. F., Anglada G., Curiel S., 2009, Astrophysical Journal, Letters to the Editor, 693, L86
Carrasco-González C., et al., 2019, Astrophysical Journal, 883, 71
Casassus S., 2016, preprint, (arXiv:1602.06523)
Casassus S., Pérez S., 2019, Astrophysical Journal, Letters to the Editor, 883, L41
Casassus S., et al., 2018, Monthly Notices of the RAS, 477, 5104
Cazzoletti P., et al., 2018, preprint, (arXiv:1809.04160)
Cazzoletti P., et al., 2019, Astronomy and Astrophysics, 626, A11
Chen X. P., Henning T., van Boekel R., Grady C. A., 2006, Astronomy and Astrophysics, 445, 331
Chiang E. P., Goldreich P., 1997, ApJ, 490, 368
Chiang E. I., Joung M. K., Creech-Eakman M. J., Qi C., Kessler J. E., Blake G. A., van Dishoeck E. F., 2001, Astrophysical Journal, 547, 1077
Cieza L. A., et al., 2019, Monthly Notices of the RAS, 482, 698
Cieza L. A., et al., 2021, Monthly Notices of the RAS, 501, 2934
Clarke C. J., Lodato G., 2009, Monthly Notices of the RAS, 398, L6
Clarke C. J., Pringle J. E., 1988, Monthly Notices of the RAS, 235, 365
Clarke C. J., Pringle J. E., 1993, MNRAS, 261, 190
Clarke C., Harper-Clark E., Lodato G., 2007, MNRAS, 381, 1543
Clarke C. J., et al., 2018, Astrophysical Journal, Letters to the Editor, 866, L6
Cleeves L. I., Bergin E. A., Harries T. J., 2015, Astrophysical Journal, 807, 2
Cleeves L. I., Öberg K. I., Wilner D. J., Huang J., Loomis R. A., Andrews S. M., Guzman V. V., 2018, Astrophysical Journal, 865, 155
Collins K. A., et al., 2009, Astrophysical Journal, 697, 557
Cossins P., Lodato G., Clarke C. J., 2009a, MNRAS, 393, 1157
Cossins P., Lodato G., Clarke C. J., 2009b, Monthly Notices of the RAS, 393, 1157
Cossins P., Lodato G., Clarke C. J., 2010, MNRAS, 401
Crida A., Morbidelli A., 2007, Monthly Notices of the RAS, 377, 1324
Crida A., Morbidelli A., Masset F., 2006, Icarus, 181, 587
Cuello N., et al., 2019, Monthly Notices of the RAS, 483, 4114
Cuello N., et al., 2020, Monthly Notices of the RAS, 491, 504
Cuzzi J., Dobrovolski A. R., Champney J. M., 1993, Icarus, 106, 102
Cuzzi J. N., Hogan R. C., Shariff K., 2008, Astrophysical Journal, 687, 1432

D'Alessio P., Cantö J., Calvet N., Lizano S., 1998, Astrophysical Journal, 500, 411

D'Alessio P., Calvet N., Hartmann L., 2001, Astrophysical Journal, 553, 321

D'Angelo G., Lubow S. H., 2008, Astrophysical Journal, 685, 560

D'Angelo G., Bate M. R., Lubow S. H., 2005, Monthly Notices of the RAS, 358, 316

Dawson R. I., Johnson J. A., 2018, Annual Review of Astronomy and Astrophysics, 56, 175

DeWarf L. E., Sepinsky J. F., Guinan E. F., Ribas I., Nadalin I., 2003, Astrophysical Journal, 590, 357

Deng H., Mayer L., Meru F., 2017, Astrophysical Journal, 847, 43

Dent W. R. F., Greaves J. S., Coulson I. M., 2005, Monthly Notices of the RAS, 359, 663

Dipierro G., Laibe G., 2017, Monthly Notices of the RAS, 469, 1932

Dipierro G., Lodato G., Testi L., de Gregorio Monsalvo I., 2014, MNRAS, 444, 1919

Dipierro G., Pinilla P., Lodato G., Testi L., 2015a, MNRAS, 451, 974

Dipierro G., Price D., Laibe G., Hirsh K., Cerioli A., Lodato G., 2015b, Monthly Notices of the RAS, 453, L73

Dipierro G., Laibe G., Price D. J., Lodato G., 2016, Monthly Notices of the RAS, 459, L1

Dipierro G., et al., 2018a, Monthly Notices of the RAS, 475, 5296

Dipierro G., Laibe G., Alexander R., Hutchison M., 2018b, Monthly Notices of the RAS, 479, 4187

Dipierro G., Laibe G., Alexander R., Hutchison M., 2018c, Monthly Notices of the RAS, 479, 4187

Disk Dynamics Collaboration et al., 2020, arXiv e-prints, p. arXiv:2009.04345

Dodson-Robinson S. E., Salyk C., 2011, Astrophysical Journal, 738, 131

Dominik C., Dullemond C. P., 2008, Astronomy and Astrophysics, 491, 663

Dominik C., Blum J., Cuzzi J. N., Wurm G., 2007, in Reipurth B., Jewitt D., Keil K., eds, Protostars and Planets V. p. 783 (arXiv:astro-ph/0602617)

Dong R., Fung J., 2017a, Astrophysical Journal, 835, 146

Dong R., Fung J., 2017b, Astrophysical Journal, 835, 38

Dong R., Zhu Z., Whitney B., 2015a, Astrophysical Journal, 809, 93

Dong R., Zhu Z., Rafikov R. R., Stone J. M., 2015b, Astrophysical Journal, Letters to the Editor, 809, L5

Dong R., Hall C., Rice K., Chiang E., 2015c, ApJ, 812, L32

Dong R., Zhu Z., Fung J., Rafikov R., Chiang E., Wagner K., 2016, Astrophysical Journal, Letters to the Editor, 816, L12

Dong R., Li S., Chiang E., Li H., 2017, Astrophysical Journal, 843, 127

Dong R., et al., 2018a, Astrophysical Journal, 860, 124

Dong R., Li S., Chiang E., Li H., 2018b, Astrophysical Journal, 866, 110

Dong R., Liu S.-Y., Fung J., 2019, Astrophysical Journal, 870, 72

Draine B. T., 2003, Annual Review of Astronomy and Astrophysics, 41, 241

Draine B. T., 2006, Astrophysical Journal, 636, 1114

Dubrulle B., Morfill G., Sterzik M., 1995, Icarus, 114, 237

Duffell P. C., 2015, Astrophysical Journal, Letters to the Editor, 807, L11

Duffell P. C., MacFadyen A. I., 2013, Astrophysical Journal, 769, 41

Duffell P. C., Haiman Z., MacFadyen A. I., D'Orazio D. J., Farris B. D., 2014, Astrophysical Journal, Letters to the Editor, 792, L10

Dullemond C. P., Dominik C., 2004, Astronomy and Astrophysics, 421, 1075

Dullemond C. P., Hollenbach D., Kamp I., D'Alessio P., 2007, in Reipurth B., Jewitt D., Keil K., eds, Protostars and Planets V. p. 555 (arXiv:astro-ph/0602619)

Dullemond C. P., Juhasz A., Pohl A., Sereshti F., Shetty R., Peters T., Commercon B., Flock M., 2012, RADMC-3D: A multi-purpose radiative transfer tool, Astrophysics Source Code Library (ascl:1202.015)

Dullemond C. P., et al., 2018, Astrophysical Journal, Letters to the Editor, 869, L46

Dullemond C. P., Küffmeier M., Goicovic F., Fukagawa M., Oehl V., Kramer M., 2019, Astronomy and Astrophysics, 628, A20

Durisen R. H., Boss A. P., Mayer L., Nelson A. F., Quinn T., Rice W. K. M., 2007, in Reipurth B., Jewitt D., Keil K., eds, Protostars and Planets V. p. 607

Dürmann C., Kley W., 2015, Astronomy and Astrophysics, 574, A52

Dutrey A., Guilloteau S., Prato L., Simon M., Duvert G., Schuster K., Menard F., 1998, Astronomy and Astrophysics, 338, L63

Dutrey A., et al., 2008, Astronomy and Astrophysics, 490, L15

Epstein P. S., 1924, Physical Review, 23, 710

Ercolano B., Pascucci I., 2017, Royal Society Open Science, 4, 170114

Evans Neal J. I., et al., 2009, Astrophysical Journal, Supplement, 181, 321

Facchini S., Birnstiel T., Bruderer S., van Dishoeck E. F., 2017, Astronomy and Astrophysics, 605, A16

Facchini S., Juhász A., Lodato G., 2018a, Monthly Notices of the RAS, 473, 4459

Facchini S., Pinilla P., van Dishoeck E. F., de Juan Ovelar M., 2018b, Astronomy and Astrophysics, 612, A104

Facchini S., et al., 2019, Astronomy and Astrophysics, 626, L2

Fan Z., Lou Y.-Q., 1999, Monthly Notices of the RAS, 307, 645

Favre C., Cleeves L. I., Bergin E. A., Qi C., Blake G. A., 2013, Astrophysical Journal, Letters to the Editor, 776, L38

Fedele D., van den Ancker M. E., Henning T., Jayawardhana R., Oliveira J. M., 2010, Astronomy and Astrophysics, 510, A72

Fedele D., et al., 2017, Astronomy and Astrophysics, 600, A72

Fedele D., et al., 2018, Astronomy and Astrophysics, 610, A24

Flaherty K. M., Hughes A. M., Rosenfeld K. A., Andrews S. M., Chiang E., Simon J. B., Kerzner S., Wilner D. J., 2015, Astrophysical Journal, 813, 99

Flaherty K. M., et al., 2017, Astrophysical Journal, 843, 150

Flaherty K., et al., 2020, Astrophysical Journal, 895, 109
Flock M., Ruge J. P., Dzyurkevich N., Henning T., Klahr H., Wolf S., 2015, Astronomy and Astrophysics, 574, A68
Follette K. B., et al., 2013, Astrophysical Journal, 767, 10
Follette K. B., et al., 2017, Astronomical Journal, 153, 264
Foreman-Mackey D., 2016, The Journal of Open Source Software, 1, 24
Foreman-Mackey D., Hogg D. W., Lang D., Goodman J., 2013, Publications of the Astronomical Society of the Pacific, 125, 306
Forgan D., Rice K., Cossins P., Lodato G., 2011, Monthly Notices of the RAS, 410, 994
Forgan D. H., Ilee J. D., Meru F., 2018, Astrophysical Journal, Letters to the Editor, 860, L5
Frank J., King A., Raine D., 2002, Accretion Power in Astrophysics. Cambridge University Press, Cambridge
Fromang S., Nelson R. P., 2009, Astronomy and Astrophysics, 496, 597
Fromang S., Papaloizou J., 2006, Astronomy and Astrophysics, 452, 751
Fu W., Li H., Lubow S., Li S., Liang E., 2014, Astrophysical Journal, Letters to the Editor, 795, L39
Fung J., Chiang E., 2016, Astrophysical Journal, 832, 105
Fung J., Dong R., 2015, Astrophysical Journal, Letters to the Editor, 815, L21
Fung J., Shi J.-M., Chiang E., 2014, Astrophysical Journal, 782, 88
Furlan E., et al., 2006, Astrophysical Journal, Supplement, 165, 568
Gaia Collaboration et al., 2018, Astronomy and Astrophysics, 616, A1
Galli D., 2005, Astrophysics and Space Science, 295, 43
Gammie C. F., 1996, ApJ, 457, 355
Gammie C. F., 2001, ApJ, 553, 174
Garaud P., Barrière-Fouchet L., Lin D. N. C., 2004, Astrophysical Journal, 603, 292
Garufi A., et al., 2013, Astronomy and Astrophysics, 560, A105
Garufi A., Quanz S. P., Schmid H. M., Avenhaus H., Buenzli E., Wolf S., 2014, Astronomy and Astrophysics, 568, A40
Garufi A., et al., 2018, preprint, (arXiv:1810.04564)
Gingold R. A., Monaghan J. J., 1977, Monthly Notices of the RAS, 181, 375
Ginski C., et al., 2016, Astronomy and Astrophysics, 595, A112
Ginski C., et al., 2021, Astrophysical Journal, Letters to the Editor, 908, L25
Goldreich P., Tremaine S., 1979, Astrophysical Journal, 233, 857
Goldreich P., Tremaine S., 1980, Astrophysical Journal, 241, 425
Goldreich P., Ward W. R., 1973, Astrophysical Journal, 183, 1051
Gonzalez J.-F., et al., 2020, Monthly Notices of the RAS, 499, 3837
Goodman A. A., Benson P. J., Fuller G. A., Myers P. C., 1993, Astrophysical Journal, 406, 528
Gradshteyn I. S., Ryzhik I. M., 1980, Table of integrals, series and products
Grady C. A., et al., 2007, Astrophysical Journal, 665, 1391

Grady C. A., et al., 2009, Astrophysical Journal, 699, 1822
Grady C. A., et al., 2013, Astrophysical Journal, 762, 48
Greaves J. S., Rice W. K. M., 2010, Monthly Notices of the RAS, 407, 1981
Greaves J. S., Richards A. M. S., Rice W. K. M., Muxlow T. W. B., 2008, Monthly Notices of the RAS, 391, L74
Guillot T., Lin D. N. C., Morel P., Havel M., Parmentier V., 2014, in EAS Publications Series. pp 327–336 (arXiv:1409.7477), doi:10.1051/eas/1465009
Guilloteau S., Dutrey A., Piétu V., Boehler Y., 2011, Astronomy and Astrophysics, 529, A105
Guilloteau S., Dutrey A., Wakelam V., Hersant F., Semenov D., Chapillon E., Henning T., Piétu V., 2012, Astronomy and Astrophysics, 548, A70
Gullbring E., Hartmann L., Briceño C., Calvet N., 1998, ApJ, 492, 323
Guzmán V. V., et al., 2018, Astrophysical Journal, Letters to the Editor, 869, L48
Haffert S. Y., Bohn A. J., de Boer J., Snellen I. A. G., Brinchmann J., Girard J. H., Keller C. U., Bacon R., 2019, Nature Astronomy, 3, 749
Haghighipour N., Boss A. P., 2003a, ApJ, 583, 996
Haghighipour N., Boss A. P., 2003b, ApJ, 598, 1301
Hall C., Forgan D., Rice K., Harries T. J., Klaassen P. D., Biller B., 2016, Monthly Notices of the RAS, 458, 306
Hall C., Rice K., Dipierro G., Forgan D., Harries T., Alexander R., 2018, Monthly Notices of the RAS, 477, 1004
Hall C., Dong R., Rice K., Harries T. J., Najita J., Alexander R., Brittain S., 2019, Astrophysical Journal, 871, 228
Hall C., et al., 2020, Astrophysical Journal, 904, 148
Hartmann L., 2009, Accretion Processes in Star Formation: Second Edition. Cambridge University Press
Hartmann L., Calvet N., Gullbring E., D'Alessio P., 1998, ApJ, 495, 385
Hartmann L., Herczeg G., Calvet N., 2016, Annual Review of Astronomy and Astrophysics, 54, 135
Hashimoto J., et al., 2011, Astrophysical Journal, 729, L17
Hashimoto J., Aoyama Y., Konishi M., Uyama T., Takasao S., Ikoma M., Tanigawa T., 2020, Astronomical Journal, 159, 222
Hawley J. F., Balbus S. A., 1991, ApJ, 376, 223
Haworth T. J., et al., 2016, preprint, (arXiv:1608.01315)
Hendler N. P., et al., 2017, arXiv e-prints, p. arXiv:1711.09933
Hendler N. P., et al., 2018, Monthly Notices of the RAS, 475, L62
Herczeg G. J., Hillenbrand L. A., 2008, Astrophysical Journal, 681, 594
Hoyle F., 1960, Quarterly Journal of the Royal Astronomical Society, 1, 28
Huang J., et al., 2018a, Astrophysical Journal, 852, 122
Huang J., et al., 2018b, Astrophysical Journal, Letters to the Editor, 869, L43
Huang J., et al., 2018c, Astrophysical Journal, Letters to the Editor, 869, L42
Huang J., et al., 2020, Astrophysical Journal, 898, 140
Hughes A. M., Wilner D. J., Andrews S. M., Qi C., Hogerheijde M. R., 2011,

Astrophysical Journal, 727, 85
Hughes A. M., Duchêne G., Matthews B. C., 2018, Annual Review of Astronomy and Astrophysics, 56, 541
Hunter J. D., 2007, Computing in Science and Engineering, 9, 90
Hutchison M., Price D. J., Laibe G., 2018, Monthly Notices of the RAS, 476, 2186
Ilee J. D., et al., 2017, Monthly Notices of the RAS, 472, 189
Isella A., Carpenter J. M., Sargent A. I., 2010, Astrophysical Journal, 714, 1746
Isella A., Pérez L. M., Carpenter J. M., Ricci L., Andrews S., Rosenfeld K., 2013, Astrophysical Journal, 775, 30
Isella A., et al., 2018, Astrophysical Journal, Letters to the Editor, 869, L49
Isella A., Benisty M., Teague R., Bae J., Keppler M., Facchini S., Pérez L., 2019, Astrophysical Journal, Letters to the Editor, 879, L25
Ivanov P. B., Papaloizou J. C. B., Polnarev A. G., 1999, Monthly Notices of the RAS, 307, 79
Jacquet E., Balbus S., Latter H., 2011, Monthly Notices of the RAS, 415, 3591
Jeans J. H., 1902, Philosophical Transactions of the Royal Society of London Series A, 199, 1
Jin S., Li S., Isella A., Li H., Ji J., 2016, Astrophysical Journal, 818, 76
Johansen A., Klahr H., 2005, Astrophysical Journal, 634, 1353
Johansen A., Oishi J. S., Low M.-M. M., Klahr H., Henning T., Youdin A., 2007, Nature, 448, 1022
Johansen A., Youdin A., Klahr H., 2009, Astrophysical Journal, 697, 1269
Johnston K. G., et al., 2020, Astronomy and Astrophysics, 634, L11
Juhász A., Benisty M., Pohl A., Dullemond C. P., Dominik C., Paardekooper S. J., 2015, Monthly Notices of the RAS, 451, 1147
Kanagawa K. D., Muto T., Tanaka H., Tanigawa T., Takeuchi T., Tsukagoshi T., Momose M., 2015, Astrophysical Journal, Letters to the Editor, 806, L15
Kanagawa K. D., Tanaka H., Muto T., Tanigawa T., 2017, , 69, 97
Kanagawa K. D., Muto T., Okuzumi S., Tanigawa T., Taki T., Shibaike Y., 2018, Astrophysical Journal, 868, 48
Kataoka A., Okuzumi S., Tanaka H., Nomura H., 2014, Astronomy and Astrophysics, 568, A42
Kataoka A., Muto T., Momose M., Tsukagoshi T., Dullemond C. P., 2015, preprint, (arXiv:1507.08902)
Kenyon S. J., Hartmann L., 1987, ApJ, 323, 714
Keppler M., et al., 2018, Astronomy and Astrophysics, 617, A44
Keppler M., et al., 2019, Astronomy and Astrophysics, 625, A118
Keppler M., et al., 2020, Astronomy and Astrophysics, 639, A62
Kitamura Y., Momose M., Yokogawa S., Kawabe R., Tamura M., Ida S., 2002, Astrophysical Journal, 581, 357
Klahr H. H., Henning T., 1997, Icarus, 128, 213
Kley W., Dirksen G., 2006, Astronomy and Astrophysics, 447, 369
Kley W., Nelson R. P., 2012, Annual Review of Astronomy and Astrophysics, 50,

211
Kratter K., Lodato G., 2016, Annual Review of Astronomy and Astrophysics, 54, 271
Kratter K. M., Murray-Clay R. A., 2011, Astrophysical Journal, 740, 1
Kratter K. M., Matzner C. D., Krumholz M. R., Klein R. I., 2010, Astrophysical Journal, 708, 1585
Kuffmeier M., Haugbølle T., Nordlund Å., 2017, Astrophysical Journal, 846, 7
Kuffmeier M., Frimann S., Jensen S. S., Haugbølle T., 2018, Monthly Notices of the RAS, 475, 2642
Kurtovic N. T., et al., 2018, Astrophysical Journal, Letters to the Editor, 869, L44
Kwon W., Looney L. W., Mundy L. G., 2011, Astrophysical Journal, 741, 3
Lacour S., et al., 2016, Astronomy and Astrophysics, 590, A90
Lada C. J., 1987, in Peimbert M., Jugaku J., eds, Vol. 115, Star Forming Regions. p. 1
Lada C. J., Wilking B. A., 1984, ApJ, 287, 610
Lagage P.-O., et al., 2006, Science, 314, 621
Laibe G., Price D. J., 2012a, MNRAS, 420, 2345
Laibe G., Price D. J., 2012b, Monthly Notices of the RAS, 420, 2365
Laibe G., Price D. J., 2014a, Monthly Notices of the RAS, 440, 2136
Laibe G., Price D. J., 2014b, Monthly Notices of the RAS, 440, 2147
Laibe G., Price D. J., 2014c, MNRAS, 444, 1940
Laibe G., Gonzalez J. F., Maddison S. T., 2012, Astronomy and Astrophysics, 537, A61
Laibe G., Gonzalez J.-F., Maddison S. T., Crespe E., 2014, Monthly Notices of the RAS, 437, 3055
Langlois M., et al., 2018, Astronomy and Astrophysics, 614, A88
Larson R. B., 2003, Reports on Progress in Physics, 66, 1651
Lau Y. Y., Bertin G., 1978, ApJ, 226, 508
Lay O. P., Carlstrom J. E., Hills R. E., 1997, Astrophysical Journal, 489, 917
Lesur G., Hennebelle P., Fromang S., 2015, Astronomy and Astrophysics, 582, L9
Li H., Lubow S. H., Li S., Lin D. N. C., 2009, Astrophysical Journal, Letters to the Editor, 690, L52
Lin D. N. C., Papaloizou J., 1979a, Monthly Notices of the RAS, 186, 799
Lin D. N. C., Papaloizou J., 1979b, Monthly Notices of the RAS, 188, 191
Lin D. N. C., Papaloizou J., 1986, Astrophysical Journal, 309, 846
Lin D. N. C., Papaloizou J. C. B., 1993, in Levy E. H., Lunine J. I., eds, Protostars and Planets III. pp 749–835
Lin D. N. C., Pringle J. E., 1987, Monthly Notices of the RAS, 225, 607
Lin C. C., Shu F. H., 1964, Astrophysical Journal, 140, 646
Lin S.-Y., Ohashi N., Lim J., Ho P. T. P., Fukagawa M., Tamura M., 2006, Astrophysical Journal, 645, 1297
Liu Y., et al., 2018a, preprint, (arXiv:1811.04074)

Liu Y., et al., 2018b, preprint, p. arXiv:1811.04074 (arXiv:1811.04074)
Liu Y., et al., 2019, Astronomy and Astrophysics, 622, A75
Lodato G., 1998, Master's thesis, Università degli Studi, Pisa
Lodato G., 2007, Nuovo Cimento Rivista Serie, 30, 293
Lodato G., 2008, New Astronomy Review, 52, 21
Lodato G., Bertin G., 2003, Astronomy and Astrophysics, 398, 517
Lodato G., Clarke C. J., 2011, Monthly Notices of the RAS, 413, 2735
Lodato G., Price D. J., 2010a, Monthly Notices of the RAS, 405, 1212
Lodato G., Price D. J., 2010b, Monthly Notices of the RAS, 405
Lodato G., Rice W. K. M., 2004, Monthly Notices of the RAS, 351, 630
Lodato G., Rice W. K. M., 2005, Monthly Notices of the RAS, 358, 1489
Lodato G., Nayakshin S., King A. R., Pringle J. E., 2009, Monthly Notices of the RAS, 398, 1392
Lodato G., Scardoni C. E., Manara C. F., Testi L., 2017, Monthly Notices of the RAS, 472, 4700
Lodato G., et al., 2019, Monthly Notices of the RAS, 486, 453
Lombart M., Laibe G., 2020, Monthly Notices of the RAS,
Long F., et al., 2017, Astrophysical Journal, 844, 99
Long Z. C., et al., 2018a, Astrophysical Journal, 858, 112
Long F., et al., 2018b, Astrophysical Journal, 869, 17
Long F., et al., 2019, Astrophysical Journal, 882, 49
Long F., et al., 2020, Astrophysical Journal, 898, 36
Loomis R. A., Öberg K. I., Andrews S. M., MacGregor M. A., 2017, Astrophysical Journal, 840, 23
Looney L. W., Mundy L. G., Welch W. J., 2000, Astrophysical Journal, 529, 477
Lorén-Aguilar P., Bate M. R., 2014, Monthly Notices of the RAS, 443, 927
Lorén-Aguilar P., Bate M. R., 2015a, Monthly Notices of the RAS, 453, L78
Lorén-Aguilar P., Bate M. R., 2015b, Monthly Notices of the RAS, 454, 4114
Lovelace R. V. E., Li H., Colgate S. A., Nelson A. F., 1999, Astrophysical Journal, 513, 805
Lubow S. H., D'Angelo G., 2006, apj, 641, 526
Lubow S. H., Martin R. G., Nixon C., 2015, Astrophysical Journal, 800, 96
Lucy L. B., 1977, Astronomical Journal, 82, 1013
Luhman K. L., Rieke G. H., 1999, Astrophysical Journal, 525, 440
Lynden-Bell D., Pringle J. E., 1974, MNRAS, 168, 603
Lyra W., Umurhan O. M., 2019, Publications of the Astronomical Society of the Pacific, 131, 072001
Lyra W., Johansen A., Zsom A., Klahr H., Piskunov N., 2009, Astronomy and Astrophysics, 497, 869
Macías E., Anglada G., Osorio M., Torrelles J. M., Carrasco-González C., Gómez J. F., Rodríguez L. F., Sierra A., 2017, Astrophysical Journal, 838, 97
Macías E., et al., 2019, Astrophysical Journal, 881, 159
Macias E., Guerra-Alvarado O., Carrasco-Gonzalez C., Ribas A., Espaillat C. C.,

Huang J., Andrews S. M., 2021, arXiv e-prints, p. arXiv:2102.04648
Maire A.-L., et al., 2017, Astronomy and Astrophysics, 601, A134
Malik M., Meru F., Mayer L., Meyer M., 2015, Astrophysical Journal, 802, 56
Manara C. F., Testi L., Natta A., Rosotti G., Benisty M., Ercolano B., Ricci L., 2014, Astronomy and Astrophysics, 568, A18
Manara C. F., Fedele D., Herczeg G. J., Teixeira P. S., 2016a, Astronomy and Astrophysics, 585, A136
Manara C. F., et al., 2016b, Astronomy and Astrophysics, 591, L3
Manara C. F., et al., 2017, Astronomy and Astrophysics, 604, A127
Manara C. F., Morbidelli A., Guillot T., 2018, Astronomy and Astrophysics, 618, L3
Manara C. F., et al., 2019a, Astronomy and Astrophysics, 628, A95
Manara C. F., Mordasini C., Testi L., Williams J. P., Miotello A., Lodato G., Emsenhuber A., 2019b, Astronomy and Astrophysics, 631, L2
Manara C. F., et al., 2020, Astronomy and Astrophysics, 639, A58
Marino S., Perez S., Casassus S., 2015, Astrophysical Journal, Letters to the Editor, 798, L44
Marshall M. D., Avara M. J., McKinney J. C., 2018, Monthly Notices of the RAS, 478, 1837
Martin R. G., Lubow S. H., 2011, Astrophysical Journal, Letters to the Editor, 740, L6
Mason B. D., Wycoff G. L., Hartkopf W. I., Douglass G. G., Worley C. E., 2001, Astronomical Journal, 122, 3466
Masset F. S., Papaloizou J. C. B., 2003, Astrophysical Journal, 588, 494
Masset F. S., Morbidelli A., Crida A., Ferreira J., 2006, Astrophysical Journal, 642, 478
Mathis J. S., Rumpl W., Nordsieck K. H., 1977, Astrophysical Journal, 217, 425
Matsumoto T., Hanawa T., 2003, Astrophysical Journal, 595, 913
Maury A. J., et al., 2019, Astronomy and Astrophysics, 621, A76
Mayor M., Queloz D., 1995, Nature, 378, 355
McCaughrean M. J., et al., 1998, Astrophysical Journal, Letters to the Editor, 492, L157
McClure M. K., et al., 2016, Astrophysical Journal, 831, 167
McMullin J. P., Waters B., Schiebel D., Young W., Golap K., 2007, in Shaw R. A., Hill F., Bell D. J., eds, Astronomical Society of the Pacific Conference Series Vol. 376, Astronomical Data Analysis Software and Systems XVI. p. 127
Meeus G., et al., 2012, Astronomy and Astrophysics, 544, A78
Ménard F., et al., 2020, Astronomy and Astrophysics, 639, L1
Mentiplay D., Price D. J., Pinte C., 2019, Monthly Notices of the RAS, 484, L130
Meru F., Bate M. R., 2010, Monthly Notices of the RAS, 406, 2279
Meru F., Bate M. R., 2011, Monthly Notices of the RAS, 411, L1
Meru F., Bate M. R., 2012, Monthly Notices of the RAS, 427, 2022
Meru F., Juhász A., Ilee J. D., Clarke C. J., Rosotti G. P., Booth R. A., 2017,

Astrophysical Journal, Letters to the Editor, 839, L24
Meru F., Rosotti G. P., Booth R. A., Nazari P., Clarke C. J., 2019, Monthly Notices of the RAS, 482, 3678
Mesa D., et al., 2019, Astronomy and Astrophysics, 632, A25
Mestel L., 1963, Monthly Notices of the RAS, 126, 553
Meyer D. M. A., Kuiper R., Kley W., Johnston K. G., Vorobyov E., 2018, Monthly Notices of the RAS, 473, 3615
Meyer D. M. A., Kreplin A., Kraus S., Vorobyov E. I., Haemmerle L., Eislöffel J., 2019, Monthly Notices of the RAS, 487, 4473
Min M., Rab C., Woitke P., Dominik C., Ménard F., 2016, Astronomy and Astrophysics, 585, A13
Miotello A., Robberto M., Potenza M. A. C., Ricci L., 2012, Astrophysical Journal, 757, 78
Miotello A., Bruderer S., van Dishoeck E. F., 2014, Astronomy and Astrophysics, 572, A96
Miotello A., van Dishoeck E. F., Kama M., Bruderer S., 2016, preprint, (arXiv:1605.07780)
Miotello A., et al., 2017, Astronomy and Astrophysics, 599, A113
Miranda R., Lai D., 2015, Monthly Notices of the RAS, 452, 2396
Miranda R., Rafikov R. R., 2019a, Astrophysical Journal, 875, 37
Miranda R., Rafikov R. R., 2019b, Astrophysical Journal, Letters to the Editor, 878, L9
Mizuno H., Markiewicz W. J., Voelk H. J., 1988, Astronomy and Astrophysics, 195, 183
Moeckel N., Throop H. B., 2009, Astrophysical Journal, 707, 268
Molinari S., et al., 2010, Astronomy and Astrophysics, 518, L100
Monaghan J. J., 1992, Annual Review of Astronomy and Astrophysics, 30, 543
Monaghan J. J., Lattanzio J. C., 1985, Astronomy and Astrophysics, 149, 135
Monnier J. D., et al., 2019, Astrophysical Journal, 872, 122
Montesinos M., Cuello N., 2018, Monthly Notices of the RAS, 475, L35
Montesinos M., Perez S., Casassus S., Marino S., Cuadra J., Christiaens V., 2016, Astrophysical Journal, Letters to the Editor, 823, L8
Moór A., et al., 2015, Astrophysical Journal, 814, 42
Morbidelli A., 2020, Astronomy and Astrophysics, 638, A1
Morbidelli A., Raymond S. N., 2016, Journal of Geophysical Research (Planets), 121, 1962
Morbidelli A., Szulágyi J., Crida A., Lega E., Bitsch B., Tanigawa T., Kanagawa K., 2014, Icarus, 232, 266
Morris J. P., Monaghan J. J., 1997, Journal of Computational Physics, 136, 41
Mulders G. D., Pascucci I., Manara C. F., Testi L., Herczeg G. J., Henning T., Mohanty S., Lodato G., 2017a, Astrophysical Journal, 847, 31
Mulders G. D., Pascucci I., Manara C. F., Testi L., Herczeg G. J., Henning T., Mohanty S., Lodato G., 2017b, Astrophysical Journal, 847, 31

Muley D., Fung J., van der Marel N., 2019, Astrophysical Journal, Letters to the Editor, 879, L2

Müller A., et al., 2018, Astronomy and Astrophysics, 617, L2

Mundy L. G., et al., 1996, Astrophysical Journal, Letters to the Editor, 464, L169

Muro-Arena G. A., et al., 2018, Astronomy and Astrophysics, 614, A24

Muro-Arena G. A., et al., 2020a, Astronomy and Astrophysics, 635, A121

Muro-Arena G. A., et al., 2020b, Astronomy and Astrophysics, 636, L4

Muto T., et al., 2012a, Astrophysical Journal, Letters to the Editor, 748, L22

Muto T., et al., 2012b, Astrophysical Journal, Letters to the Editor, 748, L22

Najita J. R., Bergin E. A., 2018, Astrophysical Journal, 864, 168

Nakagawa Y., Sekiya M., Hayashi C., 1986, Icarus, 67, 375

Narayan R., Igumenshchev I. V., Abramowicz M. A., 2003, , 55, L69

Natta A., Grinin V. P., Mannings V., 2000, in Mannings V., Boss A., Russell S., eds, Protostars and Planets IV. Arizona University Press, Tucson

Natta A., Testi L., Neri R., Shepherd D. S., Wilner D. J., 2004, A&A, 416, 179

Natta A., Testi L., Calvet N., Henning T., Waters R., Wilner D., 2007, in Reipurth B., Jewitt D., Keil K., eds, Protostars and Planets V. p. 767

Nealon R., Dipierro G., Alexander R., Martin R. G., Nixon C., 2018, Monthly Notices of the RAS, 481, 20

Nealon R., Pinte C., Alexander R., Mentiplay D., Dipierro G., 2019, Monthly Notices of the RAS, 484, 4951

Nealon R., Price D. J., Pinte C., 2020a, Monthly Notices of the RAS, 493, L143

Nealon R., Cuello N., Gonzalez J.-F., van der Plas G., Pinte C., Alexander R., Ménard F., Price D. J., 2020b, Monthly Notices of the RAS, 499, 3857

Nelson R. P., Papaloizou J. C. B., 2000, MNRAS, 315, 570

Nelson R. P., Papaloizou J. C. B., 2004, Monthly Notices of the RAS, 350, 849

Ober F., Wolf S., Uribe A. L., Klahr H. H., 2015, Astronomy and Astrophysics, 579, A105

Ogilvie G. I., Lubow S. H., 2002, Monthly Notices of the RAS, 330, 950

Ohta Y., et al., 2016, , 68, 53

Okuzumi S., Momose M., Sirono S.-i., Kobayashi H., Tanaka H., 2016, Astrophysical Journal, 821, 82

Ormel C. W., 2017, The Emerging Paradigm of Pebble Accretion. p. 197, doi:10.1007/978-3-319-60609-5˙7

Ormel C. W., Cuzzi J. N., 2007, Astronomy and Astrophysics, 466, 413

Paardekooper S.-J., 2012, Monthly Notices of the RAS, 421, 3286

Paardekooper S. J., Mellema G., 2004, Astronomy and Astrophysics, 425, L9

Paardekooper S.-J., Mellema G., 2006, Astronomy and Astrophysics, 453, 1129

Paardekooper S.-J., Baruteau C., Meru F., 2011, Monthly Notices of the RAS, 416, L65

Paczynski B., 1978, , 28, 91

Padgett D. L., Brandner W., Stapelfeldt K. R., Strom S. E., Terebey S., Koerner D., 1999, Astronomical Journal, 117, 1490

Paneque-Carreno T., Perez L., Benisty M., Hall C., Veronesi B., Lodato G. e. a., 2021,

Papaloizou J., Pringle J. E., 1977, Monthly Notices of the RAS, 181, 441

Pardo J., Cernicharo J., Serabyn E., 2002, in Vernin J., Benkhaldoun Z., Muñoz-Tuñón C., eds, Astronomical Society of the Pacific Conference Series Vol. 266, Astronomical Site Evaluation in the Visible and Radio Range. p. 188

Pascucci I., et al., 2006, Astrophysical Journal, 651, 1177

Pascucci I., et al., 2016, Astrophysical Journal, 831, 125

Pascucci I., et al., 2020, Astrophysical Journal, 903, 78

Perez S., et al., 2015a, Astrophysical Journal, 798, 85

Perez S., Dunhill A., Casassus S., Roman P., Szulágyi J., Flores C., Marino S., Montesinos M., 2015b, Astrophysical Journal, Letters to the Editor, 811, L5

Pérez L. M., et al., 2016, Science, 353, 1519

Pérez S., Casassus S., Benítez-Llambay P., 2018a, Monthly Notices of the RAS, 480, L12

Pérez L. M., et al., 2018b, Astrophysical Journal, 869, L50

Pérez S., Casassus S., Baruteau C., Dong R., Hales A., Cieza L., 2019, Astronomical Journal, 158, 15

Pérez S., et al., 2020, Astrophysical Journal, Letters to the Editor, 889, L24

Piétu V., Guilloteau S., Di Folco E., Dutrey A., Boehler Y., 2014, Astronomy and Astrophysics, 564, A95

Pinilla P., Birnstiel T., Ricci L., Dullemond C. P., Uribe A. L., Testi L., Natta A., 2012a, Astronomy and Astrophysics, 538, A114

Pinilla P., Benisty M., Birnstiel T., 2012b, Astronomy and Astrophysics, 545, A81

Pinilla P., et al., 2015, Astronomy and Astrophysics, 584, A16

Pinilla P., Flock M., Ovelar M. d. J., Birnstiel T., 2016, Astronomy and Astrophysics, 596, A81

Pinilla P., et al., 2017, Astrophysical Journal, 839, 99

Pinilla P., et al., 2018a, Astrophysical Journal, 859, 32

Pinilla P., et al., 2018b, Astrophysical Journal, 868, 85

Pinte C., Laibe G., 2014, Astronomy and Astrophysics, 565, A129

Pinte C., Ménard F., Duchêne G., Bastien P., 2006, Astronomy and Astrophysics, 459, 797

Pinte C., Harries T. J., Min M., Watson A. M., Dullemond C. P., Woitke P., Ménard F., Durán-Rojas M. C., 2009, Astronomy and Astrophysics, 498, 967

Pinte C., Dent W. R. F., Ménard F., Hales A., Hill T., Cortes P., de Gregorio-Monsalvo I., 2016, Astrophysical Journal, 816, 25

Pinte C., et al., 2018a, Astronomy and Astrophysics, 609, A47

Pinte C., et al., 2018b, Astrophysical Journal, Letters to the Editor, 860, L13

Pinte C., et al., 2019, Nature Astronomy, p. 419

Pinte C., et al., 2020, Astrophysical Journal, Letters to the Editor, 890, L9

Poblete P. P., Calcino J., Cuello N., Macías E., Ribas Á., Price D. J., Cuadra J., Pinte C., 2020, Monthly Notices of the RAS, 496, 2362

Pohl A., et al., 2017, Astrophysical Journal, 850, 52

Pollack J. B., Hollenbach D., Beckwith S., Simonelli D. P., Roush T., Fong W., 1994, Astrophysical Journal, 421, 615

Powell D., Murray-Clay R., Pérez L. M., Schlichting H. E., Rosenthal M., 2019, arXiv e-prints,

Price D., 2005, PhD Thesis. ArXiv Astrophysics e-prints, 0507472

Price D. J., 2007, Publications of the Astronomical Society of Australia, 24, 159

Price D. J., 2012a, Journal of Computational Physics, 231, 759

Price D. J., 2012b, in Capuzzo-Dolcetta R., Limongi M., Tornambè A., eds, Astronomical Society of the Pacific Conference Series Vol. 453, Advances in Computational Astrophysics: Methods, Tools, and Outcome. p. 249 (arXiv:1111.1259)

Price D. J., Laibe G., 2015, MNRAS, 451, 813

Price D. J., et al., 2018a, PASA, 35, e031

Price D. J., et al., 2018b, Monthly Notices of the RAS, 477, 1270

Principe D. A., et al., 2018, Monthly Notices of the RAS, 473, 879

Pringle J. E., 1981, ARA&A, 19, 137

Pringle J. E., King A., 2007, Astrophysical Flows

Qi C., Öberg K. I., Wilner D. J., 2013, Astrophysical Journal, 765, 34

Qi C., Öberg K. I., Andrews S. M., Wilner D. J., Bergin E. A., Hughes A. M., Hogherheijde M., D'Alessio P., 2015, Astrophysical Journal, 813, 128

Quénard D., Jiménez-Serra I., Viti S., Holdship J., Coutens A., 2018, Monthly Notices of the RAS, 474, 2796

Rabago I., Zhu Z., 2021, Monthly Notices of the RAS,

Rafikov R. R., 2002, Astrophysical Journal, 569, 997

Rafikov R., 2005, ApJ, 621, 69

Rafikov R. R., 2015, Astrophysical Journal, 804, 62

Rafikov R. R., 2017, Astrophysical Journal, 837, 163

Ragusa E., Lodato G., Price D. J., 2016, Monthly Notices of the RAS, 460, 1243

Ragusa E., Dipierro G., Lodato G., Laibe G., Price D. J., 2017, Monthly Notices of the RAS, 464, 1449

Ragusa E., Alexander R., Calcino J., Hirsh K., Price D. J., 2020, Monthly Notices of the RAS, 499, 3362

Regály Z., Juhász A., Sándor Z., Dullemond C. P., 2012, Monthly Notices of the RAS, 419, 1701

Reynolds N. K., et al., 2021, Astrophysical Journal, Letters to the Editor, 907, L10

Ricci L., Testi L., Natta A., Neri R., Cabrit S., Herczeg G. J., 2010, A&A, 512, A15

Rice W. K. M., Lodato G., Pringle J. E., Armitage P. J., Bonnell I. A., 2004, MNRAS, 355, 543

Rice W. K. M., Lodato G., Armitage P. J., 2005, MNRAS, 364, L56

Rice W. K. M., Lodato G., Pringle J. E., Armitage P. J., Bonnell I. A., 2006a, Monthly Notices of the RAS, 372, L9

Rice W. K. M., Armitage P. J., Wood K., Lodato G., 2006b, Monthly Notices of the RAS, 373, 1619

Rice W. K. M., Mayo J. H., Armitage P. J., 2010, MNRAS, 402, 1740

Rice W. K. M., Armitage P. J., Mamatsashvili G. R., Lodato G., Clarke C. J., 2011, Monthly Notices of the RAS, 418, 1356

Rice W. K. M., Forgan D. H., Armitage P. J., 2012, Monthly Notices of the RAS, 420, 1640

Rice W. K. M., Paardekooper S. J., Forgan D. H., Armitage P. J., 2014, Monthly Notices of the RAS, 438, 1593

Riols A., Lesur G., 2019, Astronomy and Astrophysics, 625, A108

Riols A., Lesur G., Menard F., 2020, Astronomy and Astrophysics, 639, A95

Rodriguez L. F., Canto J., Torrelles J. M., Gomez J. F., Anglada G., Ho P. T. P., 1994, Astrophysical Journal, Letters to the Editor, 427, L103

Rodriguez J. E., et al., 2018, Astrophysical Journal, 859, 150

Ros K., Johansen A., 2013, Astronomy and Astrophysics, 552, A137

Rosenfeld K. A., Andrews S. M., Wilner D. J., Kastner J. H., McClure M. K., 2013, Astrophysical Journal, 775, 136

Rosotti G. P., Juhasz A., Booth R. A., Clarke C. J., 2016, Monthly Notices of the RAS, 459, 2790

Rosotti G. P., Clarke C. J., Manara C. F., Facchini S., 2017, Monthly Notices of the RAS, 468, 1631

Rosotti G. P., Booth R. A., Tazzari M., Clarke C., Lodato G., Testi L., 2019a, Monthly Notices of the RAS, 486, L63

Rosotti G. P., Tazzari M., Booth R. A., Testi L., Lodato G., Clarke C., 2019b, Monthly Notices of the RAS, 486, 4829

Rosotti G. P., et al., 2020a, Monthly Notices of the RAS, 491, 1335

Rosotti G. P., Teague R., Dullemond C., Booth R. A., Clarke C. J., 2020b, Monthly Notices of the RAS, 495, 173

Rowther S., Meru F., 2020, Monthly Notices of the RAS, 496, 1598

Ruge J. P., Flock M., Wolf S., Dzyurkevich N., Fromang S., Henning T., Klahr H., Meheut H., 2016, Astronomy and Astrophysics, 590, A17

Rybicki G. B., Lightman A. P., 1979, Radiative Processes in Astrophysics. Wiley & sons, New York

Safronov V. S., 1969, Evoliutsiia doplanetnogo oblaka.

Safronov V. S., 1972, Evolution of the protoplanetary cloud and formation of the earth and planets.

Sanchis E., Picogna G., Ercolano B., Testi L., Rosotti G., 2020, Monthly Notices of the RAS, 492, 3440

Sanchis E., et al., 2021, arXiv e-prints, p. arXiv:2101.11307

Sargent A. I., Beckwith S., 1987, Astrophysical Journal, 323, 294

Scally A., Clarke C., 2001, Monthly Notices of the RAS, 325, 449

Scardoni C. E., Rosotti G. P., Lodato G., Clarke C. J., 2020, Monthly Notices of the RAS, 492, 1318

Segura-Cox D. M., et al., 2020, Nature, 586, 228
Sellek A. D., Booth R. A., Clarke C. J., 2020a, Monthly Notices of the RAS, 492, 1279
Sellek A. D., Booth R. A., Clarke C. J., 2020b, Monthly Notices of the RAS, 498, 2845
Shakura N. I., Sunyaev R. A., 1973, A&A, 24, 337
Sheehan P. D., Eisner J. A., 2018, Astrophysical Journal, 857, 18
Shu F. H., 1970, ApJ, 160, 99
Simon J. B., Armitage P. J., 2014, Astrophysical Journal, 784, 15
Sinclair C. A., Rosotti G. P., Juhasz A., Clarke C. J., 2020, Monthly Notices of the RAS, 493, 3535
Smoluchowski M. V., 1916, Zeitschrift fur Physik, 17, 557
Somigliana A., Toci C., Lodato G., Rosotti G., Manara C. F., 2020, Monthly Notices of the RAS, 492, 1120
Spitzer Lyman J., 1942, Astrophysical Journal, 95, 329
Springel V., Hernquist L., 2002, Monthly Notices of the RAS, 333, 649
Stammler S. M., Birnstiel T., Panić O., Dullemond C. P., Dominik C., 2017, Astronomy and Astrophysics, 600, A140
Stepinski T. F., Valageas P., 1996, Astronomy and Astrophysics, 309, 301
Stolker T., et al., 2016, Astronomy and Astrophysics, 595, A113
Sturm J. A., Rosotti G. P., Dominik C., 2020, Astronomy and Astrophysics, 643, A92
Suriano S., Li Z.-Y., Krasnopolsky R., Shang H., 2018, in American Astronomical Society Meeting Abstracts #231. p. 330.03
Syer D., Clarke C. J., 1995, Monthly Notices of the RAS, 277, 758
Szulágyi J., Morbidelli A., Crida A., Masset F., 2014, Astrophysical Journal, 782, 65
Takahashi S. Z., Inutsuka S.-i., 2016, Astronomical Journal, 152, 184
Takeuchi T., Lin D. N. C., 2002, Astrophysical Journal, 581, 1344
Takeuchi T., Lin D. N. C., 2005, Astrophysical Journal, 623, 482
Tanaka H., Inaba S., Nakazawa K., 1996, Icarus, 123, 450
Tanaka H., Takeuchi T., Ward W. R., 2002, Astrophysical Journal, 565, 1257
Tanaka H., Himeno Y., Ida S., 2005, Astrophysical Journal, 625, 414
Tang Y. W., Guilloteau S., Piétu V., Dutrey A., Ohashi N., Ho P. T. P., 2012, Astronomy and Astrophysics, 547, A84
Tang Y.-W., et al., 2017, Astrophysical Journal, 840, 32
Tazzari M., et al., 2017, Astronomy and Astrophysics, 606, A88
Tazzari M., et al., 2020a, arXiv e-prints, p. arXiv:2010.02248
Tazzari M., Clarke C. J., Testi L., Williams J. P., Facchini S., Manara C. F., Natta A., Rosotti G., 2020b, arXiv e-prints, p. arXiv:2010.02249
Teague R., Bae J., Bergin E. A., Birnstiel T., Foreman-Mackey D., 2018, Astrophysical Journal, Letters to the Editor, 860, L12
Teague R., Bae J., Bergin E. A., 2019a, Nature, 574, 378

Teague R., Bae J., Huang J., Bergin E. A., 2019b, Astrophysical Journal, Letters to the Editor, 884, L56

Terebey S., Shu F. H., Cassen P., 1984, Astrophysical Journal, 286, 529

Testi L., Natta A., Shepherd D. S., Wilner D. J., 2003, Astronomy and Astrophysics, 403, 323

Testi L., et al., 2014, Protostars and Planets VI, pp 339–361

Thi W.-F., et al., 2010, Astronomy and Astrophysics, 518, L125

Tielens A. G. G. M., Tokunaga A. T., Geballe T. R., Baas F., 1991, Astrophysical Journal, 381, 181

Tobin J. J., et al., 2019, Astrophysical Journal, 886, 6

Tobin J. J., et al., 2020, Astrophysical Journal, 890, 130

Toci C., Galli D., 2015, Monthly Notices of the RAS, 446, 2110

Toci C., Lodato G., Christiaens V., Fedele D., Pinte C., Price D. J., Testi L., 2020a, Monthly Notices of the RAS, 499, 2015

Toci C., Lodato G., Fedele D., Testi L., Pinte C., 2020b, Astrophysical Journal, Letters to the Editor, 888, L4

Toomre A., 1964, Astrophysical Journal, 139, 1217

Toomre A., 1969, ApJ, 158, 899

Trapman L., Miotello A., Kama M., van Dishoeck E. F., Bruderer S., 2017, Astronomy and Astrophysics, 605, A69

Trapman L., Facchini S., Hogerheijde M. R., van Dishoeck E. F., Bruderer S., 2019, Astronomy and Astrophysics, 629, A79

Trapman L., Ansdell M., Hogerheijde M. R., Facchini S., Manara C. F., Miotello A., Williams J. P., Bruderer S., 2020, Astronomy and Astrophysics, 638, A38

Tricco T. S., Price D. J., Laibe G., 2017, Monthly Notices of the RAS, 471, L52

Tripathi A., Andrews S. M., Birnstiel T., Wilner D. J., 2017, Astrophysical Journal, 845, 44

Tripathi A., et al., 2018, Astrophysical Journal, 861, 64

Turner N. J., Fromang S., Gammie C., Klahr H., Lesur G., Wardle M., Bai X. N., 2014, in Beuther H., Klessen R. S., Dullemond C. P., Henning T., eds, Protostars and Planets VI. p. 411 (arXiv:1401.7306), doi:10.2458/azu˙uapress˙9780816531240-ch018

Tychoniec Ł., et al., 2020, Astronomy and Astrophysics, 640, A19

Ubeira Gabellini M. G., et al., 2019, Monthly Notices of the RAS, 486, 4638

Ubeira-Gabellini M. G., Christiaens V., Lodato G., Ancker M. v. d., Fedele D., Manara C. F., Price D. J., 2020, Astrophysical Journal, Letters to the Editor, 890, L8

Uyama T., et al., 2018, Astronomical Journal, 156, 63

Uyama T., et al., 2020, Astronomical Journal, 159, 118

Varnière P., Tagger M., 2006, Astronomy and Astrophysics, 446, L13

Varnière P., Quillen A. C., Frank A., 2004, Astrophysical Journal, 612, 1152

Veronesi B., Lodato G., Dipierro G., Ragusa E., Hall C., Price D. J., 2019, Monthly Notices of the RAS, 489, 3758

Veronesi B., et al., 2020, Monthly Notices of the RAS, 495, 1913
Veronesi B., Paneque-Carreno T., Lodato G., Perez L., Testi L., Bertin G., Hall C., 2021,
Vigan A., et al., 2020, arXiv e-prints, p. arXiv:2007.06573
Villenave M., et al., 2020, Astronomy and Astrophysics, 642, A164
Vioque M., Oudmaijer R. D., Baines D., Mendigutía I., Pérez-Martínez R., 2018, Astronomy and Astrophysics, 620, A128
Visser R., van Dishoeck E. F., Black J. H., 2009, Astronomy and Astrophysics, 503, 323
Vorobyov E. I., Basu S., 2005, ApJ, 633, L137
Vorobyov E. I., Basu S., 2006, ApJ, 650, 956
Wagner K., et al., 2018, Astrophysical Journal, 854, 130
Wagner K., Stone J. M., Spalding E., Apai D., Dong R., Ertel S., Leisenring J., Webster R., 2019, Astrophysical Journal, 882, 20
Walker M. F., 1956, Astrophysical Journal, Supplement, 2, 365
Ward W. R., 1997, Icarus, 126, 261
Waters L. B. F. M., Waelkens C., 1998, ARA&A, 36, 233
Weidenschilling S. J., 1977, Monthly Notices of the RAS, 180, 57
Weidenschilling S. J., 1980, Icarus, 44, 172
Weinberger A. J., Anglada-Escudé G., Boss A. P., 2013, Astrophysical Journal, 762, 118
Whipple F. L., 1972, in Elvius A., ed., From Plasma to Planets. Wiley, London
Williams J. P., Best W. M. J., 2014, Astrophysical Journal, 788, 59
Williams J. P., Cieza L. A., 2011, Annual Review of Astronomy and Astrophysics, 49, 67
Wilner D. J., Ho P. T. P., Rodriguez L. F., 1996, Astrophysical Journal, Letters to the Editor, 470, L117
Windmark F., Birnstiel T., Güttler C., Blum J., Dullemond C. P., Henning T., 2012, Astronomy and Astrophysics, 540, A73
Winn J. N., Fabrycky D. C., 2015, Annual Review of Astronomy and Astrophysics, 53, 409
Winter A. J., Clarke C. J., Rosotti G., Ih J., Facchini S., Haworth T. J., 2018a, Monthly Notices of the RAS, 478, 2700
Winter A. J., Booth R. A., Clarke C. J., 2018b, Monthly Notices of the RAS, 479, 5522
Winter A. J., Ansdell M., Haworth T. J., Kruijssen J. M. D., 2020, Monthly Notices of the RAS, 497, L40
Woitke P., et al., 2016, Astronomy and Astrophysics, 586, A103
Wolcott-Green J., Haiman Z., Bryan G. L., 2011, Monthly Notices of the RAS, 418, 838
Wolf S., Klahr H., 2002, Astrophysical Journal, Letters to the Editor, 578, L79
Wölfer L., et al., 2020, arXiv e-prints, p. arXiv:2012.04680
Wurster J., 2021, arXiv e-prints, p. arXiv:2101.04129

Wyatt M. C., 2018, Debris Disks: Probing Planet Formation. p. 146, doi:10.1007/978-3-319-55333-7˙146

Wyatt M. C., Panić O., Kennedy G. M., Matrà L., 2015, Astrophysics and Space Science, 357, 103

Yorke H. W., Bodenheimer P., Laughlin G., 1993, Astrophysical Journal, 411, 274

Youdin A. N., 2010, in Montmerle T., Ehrenreich D., Lagrange A. M., eds, EAS Publications Series Vol. 41, EAS Publications Series. pp 187–207 (arXiv:0807.1114), doi:10.1051/eas/1041016

Youdin A. N., Goodman J., 2005, Astrophysical Journal, 620, 459

Youdin A. N., Lithwick Y., 2007, Icarus, 192, 588

Youdin A. N., Shu F. H., 2002, Astrophysical Journal, 580, 494

Young M. D., Clarke C. J., 2015, Monthly Notices of the RAS, 451, 3987

Yu C., Li H., Li S., Lubow S. H., Lin D. N. C., 2010, Astrophysical Journal, 712, 198

Zhang K., Isella A., Carpenter J. M., Blake G. A., 2014, Astrophysical Journal, 791, 42

Zhang K., Blake G. A., Bergin E. A., 2015, Astrophysical Journal, Letters to the Editor, 806, L7

Zhang S., et al., 2018, Astrophysical Journal, Letters to the Editor, 869, L47

Zhu Z., Nelson R. P., Hartmann L., Espaillat C., Calvet N., 2011, Astrophysical Journal, 729, 47

Zhu Z., Hartmann L., Nelson R. P., Gammie C. F., 2012a, Astrophysical Journal, 746, 110

Zhu Z., Nelson R. P., Dong R., Espaillat C., Hartmann L., 2012b, Astrophysical Journal, 755, 6

Zhu Z., Stone J. M., Rafikov R. R., Bai X.-n., 2014, Astrophysical Journal, 785, 122

Zhu Z., Dong R., Stone J. M., Rafikov R. R., 2015, preprint, (arXiv:1507.03599)

de Boer J., et al., 2016, Astronomy and Astrophysics, 595, A114

de Boer J., et al., 2020, arXiv e-prints, p. arXiv:2010.12202

de Gregorio-Monsalvo I., et al., 2013, Astronomy and Astrophysics, 557, A133

van Boekel R., et al., 2016, preprint, (arXiv:1610.08939)

van Boekel R., et al., 2017, Astrophysical Journal, 837, 132

van Dishoeck E. F., Black J. H., 1988, Astrophysical Journal, 334, 771

van Holstein R. G., et al., 2021, arXiv e-prints, p. arXiv:2101.04033

van Terwisga S. E., et al., 2018, Astronomy and Astrophysics, 616, A88

van Zadelhoff G. J., van Dishoeck E. F., Thi W. F., Blake G. A., 2001, Astronomy and Astrophysics, 377, 566

van der Marel N., et al., 2013, Science, 340, 1199

van der Marel N., van Dishoeck E. F., Bruderer S., Pérez L., Isella A., 2015, Astronomy and Astrophysics, 579, A106

van der Marel N., van Dishoeck E. F., Bruderer S., Andrews S. M., Pontoppidan K. M., Herczeg G. J., van Kempen T., Miotello A., 2016a, Astronomy and

Astrophysics, 585, A58
van der Marel N., Cazzoletti P., Pinilla P., Garufi A., 2016b, Astrophysical Journal, 832, 178
van der Marel N., Cazzoletti P., Pinilla P., Garufi A., 2016c, Astrophysical Journal, 832, 178
van der Marel N., et al., 2018a, Astrophysical Journal, 854, 177
van der Marel N., Williams J. P., Bruderer S., 2018b, Astrophysical Journal, Letters to the Editor, 867, L14
van der Marel N., Dong R., di Francesco J., Williams J. P., Tobin J., 2019, Astrophysical Journal, 872, 112
van der Marel N., et al., 2020, arXiv e-prints, p. arXiv:2010.10568
van der Plas G., et al., 2017, Astronomy and Astrophysics, 597, A32
van der Plas G., et al., 2019, Astronomy and Astrophysics, 624, A33

List of Publications

As of April 2020

Refereed publications

1. T. Paneque-Carreño, L. M. Pérez, M. Benisty, C. Hall, **B. Veronesi**, G. Lodato et al.: "Spiral arms and a massive dust disk with non-Keplerian kinematics: Possible evidence for gravitational instability in Elias 2-27", ApJL paper, in prep., 2020.

2. C. Hall, R. Dong, R. Teague, J. Terry, C. Pinte, T. Paneque-Carreño, **B. Veronesi**, R. D. Alexander, G. Lodato: "Predicting the kinematic evidence of gravitational instability", ApJL paper, in press, 2020.

3. **B. Veronesi**, E. Ragusa, G. Lodato, H. Aly, C. Pinte, D. J. Price, F. Long, G. Herczeg and V. Christiaens: "Is the gap in the DS Tau disc hiding a planet?", MNRAS paper, publ., 2020, 495, 1913-1926.

4. **B. Veronesi**, G. Lodato, G. Dipierro, E. Ragusa, C. Hall, D. J. Price: "Multi-wavelength observations of protoplanetary discs as a proxy for the gas disc mass", MNRAS paper, publ., 2019, 489, 3758-3768.

5. G. Ballabio, G. Dipierro, **B. Veronesi**, G. Lodato, M. Hutchison, G. Laibe, D. J. Price: "Enforcing dust mass conservation in 3D simulations of tightly-coupled grains with the PHANTOM SPH code", MNRAS paper, publ., 2018, 477, 2766-2771.

Publications under review

1. **B. Veronesi**, et al.: "A dynamical mass estimate for Elias 2-27", ApJL paper, submitted, 2021.

Publications in preparation Publications in conference proceedings

1. G. Lodato, **B. Veronesi**, M. G. Ubeira Gabellini, E. Ragusa, A. Franchini, G. Dipierro: "Planet formation in the ALMA era", Toward a Science Campus in Milan: A Snapshot of Current Research at the Physics Department Aldo Pontremoli, Springer International Publishing, 2018.

Acknowledgements

Footprints and waves on a beach along the Great Ocean Road (Australia 2019).

Below, I report for completeness the formal acknowledgements sections of the individual projects presented in this thesis.

Chapter 6: We wish to thank the referee for an insightful report of the manuscript. We thank Nienke van der Marel for fruitful discussions that gave new perspective to this work. We also want to thank Anna Miotello for enlightening discussion about gas measurements from observations. GL and BV have

received funding from the European Union's Horizon 2020 research and innovation programme under the Marie Skłodowska-Curie grant agreement No 823823 (RISE DUSTBUSTERS project). GD and ER acknowledge financial support from the European Research Council (ERC) under the European Union's Horizon 2020 research and innovation programme (grant agreement No 681601). CH is a Winton Fellow, and this research has been supported by Winton Philanthropies/The David and Claudia Harding Foundation. DP acknowledges funding from the Australian Research Council via FT130100034 and DP180104235. For our work we adopted different codes and software. We used PHANTOM (Price et al. 2018a) for the hydrodynamic simulations and RADMC-3D (Dullemond et al. 2012) for the radiative trasnfer calculations. We utilized DIANA OPACITYTOOL (Woitke et al. 2016) for the dust opacities coefficients and CASA (McMullin et al. 2007) for the simulations of ALMA observations. We used SPLASH (Price 2007) for rendered images of our simulated hydrodynamic systems, while the remaining figures have been generated using the PYTHON-based MATPLOTLIB package (Hunter 2007).

Chapter 7: We thank the referee Ruobing Dong for an insightful report of the manuscript. We thank the SPHgroup at the Monash University in Melbourne for fruitful discussions that improved the manuscript. GL and BV have received funding from the European Union's Horizon 2020 research and innovation programme under the Marie Skłodowska-Curie grant agreement No 823823 (RISE DUSTBUSTERS project). ER acknowledges financial support from the European Research Council (ERC) under the European Union's Horizon 2020 research and innovation programme (grant agreement No 681601). DP, CP and VC acknowledge funding from the Australian Research Council via FT130100034 and DP180104235. For this project we used OzStar, funded by Swinburne University of Technology and the Australian government. We used PHANTOM (Price et al. 2018a) for the hydrodynamic simulations and MCFOST (Pinte et al. 2006, 2009) for the radiative trasnfer calculations. We used SPLASH (Price 2007) for rendered images of our simulated hydrodynamic systems, the PYMCFOST tool provided by Christophe Pinte for the rendering of the channel maps, while the remaining figures have been generated using the PYTHON-based MATPLOTLIB package (Hunter 2007).

Chapter 8: The authors want to thank the referee for constructive comments that improved this manuscript. BV thanks Guglielmo Mastroserio for fruitful discussions that improved the quality of the coding. This paper makes use of the following ALMA data: #2013.1.00498.S, #2016.1.00606.S and #2017.1.00069.S. ALMA is a partnership of ESO (representing its member states), NSF (USA), and NINS (Japan), together with NRC (Canada), NSC and ASIAA (Taiwan), and KASI (Republic of Korea), in cooperation with the Republic of Chile. The Joint ALMA Observatory is operated by ESO, AUI/NRAO, and NAOJ. This work has received funding from the European Union's Horizon 2020 research and innovation programme under the Marie Skłodowska-Curie grant agreement No 823823 (RISE DUSTBUSTERS project). L.M.P. acknowledges support from ANID project Basal AFB-170002 and from ANID FONDECYT Iniciación project #11181068. We used the EMCEE algorithm (Foreman-Mackey et al. 2013), the CORNER package Foreman-Mackey (2016) to produce corner plots and PYTHON-

based MATPLOTLIB package (Hunter 2007) for all the other figures.

Appendix C: We are grateful to an anonymous referee for constructive suggestions that improved our paper. The authors would like to thank Richard Alexander and Chris Nixon for fruitful discussions. This project has received funding from the European Research Council (ERC) under the European Union's Horizon 2020 research and innovation program (grant agreement No 681601). This research used the ALICE High Performance Computing Facility and the DiRAC Complexity system, funded by BIS National E-Infrastructure capital grant ST/K000373/1 and STFC DiRAC Operations grant ST/K0003259/1. We used SPLASH (Price 2007).

Finally, and more personally, I would like to thank all the people I have met and who have accompanied me during this three-year (and a bit) adventure called PhD. These people have contributed to my personal and scientific growth, and have brought me to the person I am now.

First of all, I would like to thank my supervisor, Prof. Giuseppe Lodato, for always pushing me to do better, and for encouraging me when I felt discouraged and demotivated. Thank you for the trust you have placed in my abilities, also sometimes leaving me without boundaries and deadlines, at the end all this strengthened me both scientifically and on a more personal level. Thank you for paving me the way in different collaborations, and for allowing me to travel, from the conference in Arizona, to Australia. For being critical when needed, and for helping me to build my scientific and more "investigative" side. Also, it has been a pleasure to exchange music and movies opinions with you during these three years.

I would also like to thank Prof. Daniel Price, my supervisor of the down-under land. Thank you for the incredible hospitality you gave us during the 3+2 months in Melbourne. Thank you for the home made pizza, for the day out with the strawberry picking and swimming in Melbourne Bay. Scientifically, thank you for having often overturned the results of my work, in the end it was always instructive and always helped to improve the quality of my work and my critical thinking. On a personal level, thank you for your discrete but friendly presence during the last period in Australia at the beginning of the pandemic. And thank you for the incredible enthusiasm that you always manage to transmit, it has contributed in a significant way to improve my self-confidence and the attitude with which I present my work... I still keep the email of congratulations for my first "push" of PHANTOM!

I want to thank Dr. Leonardo Testi and Dr. Carlo Manara, who refereed this thesis, for their valuable comments and suggestions that improved the quality of the manuscript. I want also to thank Prof. Richard Alexander and Prof. Philip Armitage for accepting to be the examiners of my thesis defense.

I thank my mentors, Gianni and Enrico. You have always been a "guiding light" to look up to, an example to (at least) try to emulate, and you have always enriched me scientifically and on a more human level. I am grateful to be able to consider you not only colleagues, but also friends.

I would like to thank all those I had the opportunity to meet during conferences or during stays abroad. In particular, I thank some of my collaborators with whom I worked in Melbourne, Christophe and Valentin. Thank you also for the coffees and lunches together, and thank you for the scientific contribution you have brought to my work. Thank you Val for being a fantastic travelling companion! I had so much fun exploring Australia together. I thank Cass, Teresa and Prof. Laura Pérez with whom I have collaborated, and hope to collaborate in the future. I also thank all my other co-authors in the projects presented in this thesis: your contribution has always been valuable and improved a lot the quality of my work. Thanks to Maxime and Arnaud, who were great mates during my second stay at Monash, on se rencontre à Lyon! I would also like to thank Daniel, the PYTHON handyman. Thank you for the Australian welcome, and for making me feel at home with the chats about life, university, and much more. Thank you especially for the moral and practical support you gave me in February, it meant a lot. I'm glad to have met you and I hope that the "time-space distance" will allow us to chat every now and then! Thank you Nico, for the book exchanges, for having brought me back to French (even before I applied in Lyon), and for a friendship started in Australia, which I hope will continue.

I am grateful to the colleagues who have crossed my way in the office of Via Celoria 16. From Ale and Hossam in the early days, to the new generations of PhD students and postdocs. Claudia, with her genuine Tuscan character, her overwhelming friendship and wholehearted support, Margi, with her incredible strength and willpower that has inspired me in this last period, and Marti, the youngest of the group, who is now the eldest and who, although she doesn't believe it, has all the potential to become a brilliant astrophysicist. Also, Margi and Marti you've bean great flatmate in the down-under, and I like to remember our little (mouse) host too! Thanks to the Biscottyny people, you have cheered up many lunches and coffee breaks, and made the university a more pleasant and friendly place. A big thanks also to Cristiano and (again) Claudia (and Gianni) for scientific discussion in these lasts months, and for a careful proofreading of some chapters of this thesis. Cristiano, also thanks for the "artistic" support in developing the cover and the photographies choice.

Molte sono le persone che vorrei ringraziare anche al di fuori dell'ambito lavorativo che hanno lasciato un segno nella mia persona in questi tre anni. Gli amici di una vita, che seppur le strade sono diverse, si continua a camminare insieme: Vero e Anna, grazie soprattutto per la pazienza che avete nei miei periodi più impegnati. Grazie a Chiara, Michi e Gullo (e Deneb), i miei lemmini preferiti. Soprattutto per questo ultimo anno in cui siamo stati più vicini "spazialmente", per le passeggiate nel vicinato, le chiacchierate e per esserci sempre! Ringrazio anche Chiara M., Maria, Ele, Lori ed Ele, Gabri, Celo and Fede (e molti altri) perché in tempi e modi diversi mi avete accompagnato in questo viaggio, bello, intenso e faticoso. Ringrazio la Scuola di Italiano di Villapallavicini, che mi ha accompagnato fino all'anno scorso, e tutti i volontari e gli studenti che qui ho conosciuto. Siete stati una presenza calorosa e bella, e ricordo tutti con affetto e fraterna amicizia. In futuro, spero di tornare fra quei banchi affollati di tante storie e speranze.

Un grande grazie alla mia famiglia. Un grazie ai miei genitori, per avermi sempre sostenuto, anche quando ero dall'altra parte del mondo. Mamma, grazie per avermi trasmesso la passione per l'astrofisica, che mi ha portato fino a qui, e per l'arte, che in quest ultimo anno ho deciso di rispolverare! Grazie per avermi insegnato a non fermarmi alla superficie, ma a scavare sempre fino al nocciolo delle cose. Papà, grazie soprattutto per avermi trasmesso la tua passione per la fotografia, e per averla nutrita. Mi ha permesso di vedere la realtà in un modo diverso e di cogliere sottigliezze e bellezza anche nella quotidianità (come quella estrema di un lockdown in solitaria!). Franci, grazie perché in questi ultimi anni ci siamo riavvicinate tanto, fra telefonate, consigli culinari, aggiornamenti sulle nostre piante e vite, e grazie al piccolo Sam, che ha portato un po' di simpatico scompiglio in più! Questo periodo, strano e difficile per tutti, penso ci abbia avvicinato ancor di più come famiglia. Un grazie a te nonna, che hai sofferto l'isolamento e la lontananza da noi nipoti, e che però nonostante tutto ancora ti ricordi della mia tesi triennale e di quei buchi neri che tanto ti avevano impressionata.

Grazie anche a Daniele, Luisa, Giorgio e Martina, per la vicinanza e per i bei momenti trascorsi insieme. Grazie a Ire, Gherard e a Miriamina per l'ospitalità viennese e per le chiamate alle 7 del mattino! Un grazie a Zero che nonostante gli acciacchi e l'età, non molla e rimarrà il nostro preferito!

Un grazie enorme a te, che mi hai sempre sostenuto e spronato (soprattutto in questi ultimi mesi), perché insieme siamo cresciuti in questi anni, e spero che ancora continueremo a crescere. Abbiamo iniziato ad abitare insieme una casa, che ora lasceremo, ma che sarà sempre la nostra prima casa. Ora una nuova avventura ci attende, fra Lione e Pescara, e poi chissà dove. On y va!

E infine, Tilla, piccola teppista a macchie e dispensatrice di fusa, grazie.